



RETURNING MATERIALS:

Place in book drop to
remove this checkout from
your record. FINES will
be charged if book is
returned after the date
stamped below.

--	--	--

**EXPERIMENTAL AND THEORETICAL STUDIES OF
DUAL LASER IONIZATION (DLI) IN FLAMES**

Volume I

by

Yen-Yuan James Wu

A DISSERTATION

**Submitted to
Michigan State University
in partial fulfillment of the requirements
for the degree of**

DOCTOR OF PHILOSOPHY

Department of Chemistry

1988

5676022

ABSTRACT

EXPERIMENTAL AND THEORETICAL STUDIES OF DUAL LASER IONIZATION (DLI) IN FLAMES

by

Yen-Yuan James Wu

Dual or Direct Laser Ionization (DLI) spectroscopy is a recently developed flame spectrometric technique for trace element detection. In the DLI experiment the analyte is first resonantly excited by a dye laser, then is promoted to the ionization continuum by a separate nitrogen laser, and the subsequent ionization signal is collected by a set of biased probes. In this study, DLI was used to simultaneously measure the mobility coefficients and the diffusion coefficients of various ions in laminar-flow $\text{H}_2\text{-O}_2\text{-Ar}$ flames, and hence the temperature of flames can be calculated by the Einstein relation.

Recent studies in our laboratory have shown that the time-resolved DLI signal consists two temporal components, i.e. a short and strong electron signal followed some microseconds later by a longer and weaker ion signal. Our studies also have shown that the time-resolved DLI signals can be modeled effectively by one-dimensional Fokker-Planck equations with various drift functions. Through proper non-

linear least-square curve-fitting procedures, details of ion transport processes under the influence of an electric field in flames can be revealed. It is particularly of interest that this study shows a relationship between the diffusion coefficient of cations and the bias-voltage applied to the probes. Theoretical treatment of this phenomenon indicates that it is mainly due to ion-ion repulsion. A computer simulation has partially confirmed this argument. The diffusion coefficients and mobility coefficients of different ions in various flame compositions obtained agree reasonably with one another and also with the values reported by other workers. The vertical temperature profile of stoichiometric and fuel-rich $\text{H}_2\text{-O}_2\text{-Ar}$ flames were measured with various ions, such as sodium, lithium, calcium, and strontium. The results are in agreement with one another and literature values.

To Mom and Dad

ACKNOWLEDGMENTS

I would like to express my deepest appreciation to my advisors, Dr. Stanley R. Crouch, Dr. George E. Leroi, and Dr. Paul M. Hunt for their intelligent advice and helpful discussions over all the aspects of the thesis. Without their joint direction and patience, this thesis would not have been accomplished.

Simple acknowledgment of Dr. Paul M. M. Hunter and Professor James L. Dye for their guidance and support in everything is absolutely insufficient here. It is quite obvious to me that without Dr. Hunter's encouragements, I will never chose teaching as my profession. Big thanks should go to Dr. Thomas V. Atkinson for his help in computer techniques, too. I am also deeply grateful for Dr. Paul D. Cratin and Mrs. Barb Cratin. You both are great.

I am indebted in John D. Stanley for his valuable helps in my research. Special thanks should go to my guardian angel Dr. Ms. Helen Archontaki (I spelled it right this time), and my old roommates Dr. Tony Oertling, and Dr. Nelson Herron.

The help and patience of Ms. Beverly Jean Bramer in the Library, Ron Haas and Scott Sanderson in the Electronics shop, Helen Rushing in the General Chemistry Office, and a lot other people who have helped.

In my years at MSU I have been lucky enough to meet and work with a number of people who have become my close friends. I doubt a better group could be found anywhere. Thanks to King, Charlie, Keith, Pat, Marguerite, Bob, Kim, Peter, and Max.

Finally, I would like to thank my Chinese friends, especially I-Jy and Shin-Chu. Without that shortly existing Three-Company Co., I would have been starving to death long time ago.

TABLE OF CONTENTS

Chapter	Page
LIST OF TABLES	x
LIST OF FIGURES	xii
I INTRODUCTION	1
A. Overview	1
B. Review and Historical	5
1. Ion mobilities	5
2. Diffusion Coefficient	13
3. Dual Laser Ionization	18
4. The Fokker-Planck Equation	27
C. Overview of the Dissertation	36
References	40
II EXPERIMENTAL	49
A. Overview	49
B. Laser System	51
C. Flame Cell	60
D. Signal Detection	62
E. Boxcar Integrator	68
F. Microcomputer and Boxcar Integrator Interface	74

Chapter		Page
II	References	79
III	DUAL LASER IONIZATION SIGNALS	80
	A. Introduction	80
	B. Theoretical	83
	1. Ion Mobilities	83
	2. Electric Fields in Flames	84
	3. Behavior of Charged Particles in Flames	92
	C. Experimental	95
	1. Apparatus	95
	2. Reagents	96
	D. Results and Discussions	97
	1. Temporal Behavior of DLI Signals	97
	2. Electron Signals	117
	3. Charge Separation Process	124
	4. Ion signals	130
	5. Shape of the Electric Field	132
	E. Conclusion	137
	References	139
IV	THE FOKKER-PLANCK EQUATION	141
	A. Introduction	141
	B. Derivation of the Fokker-Planck equation ..	144
	C. Analytical Solutions	147
	1. Steady-State Approximations	147
	2. Path Integral Formalism	149
	3. Constant Drift Function	151

Chapter		Page
IV	C. 4. Practical Modification	153
	5. Linear Drift Function	158
	6. Piece-wise Linear Drift Function	158
	D. Further Treatments	161
	1. Introduction	161
	2. Convolution Method	163
	E. Numerical Solutions	165
	1. Introduction	165
	2. Computer Algorithm	165
	F. Conclusion	169
	References	171
V	FLAME TEMPERATURE MEASUREMENT	173
	A. Introduction	173
	B. Theoretical	174
	C. Experimental	178
	1. Apparatus	178
	2. Reagents	180
	3. Experimental Conditions	181
	D. Data Treatment	182
	E. Results	185
	F. Discussion	191
	G. Conclusion	199
	References	205
VI	SIMULATION STUDIES OF MUTUAL REPULSION OF IONS	201
	A. INTRODUCTION	207

Chapter		Page
VI	B. THE FOKKER-PLANCK EQUATION	209
	C. ALGORITHM FOR DIFFUSION	210
	1. Introduction	210
	2. Basic Definitions	210
	3. Conventional methods	213
	4. Development of a New Algorithm	221
	D. DRIFT FUNCTION	232
	1. Introduction	232
	2. Basic Definitions	237
	3. Conventional Algorithm	238
	4. Development of a New Algorithm	241
	E. THE SIMULATION PROGRAM	243
	1. Introduction	243
	2. Description of the Simulation Program	245
	F. RESULTS AND DISCUSSION	246
	G. CONCLUSIONS	251
	References	252
VII	FLAME TEMPERATURE PROFILES	254
	A. INTRODUCTION	254
	B. EXPERIMENTAL	255
	1. Flame Cell	255
	2. Apparatus	256
	3. Reagents	257
	C. RESULTS OF VERTICAL FLAME TEMPERATURE PROFILE MEASUREMENTS	258

Chapter		Page
VII	C. 1. Non-Stoichiometric Hydrogen-Oxygen- Argon Flame	259
	2. Stoichiometric Hydrogen-Oxygen- Argon Flame	267
	D. DISCUSSION	272
	E. CONCLUSIONS	283
	References	286
VIII	CONCLUSIONS AND FUTURE PROSPECTS	288
	A. REVIEW AND CONCLUSIONS	288
	1. Dual Laser Ionization Signals	288
	2. The Fokker-Planck Equation	290
	B. FUTURE PROSPECTS	291
	1. DLI Techniques	291
	2. Fokker-Planck Formalism	293
	References	296
	APPENDIX A - FOKKER-PLANCK EQUATION NUMERICAL SOLVER ..	297
	APPENDIX B - CURVE FITTING PROGRAM WITH MINPACK-1	331
	APPENDIX C - SIMULATION PROGRAM	347
	APPENDIX D - APPLICATIONS OF THE FOKKER-PLANCK EQUATION TO HPLC DATA	362

LIST OF TABLES

Table	Page
2-1. Specifications of the Nitrogen Laser	54
2-2. Characteristics of the Dye Laser	57
5-1. A Comparison of Mobility Coefficients for Sodium Cations in $H_2/O_2/Ar$ Flames	188
5-2. A Comparison of Diffusion Coefficients for Sodium Cations in $H_2/O_2/Ar$ Flames	190
5-3. A Comparison of $H_2/O_2/Ar$ Flame Temperatures	192
6-1. Parameters Chosen for Simulation of Diffusion	217
7-1. Non-stoichiometric H_2-O_2-Ar Flame Temperature Profile Measurements with Sodium Ions	260
7-2. Non-stoichiometric H_2-O_2-Ar Flame Temperature Profile Measurements with Lithium Ions	263
7-3. Non-stoichiometric H_2-O_2-Ar Flame Temperature Profile Measurements with Calcium Ions	265
7-4. Non-stoichiometric H_2-O_2-Ar Flame Temperature Profile Measurements with Various Ions	268
7-5. Stoichiometric H_2-O_2-Ar Flame Temperature Profile Measurements with Sodium Ions	270

Table	Page
7-6. Stoichiometric H_2-O_2 -Ar Flame Temperature Profile Measurements with Strontium Ions	273
7-7. Stoichiometric H_2-O_2 -Ar Flame Temperature Profile Measurements with Various Ions	275
7-8. A Comparison of Diffusion and Mobility Coefficients of Sodium in Various Flames	278
7-9. A Comparison of Diffusion and Mobility Coefficients of Lithium in Various Flames	279
7-10. A Comparison of Diffusion and Mobility Coefficients of Calcium in Various Flames	281
7-11. A Comparison of Diffusion and Mobility Coefficients of Strontium in Various Flames ...	282
7-12. A Comparison of H_2-O_2 -Ar Flame Temperatures	284

LIST OF FIGURES

Figure	Page
2-1. Block diagram of dual laser ionization experimental set-up.	50
2-2. Simplified schematic diagram of the dual laser system. B, boxcar; DL, dye laser; F, flame; L, lens; M, mirror; O, oscilloscope; PL, pump laser (nitrogen laser); R, x-t chart recorder, S, signal; TL, trigger line.	53
2-3. The wavelength range of various organic dyes pumped by a 337.1 nm nitrogen laser (Molelectron). (Taken from the catalog of the Exciton Chemical Co., Inc., Dayton, OH)	58
2-4. Temporal overlap and pulse shapes of the N ₂ () and dye (o) lasers. (Taken from F.M. Curran, Ph.D. dissertation, Michigan State University, 1983).	59
2-5. Block diagram of the ionization signal collection circuit.	63
2-6. Schematic diagram of the probe configuration. The anode and cathode were positioned horizontally and parallel to the colinear dye and	

- N_2 laser beams L_1 and L_2 . The center of the laser beams usually are focused about 10 mm above the burner head. The vertical "displacement from beam center" distance q is defined such that $q_a > 0 > -q_c > -q_b$ 65
- 2-7. Ionization signal collection circuitry.
(Taken from F.M. Curran, Ph.D. dissertation, Michigan State University, 1983). 67
- 2-8. Block diagram of a boxcar integrator. 69
- 2-9. The instrumentation block diagram of a micro-processor interfaced boxcar system. (Taken from J.D. Stanley, Masters thesis, Michigan State University, 1982). 76
- 2-10. Dual laser ionization signals of sodium cation at 5890 Å and 5896 Å. 77
- 3-1. Pictorial representation of Lawton's model concerning the sub-saturated electric field in a flame environment. The symbol x indicates the laser focal point. 85
- 3-2. (a) The calculated spatial distribution of electric field and electrical potential in a flame environment with various ionization rates (r_c) under the sub-saturated condition. The bias potential applied is -750 V on the cathode. A, A', $10^{11} \text{ cm}^{-3} \cdot \text{sec}^{-1}$; B, B', $10^{12} \text{ cm}^{-3} \cdot \text{sec}^{-1}$; C, C', $10^{13} \text{ cm}^{-3} \cdot \text{sec}^{-1}$. The dashed lines indicate distributions in

the absence of a flame ($r_c = 0$). (b) The calculated spatial distribution of electric field and electrical potential in a flame environment with various applied voltages (V_a) under the sub-saturated condition. The ionization rate is $10^{12} \text{ cm}^{-3} \cdot \text{sec}^{-1}$. A, A', -750 V on the cathode; B, B', -1000 V; C, C', -1250 V; D, D', -1500 V.	87
3-3. The spatial distribution of the electric field and the electrical potential for the super-saturated condition.	91
3-4. A typical DLI signal for sodium cations. The positions of both probes were adjusted to obtain maximum DLI signal. ($q_c \approx 0.50 \text{ mm}$, $q_a \approx 2.00 \text{ mm}$, $V_a = 100 \text{ V}$).	98
3-5. DLI signal for sodium cations when the lower probe was placed just below the laser focal point ($q_c = 0.0 \text{ mm}$) with a 600 V bias voltage applied. Each plotted point was an average of 30 data points recorded by the microcomputer. The solid line was drawn from the results of a fit to an exponential decay. The lifetime from the curve fitting is 10.292 μs	100
3-6. DLI signal for sodium cations when the lower probe was located 2.00 mm below the laser focal point ($q_c = 2.0 \text{ mm}$) with a 500 V bias	

voltage applied. Each plotted point was an average of 30 data points recorded by the microcomputer. The solid line was drawn from the results of a fit to an exponential decay. The lifetime from the curve fitting is 17.740 μ s..... 102

3-7. DLI signal for sodium cations recorded with a strip-chart recorder. Notice that the signal is inverted, i.e. a downward signal is a stronger DLI signal. The second temporal peak can be seen clearly from this plot. ($V_a=100$ V, $q_c=2.00$ mm, $q_a=3.00$ mm). 105

3-8. DLI signal for sodium cations from 3-7 with averaged signal points. The solid line was drawn from the results of a curve fitting of the data to an exponential-decay model. The life-time of the exponential decay of the DLI signal is 11.079 μ s when the data points were smoothed by deleting all the points that formed the second peak. 106

3-9. The DLI signals for sodium cations taken at various distances (q_c) between the laser focal point and the lower probe (i.e., the cathode). ($V_a=180$ V, $q_a=1.00$ mm, $A_r=50.0$ μ s, $R=5.0$ μ s, $\%I=2.0\%$, $t_r=0.9766$ μ s, $N_s=15$). A, $q_c=1.02$ mm; B, $q_c=1.12$ mm; C, $q_c=1.22$ mm; D, $q_c=1.32$ mm; E, $q_c=1.42$ mm; F, $q_c=1.52$ mm;

Figure	Page
G, $q_c=1.62$ mm; H, $q_c=1.82$ mm.	108
3-10. The DLI signals for sodium cations taken at various distances (q_a) between the laser focal point and the upper probe (i.e., the anode). ($V_a = 180$ V, $q_c=2.00$ mm, $A_r=50.0$ μ s, $R=5.0$ μ s, $\%I=2.0\%$, $t_r=0.9766$ μ s, $N_s=15$). A, $q_a=0.00$ mm; B, $q_a=1.50$ mm; C, $q_a=2.50$ mm; D, $q_a=3.50$ mm; E, $q_a=4.50$ mm.	111
3-11. A typical DLI signal for sodium cations. The experimental parameters were chosen in order to obtain maximum amount of ion signals. ($V_a = 200$ V, $q_c=3.00$ mm, $q_a=1.00$ mm, $A_r=50.0$ μ s, $R=5.0$ μ s, $\%I=3.0\%$, $t_r=0.5882$ μ s, $N_s=10$).	114
3-12. Pictorial representation of charge separation of a plasma cluster due to ambipolar diffusion.	119
3-13. The physical interpretation of equation [35]. This plot shows that the model of separation of variables assumes that there is a steady-state distribution between the laser focal point and the anode which builds up at the very moment when both lasers go off ($t_f=0$). The anode behaves like an infinite sink and the electron populations thus decays exponentially versus time. The solid line is the spatial distribution of electrons at $t_f=0$ and the dash lines are the electron	

- distribution at later times. Notice that the area under each curve stands for the total population of electrons and it decays exponentially versus time. 125
- 3-14. A sketch of the charge separation processes under the influence of a high bias voltage at $t_f > 0$. This process started immediately after the laser pulses went off. Lawton's model of "charge sheath" is adopted here and the electric field (the solid line) is thus piece-wise linear. The distribution curves of ions electrons were calculated by the Fokker-Planck equation with a piece-wise linear drift function. The ambipolar diffusion effect was ignored. Notice that the the shape of the distribution curves for ions and electrons are not pure Gaussian. 128
- 4-1. Ion distribution versus time diagram. This diagram was drawn from equation [24] by assuming $D = 11.3 \text{ cm}^2 \cdot \text{sec}^{-1}$ and $u = 30.4 \text{ cm}^2 \cdot \text{sec}^{-1} \cdot \text{volt}^{-1}$. A, 5 μs ; B, 10 μs ; C, 15 μs ; D, 20 μs after the laser pulse. 154
- 4-2. Calculated ion signal versus time. This diagram is calculated from equation [30] by assuming $D = 11.3 \text{ cm}^2 \cdot \text{sec}^{-1}$ and $u = 30.4 \text{ cm}^2 \cdot \text{sec}^{-1} \cdot \text{volt}^{-1}$. Notice the skewness of the calculated signal. 157

- 5-1. Ion velocity versus bias voltage diagram for sodium cations. The slope of the straight line is $54.06 \text{ cm}\cdot\text{sec}^{-1}\cdot\text{volt}^{-1}$, which gives a mobility coefficient of $24.33 \text{ cm}^2\cdot\text{sec}^{-1}\cdot\text{V}^{-1}$. The intercept is about $-680 \text{ cm}\cdot\text{sec}^{-1}$, which gives a burning velocity of $680 \text{ cm}\cdot\text{sec}^{-1}$ 186
- 5-2. Diffusion coefficient versus bias voltage for sodium cations. Extrapolation back to zero voltage gives an ambipolar diffusion coefficient of $8.24 \text{ cm}^2\cdot\text{sec}^{-1}$ 189
- 5-3. Ion repulsion versus space coordinate at various times. The laser focal point is located at the position $x=0$, the cathode is placed at the positive x -coordinate and the anode is placed at negative. The ion repulsion is a measure of the electric field due to neighbor ions and each grid scale on the y -axis stands for $1.0 \times 10^6 \text{ volts}\cdot\text{cm}^{-1}$. Positive ion repulsion values means that the electric field due to mutual ion repulsion will push ions toward the cathode. Notice that the ion clusters moves toward cathode and disperses when time elapses. A, $0.167 \mu\text{s}$; B, $1.00 \mu\text{s}$; C, $10.0 \mu\text{s}$; D, $30.0 \mu\text{s}$ after laser pulses went off. 200
- 5-4. Time-averaged diffusion coefficient $(D_i)_t$ versus applied voltages V_a for various ion

mobilities. This plot is drawn from equation [39]. Notice that even if the ion mobility is small, the time-averaged diffusion coefficient $(D_i)_t$ still changes dramatically with V_a and gives values over $100 \text{ cm}^2 \cdot \text{sec}^{-1}$, in contrast with the $4.1 \text{ cm}^2 \cdot \text{sec}^{-1}$ for sodium cation. ($c_0 \approx 1.0 \times 10^{11} \text{ esu} \cdot \text{cm}^{-3}$, $q_c = 0.2 \text{ cm}$, $q_a = 0.3 \text{ cm}$, $d_i \approx 0.1 \text{ cm}$) 203

- 6-1. Deviations of the maximum peak height versus the logarithm of the model diffusion coefficient. The simulated peak heights were obtained by implementing equation [11] in the simulation program. The theoretical peak height was calculated by equation [3]. 219
- 6-2. Peak width at baseline versus the logarithm of the model diffusion coefficient. The simulated peak widths were obtained by implementing equation [11] in the simulation program. The theoretical peak width was calculated by equation [3]. A, simulated data; B, theoretical values. 220
- 6-3. Deviations of the maximum peak height versus the logarithm of the model diffusion coefficient. The simulated peak heights were obtained by implementing equation [14] in the simulation program with different degrees of implicitness. The theoretical peak height

- was calculated by equation [3]. A: 40 %
implicitness ($\Omega=0.4$) B: 50 % implicitness
($\Omega=0.5$) C: 60 % implicitness ($\Omega=0.6$). 227
- 6-4. Peak width at baseline versus the logarithm
of the model diffusion coefficient. The
simulated peak widths were obtained by
implementing equation [14] in the simulation
program with different degrees of
implicitness. The theoretical peak width was
calculated by equation [3]. A: 40 %
implicitness ($\Omega=0.4$) B: 50 % implicitness
($\Omega=0.5$) C: 60 % implicitness ($\Omega=0.6$). D:
Theoretical value. 229
- 6-5. The logarithm of the average of the squares
of the deviations between the simulated and
theoretical values versus the logarithm of
the model diffusion coefficient. The
simulated values were obtained by
implementing equation [14] in the simulation
program with different degrees of
implicitness. The theoretical values were
calculated by equation [3]. A: 60 %
implicitness ($\Omega=0.4$) B: 50 % implicitness
($\Omega=0.5$) C: 40 % implicitness ($\Omega=0.6$). 233
- 6-6. A comparison of the deviations of the maximum
peak heights from different simulation
algorithms. The x-axis is the logarithm of

the model diffusion coefficient. A: 50 % implicitness ($Q=0.4$), equation [11]; B: 40 % implicitness ($Q=0.4$), equation [14]; C: 50 % implicitness ($Q=0.5$), equation [14]; D: 60 % implicitness ($Q=0.6$), equation [14].	235
6-7. Ion velocity versus bias voltage plot. The velocities were obtained from the simulation program. The slope of the plot is $51.71 \pm$ 0.48 which yields a mobility coefficient of $25.86 \pm 0.24 \text{ cm}^2 \cdot \text{volt}^{-1} \cdot \text{sec}^{-1}$	248
6-8. Ion diffusion coefficient versus bias voltage plot. The ion diffusion coefficient were obtained from the simulation program. A: ion density is $1.0 \times 10^{11} \text{ ions} \cdot \text{cm}^{-3}$; B: ion density is $1.0 \times 10^{10} \text{ ions} \cdot \text{cm}^{-3}$	249
7-1. Non-stoichiometric $\text{H}_2\text{-O}_2\text{-Ar}$ flame temperature profile measurements with sodium ions at different heights above the burner head.	261
7-2. Non-stoichiometric $\text{H}_2\text{-O}_2\text{-Ar}$ flame temperature profile measurements with lithium ions at different heights above the burner head.	264
7-3. Non-stoichiometric $\text{H}_2\text{-O}_2\text{-Ar}$ Flame temperature profile measurements with calcium ions at different heights above the burner head.	266
7-4. Non-stoichiometric $\text{H}_2\text{-O}_2\text{-Ar}$ flame temperature profile measurements with various ions at different heights above the burner head. (:	

Figure	Page
sodium; : lithium; :calcium).	269
7-5. Stoichiometric H_2-O_2 -Ar flame temperature profile measurements with sodium ions at different heights above the burner head.	271
7-6. Stoichiometric H_2-O_2 -Ar flame temperature profile measurements with strontium ions at different heights above the burner head.	274
7-7. Stoichiometric H_2-O_2 -Ar flame temperature profile measurements with various ions at different heights above the burner head. (: sodium; : Strontium; :calcium).	276
D-1. Analyte flow speed versus flow rate plot.	366
D-2. Pesudo diffusion coefficient versus flow rat plot.	367

CHAPTER I

INTRODUCTION

A. Overview

Early experimental and theoretical studies of the diffusion and drift of ions in gases were started soon after the publication by Roentgen in 1895 of his discovery of X-rays. Several physicists (1,2), including Roentgen himself, observed that X-rays render gases electrically conducting. The properties of gaseous conductivity were explained by Thompson and Rutherford on the hypothesis that the conduction is due to the production of small charged particles, i.e. ions and electrons. In their 1896 paper, Thompson and Rutherford indicated a method for measuring the sum of the mobilities of the positive and negative ions. Three years later, Townsend (3) published the first attempt to measure the diffusion coefficients of gaseous ions. These investigations marked the beginning of quantitative studies of ionized gases and have made important contributions to the growth of modern physics, both in the development of theories and experimental techniques.

In spite of the concentration of effort in this area for more than half a century, many of the long-recognized problems have been only partly solved. Notwithstanding the ingenuity and skill of the early workers, most of the mobility data obtained before 1960 are of no more than historical interest today. Apparently no reliable direct measurements of diffusion coefficients of gaseous ions were made until the 1960's (4).

Some of the recent measurements of ion mobilities were done in flames (5-7). Often a Langmuir probe was applied to relate the measured current to ionic mobilities (8-11). In recent years, a laser beam has been employed to generate an ion source in the flame (12,13).

Laser-enhanced ionization (LEI) is a relatively new technique which can detect analytes in a flame by forming ions with the aid of a laser and a pair of electrodes, which have a bias voltage applied to them (14). With this technique, time-resolved signals can be obtained (7), which can be used to determine the ion mobilities. Smyth and Mallard have used this technique to determine the mobility coefficients of various ions with a wide range of atomic weights in different flames. The results were compared with the results from the Langevin theory of ion mobility. Lin, Hunt and Crouch (15) applied a technique similar to LEI, which is now called Dual or Direct Laser Ionization (DLI),

and were able to determine both mobility coefficients and diffusion coefficients of ions without using the Langmuir probe theory, from these the flame temperature could be determined with the Einstein equation (16). The results agree with the measurements of other workers very well.

Further investigations of time-resolved DLI signals in our laboratory have shown that there exist two temporal components, i.e. an early electron signal followed some microseconds later by a longer and weaker ion signal. Other workers have observed similar features in LEI (7,17). Two temporal components in the DLI signals imply that the model of ambipolar diffusion, which is one of the basic assumptions Lin made in his work, is not a complete treatment. The Fokker-Planck equation with appropriate drift functions turns out to be a superior model. The biggest advantage of the Fokker-Planck equation is that it can treat ion mobility and diffusion simultaneously. Through proper modelling of the DLI signals with a set of one-dimensional Fokker-Planck equations, curve fitting techniques can help reveal all details of the ion transport processes in the flame under the influence of an electric field.

To verify the validity of a Fokker-Planck model for DLI signals, a study has been made by varying two parameters: the dc voltage applied on the electrodes and the position of

the laser focal point in the flame. Modelling and curve fitting unveiled a dependence between the diffusion coefficient and the applied electric field. However, extrapolation to zero voltage gave reasonable values for the diffusion coefficients of various metal ions, provided that ambipolar diffusion is still assumed. These results showed that the interaction among charged particles in the flame should be taken into account, also. To treat the interaction among ions quantitatively, a FORTRAN program was constructed to simulate the DLI processes in the flame. Results from simulations showed that the repulsion forces among ions play an extremely important role, which was not anticipated previously.

Using the ion mobilities and diffusion coefficients determined by the newly developed model, flame temperatures were calculated via the Einstein relation (16). Various ions were tested and the temperatures at different heights in the flame were measured. All measurements agreed with one another and other investigators' works reasonably.

In addition to the investigations of the applications of the Fokker-Planck equation to DLI, the same idea was also applied to HPLC signals, since the equilibrium of solutes between stationary and mobile phases simulates a diffusion process and the mobile phase movement simulates the ion mobility. It has been found that the exponentially modified

Gaussian function (EMG), which is a popular semiempirical formula for modelling chromatographic peaks (18), is the solution of a particular Fokker-Planck equation. This derivation implies that most of the chromatographic processes can be treated much more precisely by rigorous mathematical models, rather than semiempirical equations. The treatment of HPLC signals with the Fokker-Planck model provided better curve fitting results than those from using the EMG.

B. Review and Historical

B-1 Ion mobilities

Data on ion mobilities and diffusion coefficients are of both theoretical and practical interest. Research on this subject was started nearly a century ago and a substantial volume of literature has now accumulated. However, recent studies of atmospheric and astrophysical phenomena have revealed that gaseous ions play a much more important role in nature than was previously suspected. The present understanding is still insufficient to explain many of the observations (19).

As mentioned previously, one year after X-rays were discovered, Thompson and Rutherford (1) invented a method

for measuring the sum of the mobilities of positive and negative ions. The first measurements of ion mobilities in gases were made by Rutherford in 1897 (20). In that paper, he gave the mean of the values of the mobilities of positive and negative ions for air, oxygen, carbon dioxide, and nitrogen. However, Rutherford's measurements were soon superseded by the more accurate measurements of Zeleny (21) in 1900.

As an ion moves through a gas under a uniform electric field, it gains energy from the field but loses energy during collisions with other molecules. The drift velocity, v_d , of ions ($\text{cm}\cdot\text{sec}^{-1}$) is thus defined as follows:

$$v_d = \mu E \quad [1]$$

where μ is the mobility coefficient ($\text{cm}^2\cdot\text{volt}^{-1}\cdot\text{sec}^{-1}$) and E is the electric field strength ($\text{volt}\cdot\text{cm}^{-1}$). The mobility coefficient μ is independent of the electric field strength E . Equation [1] is valid only when the energy acquired from the electric field between collisions is small relative to the thermal energy (22). A quantitative criterion for the limits of its applicability can thus be described as follows:

$$\frac{mv_d^2}{3kT} \ll 1 \quad [2]$$

where m is the mass of the gaseous ion. The condition

defined by equation [2] is called the "low field limit". If the relative importance of the thermal and field energies is reversed, it is called the "high field limit". It is not difficult to show that the ratio of the electric field intensity to the gas pressure, E/p , is an extremely important parameter since it determines the mean energy acquired from the electric field, and hence the value of ion mobilities (22). The dependence of mobility upon the pressure p of the gas was investigated first by Rutherford. Since in his method ions were produced through photoelectric emission from a plane cathode, only the behavior of negative ions was observed. He found that in a pressure range from 34 to 765 torr, the product of pressure p and ion mobility μ^-p was effectively a constant. Langevin (23), in his more extensive experiments, arrived at a similar conclusion. Since then, most experimentalists have reported the results of their measurements in terms of E/p , or E/p_0 , where p_0 is the "reduced pressure," normalized to 0°C . Upon closer examination, it is obvious that the ion mobilities can be accounted for more precisely by the gas number density, N , rather than p . McDaniel and Mason (22) have suggested replacement of the E/p term by E/N to avoid ambiguity in comparing experimental results. Huxley, Crompton and Elford (24) suggested that the units of E/N be named the "Townsend" or "Td". This designation of the new unit has attained widespread usage in the last twenty years (22).

In 1903, Soon after the first measurements of the mobility of gaseous ions, Langevin (25) published a theory of ionic mobility based on the kinetic theory of gases. It now appears to be the most useful and significant classical treatment of the mobility problem. The equation obtained by Langevin is:

$$\mu = \frac{eL}{mv_t} \quad [3]$$

where L denotes the mean free path, m is the ionic mass, and v_t is the mean thermal speed of ions. Comparison with experiments showed equation [3] to be deficient. The calculated values are always too high by about a factor of four (19). It was obvious to Langevin that one source of error was the assumption that the mean free path of the ion is the same as that of a molecule of the same species. A mechanism which would shorten the ionic mean free path substantially would definitely have to be developed. Furthermore, the crude nature of the mean free path calculations was apparent, and it was evident that more rigorous methods should be applied.

In 1905, Langevin (26) extended the dynamical theory of gases as founded by Maxwell and Boltzmann to derive accurate formulae for the coefficient of inter-diffusion of pairs of gases. He then proceeded to derive a formula for the mobility of a gaseous ion on the assumption that a neutral

molecule of the gas behaves as a perfectly elastic sphere which becomes polarized under the influence of the electrostatic field of the ions. Langevin also assumed that the random thermal speeds of the ions followed Maxwell's distribution law, in other words, the field energy is negligible compared with the thermal energy. The complete Langevin equation (in Hasse's notation) is:

$$\mu = A \left(\frac{1 + (m/M)}{\rho (\epsilon - 1)} \right)^{1/2} \quad [4]$$

where m and M are the masses of the ion and molecule, respectively, ρ is the density of the gas, and ϵ is the dielectric constant of the gas. A is a function of the sum of the radii of ion and molecule in a collision, which had been recalculated by Hasse (27). Notice the fact that the mobility expressed in equation [4] contains no dependence on the charge of the ion; however, temperature dependence is implied in a constant pressure environment.

Two distinctly different theories (23) involving the concept of polarization attraction were then developed. One proposal, which is called the "cluster-ion theory," was that neutral molecules are attracted to and permanently bound by the ion because of its charge. Also, the increased size and mass of the ion which result from this attachment are responsible for the low observed value of the mobility. An opposing view was the "small-ion theory," in which the

assumption was made that the size of the ion is relatively unimportant, since the ions are retarded in their motion principally by momentum transfers which are due to the action of the attractive forces. The concept of the ionic cluster is rarely useful. Experimental evidence shows ion clusters can be formed in some gases under certain conditions, however, only at low temperatures (22). For most applications the "small-ion limit" of equation [4] has been utilized. As the sum of the radii of the ion and molecule in a collision approaches zero, the value of the function A in equation [4] approaches 0.5105 (Langevin gave 0.505) and the equation simplifies to a form dependent only on the bulk properties of the gas and the atomic or molecular weight of the ion. This theory has been applied to a large number of atomic and small molecular ions in nonreacting gases at room temperature and also in flame environments, and provides an excellent description of ion mobilities (22).

The study of ion mobilities has made considerable progress since 1905. However, it is interesting to point out that Langevin's work remained unnoticed for about twenty years, until Hasse (27) published his paper in 1926 with some modifications of his calculations. During the period before 1926, the most important investigations of the theories of ion mobility were done by Chapman (28) and Enskog (29). They developed a rigorous kinetic theory for

gases composed of spherically symmetric (monatomic) particles. Their expression for the mutual diffusion coefficient lead to excellent predictions of ion mobilities; (28-30). In 1931, Hasse and Cook (31,32) used the Chapman-Enskog theory to improve the calculation of ion mobilities, however, their attempt does not seem to represent a general refinement over Langevin's model.

In 1934, the earliest investigation of ion mobilities based upon quantum mechanics was published by Massey and Mohr (33). Dalgarno and Williams (34) have investigated the second-order correction term in the Chapman-Enskog expression for the mutual diffusion coefficient and obtained approximate solutions for lithium and helium ions. This results indicated that the ion mobilities increased with increasing temperature (35), in contrast to gas molecules.

Wannier (36,37) extended the theory of ion mobilities to the high E/p region, in which the energy derived from the field is comparable to the thermal energy. Although his theory is mainly applicable to the high-field region, it also yielded results of considerable interest at low E/p . His theory indicated that the drift velocity should show no dependence on temperature in the high-field region. However, in the low-field region, the drift velocity should vary directly with E/p regardless of the interactions among gas particles. Wannier's theory concerning the variation of

drift velocity with E/p has been verified by Hornbeck (38) and Varney (39) in studies of the noble gases, oxygen, nitrogen, and carbon monoxide. More refined models then were used by Kihara (40), Mason and Schamp (41), and Perel (42). All results showed that Langevin's treatment, which now is usually referred to as the first-order approximation, is often accurate enough. Higher-order corrections to the mobility were shown to be small.

The measurement of ion mobilities was considerably advanced in precision and reliability by the introduction of time-of-flight methods in 1928. Tyndall, Starr, and Powell (43) invented a four-gauze electrical shutter apparatus and measured the mobilities of alkali metal ions in various noble gas environments. Beaty (44-47) has improved this apparatus and measured the mobility of positive ions of argon in the parent gas over an E/p_0 range extending from about 1 to 80 $\text{volt}\cdot\text{cm}^{-1}\cdot\text{mmHg}^{-1}$. Hornbeck (38,48) invented a method which uses an ultraviolet light source to generate pulses of photoelectrons and produces a Townsend avalanche. The ionic drift velocity is also determined by measuring the arrival time of ions. Hornbeck extended the E/p_0 range to 1000 $\text{volt}\cdot\text{cm}^{-1}\cdot\text{mmHg}^{-1}$. Other accurate measurements were made by Bionde and Chanin (49-52), McAfee et al. (53), Miller et al. (54), Young and Edelson, et al. (55), and Smith et al. (56). Those people applied the afterglow method and the mass spectrometer extensively. Since then

the general consensus is that experimental values of ion mobilities should not be formally accepted unless a mass spectrometer has been employed (22).

Direct determinations of ion mobilities in flames have been very limited (6,7,10) despite the interest in gas reactions at high temperatures. Most determinations have used a Langmuir probe (11) to derive mobilities from the measured current. However, since the dependence of the ion current on mobility is not clearly established, the reported ion mobilities have shown large variations (57). Smyth and Mallard (6,7) applied the LEI techniques to measure the ion mobilities of alkali metal ions in air-acetylene and oxygen-carbon monoxide flames. The results were compared with Langevin's theoretical values.

B-2 Diffusion Coefficient

Diffusion is the process by which matter is transported from one part of a system to another as a result of random motion. Transfer of heat by conduction is also due to random motions of molecules and there is an obvious analogy between the two processes. Fick (58), who recognized this resemblance and then adopted the mathematical equation of heat conduction derived by Fourier in 1822, made the first treatment of the diffusion processes on a quantitative basis

in 1855. The mathematical theory of diffusion in isotropic substances is therefore based on the hypothesis that the rate of transfer of a diffusive subject through a unit area in an arbitrarily chosen frame is proportional to the concentration gradient measured normal to the unit area plane. This hypothesis can be written in mathematical terms as:

$$J = - D \frac{\partial P}{\partial q} \quad [5]$$

where J ($\text{sec}^{-1} \cdot \text{cm}^{-2}$), sometimes called the "flux", is the rate of transfer of the diffusive subject per unit area, D is the diffusion coefficient ($\text{cm}^2 \cdot \text{sec}^{-1}$), and P can be interpreted as the concentration (cm^{-3}) of the diffusive subject at coordinate q and time t . The negative sign in equation [5] is due to the fact that the direction of diffusion is always opposite to the direction of increasing concentration. The change of concentration P versus time thus can be written as follows:

$$\frac{\partial P}{\partial t} = \frac{\partial}{\partial q} [J(q,t) - J(q+dq,t)] \quad [6]$$

where

$$J(q+dq,t) = J(q,t) + \left(\frac{\partial J(q,t)}{\partial q} \right) dq. \quad [7]$$

On combining equations [5] through [7], the well-known

equation of continuity can be derived.

$$\frac{\partial P}{\partial t} = D \frac{\partial^2 P}{\partial q^2} \quad [8]$$

Equation [8] is also called the time-dependent diffusion equation of Fick's Second Law, while equation [5] is known as Fick's First Law. Numerous books and review articles devoted to diffusion processes are available (59).

The theoretical investigation of diffusion processes in ionized gases and the measurement of diffusion coefficients of ions were never easy tasks. Most measurements of diffusion coefficients were carried out along with the measurements of ion mobilities, in fact, as a by-product of the measurements of ion mobilities. Hence equation [8] is usually used along with a mobility term to describe the essential part of the transport phenomena of gaseous ions. The details will be covered later in this chapter. As mentioned before, it is generally acceptable that no reliable direct measurements of ionic diffusion coefficients were made before the 1960's. In fact, the first precise and accurate measurement of ionic diffusion coefficients may be dated back only to 1968 (22). However, the studies on this subject were started much earlier. In 1899, Townsend (3) published the first attempt to measure the diffusion coefficients. He was able to deduce the diffusion coefficients by measuring the ratio of losses of ions when

the ionized gas travelled through narrow metal tubes of different lengths. The somewhat difficult theory deduced from Maxwell's equations of transport was also given by Townsend. The result can be written as follows with modern symbols:

$$\frac{\mu}{D} = \frac{e}{kT} \quad [9]$$

where μ is the mobility coefficient ($\text{cm}^2 \cdot \text{volt}^{-1} \cdot \text{sec}^{-1}$) of the ions, D is the diffusion coefficient ($\text{cm}^2 \cdot \text{sec}^{-1}$), e is the electron charge, k is the Boltzmann constant, and T is the absolute temperature. It is interesting to point out that equation [9] had previously been deduced by Nernst (19) in 1889 for electrolytic ions, although his theoretical treatment was not strictly applicable to ionized gases. However, for some unknown reasons equation [9] is often called the "Einstein Formula." Einstein certainly employed this formula in his research on Brownian motion, as will be mentioned later in this chapter; however, equation [9] was already well known at that time. In actuality, Einstein himself has acknowledged this fact (16). Conventionally, equation [9] is used to derive the ionic diffusion coefficients if the mobility coefficient is known (19).

The direct measurements of diffusion coefficients were mainly by the drift-tube method along with the measurements of ion mobilities, as mentioned earlier. Drift tubes were

first used at the end of the nineteenth century and have been applied to the study of ionic drift velocities almost continuously since then (3). A conventional ionic drift tube usually consists of a gas container, an ion source, a set of electrodes that establishes a uniform axial electrostatic field along which the ions drift, and a detector at the end of the tube. The drift field E causes the ions to "swarm" through the gas. The drift velocity and diffusion rate of a gaseous ion are functions of the field strength, pressure, and temperature. A time-resolved spectrum is usually taken for the determination of ion mobilities and diffusion coefficients (19). It is expected that the shape and width of the time-resolved spectrum would depend strongly on the value of the diffusion coefficient D . With this idea, the first reliable measurement was made by Moseley (60), subsequently followed by McDaniel et al. (61). Soon after Moseley's publication, the drift-tube mass spectrometer was introduced and the time-resolved spectrum of gaseous ion could be measured much more precisely. However, due to the inherent difficulty of relating the time-resolved signals to diffusion coefficients, this probably could not be much better determined (19).

Recently, Lin, Crouch and Hunt (15) has used simple models to determine both mobility and diffusion coefficients of ions, as mentioned before.

The real challenge in this subject is to find the solution of the transport equation describing the drift and diffusion of the ions in the apparatus used for an experiment. This can be treated most efficiently by solving the Fokker-Planck equation with suitable drift functions. The essence, development, and application of the Fokker-Planck equation will be covered in later sections of this chapter.

B-3 Dual Laser Ionization

Among the many laser-based analytical techniques developed in the last two decades, laser-enhanced ionization (LEI) has proven to be particularly useful for the determination of trace metal elements. A closely related technique, dual or direct laser ionization (DLI), which has improved the sensitivity of LEI under circumstances, is under investigation in our laboratory.

The irradiation of a sample reservoir, such as a flame or discharge plasma, by a light beam at a frequency selected right at the resonant transition of the analyte may induce a variation of local charge density, which usually can be measured as a voltage or current change. This variation of electric phenomena is due to the change of the ionization rate within the sample reservoir, and is commonly called the

opto-galvanic effect (OGE). The first observation of the OGE was published in 1925 by Foote and Mohler (62,63). In their investigations of the photoionization of alkali metal elements, they observed cesium ions by using space-charge amplification in a thermionic diode which was irradiated with a tungsten lamp at wavelengths chosen below the photoionization threshold. Due to the limited signal magnitudes obtainable with conventional light sources, the OGE was nearly completely overlooked for 50 years until very powerful light sources, namely lasers, became popular in analytical laboratories. With a laser as the light source, OGE was first applied to analytes in a flame environment in 1976 by Green et al. (64) at the National Bureau of Standards (NBS), and this new application of OGE is now more aptly called LEI. Dramatic progress has been achieved since 1976 (65).

The basic principles of the LEI technique have been described in numerous articles (65-73). Briefly, the mechanism of LEI process can be portrayed as follows: gas phase analytes in a flame are first promoted to a selected excited state by a dye laser tuned at the resonant frequency; then, the excited atoms are further elevated to the ionization continuum, mainly by collisions with foreign gas molecules in the flame. The ions formed in the flame are collected by a pair of electrodes with bias voltages. LEI differs from conventional flame spectroscopic methods,

such as absorption, emission, and laser-induced fluorescence, in at least two ways. First, the ionization continuum states of analytes are involved, in contrast to the conventional optical methods which deal exclusively with the discrete states. Second, the detector of LEI is a pair of electrodes instead of an optical detector, such as a photomultiplier. This difference in detector can provide many advantages over the conventional optical methods. Thorough reviews of the development of laser-induced analytical spectroscopies, including LEI, have been given by Lin (74) and Curran (75), hence, later in this section only recent advances in LEI methods are reviewed.

Dual or direct laser ionization (DLI), which has been under investigation in our laboratory since 1979 (76), is closely related to LEI in instrument design. However, in basic principles it is, in fact, an extension of resonance ionization spectroscopy (RIS) to the flame cell. In RIS laser radiation is used to photoionize the atoms or molecules directly (77), while in LEI the ionization process is assisted by collisions among excited analytes and foreign gas molecules in the flame. DLI differs from LEI in that a second laser is applied to promote the excited analytes to the ionization continuum. However, for some elements the collisional ionization mechanism still can compete, or even dominate over the photoionization mechanism and effectively turn DLI back, in principle, to LEI (78). In the DLI

experiment performed in our laboratory the analyte, after being nebulized into the flame cell, is first resonantly excited by a dye laser tuned to a wavelength at the resonant transition. Then is promoted to the ionization continuum by a separate nitrogen laser (337.1 nm). The subsequent ionization signal is collected by a pair of voltage-biased nichrome-wire probes. The electrical, rather than optical, nature of signal detection leads to high sensitivity, as many of the common limitations on signal collection that are found in conventional spectroscopic techniques are avoided (74).

There are at least two advantages of DLI, compared with the conventional optical methods, worth mentioning. First, DLI is definitely free from most of the optical interferences, such as scattering of the laser light, stray light, and flame background emission. This is part of the reason why DLI usually provides very good detection limits and high sensitivity (79), provided that the interferences caused by easily ionized matrix constituents are kept low, as they usually are. Second, DLI supplies a very convenient, inexpensive and high-intensity ion source in the flame environment. Since there is an electric field built up between the electrodes, ion transport between the laser focal point (the ion source) and the electrodes involves both mobility and diffusion. Hence DLI provides a very good tool to study ion transport processes in the flame

environment. The high efficiency of ion collection, coupled with a high intensity ion source, gives very stable and reproducible time-resolved DLI signals, from which both the ion mobility and diffusion coefficient can be deduced.

Recent developments in LEI have focused on the practical aspects, and various methods have been used to improve the performance of LEI. One major concern has been poor sample transport efficiency, which is inherent with premixed sample introduction into flames or plasmas (80). Hall and Green (81) reported the use of a total consumption burner and showed that it can enhance the collisional ionization for copper and give better detection limits. They also compared premixed burners with total consumption burners for sample analysis by LEI (82). Also, Hall and Green (83) used a total consumption burner with prior desolvation of discrete sample volumes in a home-made microcondenser or a commercial graphite furnace. The desolvation with a graphite furnace was examined in much greater detail; however, the microcondenser generally performed better and gave a lower detection limit. In the best case, sample desolvation permitted the improvement of detection limits for manganese by two orders of magnitude. With both the graphite furnace and the microcondenser, the discrete sampling gives a low concentration environment and effectively reduces the electrical interference. Also, Turk and Watters have tried an ICP as the atomization source (84)

and Bykov et al. (85) have used various flames and a graphite furnace as atomization sources to evaluate certain interfering matrices. A new interface that can lower the pressure of the gas analyte from the flame was also reported (86). Replacing the dc detection system with the microwave detection frequencies for LEI to minimize the perturbation on the flame combustion has been suggested, as well (87). Axner et al. (88) reported on detection limits for LEI in flames for several metal elements. They used a pulsed excimer laser for excitation. Detection limits in the part-per-billion to part-per-trillion range were obtained for 13 elements. Some detection limits from their work compare favorably with those reported previously in the literature.

Stepwise LEI techniques have also been investigated by people. Omenetto et al. (89) have employed two lasers, one tuned at 291.832 nm and the other at either 377.572 or 276.781 nm, to excite the analyte. By increasing the population at the metastable $^2P_{3/2}$ level, a 38-fold enhancement of the LEI signal was obtained. Axner et. al (90) also showed that by a two-laser excitation method, the LEI signal for Mg can be enhanced at least two orders of magnitude. Smith et al. (91) reported that, for lithium, the ionization yield from a single-step excitation at 670.784 nm increased from 0.26%, to 58% from a two-step excitation (670.784 + 460.286 nm) mechanism. They also have presented a simple theoretical treatment of the ionization

process in order to estimate the effective collisional ionization rate coefficients by order of magnitude. Havrilla and Choi (92) have employed both of the single and stepwise excitation schemes to measure the detection limit of zinc. They tried seven zinc transitions, including resonance lines at 213.8 and 307.6 nm, and obtained detection limits ranging from 10 ppm to 1 ppb. Generally speaking, the stepwise scheme is more effective and selective than single step processes. However, it also leads to a substantial increase in the analysis complexity. An even more complicated system is also worth mentioning here. Turk and Omenetto (93) have used a two-step scheme to photoionize strontium directly. The strontium ions produced were then monitored by a third laser, colinear and counter-propagating in the flame, tuned to an ionic fluorescence transition, and delayed in time with respect to the ionizing beams. Although their work is beyond the scope of DLI, the fast decay of ions they have observed might be helpful in constructing better theoretical models for LEI processes.

In addition, LEI was successfully employed for isotopic analysis, and hyperfine splitting was revealed by using hollow cathode-type sampling source (94-96). LEI has also been applied to high-resolution spectroscopy in recent studies of uranium (97-98) and lutetium (99).

The complete quantum mechanical theory of LEI has still

not been fully developed. However, many characteristics of LEI can be explained by a simple rate-equation argument (100). Curran et al. (78) examined the energy schemes of DLI processes. They demonstrated that for lithium, sodium, calcium, and strontium, the second, fixed-wavelength laser can enhance the electrical signal up to three orders of magnitude. For some elements, the lack of enhancement was explained in terms of the decline of photoionization cross sections with increasing energy overshoot into the ionization continuum, and the competition between photoionization and collisional ionization. Considerations applicable to the optimization of DLI experiments were also discussed. The mechanism of the LEI signal in a glow discharge and the perturbation of the laser source on the discharge character were discussed by Burakov et al. (101). The plasma characteristics for copper (102) and uranium (103) hollow cathode lamps were examined and simple plasma models discussed.

The theoretical aspects of electrical phenomena and the electrical interferences shown in LEI and DLI processes have drawn considerable attention. Curran et al. (79) have studied the electrical interference for DLI. Reasonable signal recovery ratios were observed as long as the laser focal point was inside the ion sheath. High concentrations of easily ionizable matrix components appear to extend the linearity of analytical curves, however, the noise levels

may be higher due to photoionization of the matrix components. As previously mentioned, Nippoldt and Green (104) have shown that taking the LEI signal right after the aspiration started may effectively suppress the electrical interferences in the flame. Bykov et al. (85) have used various flames and a graphite furnace as atomization sources to evaluate certain interfering matrices, too. Havrilla et al. (105) have developed a point charge model based on induction theory to explain LEI and account for the effects of the alkali metals. Also, the signal suppression by easily ionized elements and the determination of ion fractions in the sources were studied by Hall and Green (106). Berthoud et al. (107) observed two temporal peaks from LEI signals. They believe that both of the two peaks are due to electrons. The data reported by them indicates that the mobility coefficient of electrons may be as large as $3000 \text{ cm}^2 \cdot \text{volt}^{-1} \cdot \text{sec}^{-1}$. Mallard and Smyth (6,7) have applied the same argument in order to calculate the mobility coefficients of various metal elements in flames.

There are a few very good review articles worth mentioning. Ingle and Crouch (100) have given a brief but accurate description of DLI and LEI in their recent book. Travis et al. (65,108) have given two thorough and comprehensive reviews of the development and progress, in 1982 and 1984. The 1984 review placed more emphasis on the theory and principles of the technique. In addition, Camus

(109) has reviewed the general aspects of LEI. Book chapters written by Schenck et al. (66), Travis et al. (67), and Travis et al. (71) also provided excellent descriptions about the general background of the LEI technique. Alkemade et al. (110) has given an extensive review of the behaviors of metal ions in various flames. Various aspects of LEI instrumentation and performance in trace metal analysis were discussed by Kuzyakov (111). Berthoud (112) discussed the LEI technique on the aspects of general instrumentation.

B-4 The Fokker-Planck Equation

Interest in linear and non-linear fluctuations of thermodynamic variables and in the stochastic methods for treating them has grown rapidly in the last few decades. In contrast to deterministic models, a common characteristic of all stochastic problems is that the treatment is focused on a property which is the result of superposition of a large number of variables. The values of the stochastic variables are governed by certain probability laws, but not by classical mechanics. It has been shown by van Kampen (113) that a well-defined set of deterministic kinetic equations for the classical mechanical variables can be extracted from the stochastic equations if the physical parameter which scales the fluctuations can be determined and taken to the limit of vanishing fluctuations. The most well-known

classical applications of stochastic mechanics in chemistry are the Debye-Hückel (DHL) theory of electrolyte solutions (114) and the Lindenmann-Hinshelwood-Marcus theory (now is called the RRKM theory) of uni-molecular reaction rates (115). In quantum mechanics a qualitative stochastic description is often used to justify the perturbation and variation methods of solving the Schroedinger equation for atoms that contain two or more electrons (116). A quantitative stochastic treatment of quantum mechanics still has serious difficulties, however, some would argue it has conceptual advantages over the wave mechanical approach (117).

The treatment of fluctuations of a system made up of many small units is not at all new. The first publication, which dealt with gaseous systems, was presented by Boltzmann in 1872 (118). In his work, Boltzmann derived an equation, which is now called the "Boltzmann Equation", to determine the evolution of the distribution function of molecules in the gaseous phase which are sufficiently dilute that only two-body interactions are ever important. For equilibrium states the treatment yields the Maxwell-Boltzmann distribution of molecular velocities; for non-equilibrium states, where mass and heat flow are present, it gives the macroscopic laws with kinetic coefficients, such as the viscosity coefficient and the heat conductivity.

From 1905 to 1908, Albert Einstein published five short papers about Brownian motion (16). He showed that the diffusion coefficient D ($\text{cm}^2 \cdot \text{sec}^{-1}$) and the so-called "mobility" of Brownian particles, u , are related by the following equation:

$$D = \mu k T \quad [10]$$

where k is the Boltzmann constant and T is the absolute temperature of the fluid in which Brownian particles are immersed. To test the validity of this equation, Einstein himself checked it with existing data on sugar molecules in water. The establishment of the first complete and absolute proof of the equation has been credited to Perrin (119). According to Kubo (120), it is interesting to note (16) that when Einstein was working on the theory of Brownian motion he did not know at first that such motion had already been observed by the Scottish botanist Robert Brown in 1827, when Brown was working with small particles originating from pollen floating on water (121). More interestingly, Einstein did not initiate his research on Brownian motion to develop stochastic mechanics, but for proving the atomic theory (122). However, the outcome of Einstein's theory has not only finally convinced even the strongest opponents of the validity of atomic theory, but also has motivated development of mathematical theories of stochastic processes. Numerous applications have been made in physics, chemistry, economics, and almost every other discipline of

science. Of all the diverse methods of treating stochastic processes, the remainder of this section concentrates on the development and applications of a special approximate representation of the master equation (123), namely, the one-dimensional Fokker-Planck equation.

The Fokker-Planck equation was first used by Fokker (124) and Planck (125) to describe the Brownian motion of particles. It is mainly used as an approximate description for any Markoff process in which the individual jumps are small. Einstein's model of Brownian motion, in this sense, is a special case of the Fokker-Planck equation. Planck derived the general non-linear Fokker-Planck equation from an arbitrary master equation assuming only that each jump has to be small (125). In 1931, Kolmogorov (126) contributed a mathematically rigorous derivation by reducing all jumps to infinitely small steps. Hence, the Fokker-Planck equation is also called the forward Kolmogorov equation.

The general Fokker-Planck equation for one variable q has the form:

$$\frac{\partial P}{\partial t} = \frac{\partial^2 (DP)}{\partial q^2} + \frac{\partial (hP)}{\partial q} \quad [11]$$

where P is the conditional propagator, D is the diffusion coefficient ($\text{cm}^2 \cdot \text{sec}^{-1}$) which can be a function of q , and h

is the drift function ($\text{cm}\cdot\text{sec}^{-1}$). The conditional propagator P is usually expressed as a function of both q and t :

$$P = P(q_f, t_f | q_0, t_0)$$

The Fokker-Planck equation has two alluring features. First it is a differential equation rather than a differentio-integral equation. Even though it is still difficult to obtain analytical solutions except for a few special cases (127), at least it is easier to handle. More important is the fact that it does not require knowledge of the entire kernel but merely of the diffusion coefficient D as a function of q , and the drift function h . For any real stochastic process these can be determined with a minimum of detailed knowledge about the underlying mechanism. By solving the Fokker-Planck equation one obtains distribution functions from which any averages of macroscopic variables are obtained by integration. Since the application of the Fokker-Planck equation is not restricted to systems near the equilibrium state, it has often been employed to describe the evolution of non-equilibrium thermodynamic systems for a small number of stochastic variables. More specifically, the Fokker-Planck equation, which involves fluctuations that reflect the range of the microscopic variables, can give both the proper conditional propagators which are consistent with given macroscopic constraints, and the vestige of the consequent variations in the time development of the

stochastic variables, by which the system is characterized. Many review articles and books on the Fokker-Planck equation exist (123,128,129).

A process described by equation [11] with a vanishing drift function and a constant diffusion coefficient is called a Wiener process. The equation for the conditional propagator $P=P(q_f, t_f | q_0, t_0)$ is then the diffusion equation:

$$\frac{\partial P}{\partial t} = D \frac{\partial^2 P}{\partial q^2} \quad [12]$$

with the initial condition:

$$P(q_f, t_f | q_0, t_0) = \delta(q_f - q_0) \quad [13]$$

The solution for $t_f > t_0$ reads as follows:

$$P(q_f, t_f | q_0, t_0) = \frac{1}{[4\pi D(t_f - t_0)]^{1/2}} \exp\left(-\frac{(q_f - q_0)^2}{4D(t_f - t_0)}\right) \quad [14]$$

If the drift function h is linear with a constant diffusion coefficient, it is called the Ornstein-Uhlenbeck process (130). The equation can be written as follows:

$$\frac{\partial P}{\partial t} = D \frac{\partial^2 P}{\partial q^2} + \frac{\partial(hP)}{\partial q} \quad [15]$$

where

$$h = -\alpha q \quad [16]$$

with the initial condition the same as equation [13]. The term α is a constant (sec^{-1}).

The Ornstein-Uhlenbeck process may be equally well described by a linear Langevin equation with Gaussian Langevin forces. Because for a linear transformation of variables a Gaussian distribution will remain Gaussian, the conditional propagator must also be a Gaussian distribution. The general solution of the Ornstein-Uhlenbeck process reads:

$$P(q_f, t_f | q_0, t_0) = \frac{\alpha^{1/2}}{[2\pi D(1-\gamma^2)]^{1/2}} \exp\left(-\frac{\alpha(q_f - q_0 \gamma)^2}{2D(1-\gamma^2)}\right) \quad [17]$$

where

$$\gamma = \exp(-\alpha(t_f - t_0)) \quad [18]$$

In the limit where α approaches zero, equation [17] reduced to the result for a Wiener process, equation [14]. Notice that equation [17] is valid for both negative and positive α values (130).

Onsager and Machlup have derived a similar integral method to treat linear fluctuations from the Langevin equation (131,132). They formulated this principle for linear fluctuations, with the aid of a function now called the Onsager-Machlup function. The definition and use of the Onsager-Machlup function have been extended recently by

Graham (133), and several articles have been published since then to discuss this and its theoretical consequences (134-138). Moreau (139) has applied the Onsager-Machlup function systematically to the non-linear fluctuations of a thermodynamic variable, and Dekker (140) has given a detailed derivation of the functional integral representation of general diffusion processes in curved spaces.

One powerful method for solving the Fokker-Planck equation is the use of functional path integral techniques. Pioneering research on path integrals has been done by Wiener for Brownian motion (141-144). This method was applied by Onsager and Machlup (131,132) to treat fluctuations in chemical systems near to the equilibrium state. Recent extensions of the method have made possible new applications to cluster growth in homogeneous nucleation (145), to the kinetics of phase transitions (146), and to other problems in non-equilibrium thermodynamics (147).

The path integral approach gives the expression for the conditional propagator $P(q_f, t_f | q_0, t_0)$ associated with a stochastic differential equation:

$$P(q_f, t_f | q_0, t_0) = \int D[q(t)] * \exp \left(-\frac{1}{2D} \int_{t_0}^{t_f} L(q, \dot{q}, t) dt \right) \quad [19]$$

where the integration runs over all functions $q(t)$ with $q(t_0) = q_0$ and $q(t_f) = q_f$. The conditional propagator gives the probability of observing the value q_f for the stochastic variable q at time t . The term $L(q, \dot{q}, t)$ in equation [19] is commonly called the thermodynamic Lagrangian. Several different representations of thermodynamic Lagrangians have been reported (133-135, 137, 140, 148, 149). The evaluation of the conditional propagator in equation [19] by Laplace's method was first carried out by Wiegel (150, 151) and subsequently by others (139, 152, 153). Since then the path integral techniques have been coupled frequently with the so-called Onsager-Machlup-Laplace (OML) approximation to obtain the conditional propagators associated with the Fokker-Planck equations. The OML approximation is exact for linear Gaussian processes, i.e., if the underlying mechanical force is linear (131, 132). Hongler (154) has presented a class of interesting Fokker-Planck equations for which the exact conditional propagators are analytically solvable. This has provided a standard for comparison with the results from OML approximations. K.L.C. Hunt and Ross (155) recently proved that the thermodynamic Lagrangian is unique for single-variable processes or for multi-variable processes in flat spaces. Subsequently P.M. Hunt, K.L.C. Hunt and Ross (156) discussed the validity of OML approximations. They also prescribed an algorithm that can be used to solve equation [19] numerically. This algorithm was applied in this dissertation to simulate the DLI signals

under linear and non-linear electric fields. The details are covered in later chapters and appendices.

C. Overview of the Dissertation

This dissertation contains eight chapters and four appendices. This first chapter has introduced the main idea of work. The general background and the historically related literature of the theories and measurements of ion mobility coefficients and diffusion coefficients has been reviewed. Since a detailed account of the development of laser-enhanced ionization (LEI), dual or direct laser ionization (DLI), and other related laser-based ionization techniques have been given by Lin (74) and Curran (75), only the developments from 1983 to the present were emphasized. However, all related background was briefly reviewed and most of the key literature was cited to make that section a self-contained essay. The section on the Fokker-Planck equations covered some historical accounts in order to show the essence of this important and powerful equation, and along with the coupling with path integral techniques and the Onsager-Machlup-Laplace (OML) approximation.

Chapter II describes the experimental set-up used to obtain the data presented in the main body of this thesis. The DLI experimental system is described briefly in order to

give a rough profile of the system. Since this work relied heavily on the use of a microcomputer interfaced boxcar integrator, a more detailed description of this aspect is given.

Chapter III deals with the time-resolved DLI signals. Evidence is provided to show that the DLI signal is composed of two separate, but often overlapped signals. The reasons for this phenomenon are also discussed.

Chapter IV introduces the application of the Fokker-Planck equation for the ion transport processes of DLI. The one-dimensional Fokker-Planck equation is derived from the basic assumptions of the DLI ion transport model. Various forms of the Fokker-Planck equations are derived and solved either analytically or numerically. The results are interpreted in order to explicate the essence of the time-resolved DLI signals.

Chapter V describes the theory and procedures utilized for comparisons of the theoretical model and DLI signals. The DLI signals for sodium ions under different conditions were chosen to demonstrate the validity of the theoretical model. Non-linear curve fitting techniques are applied to the sodium DLI signals in order to extract the essential parameters, such as the mobility and diffusion coefficients. The curve fitting reveals a dependence between the diffusion

coefficient and the applied electric field, which is interpretable. However, the temperature of the hydrogen-oxygen-argon flame can still be calculated by the Einstein relation.

Chapter VI describes a FORTRAN simulation program which simulates the DLI processes with different parameters in order to explain the interdependence of the diffusion coefficient and the applied electric field. However, due to the deficiencies of the one-dimensional model, this program can only show the relationship between the diffusion coefficient and the electric field. It can not duplicate actual DLI processes. New algorithms that can simulate the diffusion and drifting processes more effectively are also described.

Chapter VII presents the temperature profile of hydrogen-oxygen-argon flames measured by using different metal ions. The results agree reasonably well with the literature values.

Finally in Chapter VIII, the work is summarized and recommendations for future studies are made.

Appendix A contains the FORTRAN listing of the program which gives the numerical solutions of a Fokker-Planck equation with various piece-wise linear drift functions.

Appendix B includes the FORTRAN source code of the non-linear curve fitting programs and their output formats. Appendix C is the FORTRAN source code for the simulation program. Appendix D describes the application of the Fokker-Planck equation to an HPLC system.

CHAPTER I

REFERENCES

1. J.J. Thomson and E. Rutherford, Phil. Mag. 62, 392 (1896).
2. "Oeuvres Scientifiques de Paul Langevin", pp. 13-141 (Services des publications du Centre National de la Recherche Scientifique, Paris, 1950).
3. J.S. Townsend, Phil. Trans. A193, 129 (1899); *ibid.* A195, 259 (1900).
4. L.G.H. Huxley and R.W. Crompton, "The Diffusion and Drift of Electrons in Gases" (John Wiley & Sons, New York, 1974).
5. P.L. Lijnse and R.J. Elsenaar, J. Quantum Spectry. Radiat. Transfer 12, 1115 (1972).
6. K.C. Smyth and W.G. Mallard, Combust. Sci. Technol. 26, 35 (1981).
7. W.G. Mallard and K.C. Smyth, Combust. Flame 44, 61 (1982).
8. R. Kelly and P.J. Padley, Trans. Faraday Soc. 67, 1384 (1971).
9. R.M. Clements, C.S. MacLatchy, and P.R. Smy, J. Appl. Phys. 43, 31 (1972).
10. D. Bradley and S.M.A. Ibrahim, J. Phys. D7, 1377 (1974).
11. C.S. MacLatchy, Combust. Flame 36, 171 (1979).
12. K.C. Smyth and P.K. Schenck, Chem. Phys. Lett. 55, 466 (1978).

13. K.C. Smyth, P.K. Schenck, and W.G. Mallard, ACS Symposium Ser. 134, 175 (1980).
14. J.C. Travis, G.C. Turk, and R.B. Green, Anal. Chem. 54, 1006A (1982).
15. K.C. Lin, P.M. Hunt, and S.R. Crouch, Chem. Phys. Lett. 90, 111 (1982).
16. A. Einstein, "Investigations on the Theory of the Brownian Movement" (Dover, New York, 1956).
17. T. Berthoud, J. Linpinsky, P. Camus, and J.-L. Stehle, Anal. Chem. 55, 963 (1983).
18. D. Hanggi and P.W. Carr, Anal. Chem. 57, 2394 (1985).
19. E.W. McDaniel, "Collision Phenomena in Ionized Gases", (John Wiley & Sons, New York, 1964).
20. E. Rutherford, Phil. Mag., November (1897).
21. J. Zeleny, Phil. Trans. A 195, 193 (1900).
22. E.W. McDaniel and E.A. Mason, "The Mobility and Diffusion of Ions in Gases" (John Wiley & Sons, New York, 1973).
23. L.B. Leob, "Basic Processes of Gaseous Electronics", 2nd. ed., chapter I (University of California Press, Berkeley, 1960).
24. L.G.H. Huxley, R.W. Crompton, and M.T. Elford, Bull. Inst. Physics and Physical Soc. 17, 251 (1966).
25. P. Langevin, Ann. Chim. Phys. 28, 289 (1903).
26. P. Langevin, Ann. Chim. Phys. 5, 245 (1905). The mathematical portion of this paper is reproduced in English translation in reference (19), pp. 701-726.
27. H.R. Hasse, Phil. Mag. 1, 139 (1926).
28. S. Chapman, Phil. Trans. Roy. Soc. (London) A216, 279 (1916); *ibid.* A217, 115 (1917).
29. D. Enskog, Dissertation (Uppsala, 1917). For a more comprehensive treatment of the Chapman-Enskog theory, see S. Chapman and T.G. Cowling, "The Mathematical Theory of Non-uniform Gases," second ed. (Cambridge University Press, London, 1952).

30. A. Dalgarno, "Atomic and Molecular Processes," ed. by D.R. Bates (Academic, New York, 1962).
31. H.R. Hasse and W.R. Cook, Phil. Mag. 12, 554 (1931).
32. J.O. Hirschfelder, C.F. Curtiss, and R.B. Bird, "Molecular Theory of Gases and Liquids," Chapter 1, 12-14 (Wiley, New York, 1954).
33. H.S.W. Massey and C.B.O. Mohr, Proc. Roy. Soc. (London) A144, 188 (1934).
34. A. Dalgarno and A. Williams, Proc. Phys. Soc. (London) A72, 274 (1958).
35. A.M. Arthurs and A. Dalgarno, Proc. Roy. Soc. (London) A256, 540, 552 (1960).
36. G.H. Wannier, Phys. Rev. 83, 281 (1951); *ibid.* 87, 795 (1952).
37. G.H. Wannier, J. Bell System Tech. 32, 170 (1953).
38. J.A. Hornbeck, Phys. Rev. 83, 374 (1951); *ibid.* 84, 615 (1951).
39. R.N. Varney, Phys. Rev. 88, 362 (1952); *ibid.* 89, 708 (1953).
40. T. Kihara, Rev. Mod. Phys. 24, 45 (1952); *ibid.* 25, 844 (1953).
41. E.A. Mason and H.W. Schamp, Ann. Phys. (New York) 4, 233 (1958).
42. V.I. Perel, Soviet Phys.-JETP 5, 440 (1957).
43. A.M. Tyndall, "The Mobility of Positive Ions in Gases" (Cambridge University Press, Cambridge, 1938).
44. E.C. Beaty. Phys. Rev. 104, 17 (1957).
45. E.C. Beaty, "Proceedings of the Fifth International Conference on Ionization Phenomena in Gases, Munich, 1961", volume I, pp. 183 (North-Holland Amsterdam, 1962).
46. E.C. Beaty. and P.L. Patterson, "Sixth International Conference on Ionization Phenomena in Gases" (Paris, 1963).
47. E.C. Beaty. and P.L. Patterson, Phys. Rev. 137, A346 (1965); *ibid.* 170, 116 (1968).

48. J.A. Hornbeck and J.P. Molnar, Phys. Rev. 84, 621 (1951).
49. M.A. Biondi, Phys. Rev. 90, 730 (1953); *ibid.* 93, 1136 (1954).
50. M.A. Biondi and L.M. Chanin, Phys. Rev. 94, 910 (1954); *ibid.* 122, 843 (1961).
51. L.M. Chanin and M.A. Biondi, Phys. Rev. 107, 1219 (1957).
52. L.M. Chanin and R.D. Steen, Phys. Rev. 132, 2554 (1963).
53. K.B. McAfee, D. Sople, and D. Edelson, Phys. Rev. 160, 130 (1967).
54. T.M. Miller, J.T. Moseley, D.W. Martin, and E.W. McDaniel, Phys. Rev. 173, 115 (1968).
55. C.E. Young, D. Edelson, and W.E. Falconer, J. Chem. Phys. 53, 4295 (1970).
56. D. Smith, A.G. Dean, and N.G. Adams, Z. Physik 253, 191 (1972).
57. P.R. Smy, Adv. in Phys. 25, 517 (1976).
58. A. Fick, Ann. Phys. 170, 59 (1855).
59. J. Crank, "The Mathematics of Diffusion", 2nd ed. (Oxford University Press, London, 1975) and references there in.
60. J.T. Moseley, R.M. Sunggs, D.W. Martin, and E.W. McDaniel, Phys. Rev. Lett. 21, 873 (1968).
61. E.W. McDaniel and J.T. Moseley, Phys. Rev. A3, 1040 (1971).
62. P.D. Foote and F.L. Mohler, Phys. Rev. 26, 195 (1925).
63. F.L. Mohler, P.D. Foote, and R.L. Chenault, Phys. Rev. 27, 37 (1926).
64. R.B. Green, R.A. Keller, P.K. Schenck, J.C. Travis, and G.G. Luther, J. Amer. Chem. Soc. 98, 8517 (1976).
65. J.C. Travis, G.C. Turk, and R.B. Green, Anal. Chem. 54, 1006A (1982).
66. P.K. Schenck, D.S. King, K.C. Smyth, J.C. Travis, and G.C. Turk, "Lasers in Chemistry" M.A. West ed., pp 431 (Elsevier, New York, 1977).

67. J.C. Travis, G.C. Turk, and R.B. Green, "New Applications of Lasers to Chemistry" G.M. Hieftje ed., chapter 6 (ACS Symposium Series 85, American Chemical Society, Washington, D.C., 1978)
68. J.E.M. Goldsmith and J.E. Lowler, Comtemp. Phys. 22, 235 (1981).
69. D.S. King and P.K. Schenck, Laser Focus 14, 50 (1978).
70. P.K. Schenck and J.W. Hastie, Opt. Eng. 20, 522 (1981).
71. J.C. Travis and J.R. Devoe, "Lasers in Chemical Analysis", G.M. Hieftje, J.C. Travis, and F.E. Lytle, eds., Chapter 5 (Humana Press, Clifton, New Jersey, 1981).
72. J.C. Travis, J. Chem. Ed. 59, 909 (1982).
73. N.B. Zorov, Y.Y. Kuzyakov, and O.I. Matveen, J. Anal. Chem. USSR 37, 400 (1982).
74. K.C. Lin, Ph.D. Thesis (Michigan State University, 1982).
75. F.M. Curran, Ph.D. Thesis (Michigan State University, 1983).
76. C.A. van Dijk, F.M. Curran, K.C. Lin and S.R. Crouch, Anal. Chem. 53, 1275 (1981).
77. G.S. Hurst, M.G. Pyane, S.D. Kramer, and J.P. Young, Rev. Mod. Phys. 51, 767 (1979).
78. F.M. Curran, K.C. Lin, G.E. Leroy, P.M. Hunt, and S.R. Crouch, Anal. Chem. 55, 2382 (1983).
79. F.M. Curran, C.A. vanDijk, and S.R. Crouch, Appl. Spectrosc. 37, 385 (1983).
80. R.F. Browner and A.W. Boorn, Anal. Chem. 56, 786A, 876A (1984).
81. J.E. Hall and R.B. Green, Anal. Chem. 55, 1811 (1983).
82. R.B. Green and J.E. Hall, J. Phys., Colloq., C7, 319 (1983).
83. J.E. Hall and R.B. Green, Anal. Chem. 57, 431 (1986).
84. G.C. Turk and R.L. Watters Jr., Anal. Chem. 57, 1979 (1985).

85. I.V. Bykov, A.B. Skvortsov, Y.G. Tatsli, and N.V. Chekalin, J. Phys. Colloq. C7, 345 (1983).
86. W.B. Whitten, L.B. Koutny, T.G. Nolan, and J.M. Ramsey, Anal. Chem. 59, 2203 (1987).
87. T. Berglind, L. Casparsson, J. Phys. Colloq. C7, 329 (1983).
88. O. Axner, I. Lindgren, I. Magnusson, and H. Rubinsztein-Dunlop, Anal. Chem. 57, 776 (1985).
89. N. Omenetto, T. Berthoud, P. Cavalli, and G. Rossi, Anal. Chem. 57, 1256 (1985).
90. O. Axner, T. Berglind, J.L. Heully, I. Lindgren, and H. Rubinsztein-Dunlop, J. Appl. Phys. 55, 3215 (1984).
91. B.W. Smith, L.P. Hart, and N. Omenetto, Anal. Chem. 58, 2147 (1986).
92. G.J. Havrilla and K.-J. Choi, Anal. Chem. 58, 3095 (1986).
93. G.C. Turk and N. Omenetto, Appl. Spectrosc. 40, 1085 (1986).
94. P.L. Larkins, Spectrochim. Acta B39, 1365 (1984).
95. H.O. Behrens, G.H. Guthoehriein, and A.J. Kasper, J. Phys. Colloq. C7, 239 (1983).
96. D.S. Gough, P. Hannaford, Opt. Commun. 55, 91 (1985).
97. M. Inguscio, J. Phys. Colloq. C7, 217 (1983).
98. M. Broglia, F. Catoni, and P.J. Zampetti, J. Phys. Colloq. C7, 251 (1983).
99. R. Engleman, Jr, R.A. Keller, and C.M. Miller, J. Opt. Soc. Am. B: Opt. Phys. 2, 897 (1985).
100. J.D. Ingle, Jr. and S.R. Crouch, "Spectrochemical Analysis" (Prentice Hall, Englewood Cliffs, New Jersey, 1988).
101. V.S. Burakov, P.A. Naumenkov, G.T. Razdobarin, and N.V. Tarasenko, Chem. Abstr. 99, 18584 (1984).
102. K. Takada and K. Hirokawa, Spectrochim. Acta B39, 1113 (1984).

103. M. Broglia, F. Catoni, and P.J. Zampetti, J. Phys. Colloq. C7, 479 (1983).
104. M.A. Nippoldt and R.B. Green, Anal. Chem. 55, 554 (1983).
105. G.J. Havrilla, P.K. Schenck, J.C. Travis, and G.C. Turk, Anal. Chem. 56, 186 (1984).
106. J.E. Hall and R.B. Green, Anal. Chem. 57, 16 (1985).
107. T. Berthoud, J. Lipinsky, P. Camus, and J-.L. Stechle, Anal. Chem. 55, 959 (1983)
108. J.C. Travis, G.C. Turk, J.R. De Voe, P.K. Schenck, and C.A. vanDijk, Prog. Anal. At. Spectrosc. 7, 199 (1984).
109. P. Camus, J. Phys. Colloq. C7, 87 (1983).
110. C.Th.J. Alkemade, Tj. Hollander, W. Snelleman, and P.J.Th. Zeegers, "Metal Vapours in Flames" (Pergamon Press, Oxford, 1982).
111. Y.Y. Kuzyakov, N.B. Zorov, N.I. Chaplygin, and O.A. Novodvorskii, J. Phys. Colloq. C7335 (1983).
112. T. Berthoud, P. Camus, N. Drin, and J-.L. Stechle, J. Phys. Colloq. C7, 389 (1983).
113. N.G. van Kampen, "Stochastic Description of Many-body Systems", preprint, (Institute for Theoretical Physics of the University of Utrecht, 1979).
114. S.R. Milner, Phil. Mag. 23, 551 (1912); *ibid.* 25, 742 (1913).
115. R.A. Marcus, J. Chem. Phys. 20, 364 (1952).
116. M. Karplus and R.N. Porter, "Atoms and Molecules" Chap. 4 and 5 (Benjamin, New York, 1970).
117. L. de la Pena and A.M. Cetto, Found. Phys. 12, 1017 (1982).
118. L. Boltzmann, "Lectures on Gas Theory", trans. by S.G. Brush (Univ. of California Press, Berkeley, 1964)
119. J.P. Perrin, "The Atom" (Leipzig and Dresden, 1914).
120. R. Kubo, Science 233, 330 (1986).
121. R. Brown, Phil. Mag. 4, 161 (1828); *ibid.* 6, 161 (1829).

122. K. Huang, "Statistical Mechanics" (Wiley, New York 1963).
123. H. Risken, "The Fokker-Planck Equation, Methods of Solution and Applications" (Springer-Verlag, Berlin, 1984).
124. A.D. Fokker, Ann. Phys. 43, 810 (1914).
125. M. Planck, Sitzber. Preub. Akad. Wiss., pp. 324 (1917).
126. A. Kolmogorov, Mathem. Annalen 104, 415 (1931).
127. R.I. Cukier, K. Lakatos-Lindenberg, and K.E. Shuler, J. Statist. Phys. 9, 137 (1973).
128. N. Wax, "Selected Papers on Noise and Stochastic Processes" (Dover, New York, 1954).
129. H. Haken, Rev. Mod. Phys. 47, 67 (1975).
130. G.E. Uhlenbeck and L.S. Ornstein, Phys. Rev. 36, 823 (1930).
131. L. Onsager and S. Machlup, Phys. Rev. 91, 1505 (1953).
132. S. Machlup and L. Onsager, Phys. Rev. 91, 1512 (1953).
133. R. Graham, "Statistical Theory of Instabilities in Stationary Non-Equilibrium Systems with Applications to Lasers and Non-linear Optics", Springer Tracts in Modern Physics, 66, G. Hoehler ed. (Springer-Verlag, Berlin, 1973).
134. W. Horsthemke and A. Bach, Z. Phys. B22, 189 (1975).
135. H. Hasegawa, Progr. Theor. Phys. 55, 90 (1976); *ibid.* 56, 44 (1976).
136. M. Suzuki, Progr. Theor. Phys. 55, 383 (1976); *ibid.* 56, 77, 477 (1976).
137. H. Ueyama, Physica A84, 392, 402 (1976).
138. H. Haken, Phys. Lett. A55, 323 (1976).
139. M. Moreau, Physica A90, 410 (1978).
140. H. Dekker, Phys. Rev. A19, 2102 (1979).
141. H. Wiener, J. Math. Phys. 2, 131 (1923).

142. H. Wiener, Proc. London Math. Soc. Second Ser. 22, 454 (1924).
143. H. Wiener, Acta Math. 55, 117 (1930).
144. H. Wiener, "Nonlinear Problems in Random Theory" (MIT, Cambridge, Mass., 1958).
145. K. Kitahara, H. Metiu, and J. Ross, J. Chem. Phys. 63, 3156 (1975).
146. H. Metiu, K. Kitahara, and J. Ross, J. Chem. Phys. 64, 292 (1976); *ibid.* 65, 393 (1976).
147. H. Metiu, K. Kitahara, and J. Ross, J. Chem. Phys. 63, 5116 (1975).
148. H. Dekker, Physica A84, 205 (1976); *ibid.* A92, 438 (1978).
149. H. Dekker, Phys. Lett. A76, 8 (1980).
150. F.W. Wiegel, Physica 33, 734 (1967); *ibid.* 37, 105 (1967).
151. F.W. Wiegel, Physics Reports 16, 57 (1975).
152. F. Langouche, D. Roekaerts, and E. Tirapegui, Physica A97, 193 (1979).
153. B.H. Lavenda, Phys. Lett. A71, 304 (1979).
154. M.-O. Hongler, Physica D2, 353 (1981).
155. K.L.C. Hunt and J. Ross, J. Chem. Phys. 75, 976 (1981).
156. P.M. Hunt, K.L.C. Hunt, and J. Ross, J. Chem. Phys. 79, 3765 (1983).

CHAPTER II

EXPERIMENTAL

A. Overview

The dual laser ionization (DLI) system used in this work is analogous to that used in laser-enhanced ionization (LEI) experiments. However, in addition to the tunable dye laser, another laser beam is used to photoionize the excited atoms in the flame cell.

Figure 2-1 shows a simplified schematic diagram of the experimental system used in this work. A dye laser beam and a portion of the nitrogen pump laser beam are directed into a flame cell so that they overlap spatially and temporally. The ions generated by the laser pulses are then collected by a pair of voltage-biased probes immersed in the flame. The current detected is converted into a voltage by a current-to-voltage converter. The output voltage signal from the amplifier is the input of the boxcar integrator, which is triggered synchronously by radio frequency noise produced when the N_2 pumping laser is fired. The output from the

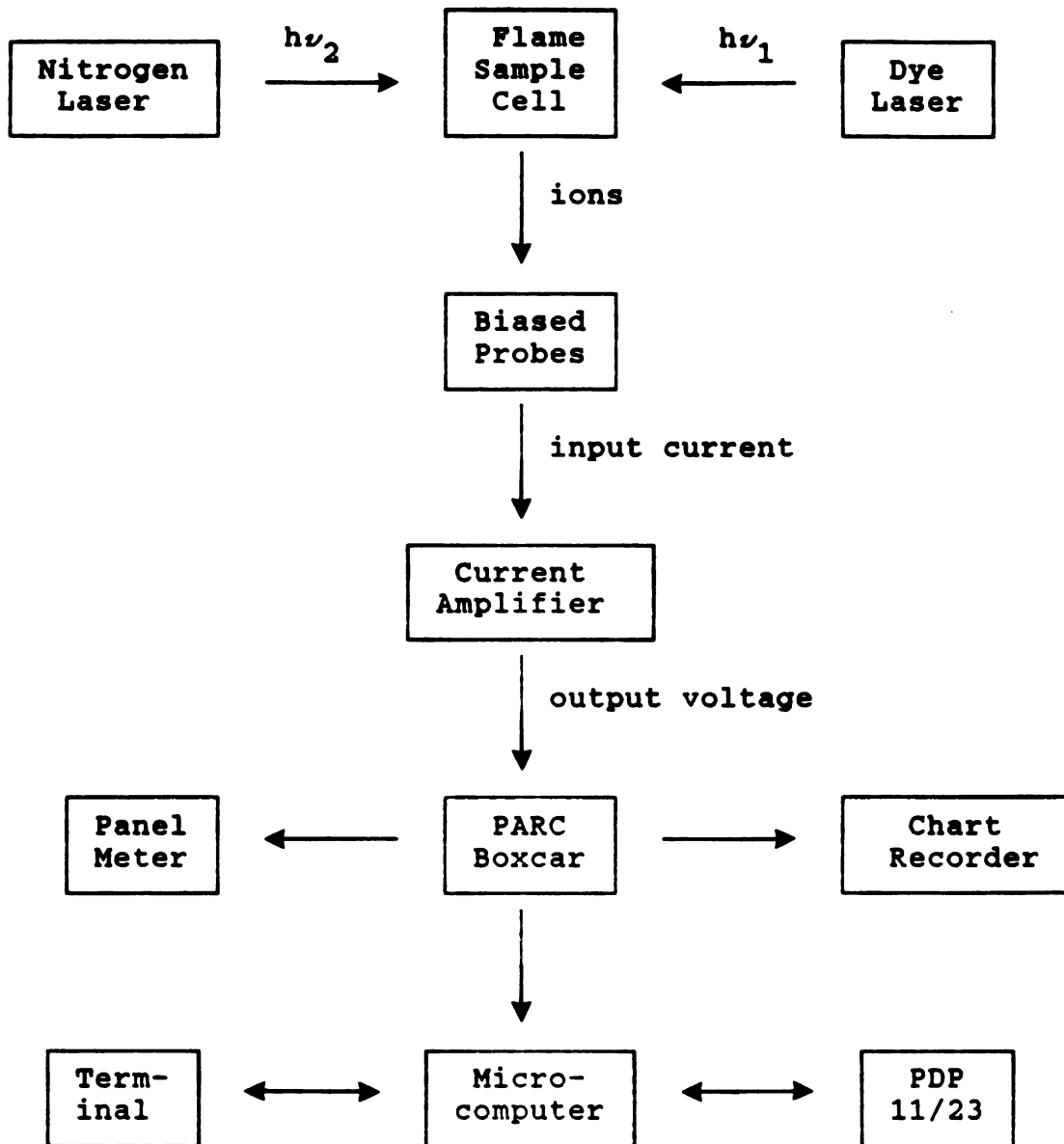


Figure 2-1. Block diagram of dual laser ionization experimental set-up.

boxcar integrator is sent to a front panel meter and a strip-chart recorder, or to a microcomputer, which is interfaced with the boxcar integrator through the back panel. The microcomputer usually (i) downloads controller programs from the mainframe PDP/11-23, (ii) takes control parameters from the user through a terminal, (iii) controls the scanning functions of the boxcar integrator, (iv) takes data from the boxcar integrator, and (v) uploads the data to the mainframe for future data processing.

Except for the microcomputer interfaced boxcar integrator system, the details of the DLI experimental setup have been described by Lin (1) and Curran (2); hence only the general characteristics of each individual component are mentioned in this chapter. However, the function of the microcomputer interfaced boxcar integrator system will be portrayed in detail in later sections.

B. Laser System

In a typical DLI experiment, a nitrogen-laser pumped, tunable dye laser is focused into the flame cell to promote atoms from the ground state to an excited state. A portion of the nitrogen laser beam is deflected by a mirror and then focused into the flame cell to be temporally and spatially coincident with the dye laser in order to photoionize the

excited atoms. A simplified schematic diagram that shows the experimental arrangement of the optical elements for the dual laser system is depicted in Figure 2-2.

The nitrogen (N_2) laser (Model 0.5-150, NRG Inc., Madison, WI), as shown in Figure 2-2, is used both as a pumping source for the tunable dye laser and as the ionizing beam in DLI experiments. The rated peak power output of the nitrogen laser at a repetition rate of 60 Hz is 500 kW; the portion of the beam split off and used for ionization had a radiant power between 100 and 150 kW. The nitrogen laser beam is focused by a quartz lens and its focal area was determined to be $(2.0 \pm 0.4) \times 10^{-4} \text{ cm}^2$. The general specifications of the nitrogen laser are given in Table 2-1. The major disadvantage of the nitrogen laser as a pumping source is the radio frequency interference (RFI) broadcast when the breakdown of the spark gap occurs. This introduces noise to all of the associated electronics. A Faraday cage made of 0.50 mm copper plates was placed around the nitrogen laser to minimize this noise. It was found that cleaning up the spark gas electrodes or replacing them sufficiently often can effectively reduce the RFI noise and reduce the pulse-to-pulse laser power fluctuations. Electrodes were usually cleaned by sandpaper, and the replacement electrodes were copied from the originals by the machine shop. A strict cleaning schedule was maintained since the stability of the nitrogen laser output is extremely important to the

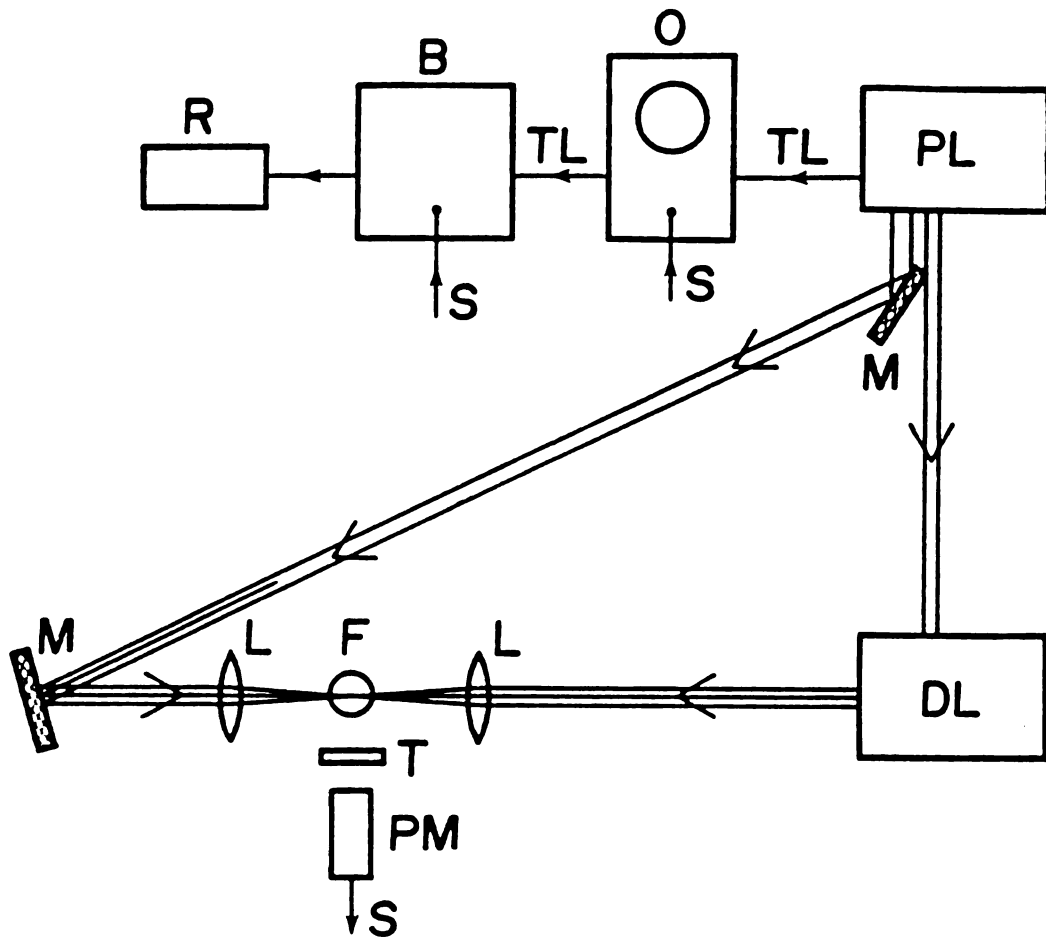


Figure 2-2. Simplified schematic diagram of the dual laser system. B, boxcar; DL, dye laser; F, flame; L, lens; M, mirror; O, oscilloscope; PL, pump laser (nitrogen laser); R, x-t chart recorder, S, signal; TL, trigger line.

Table 2-1. Specifications of the Nitrogen Laser

=====		
Repetition Rate		1 - 60 Hz
Peak Power at 60 Hz		0.5 MW
Pulse Duration		5 ns FWHM
Average Power at 60 Hz		150 mW
Power Requirement at 120 volts, 60 Hz		10 amp
Beam Divergence	3.8 mrad x 10.7 mrad	
=====		

reproducibility of the time-resolved DLI spectra.

During the operation of the nitrogen laser, the pressure of pre-purified grade nitrogen (Airco Inc., Murray Hill, NJ) was usually varied between 20 to 28 psi while the laser tube pressure was maintained at 72 torr. To avoid short term variations in the tube and spark gap pressures, a dual stage pressure regulator (Model 580, Airco Inc., Murray Hill, NJ) was adopted. The laser was operated at 20 Hz for most DLI experiments.

The nitrogen-pumped tunable dye laser used in these experiments essentially follows the original design described by Hänsch (3). A laser dye solution in a slightly tilted quartz cuvette having mono-layer anti-reflection coatings (Type 509, Precision Cells, Inc., Hicksville, NY) is incorporated into a short optical cavity formed between a diffraction grating and a partially reflecting output coupler. The organic dyes in the cuvette are optically pumped by the repetitively pulsed nitrogen laser placed at a ninety-degree angle to the cavity. A cylindrical quartz lens focuses the nitrogen laser beam to a narrow line inside the quartz cuvette. The subsequent fluorescence radiation is collected by an achromatic inverting telescope (Model 1592, Oriel Corp., Stamford, CN) which collimates and expands the incoming beam in order to cover a larger fraction of the grating surface and consequently reduce the

output radiation bandwidth. Similarly, the second order of the plane diffraction grating (48 square millimeter ruled area with 1180 lines/mm, blaze wavelength 2500 Å) is used to reduce the bandwidth of the output pulses further. The grating is mounted backwards on the sine-bar of a Czerny-Turner grating monochromator (Model EU-700, GCA/McPherson Instruments, Acton, MA) to provide the rotation function needed for tuning the dye laser. The dye laser system must be aligned routinely with a visible, 5 mW randomly polarized helium neon laser (Model 05-LHR-151, Melles Griot, Irvine, CA). A detailed alignment procedure was designed by Curran and is described elsewhere (2). The output of the dye laser can be measured by a joulemeter (Model J3-05, Molelectron Corp., Sunnyvale, CA) and an oscilloscope.

A summary of the dyes used in this work along with their wavelength ranges and typical peak output powers is given in Table 2-2. The wavelength ranges covered by various organic dyes when pumped by a nitrogen laser are shown in Figure 2-3. The temporal overlap and pulse shapes of the nitrogen and dye lasers obtained by Curran (2) with a PIN photodiode (Model 4220, Hewlett Packard, Palo Alto, CA) are shown in Figure 2-4. Figure 2-4 suggests that temporally the ion distribution at the beginning of the ion transport processes can be approximated by a Dirac delta function. In order to increase the power density of the laser, a lens with a 15-cm focal length was set at an

Table 2-2. Characteristics of the Dye Laser

=====

Excitation Beam - Hänsch design, nitrogen laser-pumped
dye laser

Typical Peak Power at Analytical Line - 5 kW

Laser Dye	Approximate Wavelength Range (nm)
-----	-----
PBBO ^a	395 - 410
Stilbene ^a	410 - 440
Coumarin 460 ^a	450 - 480
Rhodamine 6G ^b	565 - 605
DCM ^a	630 - 710

=====

^a Dyes obtained from Exciton Chemical Co., Inc., Dayton, OH.

^b Dye obtained from Eastman Kodak Co., Rochester, NY.

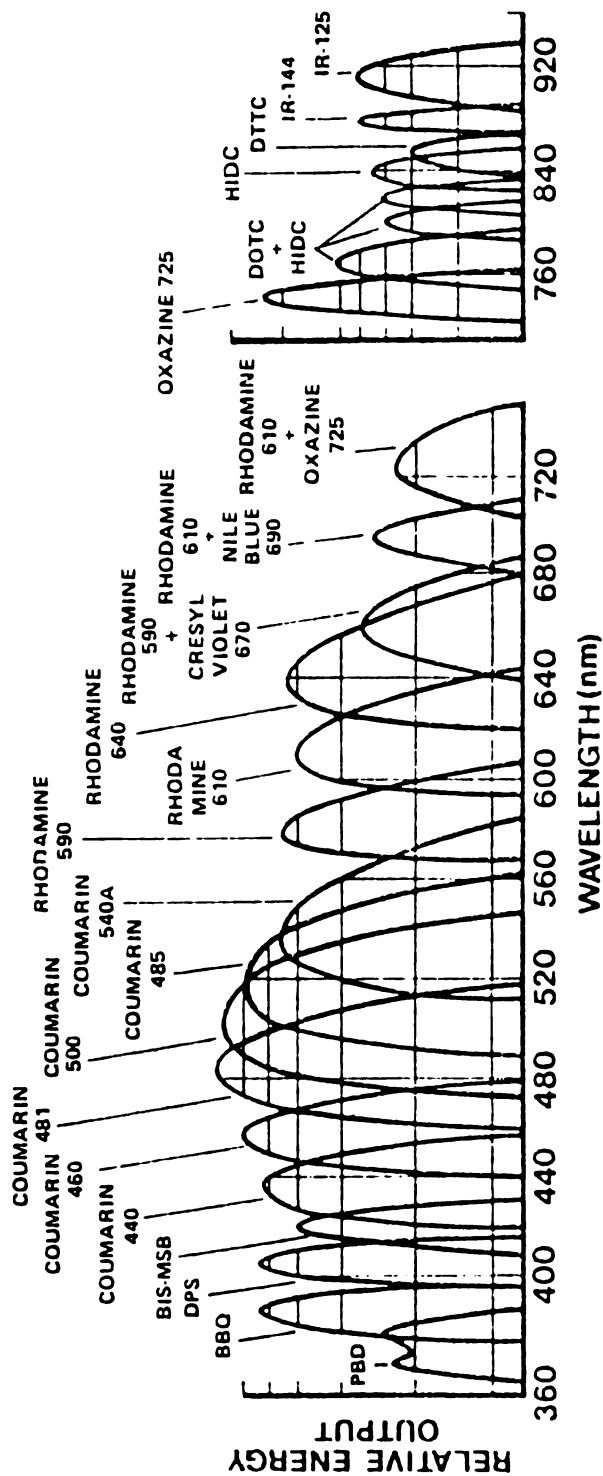


Figure 2-3. The wavelength range of various organic dyes pumped by a 337.1 nm nitrogen laser (Molelectron).
(Taken from the catalog of the Exciton Chemical Co., Inc., Dayton, OH)

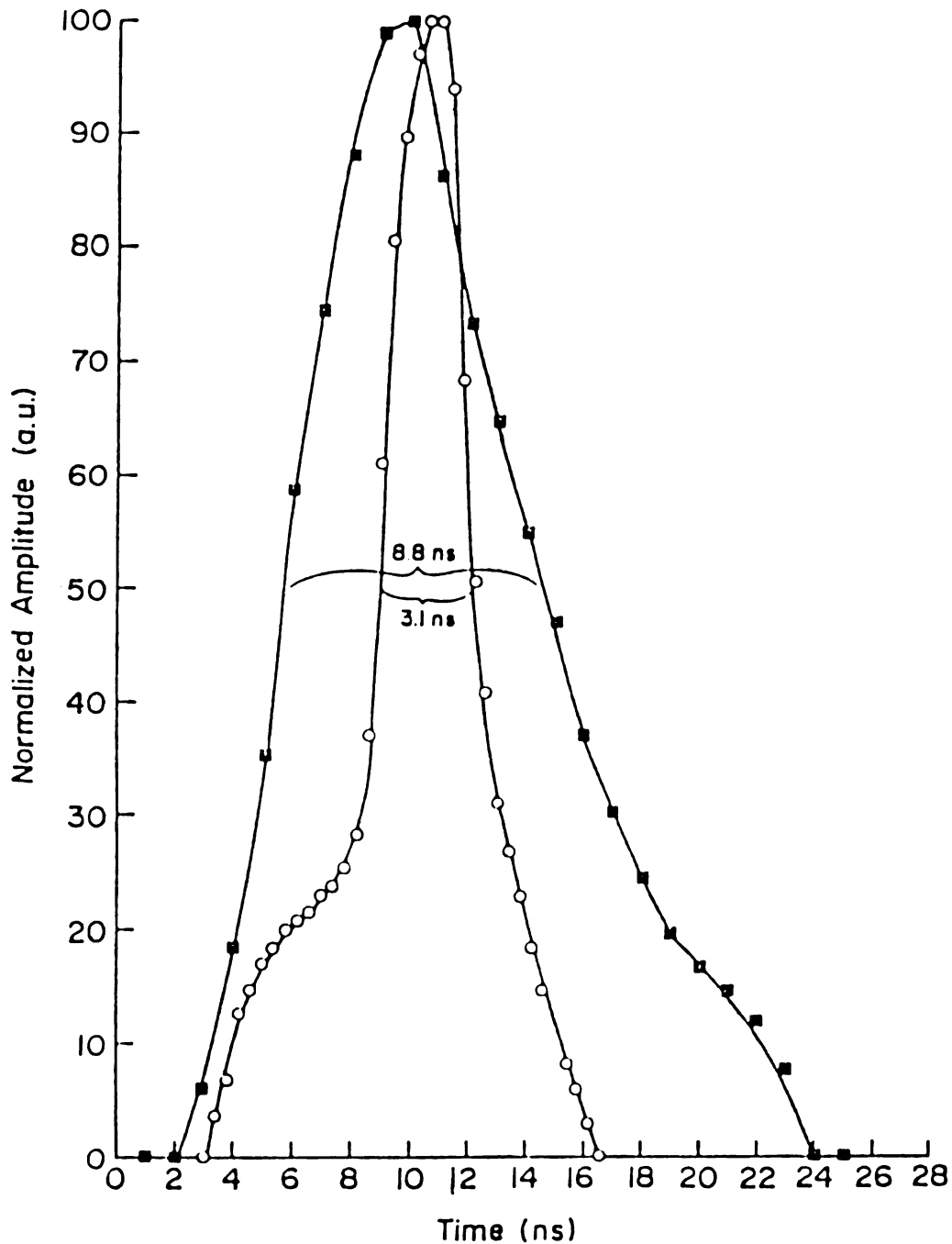


Figure 2-4. Temporal overlap and pulse shapes of the N_2 (■) and dye (o) lasers.
(Taken from F.M. Curran, Ph.D. dissertation, Michigan State University, 1983).

appropriate position between the front mirror and the flame. The focal area of the dye laser through the lens was determined to be $(1.0 \pm 0.3) \times 10^{-3} \text{ cm}^2$. From this measurement, it is clear that the initial spatial distribution of ions is not a true Dirac delta function. In fact, the initial distribution of ions should be approximated by an exponentially modified Gaussian function. More details will be covered in Chapter III.

C. Flame Cell

A laminar-flow, premixed, hydrogen-oxygen-argon flame was used in this work. This flame is similar to the one designed by Lijnse and Elsenaar (4) and has been described by both van Dijk (5) and Lin (1). Extensive reviews of the properties of this flame can be found in the books written by Ingle and Crouch (6), and Alkemade et al. (7). Hence, in this section only the significance and a general description of this flame will be provided.

The burner is of the Meker type; the gas mixture emanates from the burner head through 631 circular holes of 0.5 mm diameter and 5 mm length, which are arranged in concentric circles with a 2 mm interval between successive rings. The height of the primary combustion zone is approximately 2 mm. The burner head is cooled by a water

jacket (5).

Pre-purified grade hydrogen, oxygen, and argon gases are divided into two branches to form the inner and mantle flames, respectively. The pressures of each branch of the flame are controlled by dual pressure regulators. Oxygen and argon gases are premixed first in a mixing chamber fitted with a safety spring; the subsequent gas mixture is then mixed with hydrogen before reaching the burner head. This design can effectively eliminate the spontaneous combustion of the hydrogen and oxygen gases inside the mixing chamber and prevent flashback. The analyte is introduced into the inner flame through a pneumatic nebulizer designed by Curran (2). Argon is the nebulizing gas. The flow rates of gases are controlled by six precision flowmeters (Series FM-1050, Matheson Instruments, Horsham, PA). In general, the central and mantle argon gas settings used gave a flow rate of approximately $3.2 \text{ L}\cdot\text{min}^{-1}$. The mantle flame hydrogen and oxygen flow rate settings gave a stoichiometric mixture of $1.0 \text{ L}\cdot\text{min}^{-1}$ and $0.50 \text{ L}\cdot\text{min}^{-1}$, respectively. To obtain maximum DLI signals, the hydrogen and oxygen settings of the central flame usually were adjusted to be slightly fuel-rich.

The laminar-flow, premixed $\text{H}_2\text{-O}_2\text{-Ar}$ flame is one of the most important premixed flames (4,8). Although it gives low temperature flames, it has very low flame background

emission and less ionization interferences than air-acetylene flames. In fact, laminar-flow, premixed flames are less turbulent, less audibly noisy, and have less flame flicker than turbulent flames (9). The mantle flame prevents entrainment of air and smooths the radial temperature distribution of the inner flame. It is usually kept at the same temperature as the inner flame to avoid heat transfer between the inner and the mantle flame, and thus turbulent convection inside the inner flame. These characteristics furnish a less complicated environment for theoretical modelling of ion transport processes, as will be discussed in detail in later chapters.

D. Signal Detection

The ions formed by the laser pulses, which occur on the nanosecond scale, are collected by a pair of voltage-biased nichrome probes immersed in the flame cell. Usually the laser focal point is placed near the lower probe in order to get the maximum DLI signal. The current sensed by the probes is converted to voltage by an operational amplifier; the output of the amplifier then goes to the input port of the boxcar integrator. Figure 2-5 shows a block diagram of the experimental set-up of the DLI signal detection system. In this work, the upper probe is connected to virtual ground and serves as the anode, while a high-voltage power supply

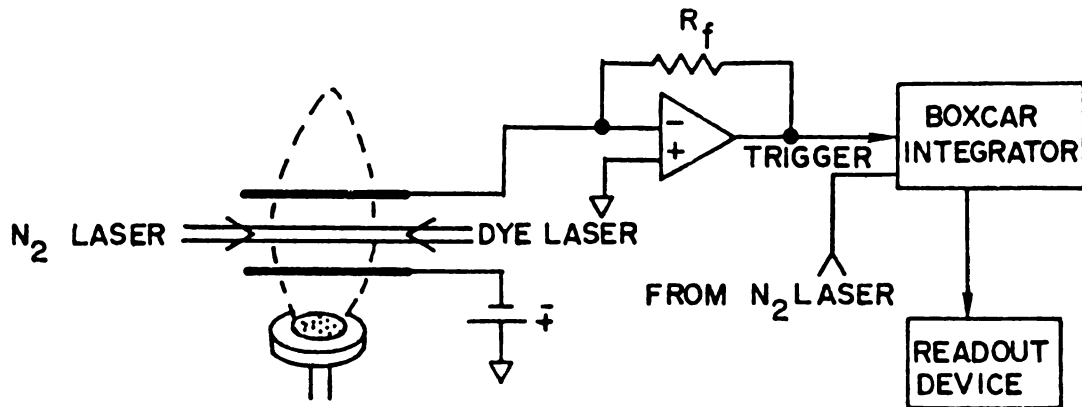


Figure 2-5. Block diagram of the ionization signal collection circuit.

(Model 3K10B, Power Designs, Inc., Westbury, NY), which is switched to supply a negative voltage, is connected to the lower probe. The lower then serves as the cathode. Hence the electrons generated by the laser pulses will be collected by the upper probe (anode) and the positive metal ions will be collected by the lower probe (cathode). The probes are placed parallel to each other in a plane perpendicular to the burner head. The probes were typically 4-10 mm apart; the lower probe is placed about 10 mm above the burner head in order to get stable and reproducible DLI signals. Each probe is mounted on a micrometer-driven translation stage with a positional accuracy of ± 0.01 mm. Both probes can be moved three-dimensionally inside the flame. Figure 2-6 shows the arrangement of the electrodes in the flame and the designation of mathematical terms used in later chapters.

The probes used to collect the ionization signal were either nichrome or iridium wires of which the diameters were almost always 0.025" (0.64 mm). Nichrome wire, which was most often used in this work, is very inexpensive. In addition, it can satisfactorily resist the high temperature environment of the flame. However, analyte contamination usually grows gradually on the surface of the nichrome wire upon continued use. Also, leaching from the probe may lead to significant electrical interference when different analytes are introduced into the flame over a short time

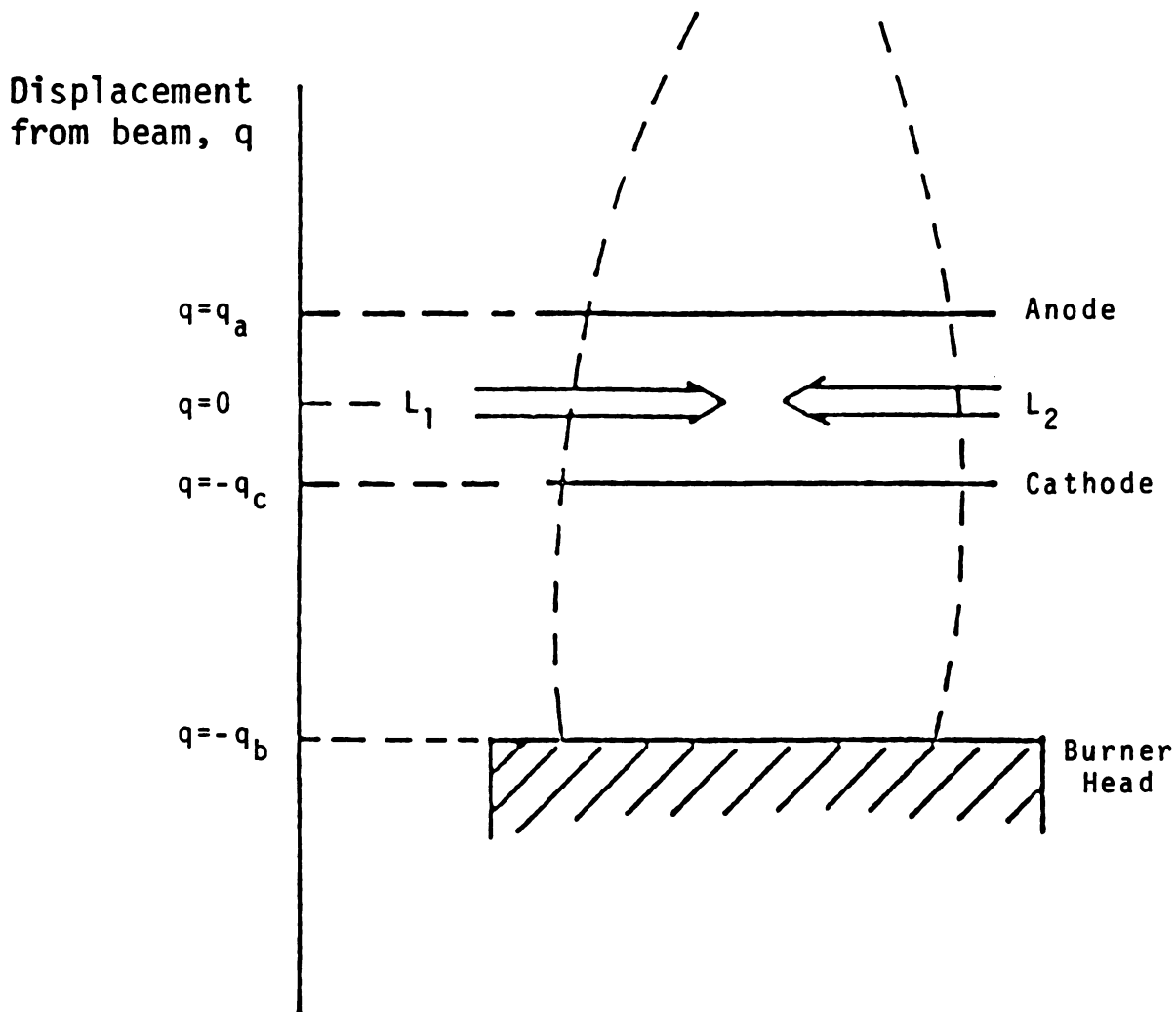


Figure 2-6. Schematic diagram of the probe configuration.

The anode and cathode were positioned horizontally and parallel to the colinear dye and N_2 laser beams L_1 and L_2 . The center of the laser beams usually are focused about 10 mm above the burner head. The vertical "displacement from beam center" distance q is defined such that $q_a > 0 > -q_c > -q_b$.

period. To ensure the reproducibility of the time-resolved DLI signals, probes must be cleaned with sandpaper or replaced frequently.

The current-to-voltage converter was designed and constructed by Curran (2); the circuitry is shown in Figure 2-7. The operational amplifier used was an "Ultra Fast" JFET amplifier (LH0032CG, National Semiconductor, Santa Clara, CA). The slew rate of this amplifier is 500 volts per micro-second, and its bandwidth is 70 MHz. The ground of the amplifier is connected to the ground of the high-voltage power supply; the whole amplifier module is mounted on the burner base in order to reduce the length of the probe cables and minimize the RFI interference. The power supply (± 15 V) for the amplifier module is made from a commercial power supply (AD902, Analog Devices, Norwood, MA) in a homemade circuit board framed in a shielded case. The input current can be conducted to the amplifier either directly or through a high pass filter network before being amplified. The gain of the amplifier is switch selectable among 10^4 , 5×10^4 , 10^5 , 5×10^5 , and 2×10^6 , with feedback resistors of 10, 50, 100, 500, and 2000 k Ω , respectively. If the filter is applied to the input signals, the gain will be frequency dependent due to the RC circuit. The filter for the amplifier was found to be essential for the low-frequency flame noise when an air-acetylene flame was used. However, it also distorts the time-resolved signal in the

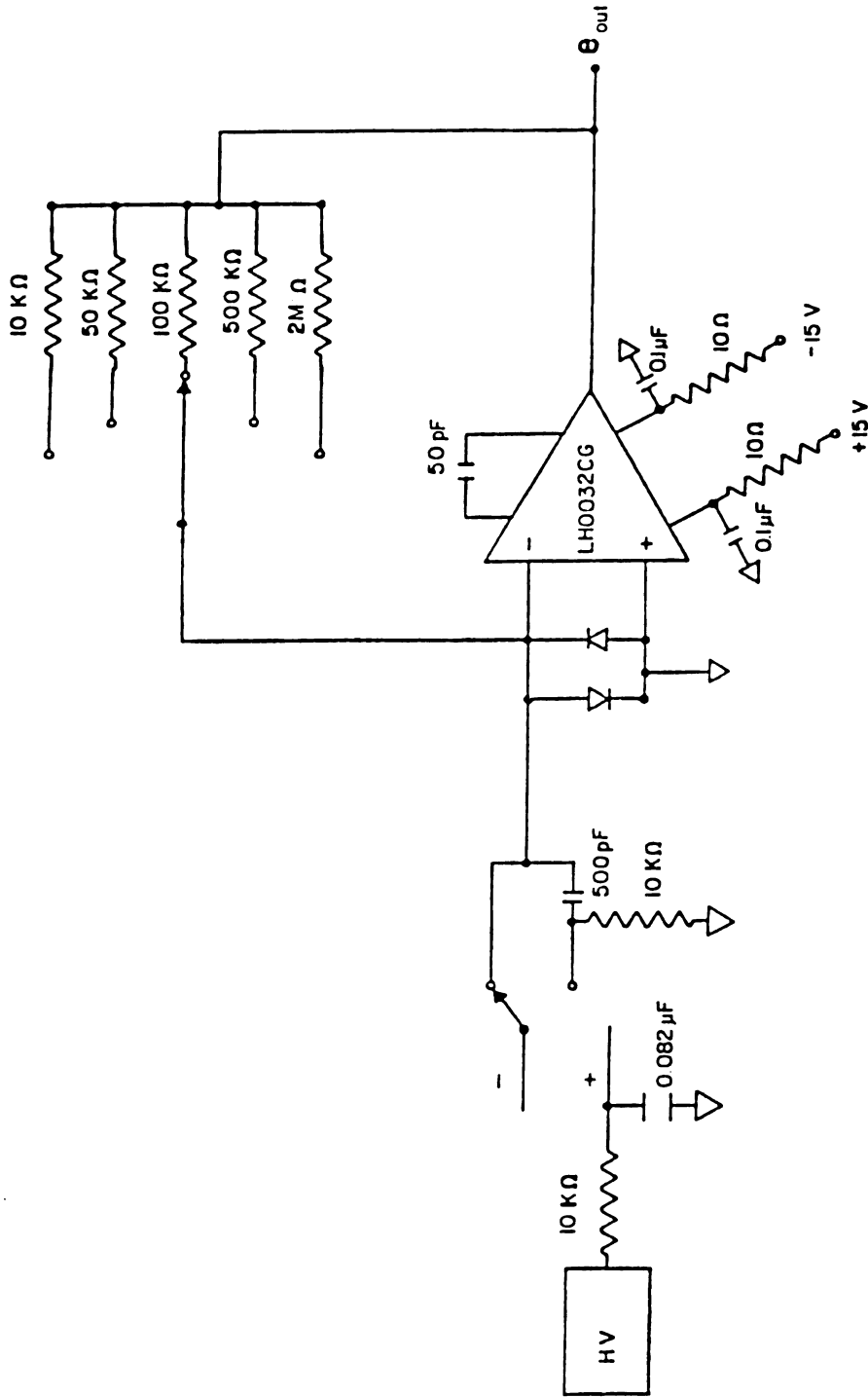


Figure 2-7. Ionization signal collection circuitry.
(Taken from F.M. Curran, Ph.D. dissertation,
Michigan State University, 1983).

H₂-O₂-Ar flame, hence in this work the filter was not applied. If the high pass filter is by-passed, the slew rate of the LH0032CG amplifier guarantees minimum distortion if the time scale of the DLI signals being observed is at microsecond level. In fact, the design of the amplifier has limited the functions of the boxcar integrator in detecting time-resolved signals with a short aperture delay range. However, since the shape of the time-resolved DLI signal during the first tenths of a microsecond, or even the first few microseconds, was not of major concern in this work, this restriction due to the amplifier could be practically ignored.

E. Boxcar Integrator

The boxcar integrator provides a relatively simple method of signal enhancement for repetitive signals, especially those with short pulse durations and low duty cycles. It allows the recovery of signals that are synchronized with external trigger pulses from random noise. With a continuously variable gate delay generator, the sampling gate can be positioned anywhere along the signal waveform to produce a time-resolved plot of the input signal. A block diagram of a boxcar integrator is shown in Figure 2-8.

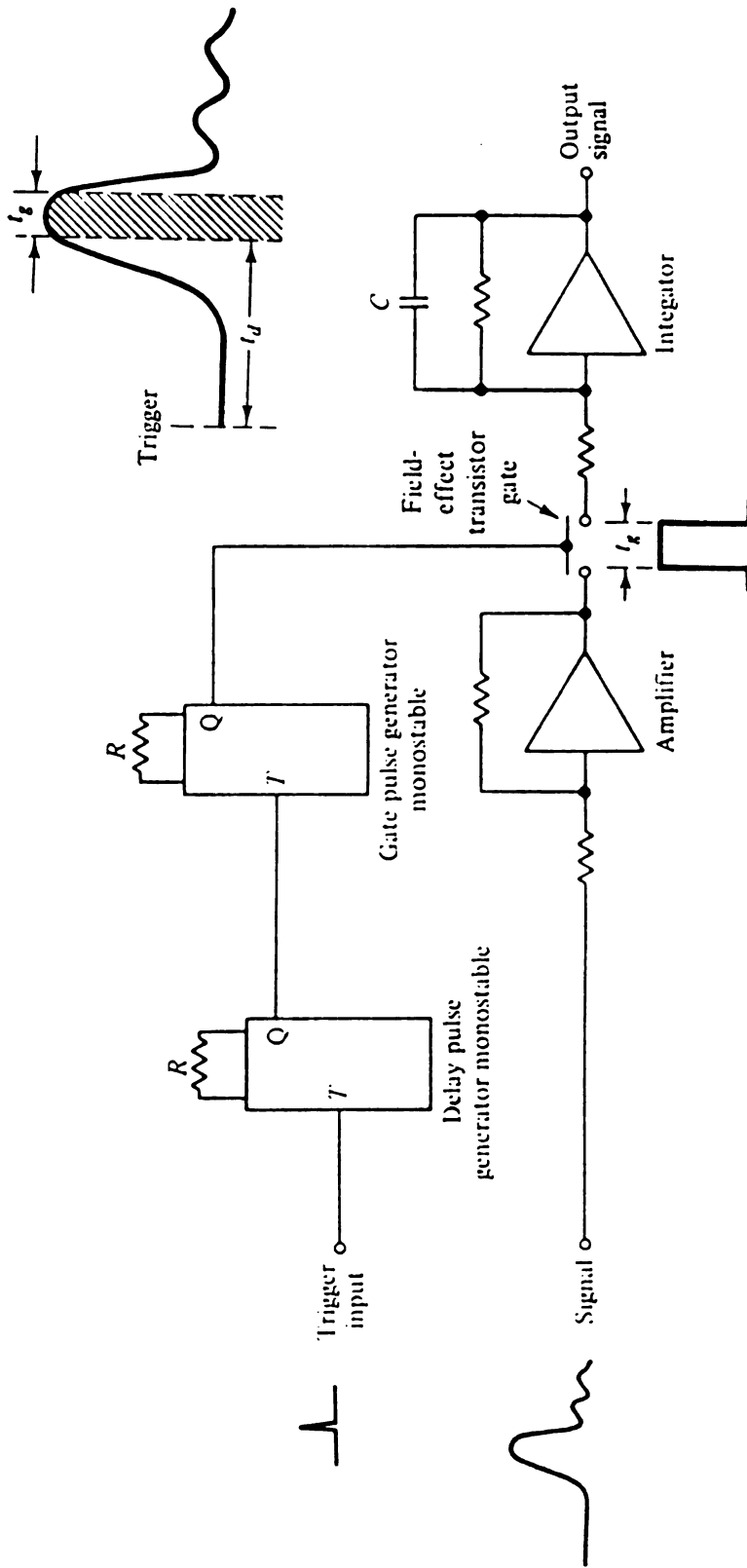


Figure 2-8. Block diagram of a boxcar integrator.

The boxcar integrator (Model 162-164, Princeton Applied Research Corp., Princeton, New Jersey) used in our laboratory is composed of three major parts: a model 162 boxcar averager main frame with a model 163 sampling integrator, and a model 164 gated integrator module. The boxcar integrator can be controlled by a microcomputer through the back panel.

The model 162 mainframe determines the time delay for the aperture and provides signal conditioning for the output. The sampling gate of both the model 163 and the model 164 can be positioned anywhere along the signal waveform by adjusting the % initial A or B dial, or it can be time-scanned across all or a portion of the signal by adjusting the scan signal.

The aperture delay is the time between the trigger pulse and the opening time of the aperture in the gated integrator. In our experiments, the boxcar integrator was triggered synchronously by radio frequency noise produced when the N_2 pumping laser is fired. The length of the aperture delay is determined by the aperture delay range and a % Initial setting. The aperture delay range determines the time duration along the waveform of the input signal that the boxcar integrator will scan through upon the trigger pulses. The aperture delay range can be set from 100 nanoseconds to 50 milliseconds by a switch on the front

panel of the boxcar integrator. The % Initial control, which determines the percentage of the aperture delay range setting that the boxcar integrator should wait for before opening the gate. It can be set by two continuously variable 10 turn precision potentiometers, the % Initial A and the % Initial B switches. In the default setup, % Initial A controls the signal from channel A, which takes signals from the Model 163, while % Initial B controls channel B, which takes signals from the model 164. In scanning mode, the aperture delay is also affected by the scan signal. When the internal scan mode is chosen, the boxcar integrator will generate a voltage ramp which slowly sweeps the aperture delay from the limit set by the % Initial control to the limit set by the aperture delay range control. In contrast, when the external scan mode is chosen, the ramp signal can be supplied externally via back panel connectors. In our experiment, the scan signal is usually controlled by the microcomputer through the interface. Mathematically, the aperture delay can be expressed as follows:

$$D = \frac{R * (\%I + 10V)}{100} \quad [1]$$

where D is the aperture delay, R is the aperture range with the same units as that of D, %I is the % Initial A or B, and V is the ramp voltage supplied by the boxcar integrator (internal scan mode) or the external circuitry (external

scan mode). In fact, there is a so-called "dead time" delay of about 75 nanoseconds before the boxcar aperture opens to manipulate the signal. This restriction, due to the design, limits the function of the boxcar integrator to a certain extent. However, since the lifetime of ions produced by the laser pulse is on the order of microseconds, it is not necessary to employ a delay line to prevent the signal from appearing prior to the gate. The aperture signal is also sent to three different comparators. The first comparator determines when the delay ramp has reached full scale, and resets the ramp generation circuitry. The other two comparators generate the gate signals for the model 163 and 164.

The second main function of the mainframe is to provide various combinations of the channel A and B outputs. For the output port, the model 162 supplies a filter to help reduce the noise components of the signal. The time constant for this filter is switch selectable from the front panel, and can vary from 0.1 millisecond to 10 seconds.

The model 164 gated integrator allows greater flexibility in the aperture duration selection than the model 163, and is the module with which the data were acquired. The gate-width of the sampling duration, or the aperture duration, can be selected from 5 nanoseconds to 5 milliseconds by a continuously variable switch. The model

164 has built-in circuitry that will integrate the input signals, upon receiving the external trigger pulse, for a time period determined by the setting of the aperture duration switch on the front panel. Two different modes of operation may be selected for the integration. When the sum averaging mode is chosen, the result of each integration is added linearly to the previous values until the output is overloaded. The output in this mode is simply the average of N repetitions. For white noise the signal-to-noise ratio (SNR) can be improved by the square root of N. The summing mode is analogous to linear integration with an analog integrator. When the exponential averaging mode is chosen, the difference between the input and output signals is integrated, and the output signal asymptotically approaches the input signal. After about 5 time constants of the integrator, the output will be essentially the same as the input, and there will be no further change in the output signal. The exponential mode is analogous to low-pass filtering with an RC filter, and is the mode normally used. The value for the time constant is switch-selectable from the front panel of the model 164 mainframe.

In contrast, the model 163 utilizes a selection of plug-in sampling units to obtain non-adjustable sampling gate widths ranging from 75 picoseconds to 1 nanosecond. Consequently, the model 163 is preferably employed to sample a fast signal such as nanosecond fluorescence decays.

However, for time-integrated signals or for longer decay times, the model 164 is preferred because its variable gate width can be adjusted to obtain a maximum signal-to-noise ratio. Although a baseline sampling gate, associated only with the model 163, would be useful to eliminate the distortion caused by baseline drift on time-scanned signals, such distortion seemed negligible in these experiments.

F. Microcomputer and Boxcar Integrator Interface

The boxcar integrator is interfaced and controlled by a microcomputer through the back panel. The details of the interface and microcomputer are described elsewhere (10-11). The processor chosen is the Intel 8085A, an 8-bit data, 16-bit address device, which runs at 3 MHz and has a maximum address of 64K bytes. The microcomputer interfaced system is always running under the external trigger mode of the boxcar integrator. It is first triggered by the gate out from the model 164, then sends out the scan signal to the model 164 and reads in the output signal. The signal is converted into digital form by a 12-bit analogue-to-digital converter and stored in the memory of the microcomputer. When the delay ramp reaches full scale, the microcomputer sends out a signal to reset the boxcar integrator. A block diagram of the various functions of the boxcar integrator and the functional board of the microcomputer is shown in

Figure 2-9.

In this work, the microcomputer generally functions in two modes. In the single-point mode, it sends out delay signals according to the aperture delay range and the % Initial A or B settings from the boxcar integrator, then reads in and stores the output signals in the memory until the memory is full. The whole process can be interrupted anytime. This mode is mainly used to scan over the effective wavelength range of the dye laser in order to get the maximum signal. A signal versus wavelength plot for sodium ions is given in Figure 2-10.

In the linear scan mode, the number of interrupts per data point (N_i), the starting point of the scan (P_s), the length the scan (L), the scan increment (S), and the number of points per scan increment (N_s) can be chosen by the user. The starting delay signal (D_s) can be calculated by the following equation:

$$D_s = A_r * \left(\frac{\%I}{100} + \frac{P_s}{255} \right) \quad [2]$$

where A_r is the aperture delay range set from the front panel of the boxcar integrator. The "effective" aperture delay range (A_r') can be calculated by the following equation:

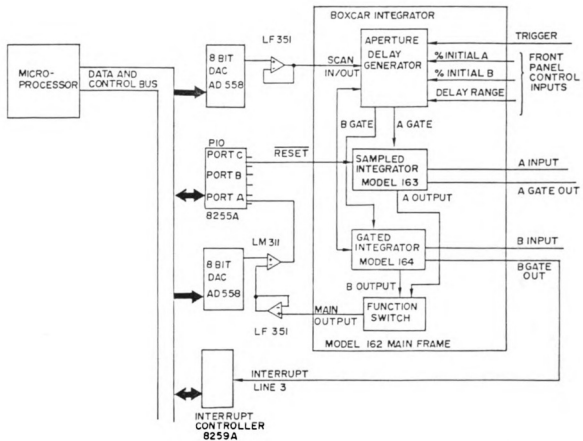


Figure 2-9. The instrumentation block diagram of a micro-processor interfaced boxcar system.

(Taken from J.D. Stanley, Masters thesis, Michigan State University, 1982).

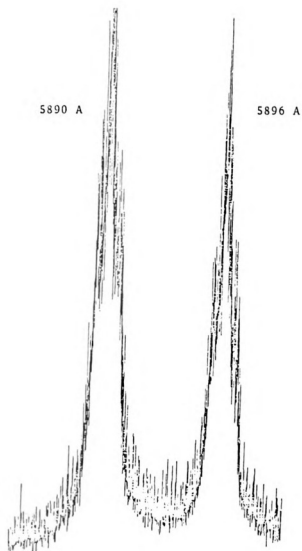


Figure 2-10. Dual laser ionization signals of sodium cation at 5890 A and 5896 A.

$$A_r' = A_r * \left(\frac{\%I}{100} + \frac{L}{255} \right) \quad [3]$$

where L ranges from 0 to 255. The relation between the scan increment and the real time (t_r) along the input signal waveform can be expressed as follows:

$$t_r = \frac{A_r * S}{255} \quad [4]$$

The number of interrupts per data point, N_i , is usually chosen to fulfill the 5 RC time constant requirement for a stable signal, and the number of points per scan increment, N_s , is chosen to account for the noise from the lasers. The time for each scan (T_s) thus can be calculated:

$$T_s = \frac{L * N_i * N_s}{S * L_f} \quad [5]$$

where L_f is the laser pulse frequency (Hertz).

The data taken by the microcomputer then is then uploaded to the PDP/11-23 mainframe for future data processing. The details of the data processing will be described in later chapters.

CHAPTER II

REFERENCES

1. K.C. Lin, Ph.D. Dissertation (Michigan State University, 1982).
2. F.M. Curran, Ph.D. Dissertation (Michigan State University, 1983).
3. T.W. Hänsch, Appl. Opt. 11, 895 (1972).
4. P.L. Lijnse and R.J. Elsenaar, J. Quant. Spectrosc. Radiat. Transfer 12, 1115 (1972).
5. C.A. van Dijk, Ph.D. Dissertation (University of Utrecht, 1978).
6. J.D. Ingle, Jr. and S.R. Crouch, "Spectrochemical Analysis" (Prentice Hall, Englewood Cliffs, New Jersey, 1988).
7. C.Th.J. Alkemade, Tj. Hollander, W. Snelleman, and P.J.Th. Zeegers, "Metal Vapours in Flames" (Pergamon Press, Oxford, 1982).
8. H.P. Hoomayers and C.Th.J. Alkemade, J. Quant. Spectrosc. Radiat. Transfer 6, 847 (1966).
9. J.D. Winefordner, S.G. Schulman, and T.C. O'Haver, "Luminescence Spectrometry in Analytical Chemistry" (Wiley, New York, 1972).
10. J.D. Stanley, Masters Thesis (Michigan State University, 1982).
11. B.H. Newcome and C.G. Enke, Rev. Sci. Instrum. 55, 2017 (1984).

CHAPTER III

DUAL LASER IONIZATION SIGNALS

A. Introduction

This chapter discusses the temporal behavior of the dual or direct laser ionization (DLI) signals in a laminar flow hydrogen-oxygen-argon flame. In DLI, two laser beams that overlap both spatially and temporally are employed to enhance the ionization processes in flame environments. The first laser is a tunable dye laser which promotes the analyte from the ground state to a resonant excited state; the second laser is a nitrogen laser with a fixed wavelength (337.1 nm) which produces photoionization from the excited atoms. Previous research and publications from our laboratory (1-6) have demonstrated that DLI, which is closely related to laser-enhanced ionization (LEI), can yield signals 2 to 3 orders of magnitude larger than those obtained with LEI (4) for some ionization schemes. DLI has shown much promise, with detection limits for some elements near the part-per-trillion level, and has been successfully utilized for the analysis of some types of real samples (6).

However, neither LEI nor DLI in flames has yet been applied to routine analysis in typical analytical laboratories. One of the major reasons is that general applications of these techniques, which are derived directly from the opto-galvanic effect (OGE), suffers from a susceptibility to severe signal depression when the sample contains even moderate levels of elements which can partially ionize via unassisted thermal ionization in the flame, most notably the alkali metals (7-9). This problem has been partially solved by Turk (10) for LEI and his description was based, in turn, on the extensive and well-documented studies of electrical phenomena in combustion systems by Lawton and Weinberg (11). Briefly, Turk found that if the laser focal point, i.e. the analyte ion source, is close enough to the surface of the cathode, or within the charge sheath around the cathode, complete signal recovery could be expected. This also applies to DLI.

Curran (3), in his studies of electrical interferences of DLI in flames, showed that the addition of easily ionized matrix components such as cesium, lithium, and potassium had little or no effect on the signal recovery for sodium, lithium and strontium. This is due to the fact that DLI employs a second photon that provides sufficient energy to ionize the analyte from a resonant excited state and, hence, for some excitation schemes, the dependence of the ionization signal upon collisional processes in the flame is

reduced substantially. In other words, a colder flame, such as the hydrogen-oxygen-argon flame used by Curran, can be adopted to suppress the unassisted thermal ionization of matrix ions and still supply the same or even better signal recovery and detection limits. However, elements with small or even moderate cross sections to nitrogen laser photons, such as indium, cesium, and potassium (4), still are dependent on the rate of collisional ionization and will show little or no improvement in signal recovery over LEI. In addition, some elements from the sample matrix might interfere even more in DLI, probably due to off-resonant multi-photon ionization.

To make DLI, which is perhaps the least expensive set-up among all dual laser techniques, applicable to real samples with complex and unknown matrices, a more selective signal collection process must be designed. Since the arrival time of sample ions is a function of the ion mobilities, investigations of the temporal behavior of DLI signals can reveal the possibility of improving the selectivity of DLI by blocking out the interference signals with an appropriate boxcar aperture. Besides, Lin (2) has established a method which can extract ion mobilities and diffusion coefficients of various ions from time-resolved DLI signals; hence flame temperatures can be determined by the well-known Einstein relation. To further confirm and

improve Lin's method, understanding more details about the temporal behavior of DLI signals is essential.

B. Theoretical

B-1 Ion Mobilities

The response of flames to external fields has been extensively studied by Lawton and Weinberg (11). At the moment an electric field is applied to a flame, positive ions begin to move toward the cathode; negative ions and electrons, in contrast, move toward the anode. The drift velocity ($\text{cm}\cdot\text{sec}^{-1}$) of each individual species depends on its mobility and can be expressed as follows:

$$v = \mu E \quad [1]$$

where μ is the mobility coefficient ($\text{cm}^2\cdot\text{volt}^{-1}\cdot\text{sec}^{-1}$) of the charged species and E is the electric field ($\text{volt}\cdot\text{cm}^{-1}$) applied to the flame. The mobility of a charged species depends inversely on its mass and thus the mobility of electrons will be much higher than those of positive ions. Since the ions and electrons are generated at the same rate in the flame, the greater electron extraction rate results in a buildup of net positive charge near the cathode in the flame. This process will continue until a steady state distribution of positive ions is built up around the cathode

which effectively neutralizes the negative potential of the cathode beyond the so-called "charge sheath". Under this circumstance, virtually the entire potential difference between the cathode and anode is sustained across the charge sheath, as shown on Figure 3-1.

B-2 Electric Fields in Flames

In an idealized, one-dimensional, and diffusion free approximation, the charge sheath around the cathode under the influence of an applied electrical potential can be expressed according to the terms designated on Figure 2-6 by the following equations:

$$E = A_s (q_s - q), \quad q \leq q_s \quad [2]$$

and

$$E = 0, \quad q_a > q > q_s \quad [3]$$

where E is the effective electric field ($\text{volt} \cdot \text{cm}^{-1}$) along the q axis, q_s is the edge of the charge sheath, and A_s ($\text{volt} \cdot \text{cm}^{-2}$) is the slope of the E - q plot. A_s can be expressed as follows:

$$A_s = \left(\frac{r_c e}{\mu_s E_0} \right)^{1/2} \quad [4]$$

where r_c is the ionization rate of the flame per unit volume

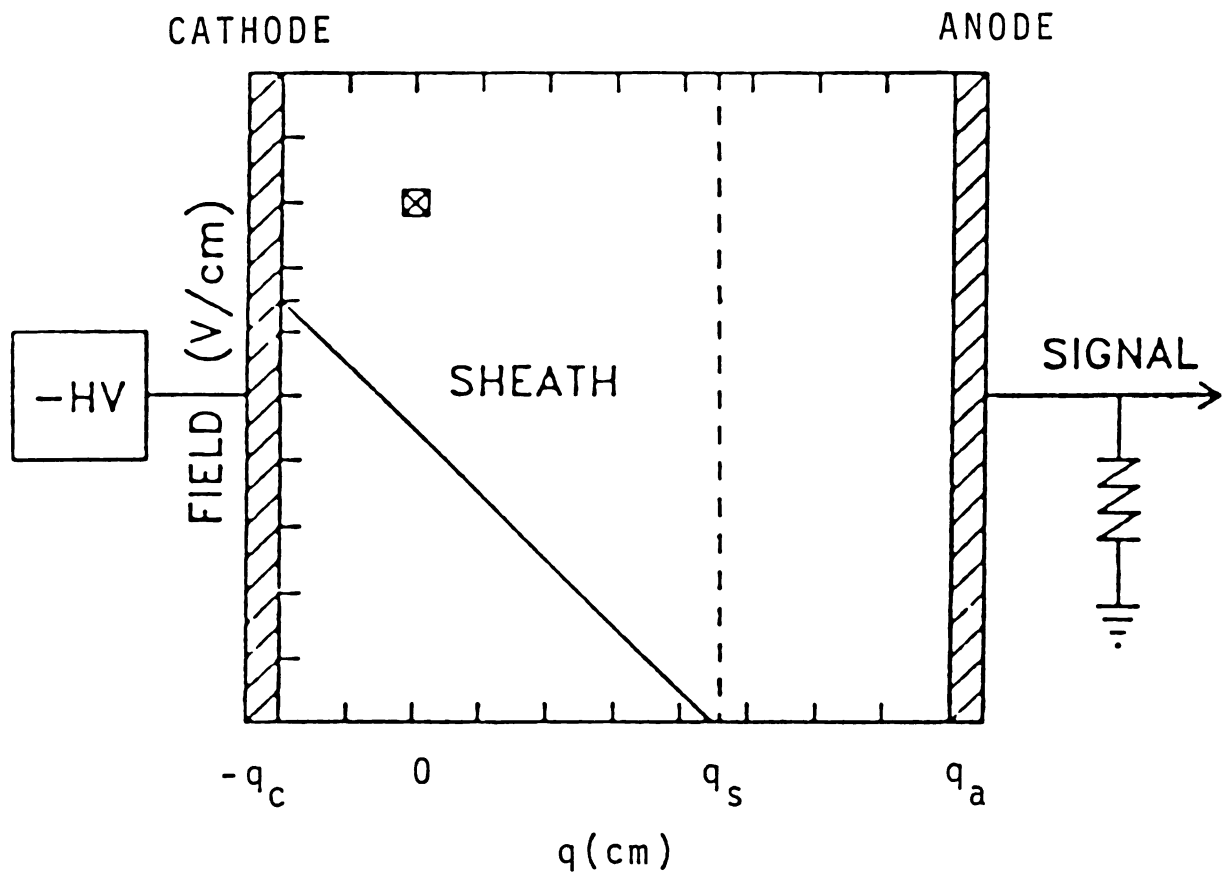


Figure 3-1. Pictorial representation of Lawton's model concerning the sub-saturated electric field in a flame environment. The symbol \boxtimes indicates the laser focal point.

($\text{cm}^{-3} \cdot \text{sec}^{-1}$), e is the electronic charge (1.62×10^{-19} coul), μ_s is the mobility coefficient ($\text{cm}^2 \cdot \text{volt}^{-1} \cdot \text{sec}^{-1}$) of the matrix ions in the flame, and E_0 is the vacuum permittivity (8.854×10^{-14} coul \cdot volt $^{-1} \cdot \text{cm}^{-1}$). The spatial distribution of electrical potential can be described as follows:

$$V = -\frac{1}{2} A_s (q_s - q)^2, \quad q_c < q < q_s \quad [5]$$

and

$$V = 0, \quad q \geq q_s \quad [6]$$

The edge of the charge sheath can be calculated by the following equation:

$$q_s = \left(-\frac{2V_a}{A_s} \right)^{1/2} - q_c \quad [7]$$

where V_a is the applied potential (volt). From equations [2] to [7], the electric field on the surface of the cathode ($q=q_b$) can be calculated by the following equation:

$$E_c = (2V_a A_s)^{1/2} \quad [8]$$

According to Lawton and Weinberg (11), equations [2] through [8] describe the so-called "sub-saturation" condition in the flame. Figure 3-2 shows the calculated spatial distribution of the electric field and electrical potential with various ionization rates (r_c) and applied voltages (V_a) under sub-saturated conditions. When V_a is large enough, the electric

Figure 3-2.

(a) The calculated spatial distribution of electric field and electrical potential in a flame environment with various ionization rates (r_c) under the sub-saturated condition. The bias potential applied is -750 V on the cathode. A, A', $10^{11} \text{ cm}^{-3} \cdot \text{sec}^{-1}$; B, B', $10^{12} \text{ cm}^{-3} \cdot \text{sec}^{-1}$; C, C', $10^{13} \text{ cm}^{-3} \cdot \text{sec}^{-1}$. The dashed lines indicate distributions in the absence of a flame ($r_c = 0$).

(b) The calculated spatial distribution of electric field and electrical potential in a flame environment with various applied voltages (V_a) under the sub-saturated condition. The ionization rate is $10^{12} \text{ cm}^{-3} \cdot \text{sec}^{-1}$. A, A', -750 V on the cathode; B, B', -1000 V; C, C', -1250 V; D, D', -1500 V.

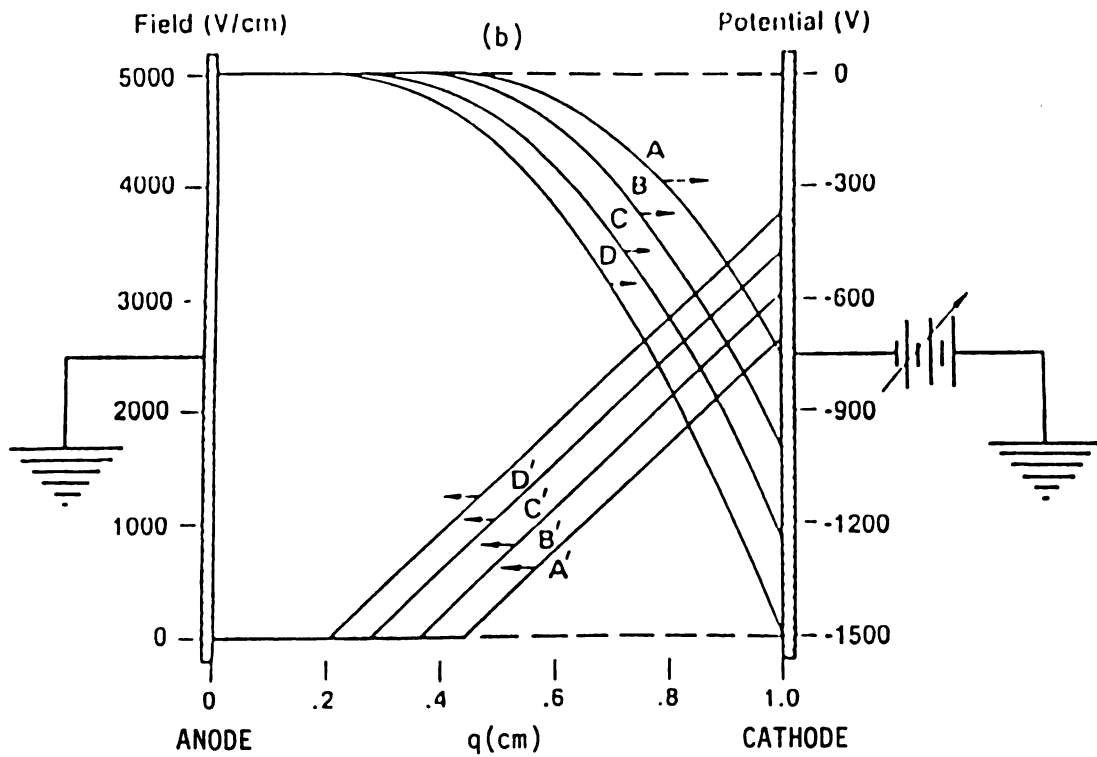
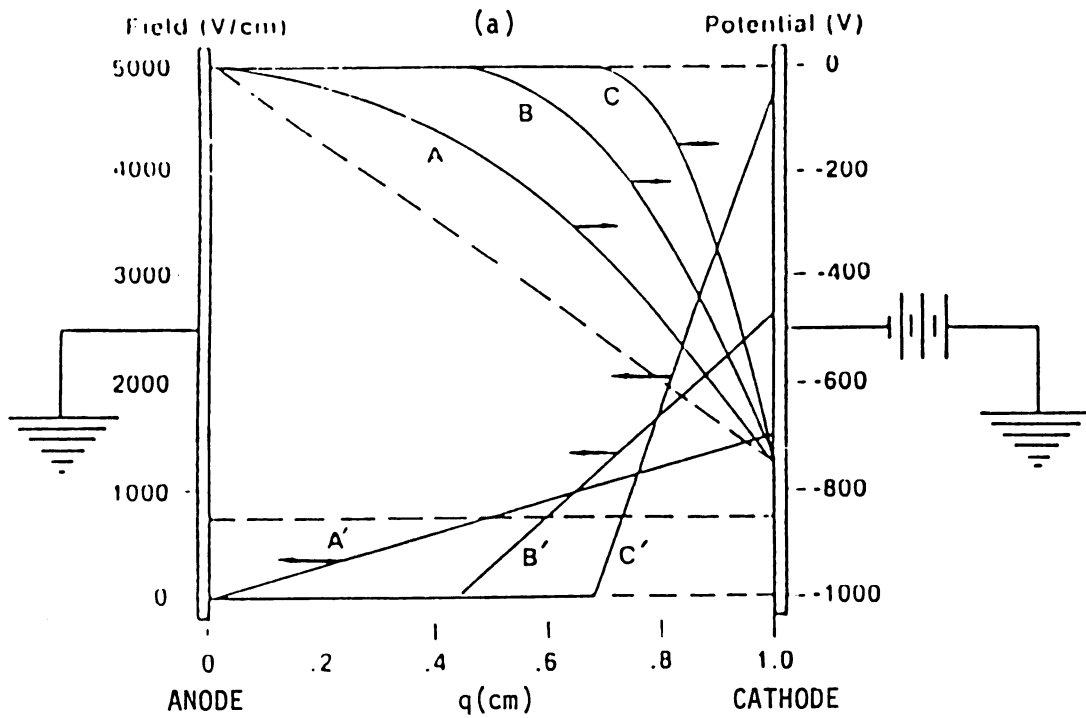


Figure 3-2.

field can be "saturated", as described by equation [9].

$$V_a = \frac{1}{2} A_s (q_c + q_a)^2 \quad [9]$$

For this condition, we have

$$q_s = q_a \quad [10]$$

where the electric field can be expressed as follows:

$$E = A_s (q_a - q), \quad -q_c \leq q \leq q_a \quad [11]$$

and the electrical potential can be described by the following equation:

$$E = \frac{1}{2} A_s (q_a - q)^2, \quad -q_c \leq q \leq q_a \quad [12]$$

However, when the electric field is very high, or,

$$V_a > \frac{1}{2} A_s (q_c + q_a)^2 \quad [13]$$

then the distribution of the electric field is "super-saturated." Under this condition, the effective electrical field should be written as follows:

$$E = [A_s^2 (q_a - q)^2 + E_a]^{1/2}, \quad q_a > q > -q_c \quad [14]$$

where E_a is the electric field at the surface of the anode.

The relation between E_a and V_a is derived as follows:

$$V_a = -\frac{1}{2} (q_c + q_a) [\Lambda_s^2 (q_c + q_a)^2 + E_a^2]^{1/2} +$$

$$-\frac{(q_c + q_a)^2}{2\Lambda_s} \ln \left\{ \frac{\Lambda_s (q_c + q_a) + [\Lambda_s^2 (q_c + q_a)^2 + E_a^2]^{1/2}}{E_a} \right\} \quad [15]$$

E_a can be obtained from equation [15] by Newton's method. The spatial distribution of the electrical potential can be expressed by the following equation:

$$V = -\frac{1}{2} (q_c + q_a) [\Lambda_s^2 (q_c + q_a)^2 + E_a^2]^{1/2} -$$

$$-\frac{1}{2} (q_c + q) [\Lambda_s^2 (q_c + q)^2 + E_a^2]^{1/2} +$$

$$-\frac{E_a^2}{2\Lambda_s} \ln \left\{ \frac{\Lambda_s (q_c + q_a) + [\Lambda_s^2 (q_c + q_a)^2 + E_a^2]^{1/2}}{\Lambda_s (q_c + q) + [\Lambda_s^2 (q_c + q)^2 + E_a^2]^{1/2}} \right\} \quad [16]$$

Figure 3-3 shows the spatial distribution of the electric field and the electrical potential for the super-saturated condition.

Generally, air/acetylene flames contain a high concentration of background ions, i.e. they have a high ionization rate, and can be described by equations [2] through [8] very well (10,12). However, the hydrogen-oxygen-argon flame used in our laboratory is a relatively

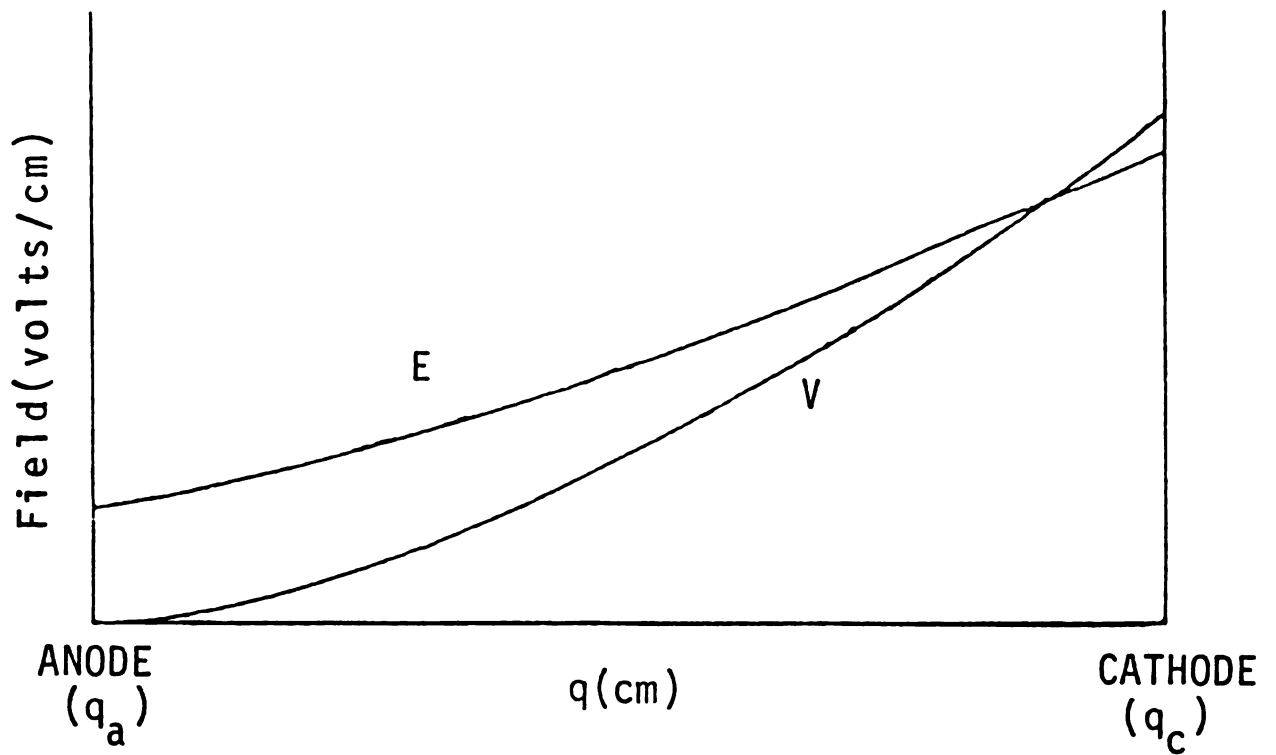


Figure 3-3. The spatial distribution of the electric field and the electrical potential for the super-saturated condition.

"clean" flame which contains fewer background ions and has a much lower ionization rate. Equation [13] shows that this kind of flame is much easier to saturate or super-saturate, even under moderate applied voltages.

B-3 Behavior of Charged Particles in Flames

A flame sample cell under the influence of an electric field can be thought of, in principle, as an electrolytic cell. Any perturbation imposed on the cell can be sensed by the electrodes. Applying voltage to an electrode can be viewed as an action of pumping electrons into or removing them from the electrode. Hence on the surface of the electrode there always exists a so-called "charge sheath" [13] if the mobilities of the positively and negatively charged particles are not the same. This charge sheath usually possesses a capacitance, C ($\text{coul} \cdot \text{volt}^{-1}$). According to the following equation:

$$V = \frac{Q}{C} \quad [17]$$

where Q is charge (coulomb). It is obvious that when a variation of local charge occurs, a relatively big voltage can be sensed by the electrodes, provided that the capacitance C is sufficiently small. This is exactly the case of the experimental set-up used in our laboratory.

Since the volume ionization rate of the hydrogen-oxygen-argon flame is low, the capacitance of the charge sheath is also low. When a laser pulses are imposed to the flame cell, it creates a change of the local charge density. Under the influence of the electrical field, charge separation occurs nearly instantly due to the big difference of the mobilities of positive ions and electrons. This effect can be viewed as a quick injection of charges to a capacitor of which the capacitance is rather small. Hence a capacitive effect which induces variations of charges and voltages can be sensed nearly momentarily by the electrode. The rapidity with which the electrode will sense the charge flow, or the voltage change, has nothing to do with the mobilities of ions and electrons, and hence is not affected by the bias voltage on the electrodes (V_a) or the distance between the laser focal point and the electrodes (q_a and q_c). The signals due to the capacitive effect has been observed by Berthoud et al. (13). They reported that it can be detected about 100 nanoseconds after the laser pulse.

At the onset of the perturbation, the velocity of the charged particle can be described by the following equation:

$$m \frac{dv}{dt} + kv = Q_e E \quad [18]$$

where m is the mass (kg) of the particle, k is the viscous force coefficient, and Q_e is the charge of the particle. At

steady state, we have:

$$m \frac{dv}{dt} = 0 \quad [19]$$

Upon substitution of equation [1] into equation [18] and integration, we have:

$$v = \mu E (1 - \exp (-Q_e t / \mu m)) \quad [20]$$

Hence, the time constant for the establishment of a steady-state current is:

$$\tau = \frac{\mu m}{Q_e} \quad [21]$$

Assuming that the mobility coefficient of sodium is 30.2 cm².volt⁻¹.sec⁻¹ (2); it can be shown that

$$\tau_{Na^+} \approx 7.09 \times 10^{-10} \text{ sec.} \quad [22]$$

Also, it has been shown that the time constant for electrons can be as small as 3 x 10⁻¹² seconds (13).

Due to the capacitive effect discussed earlier, it can be expected that when laser pulses perturb the flame system, at least two temporal signals can be observed. One is the signal due to the fast moving electrons with the capacitive effect, and the other is due to direct charge collection through the electrodes. Smyth and Mallard (14,15) have shown the existence of two temporal components of the LEI

signal with short laser pulses. They observed a short electron signal followed some microseconds later by a longer and weaker ion signal. Berthoud et al. have observed two temporal electron signals (13), both on the nanoseconds time scale.

C. Experimental

C-1 Apparatus

A complete description of the DLI experimental system used in this study has been given elsewhere (1,5-6) and a brief description of the microcomputer interfaced boxcar system has been presented in section F of Chapter II. In all cases, the resonant laser radiation was produced by a Hänsch-type dye laser pumped by a nitrogen laser (Model 0.5-150, NRG, Inc. Madison, WI). Part of the nitrogen laser beam was used to provide the the radiation for photoionization. For sodium, the dye laser was tuned to the $3S_{1/2} - 3P_{3/2}$ transition (589.0 nm). The laser powers were adjusted each time to ensure the same ionization rate of the analyte in the flame. The sample emanated from a circular Meker burner which produces a laminar-flow flame. In all cases both the central and mantle hydrogen-oxygen-argon flames were adjusted to be fuel rich (Argon $3.2 \text{ L}\cdot\text{min}^{-1}$, hydrogen $1.2 \text{ L}\cdot\text{min}^{-1}$, oxygen $0.5 \text{ L}\cdot\text{min}^{-1}$). Atomic sodium

was obtained by nebulizing 20 ppm sodium chloride solution into the flame with a pneumatic nebulizer. The probe configuration with the designation of symbols is depicted in Figure 2-6. Sodium ions were collected at the bottom probe (cathode) the position in the flame can be varied. The laser focal point was always kept 18 mm above the burner head to ensure a constant temperature environment. In all cases data were collected with a boxcar integrator in the exponential averaging mode. Multiple points were taken and stored in the microcomputer for each aperture duration in order to minimize the noise due to the pulse-to-pulse laser power variations. Since all DLI current signals were converted into voltages through the inverting input of an operational amplifier, all the signals shown in this chapter are inverted, i.e. the more negative values mean a larger signal amplitude.

C-2 Reagents

All solutions were prepared from reagent grade sodium chloride dissolved in distilled, deionized water. The laser dye chosen for this study was rhodamine 6G (Eastman Kodak Co.) with a concentration of 7.5×10^{-3} M in absolute ethanol. It was used without further purification. To maintain the stability of the dye laser, the dye solution was replaced every ten working hours.

D. Results and Discussions

D-1 Temporal Behavior of DLI Signals

In this section the time-resolved DLI signals are presented as a function of the lower probe position (q_c), the upper probe position (q_a), and the applied potential (V_a).

It has been found that the shape of the time-resolved DLI signals (hereafter simply called the DLI signals) changes dramatically with the distance (q_c) between the laser focal point and the lower probe. For a fixed q_c , the shape of the DLI signal may also change significantly with the applied voltage (V_a). Figure 3-4 shows a typical DLI signal collected when the positions of both probes were adjusted to achieve maximum DLI signal. For obtaining maximum DLI signals, the lower probe was usually located about 0.50 ± 0.10 mm below the laser focal point. The signal shows a very good exponential-decay behavior if the appropriate bias voltage is applied. The DLI signal shown in Figure 3-4, which was recorded at an applied voltage of 100 volts, has an exponential-decay lifetime of 3.707 microseconds. In fact, Figure 3-4 shows only the later part of the DLI signal; the early part of the DLI signal was not shown simply because it is too fast to be observed by our

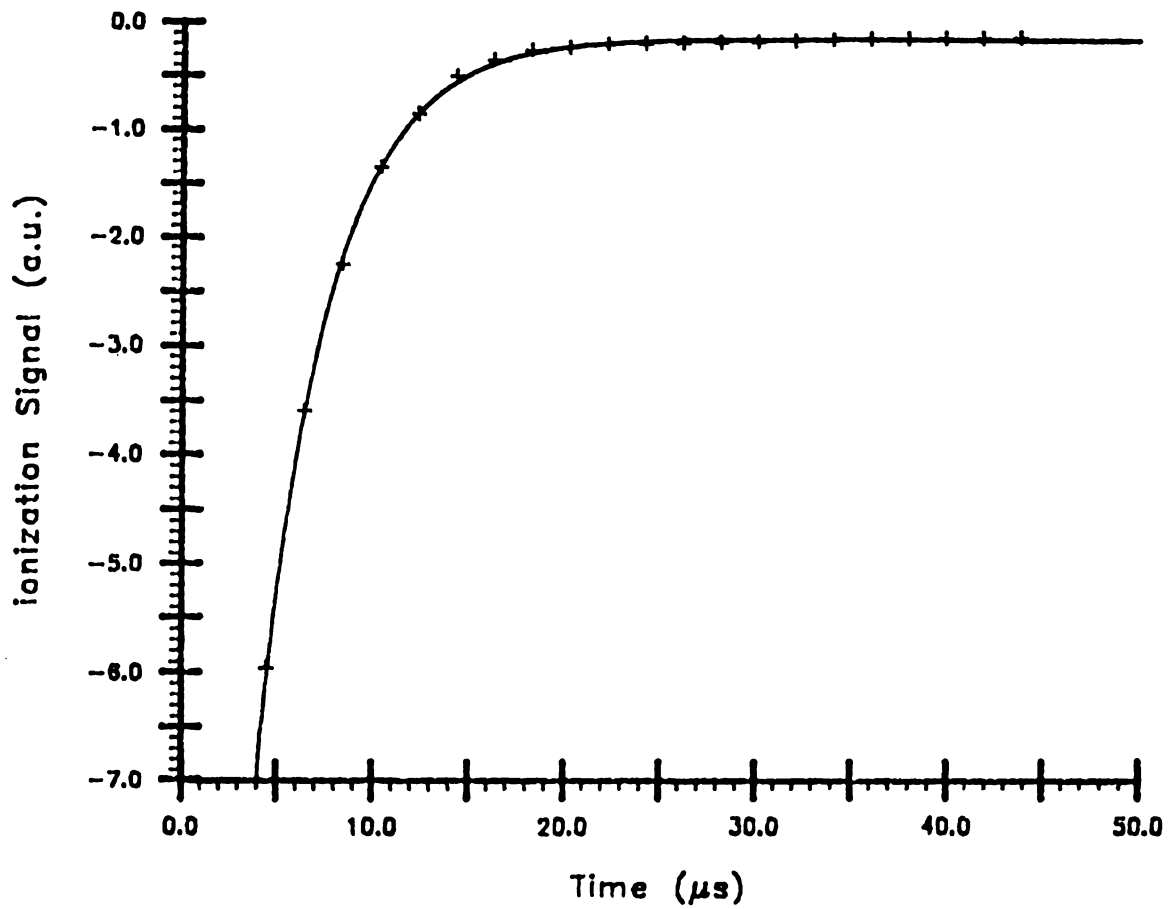


Figure 3-4. A typical DLI signal for sodium cations. The positions of both probes were adjusted to obtain maximum DLI signal. ($q_c \approx 0.50$ mm, $q_a \approx 2.00$ mm, $V_a = 100$ V).

experimental set-up. Other experiments have shown that the lifetime of the exponential decay increases with increasing distance between the lower probe (cathode) and the laser focal point (q_c). However, the signal intensity (peak amplitude) decreases with increasing q_c . To compensate for the signal loss and obtain less noisy DLI signals, higher bias voltages were applied. However, results from curve fitting showed that the DLI signals behaved differently in time when the applied voltage was increased.

Figure 3-5 shows a DLI signal obtained when the lower probe was placed just below the laser focal point and a 600 volts bias voltage was applied. Each plotted point was an average of 30 data points collected by the boxcar. The solid-line curve was drawn from the results of data fitting with an exponential decay function and gives a lifetime of 10.3 microseconds. A significant deviation between the DLI signal and the exponential decay can be observed. Other DLI signals have been collected repeatedly with more averaging and have shown rather high reproducibility. Figure 3-6 shows a DLI signal when the lower probe was located 2.00 mm below the laser focal point and a 500 V bias voltage was applied. Again, a significant deviation between the DLI signal and the exponential-decay model can be observed. The lifetime obtained from curve fitting is 13.7 microseconds. If the lower probe was placed near the combustion zone, only

Figure 3-5. DLI signal for sodium cations when the lower probe was placed just below the laser focal point ($q_c=0.0$ mm) with a 600 V bias voltage applied. Each plotted point was an average of 30 data points recorded by the microcomputer. The solid line was drawn from the results of a fit to an exponential decay. The lifetime from the curve fitting is 10.292 μ s.

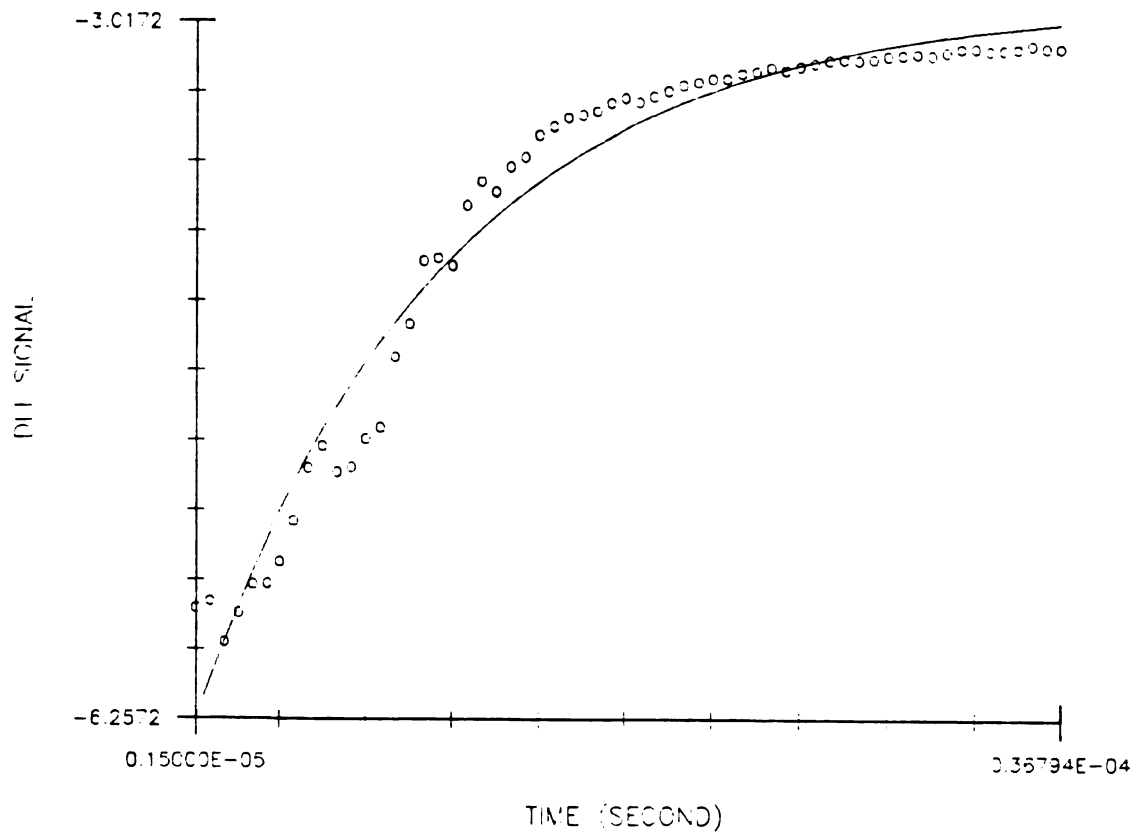


Figure 3-5.

Figure 3-6. DLI signal for sodium cations when the lower probe was located 2.00 mm below the laser focal point ($q_c=2.0$ mm) with a 500 V bias voltage applied. Each plotted point was an average of 30 data points recorded by the microcomputer. The solid line was drawn from the results of a fit to an exponential decay. The lifetime from the curve fitting is 17.740 μ s.

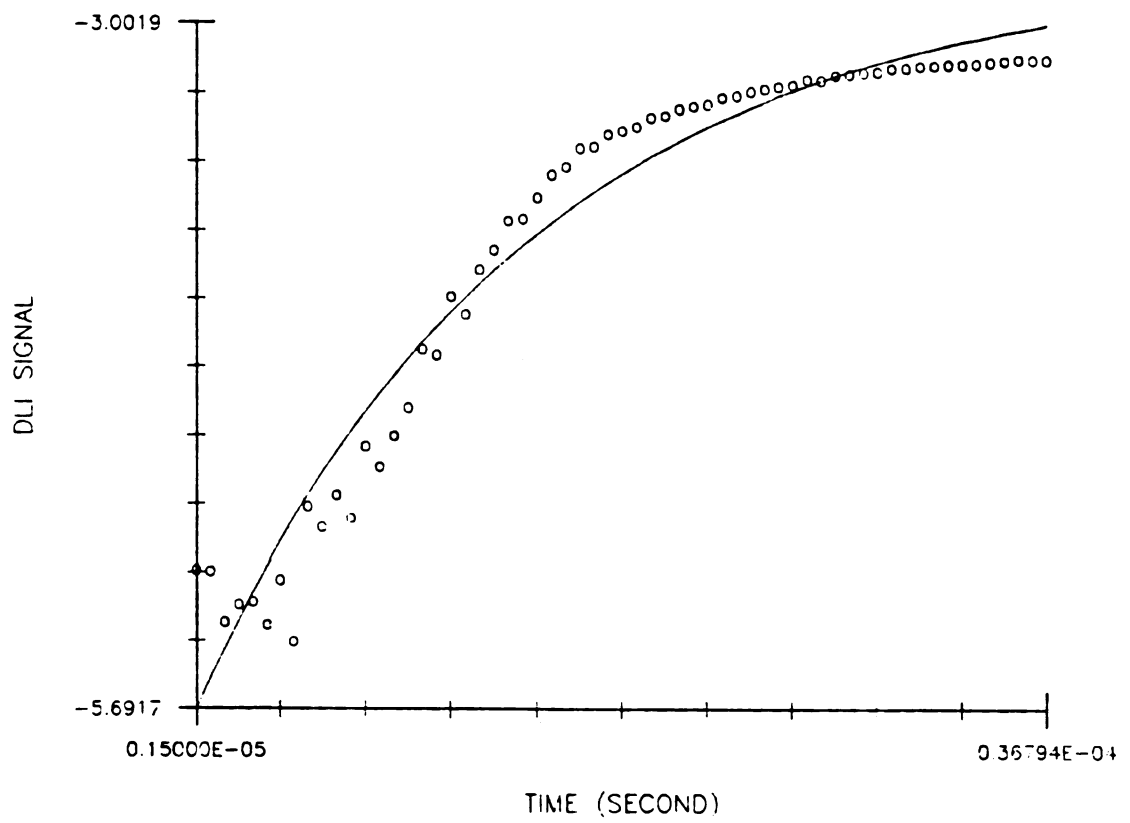


Figure 3-6.

a weak but seemingly exponential decaying DLI signal could be observed.

Figure 3-7 shows a DLI signal recorded on a strip chart recorder at 100 V bias voltage with the lower probe (cathode) located 2.00 mm below the laser focal point. The distance between the lower and upper probes was 5.00 mm. A second temporal peak which was never previously observed in our laboratory is apparent. The lifetime of the exponential decay of the DLI signal is 11.1 microseconds when the data points were curve-fitted by deleting all the points that formed the second peak. By contrast, the lifetime was 3.707 microseconds when the probe was located 0.50 mm below the laser focal point. The averaged DLI signal and the curve obtained from fitting data to an exponential-decay function are shown in Figure 3-8. The observation of two components to the temporal DLI signal implies that the exponential decay component of the DLI signal is due to the collection of electrons on the upper electrode (anode). This is consistent with the observations made by Smyth and Mallard (14,15) for LEI signals. They observed that the short electron signal usually appears earlier with much higher intensity and ion signal emerges microseconds later with a much smaller intensity and a longer lifetime.

Figure 3-9 shows a set of DLI signals for sodium ions taken at various distances, q_c , between the laser focal

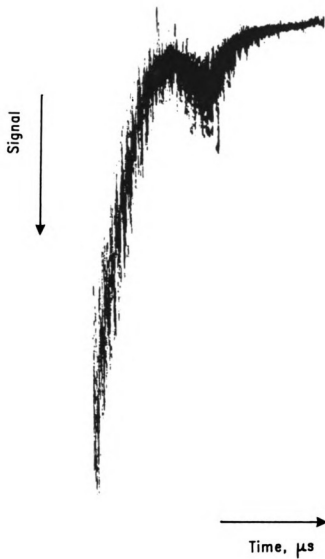


Figure 3-7. DLI signal for sodium cations recorded with a strip-chart recorder. Notice that the signal is inverted, i.e. a downward signal is a stronger DLI signal. The second temporal peak can be seen clearly from this plot. ($V_a=100$ V, $q_c=2.00$ mm, $q_a=3.00$ mm).

Figure 3-8. DLI signal for sodium cations from Figure 3-7 with averaged signal points. The solid line was drawn from the results of a curve fitting of the data to an exponential-decay model. The lifetime of the exponential decay of the DLI signal is 11.079 μ s when the data points were smoothed by deleting all the points that formed the second peak.

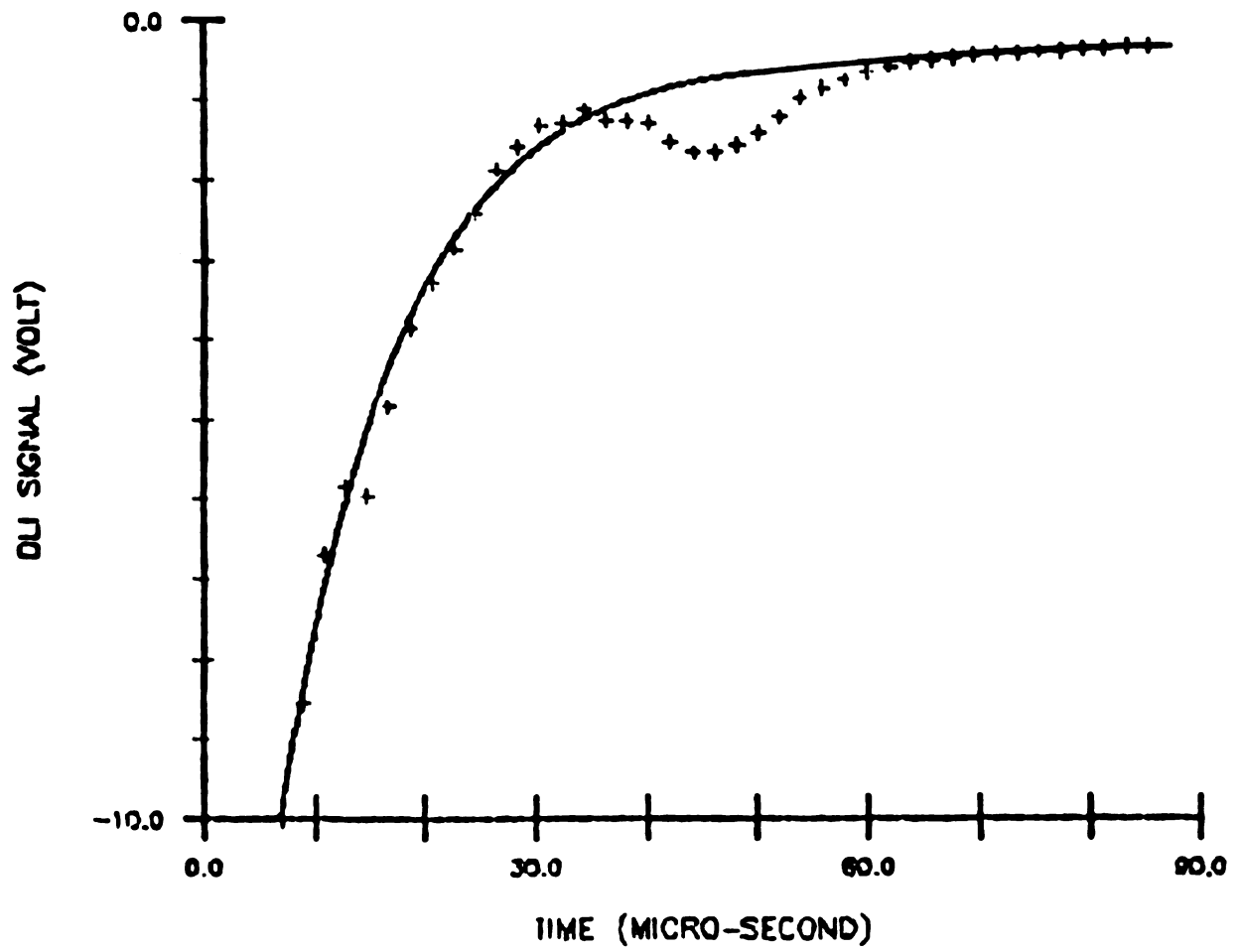


Figure 3-8.

Figure 3-9. The DLI signals for sodium cations taken at various distances (q_c) between the laser focal point and the lower probe (i.e., the cathode). ($V_a = 180$ V, $q_a = 1.00$ mm, $A_r = 50.0$ μ s, $R = 5.0$ μ s, $\%I = 2.0\%$, $t_r = 0.9766$ μ s, $N_s = 15$).

A, $q_c = 1.02$ mm; B, $q_c = 1.12$ mm; C, $q_c = 1.22$ mm;
D, $q_c = 1.32$ mm; E, $q_c = 1.42$ mm; F, $q_c = 1.52$ mm;
G, $q_c = 1.62$ mm; H, $q_c = 1.82$ mm.

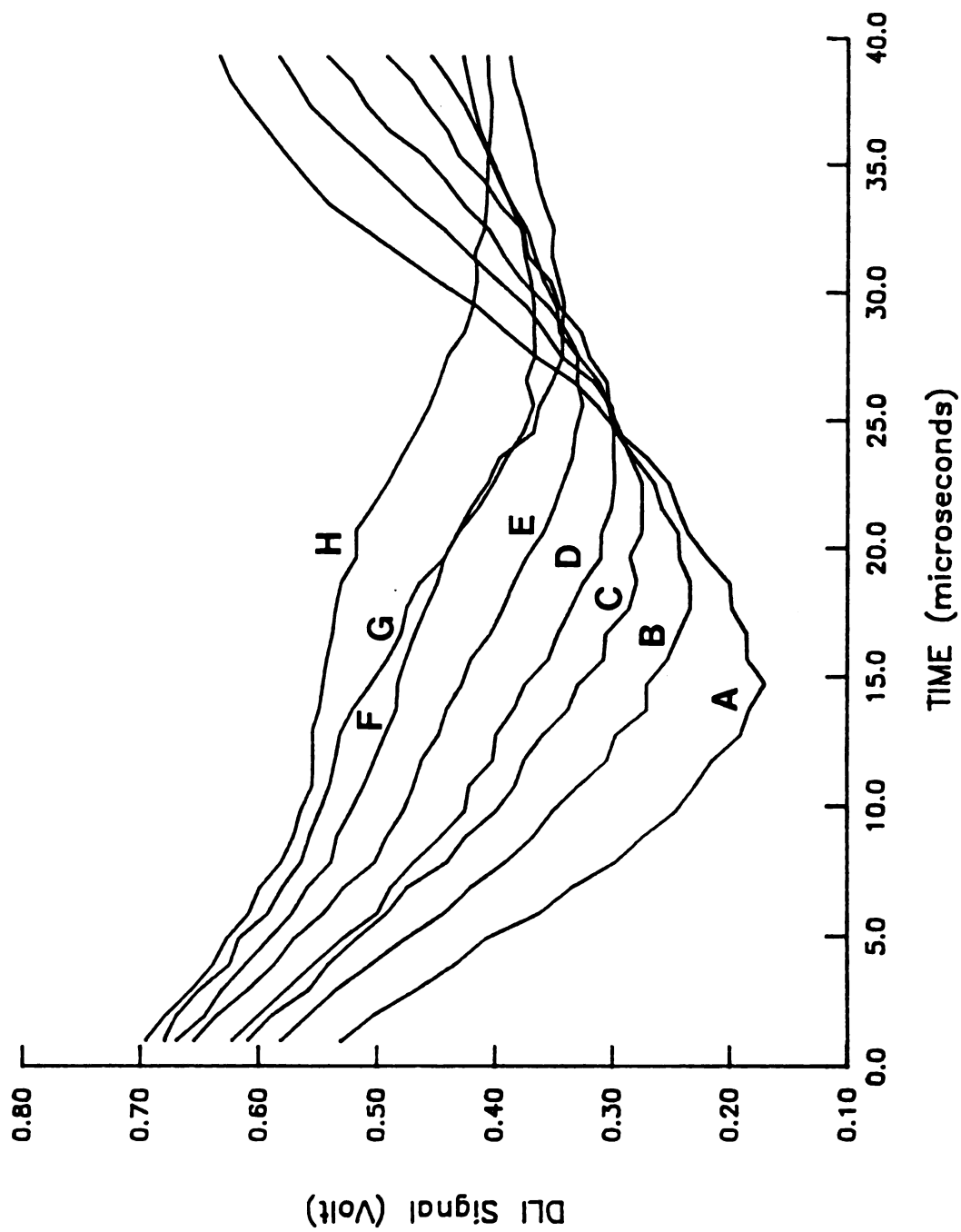


Figure 3-9.

point and the lower probe (cathode). All of the signals were taken with a bias voltage of 180 V; the upper probe (anode) was placed 1.00 mm above the laser focal point. The aperture duration was chosen to be 5 microseconds with an aperture delay range of 50 microseconds. The % Ini knob was set at 2.0 % (i.e. 1.0 microsecond initial delay). The scan increment between each data point was 0.9766 microseconds; and the microcomputer recorded 15 points per datum. With 180 volts of bias voltage, the electron peak appeared much earlier than the second peak; hence it could not be observed with the boxcar integrator. Thus the peaks shown in Figure 3-9 are only the peaks attributes to the ions. Figure 3-9 shows clearly two facts. First, the arrival time of the peak increases when the distance between the laser focal point and the lower probe increases. Second, the height of the second peak decreases significantly when q_c increases.

To confirm that the peaks shown in Figure 3-9 are truly due to sodium ions, a second series of DLI signals was taken. Figure 3-10 shows this set of DLI signals taken at various distances, q_a , between the laser focal point and the upper probe (anode). The lower probe was fixed at 2.00 mm below the laser focal point. All other parameters were chosen to be exactly the same as those in Figure 3-9. Figure 3-10 reveals even more information. First, as the anode was moved away from the laser focal point, an exponential-decay shape signal with high intensity starts to

Figure 3-10. The DLI signals for sodium cations taken at various distances (q_a) between the laser focal point and the upper probe (i.e., the anode). ($V_a = 180$ V, $q_c = 2.00$ mm, $A_r = 50.0$ μ s, $R = 5.0$ μ s, $\%I = 2.0\%$, $t_r = 0.9766$ μ s, $N_s = 15$).

A, $q_a = 0.00$ mm; B, $q_a = 1.50$ mm; C, $q_a = 2.50$ mm;
D, $q_a = 3.50$ mm; E, $q_a = 4.50$ mm.

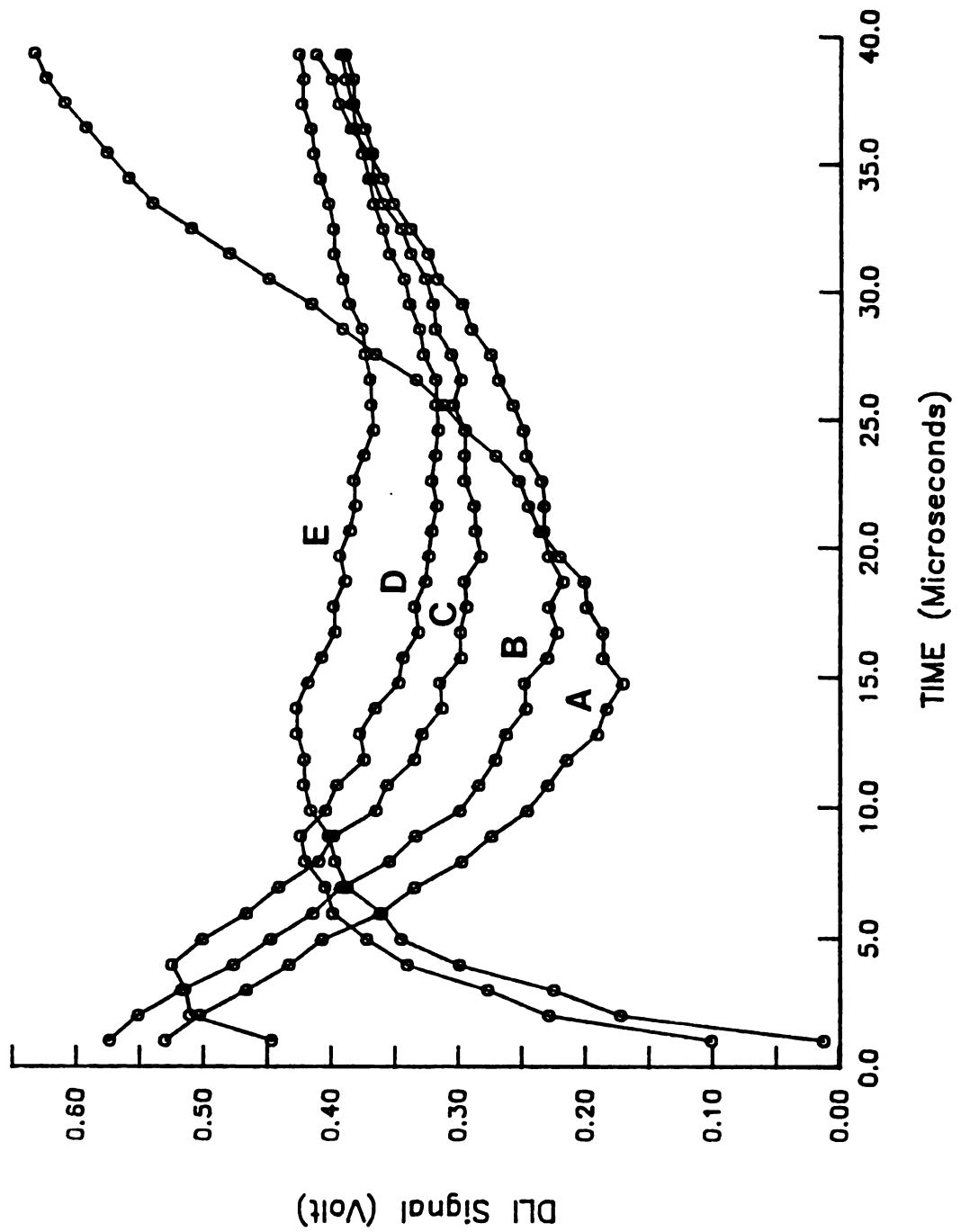


Figure 3-10.

emerge. Since the anode collects electrons, the emergence of the early part of the DLI signals with increasing probe distances (q_a) verifies that this component is due to electrons. Second, since electrons have much a higher mobility coefficient than the ions, signals due to electrons should appear much earlier in time than the ion signals. Only the later part of the electron peak can be observed if the boxcar integrator is not sufficiently fast. Figure 3-10 confirms this statement. Third, the electron signal is, in fact, very short, and decays exponentially. This statement can be further strengthened by referring to Figure 3-8. Fourth, the electron peaks possess much higher signal intensity than the ion peaks. Again Figure 3-8 helps ratify this statement.

If all parameters are chosen carefully an intense ion signal can be obtained with a yet observable electron signal as shown in Figure 3-11. From these observations, it should be possible to choose the most effective boxcar scan range in order to block out the background signals and increase the detection limits for the analysis of real samples. The cathode was placed 3.00 mm below the laser focal point and 4.00 mm below the anode. Sodium was aspirated into the flame, and the bias voltage applied was 200 volts. The aperture duration was chosen to be 5 microseconds with an aperture delay range of 50 microseconds. The % Ini knob was set at 3.0 % (i.e. 1.50 microsecond initial delay). The

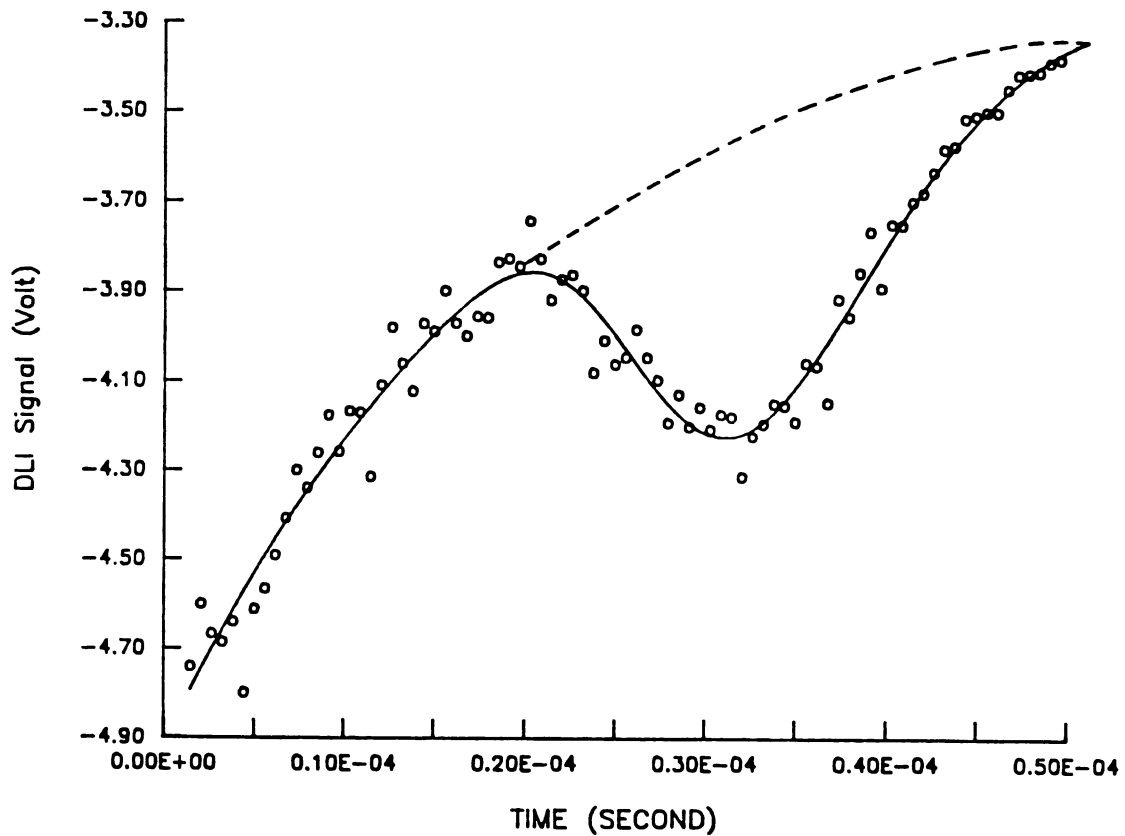


Figure 3-11. A typical DLI signal for sodium cations. The experimental parameters were chosen in order to obtain maximum amount of ion signals.

$(V_a = 200 \text{ V}, q_c = 3.00 \text{ mm}, q_a = 1.00 \text{ mm}, A_r = 50.0 \text{ } \mu\text{s}, R = 5.0 \text{ } \mu\text{s}, \%I = 3.0\%, t_r = 0.5882 \text{ } \mu\text{s}, N_s = 10).$

scan increment between each data point was 0.5882 microseconds; and the microcomputer recorded 10 points per datum. Figure 3-11 shows clearly two facts. First, there exists a time period during which the ion signal is truly the predominate component of the DLI signal. This time period can be chosen so as to discriminate against most of the background signals. Second, the curve fitting shows that the DLI signal consists of two temporal components. An electron peak with high signal intensity appears early in time under most circumstances and decays exponentially. The ion peak appears later in time with a skewed Gaussian shape. In fact, if both the ion and electron peaks can be modelled precisely, the electron signal may thus be subtracted from the DLI signal in order to further improve the detection limits of DLI technique. Smyth and Mallard have shown that different ions will appear at different times (15) if they have a significant difference in mobility coefficients. However, even if the background signal overlaps with the analyte ion signal, the entire spectrum still can be deconvolved provided a suitable mathematical model is available. The next chapter is devoted to deriving pertinent mathematical models, and the advantages and disadvantages of the various models will be examined. Chapter IV discusses the curve fitting techniques in detail.

From the above discussions and the experimental results shown in Figures 3-5 through 3-11, the following conclusions

can be reached concerning the DLI signals:

- (i) The DLI signal is composed of two temporal components. A short, but strong, electron peak which appears very early in time, followed by a weak, but broad, ion peak.
- (ii) The peak which appears early in time always decays exponentially if it is solely due to electrons.
- (iii) If the lower probe (cathode) is placed close enough to the laser focal point and an appropriate bias voltage is applied, the later part of the DLI signal shows an exponential decay. In this case the ion peak may have weakly merged into the electron peak and may not be observed separately. If the bias voltage is small, the ion peak becomes very broad and merges into the background. Again, the DLI signal decays exponentially. However, if too high a bias voltage is applied, the ion peak distorts the electron peak and the combined signal no longer decays exponentially anymore.
- (iv) If the cathode is sufficiently far from the laser focal point and an appropriate bias voltage is applied, the ion peak can be observed clearly. However, the DLI signal during that time period will

be the sum of the electron signal and the ion signal. If too high a bias voltage is applied, the ion peak will again merge into the electron peak. A small part of the ion peak usually can be seen at the very beginning of the DLI signal. Nevertheless, the later part of the DLI signal no longer shows an exponential decay.

- (v) If the cathode is too far away from the laser focal point, only the electron peak can be observed.

D-2 Electron Signals

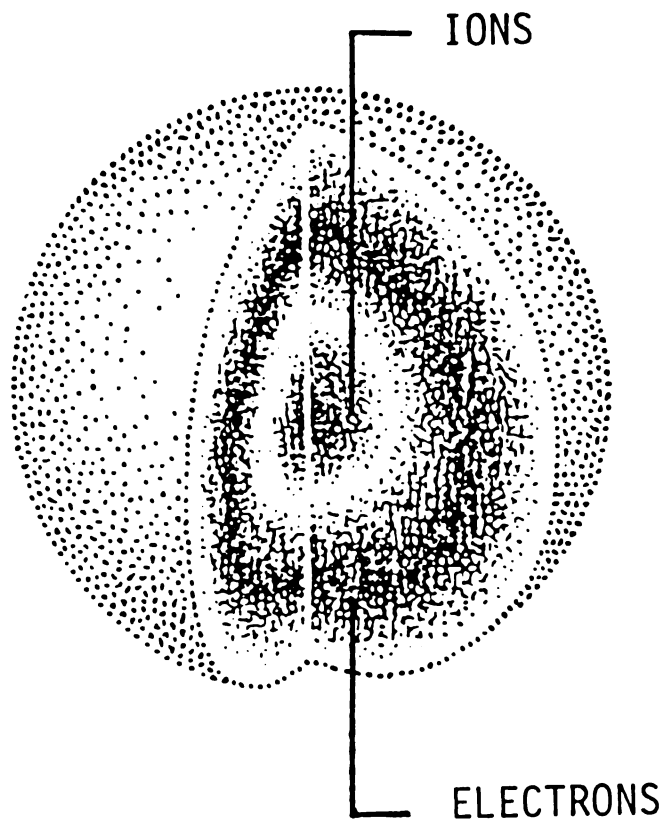
A detailed theoretical treatment of the behavior of electrons in a flame environment under the influence of a possibly very complicated electric field is beyond the scope of this thesis. Hence this section is devoted to finding a relatively simple model which can explain the behavior of electrons in DLI process.

Electrons behave very differently than ions. As might be expected, electrons usually possesses mobility and diffusion coefficients much higher than ions by orders of magnitude. Because of its small mass, the electrons can be accelerated rapidly by an electric field, and it loses very little energy in elastic collisions with other particles in

the flame (16). Therefore electrons can acquire kinetic energy from an electric field faster than ions. Even with only a weak electric field imposed on the gas through which the electrons are moving, the average energy of electrons may be far in excess of the thermal energy calculated by Boltzmann's Law. In other words, for electrons usually the drift term in the Fokker-Planck equation overrides the diffusion term. Berthoud et al. (13) have indicated that the time constant for electrons to attain steady-state mobility is about 3 picoseconds, as discussed previously in Section B-3 of this chapter.

In addition, from the results of DLI experiments in our laboratory Lin, et al. (2) have shown that in the flame environment, the behavior of ions can be modelled by ambipolar diffusion. Ambipolar diffusion usually starts from a neutral mixture of positive ions and electrons with very high density. The more mobile electrons diffuse faster and outrun the slow-moving positive ions. This causes a charge-separation electric field that acts to retard the diffusion of the electrons and to enhance the diffusion of the positive ions, thus maintaining charge neutrality. The enhanced diffusion of positive ions is called ambipolar diffusion (17). A pictorial representation of the charge separation due to ambipolar diffusion is shown in Figure 3-12. The ambipolar diffusion coefficient D_a ($\text{cm}^2 \cdot \text{sec}^{-1}$) for a high density mixture of electrons and positive ions is

AMBIPOLAR DIFFUSION



$$D_a \approx 2D$$

Figure 3-12. Pictorial representation of charge separation of a plasma cluster due to ambipolar diffusion.

twice of the magnitude of the diffusion coefficient D for ions alone, provided the kinetic temperatures of both species are the same; i.e.,

$$D_a \approx 2 D \quad [23]$$

Since the pulse widths of both lasers are about 5 nanoseconds, we may assume that at the instant when the laser pulses turned off, a steady-state ambipolar diffusion has already built up at the laser focal point.

Based on the previous discussion, we propose the following for the behavior of electrons in the DLI process:

- (i) At the moment the lasers are fired, the electrons start to move to the anode. They contribute to the early part of the electron peak through both the capacitive effect and/or direct charge collection processes on the surface of the anode.
- (ii) After a short time period, the depletion of electrons at the laser focal point causes ambipolar diffusion to be built up gradually.
- (iii) After the short time period of the depletion of electrons at the laser focal point (hereafter simply called the transition stage) described in step (ii), the electrons can be described effectively by the

ambipolar diffusion model. A steady-state ambipolar process thus governs the behavior of both ions and electrons.

From our proposed mechanism, step (i) can explain why electrons can reach the anode at such an early stage of the DLI processes. After a very complicated transition stage, step (iii) explicates the reason why the electron peak still possesses a tail at late stages of the DLI processes.

To explain why the electron peak decays exponentially, a relatively simple and straightforward model is presented here, with the assumption that at step (iii) the mobility of electrons is no longer important. We may start from the equation of continuity:

$$\frac{\partial P(q,t)}{\partial t} = D_a \frac{\partial^2 P(q,t)}{\partial q^2} \quad [24]$$

where $P(q,t)$ is the electron density function and D_a is the ambipolar diffusion constant ($\text{cm}^2 \cdot \text{sec}^{-1}$) of the electrons. Since a steady state has already been built up, we may apply the method of separation of variables:

$$P(q,t) = P(t) * P(q) \quad [25]$$

If we substitute equation [25] into equation [24], the following equation can be derived:

$$\frac{1}{P(t)} \frac{\partial P(t)}{\partial t} = \frac{D_a}{P(q)} \frac{\partial^2 P(q)}{\partial q^2} \quad [26]$$

Equating both sides of equation [26] to a time constant $-\tau^{-1}$ yields:

$$\frac{1}{P(t)} \frac{dP(t)}{dt} = - \frac{1}{\tau} \quad [27]$$

and

$$\frac{D_a}{P(q)} \frac{d^2 P(q)}{dq^2} = - \frac{1}{\tau} \quad [28]$$

Equation [27] gives:

$$P(t) = A \exp(-t/\tau) \quad [29]$$

Since A can be included as a factor in the P(q) function as part of the normalization constant, there is no loss of generality in rewriting equation [29] as follows:

$$P(t) = \exp(-t/\tau) \quad [30]$$

Either equation [29] or equation [30] can be used to describe the temporal behavior of electrons in the later stage of the DLI process. Due to the ambipolar diffusion feature of the electrons, it is reasonable to impose the following two boundary conditions as a first order approximation:

$$\frac{dP(q_0)}{dq} = 0 \quad [31]$$

where q_0 is the coordinate of the laser focal point and is defined as $q_0=0$ here. This boundary condition implies that the laser focal point possesses the highest electron density all the time. Considering the attractive force between the electrons and the much slower-moving ion cloud, we may perceive this as a reasonable approximation. Also, we may have,

$$P(q_a) = 0 \quad [32]$$

where q_a is the coordinate of the anode, as designated in Figure 2-6. Equation [32] implies that the anode behaves like an infinite sink for electrons. It is also assumed that the rate of the electrode kinetics are also infinitely rapid. Equation [28] thus gives:

$$\frac{q_a}{(D_a \tau)^{1/2}} = (2k-1) \frac{\pi}{2} \quad [33]$$

where k is an integer greater than or equal to 1. We may choose the fundamental mode solution to describe the behavior of electrons. This yields:

$$\tau = 4 \pi^{-2} D_a^{-1} q_a^2 \quad [34]$$

where τ is the lifetime of the exponential decay of the

electron peak. Assume that at the moment the lasers are turned off, the total number of ions is N . We may then write the complete solution of $P(q,t)$ for the fundamental mode as follows:

$$P(q,t) = \frac{N \pi}{2q_a} * \exp(-t/\tau) * \cos\left(\frac{\pi q}{2q_a}\right) \quad [35]$$

The physical interpretation of equation [35] is depicted in Figure 3-13. Briefly, this model assumes that there is a steady-state distribution between the laser focal point and the upper probe (anode) which builds up at the very moment when both lasers are turned off. The anode behaves like an infinite sink and the electron population thus decays exponentially with time.

D-3 Charge Separation Process

Before examining the shape of the ion peaks, it is important to understand why there exist two separate components of the DLI signals. Since a closed loop of current flow is always required, common sense will deny the idea that the electrons and ions can be collected separately, not to mention that they can be counted additively. However, if the background ionization from the matrix components and the self-ionization of the flame itself are considered, it is clear that the electron signal

Figure 3-13. The physical interpretation of equation [35].

This plot shows that the model of separation of variables assumes that there is a steady-state distribution between the laser focal point and the anode which builds up at the very moment when both lasers go off ($t_f=0$). The anode behaves like an infinite sink and the electron populations thus decays exponentially versus time. The solid line is the spatial distribution of electrons at $t_f=0$ and the dash lines are the electron distribution at later times. Notice that the area under each curve stands for the total population of electrons and it decays exponentially versus time.

RESULT FROM THE METHOD OF SEPARATION OF VARIABLES

$$P(q, t) = \frac{N \pi}{2q_a} * \exp(-t/\tau) * \cos\left(\frac{q \pi}{2q_a}\right)$$

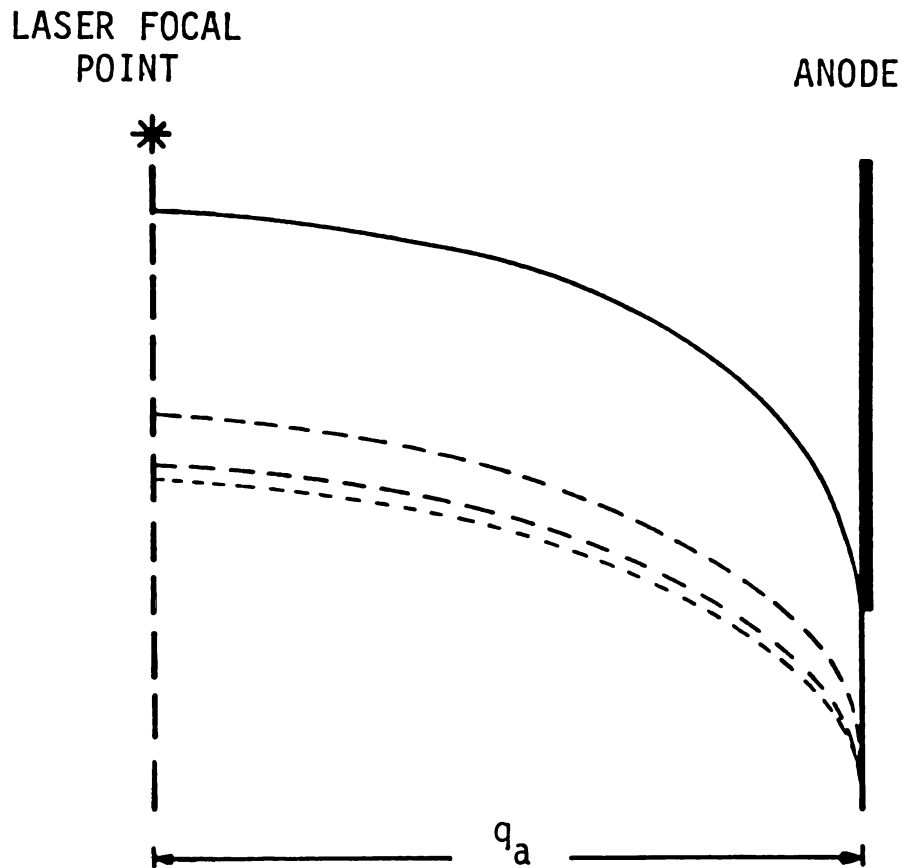


Figure 3-13.

can be detected by the anode separately since meanwhile the cathode can absorb the background ions in the flame and fulfill the requirement of constructing a closed current loop. The very same argument can also be applied to the cathode reactions. Nevertheless, this argument cannot guarantee that the electron and ion peaks will be additive all the time during a DLI signal collection process. If the volume ionization rate of the dual laser ionization is far exceeding that of the background flame, at a stage the electrodes will be collecting electrons and ions which are both formed by the dual laser ionization of the analytes. A complete treatment of the transition stage for step (ii) proposed in Section D-2 is clearly required. However, since the experimental results showed that counter compensation from the background to the signal collecting processes at both electrodes can be assumed at the later stage of the DLI processes, the signals are assumed to be always additive throughout this thesis.

In Figure 3-14 a charge separation process is sketched for a flame with biased probes. The separation is assumed to begin immediately after the lasers were turned off. Notice that in Figure 3-14, Lawton's model of "charge sheath" is adopted, and the electric field is not the same everywhere along the q -axis but rather piece-wise linear. In the sketches of the electron and ion distribution curves, it is assumed that a high bias voltage is applied and the

Figure 3-14. A sketch of the charge separation processes under the influence of a high bias voltage at $t_f > 0$. This process started immediately after the laser pulses went off. Lawton's model of "charge sheath" is adopted here and the electric field (the solid line) is thus piece-wise linear. The distribution curves of ions electrons were calculated by the Fokker-Planck equation with a piece-wise linear drift function. The ambipolar diffusion effect was ignored. Notice that the the shape of the distribution curves for ions and electrons are not pure Gaussian.

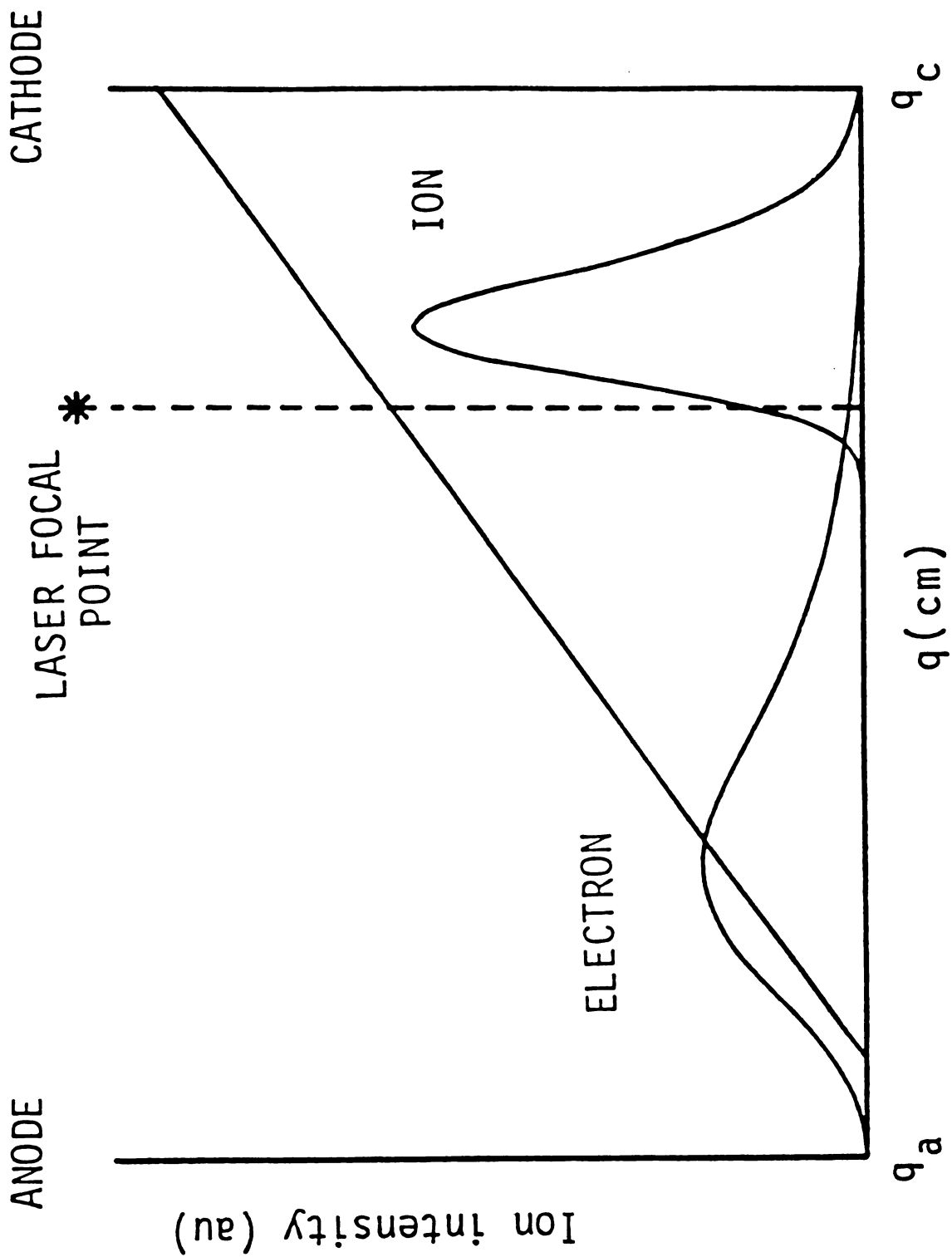


Figure 3-14.

interaction between electrons and ions (i.e. the ambipolar diffusion effect) can be safely ignored. Even so, due to the piece-wise linear electric field, the shape of the distribution curves for electrons and ions are still not purely Gaussian. The theoretical effects of the piece-wise linear electric field on the distribution curves were calculated by a simple Fokker-Planck equation, and are depicted in Figure 3-14. The implications and the formalism of the Fokker-Planck equations are discussed in detail in Chapter IV.

D-4 Ion signals

Close examination of Figures 3-9 and 3-10 reveals that the arrival times of the peak maxima of the ion signals is a function of the distance between the laser focal point and the lower probe (cathode). The width of the ion peaks is in turn a function of the peak maxima arrival time. These observations imply that the transport phenomena for ions in the DLI process are both mobility and diffusion dependent. Experimental results from our laboratory have shown that the mobility and diffusion processes are both involved, and can be treated separately by assuming the existence of steady states (2). However, when the bias voltage applied to the electrodes increases to a certain extent, it has been found that the DLI signals no longer decay exponentially. Curve

fitting has also shown that the ion signals, which are obtained by subtracting the electron peaks from the DLI signals, are significantly skewed from pure Gaussian distributions. This implies that the steady-state, pure diffusion model proposed by Lin is not suitable when the bias voltage applied to the electrodes is sufficiently high. Therefore, a new model which can treat the interactions between the mobility and diffusion processes simultaneously, for ions and electrons under different shapes of the electric fields, is clearly required. The one-dimensional Fokker-Planck equation was chosen to try to reconcile all the different mechanisms of the DLI processes under investigation in our laboratory.

One of the important applications of the the time-resolved DLI ion signal is that it can be used to disclose the values of the mobilities and diffusion coefficients of analyte ions. Lin et al. (2,5) have shown that by assuming an ambipolar model, the diffusion coefficients of various ions can be calculated. By solving a linear hyperbolic equation, Lin (1,5) was also able to calculate the mobility coefficients of various ions. With the aid of the Einstein formula given in equation [9] of Chapter I, the temperature of the flame was calculated. Lin's data agreed with literature values very well.

A close examination of Lin's model shows that Lin was,

in fact, solving the Fokker-Planck equation with a constant drift function separately while assuming that ambipolar diffusion exists. In other words, the interactions between the ion mobility and diffusion are completely ignored. The Fokker-Planck equations are capable of treating the mobility, diffusion, and the interactions between the two accurately. Hence through proper modelling and curve fitting procedures, the mobility and diffusion coefficients of ions can be extracted simultaneously from one time-resolved DLI experiment. In turn the flame temperature can be calculated. The details of the new model are covered in the next three chapters of this thesis. The treatment of ion signals and the Fokker-Planck formalism are discussed, and more experimental results are presented to portray the ion transport phenomena.

Another potential application of the ion peaks in the DLI signals is to increase the detection limit of the DLI technique for real sample analysis. This idea has already been presented in Section D-1 along with the discussion of the implications of Figure 3-11.

D-5 Shape of the Electric Field

Before closing this chapter, the electric field built up in the relatively clean hydrogen-oxygen-argon flame

produced by a laminar-flow Meker burner will be discussed.

Besides revealing several features of the electron peaks of the DLI signals, Figure 3-10 also implies that the fuel-rich hydrogen-oxygen-argon flame probably is "super-saturated" when a bias voltage of 180 volts are applied. From Figure 3-10, it is clear that as the upper electrode (anode) is displaced from the laser focal point, the peak maxima of the ion signals arrive later. Since the distance between the lower probe (cathode) and the laser focal point was kept the same, the only explanation is that the electric field changes as the anode was moved. However, equations [2] and [3] indicate that the shape of the electric field should be independent of the position of the anode. According to Lawton's model, the only explanation is that the electric field between the electrodes has been super-saturated. This phenomenon has been examined carefully. The same results were always obtained unless more than 500 ppm of cesium was added to the analyte solution. A high concentration of cesium in the analyte solution often caused the input of the boxcar to be overloaded. Hence in all of the models constructed in this thesis, a super-saturated electric field between the electrodes is always assumed.

Equations [14] through [16] describe the magnitudes of the electric field and electrical potential along the q -coordinate. They were previously given in in Section B-2

and Figure 3-3. These equations are all extremely lengthy and complicated. In addition, when the flame is perturbed by the laser pulses, the inductive effect due to the fast-moving electrons and the transport phenomena of ions and electrons moving through space will further disturb the steady-state charge distribution in the flame. The entire situation thus becomes even more complicated. In order to avoid the sophistication of mathematics, a reasonable but less complicated version of equation [14] is desired.

For a relatively clean flame like the hydrogen-oxygen-argon flame used in our laboratory, it is reasonable to assume that the ionization rate, A_s , of the background matrix per unit volume per second is very small, or

$$A_s^2 (q_a - q)^2 \ll E_a, \quad q_a > q > -q_c \quad [36]$$

Hence the series expansion of equation [14] can be obtained as follows :

$$E = E_a + \frac{1}{2} \frac{A_s^2 (q_a - q)^2}{E_a} + \dots \quad [37]$$

The first order approximation of equation [14] then is:

$$E \approx E_a + k(q_a - q)^2 \quad [38]$$

where

$$k = \frac{1}{2} \frac{A_s^2}{E_a} \quad [39]$$

Practically, equation [39] can be further simplified by assuming that the distance between the laser focal point and the cathode is reasonably small, or that the first derivative of the second term in equation [38] is reasonably small. This yields:

$$E = E_a + k'(q_a - q) \quad [40]$$

where

$$k' = \frac{A_s^2 (q_c + q_a)}{E_a} \quad [41]$$

Equation [41] has been applied to various Fokker-Planck equations with good results. To further simplify the model, we may assume that the second derivative of the second term in equation [38] is zero:

$$\frac{d^2 E}{dq^2} \approx 0 \quad [42]$$

Equation [42] yields the following:

$$A_s = 0 \quad [43]$$

which makes:

$$E = E_a \quad [44]$$

In this condition, E_a can be obtained by applying L'Hospital's rule to the right hand side of equation [16], which gives:

$$E_a = \frac{V_a}{(q_c + q_a)} \quad [45]$$

In turn equations [44] and [45] give the extremely useful approximation:

$$E = \frac{V_a}{(q_c + q_a)} \quad [46]$$

Equation [46] applies in the extreme condition under which no background ions are present in the flame. This condition also has been applied to the Fokker-Planck equation and again yields very good results in most circumstances.

Equations [14], [38], [40], and [46] offer different orders of approximation to the electric field in the flame. Their usefulness depend on how sophisticated a model that is actually needed. Notice that the derivation of equations [36] through [46] implies that if the bias voltages applied are sufficiently large in a relatively clean flame, the electric field can be safely assumed to be linear even it is truly super-saturated. This assumption may help to simplify the already complicated DLI processes.

E. Conclusion

Experimental results have been presented in this chapter to confirm that the time resolved DLI signal has two temporal components: a short and strong electron peak followed some microseconds later by a longer and weaker ion peak. The temporal behavior of DLI signals taken under various probe positions and bias voltages were discussed. General conclusions were drawn in order to give a clear picture of the temporal DLI processes. An explanation of the reason why the electron signal and ion signal can be detected separately and treated additively was given. The shape of the electron signal was investigated and described. A theoretical treatment was given to strengthen the argument that, with the experimental set-up in our laboratory, the electron signal always decays exponentially versus time. Experimental results also revealed that the interaction between ion mobility and diffusion cannot be ignored if the bias voltage is high. Discussions concerning the modelling of the ion signals were given. The necessity of adopting the Fokker-Planck equation was established.

Also, Lawton's model concerning the shape of the electric field in a flame environment was presented. Experimental results have shown that in a hydrogen-oxygen-argon flame under fuel-rich conditions, the electric field

is almost always super-saturated. Several approximations of the super-saturated electric fields in the flame environment were derived and interpreted.

The potential application of the time-resolved DLI technique to real samples was suggested. The possibility of extracting mobility and diffusion coefficients of ions from a single DLI experiment in order to determine the flame temperature was considered. This feature is examined in future chapters.

CHAPTER III

REFERENCES

1. C.A. van Dijk, F.M. Curran, K.C. Lin and S.R. Crouch, Anal. Chem. 53, 1275 (1981).
2. K.C. Lin, P.M. Hunt, and S.R. Crouch, Chem. Phys. Lett. 90, 111 (1982).
3. F.M. Curran, C.A. vanDijk, and S.R. Crouch, Appl. Spectrosc. 37, 385 (1983).
4. F.M. Curran, K.C. Lin, G.E. Leroy, P.M. Hunt, and S.R. Crouch, Anal. Chem. 55, 2382 (1983).
5. K.C. Lin, Ph.D. Thesis (Michigan State University, 1982).
6. F.M. Curran, Ph.D. Thesis (Michigan State University, 1983).
7. G.C. Turk, J.C. Travis, J.R. DeVoe, and T.C. O'Haver, Anal. Chem. 51, 1890 (1979).
8. R.B. Green, G.J. Havrilla, and T.O. Task, Appl. Spectrosc. 34, 561 (1980).
9. G.J. Havrilla, and R.B. Green, Anal. Chem. 52, 2376 (1980).
10. G.C. Turk, Anal. Chem. 53, 1187 (1981).
11. J. Lawton and F. Weinberg, "Electrical Aspects of Combustion" (Claredon Press, Oxford, 1969).
12. G.J. Havrilla, P.K. Schenck, J.C. Travis, and G.C. Turk, Anal. Chem. 56, 186 (1984).
13. T. Berthoud, J. Lipinsky, P. Camus, and J.-L. Stchle, Anal. Chem. 55, 959 (1983).

14. K.C. Smyth and W.G. Mallard, Combust. Sci. Technol. 26, 35 (1981).
15. W.G. Mallard and K.C. Smyth, Combust. Flame 44, 61 (1982).
16. L.G.H. Huxley and R.W. Crompton, "The Diffusion and Drift of Electrons in Gases" (John Wiley & Sons, New York, 1974).
17. E.W. McDaniel and E.A. Mason; "The Mobility and Diffusion of Ions in Gases" (John Wiley & Sons, New York, 1973).

CHAPTER IV

THE FOKKER-PLANCK EQUATION

A. Introduction

Dual laser ionization (DLI) spectrometry is a powerful analytical technique for the detection of trace metals (1). An N_2 -laser pumped dye laser, which is tuned to a resonant transition wavelength, is used to excite the analyte atomized in a flame. The excited analyte atoms are then photoionized by an N_2 laser beam (337.1 nm). The ions produced during the laser pulses are collected by a pair of nichrome wires (probes) immersed in the flame. Various bias voltages were applied to the probes in order to obtain optimum signal detection. An electric field is built up between probes. Ion transport to the probe (cathode) thus involves ion mobility. As indicated in the previous chapter, the ion peaks of the time-resolved DLI signals become broader when the arrival times of the peak maxima get longer. This suggests that the diffusion of ions has to be considered in addition to their mobility.

Further investigations of time-resolved DLI signals have shown that there exist two temporal components, i.e. a short electron signal followed some microseconds later by a longer and weaker ion signal. The shape of the time-resolved DLI signals can vary tremendously with the change of experimental variables such as applied voltage, flame background current, and the position of laser focal point with respect to the collection to the probes.

In order to be able to systematically predict the effect of experimental variables on the time-resolved DLI signals, a suitable mathematical model is required. As indicated in the previous chapter, the mathematical model may be used to help determine the appropriate aperture duration and aperture delay of the boxcar integrator, in order to block out most of the background interference and to obtain lower detection limits (1). It may also be used to find the experimental conditions which exclude the contribution of the electron peak to the time-resolved DLI signal, and enable further lowering of the detection limits through curve fitting techniques. In addition, a suitable mathematical model may be employed to help determine both the mobility and the diffusion coefficients of analyte ions in the flame, hence the flame temperature can be calculated.

Mathematical models which describe the signal collection processes of laser-enhanced ionization (LEI) and

DLI have been reported (2-4). Berthoud et al. (3) used a diffusion-free model to calculate the mobility of electrons. Havrilla et al. (4) treated the ion cluster as a point charge and proposed a signal detection mechanism with the aid of Lawton's model, which predicts the shapes of the electric fields in the flame. Lin et al. (2) proposed a steady-state approximation to calculate the diffusion coefficients of analyte ions in the flame. Also, a model with a linear, hyperbolic partial differential equation was employed by Lin et al. in order to measure the mobility coefficients of ions. However, none of the previous workers has investigated the interactions between ion diffusion and ion mobility. Experimental results presented in the previous chapter show that in many cases the interactions between diffusion and mobility of ions cannot be ignored if high flexibility of the DLI technique is demanded. Therefore, a new model which can simultaneously treat both factors is required. In fact, solving the Fokker-Planck equation with appropriate drift functions turns out to be an appealing choice.

The biggest advantage of the Fokker-Planck equation is that it can treat ion mobility and diffusion simultaneously under various experimental conditions. Through proper modelling of the DLI signals with a set of one-dimensional Fokker-Planck equations, curve fitting techniques can help reveal details of the ion transport processes in a flame

under the influence of an electric field. This chapter is devoted to the derivations of the Fokker-Planck equations in order to construct a more flexible and effective mathematical model for DLI processes. The interpretations of various drift functions will also be discussed.

B. Derivation of the Fokker-Planck equation

The transport phenomena of ions and electrons in a flame environment under the influence of an electric field consist of at least four factors, namely: diffusion, migration, convection, and mutual interactions of electrons and ions. In this chapter, only the first three factors are considered since presumably the interactions among electrons and ions can be treated by the ambipolar diffusion assumption (2). Also, the discussion in this chapter is devoted to the ion peaks of the time-resolved DLI signals, since the experimental results mentioned in the previous chapter have shown that the electron peaks usually decay exponentially in the later stage of the DLI processes.

The most obvious factor of the three is the migration of ions under the influence of the electric field. This factor can be expressed mathematically by the following equation:

$$J(q,t) = \mu E(q) P(q,t) \quad [1]$$

where $J(q,t)$ is the ion flux ($\text{ions} \cdot \text{sec}^{-1} \cdot \text{cm}^{-2}$), μ is the ion mobility coefficient ($\text{cm}^2 \cdot \text{sec}^{-1} \cdot \text{volt}^{-1}$), $E(q)$ is the electric field ($\text{volt} \cdot \text{cm}^{-1}$), and $P(q,t)$ is the conditional propagator or ion density ($\text{ions} \cdot \text{cm}^{-3}$). The ion flux is a function of both the q -coordinate and time, as is the ion density. According to the discussion in Section D-2, Chapter III concerning the shape of the electric field, the term $E(q)$ is assumed to be a function of the q -coordinate only in order to keep the model from getting too complicated.

The factor most often ignored in the DLI process is diffusion. The diffusion of ions due to the ion density gradients can be expressed as follows:

$$J(q,t) = - D \frac{\partial P(q,t)}{\partial q} \quad [2]$$

where D ($\text{cm}^2 \cdot \text{sec}^{-1}$) is the diffusion coefficient of the ions.

The convection factor is due to elastic collisions of the analyte ions with other flame particles. Since the flames used in this work were generated by a laminar-flow Meker burner, there is some justification for omitting this factor from the one-dimensional model proposed here. The ion flux due to convection can be written as follows:

$$J(q,t) = v(q) P(q,t) \quad [3]$$

where $v(q)$ is the burning velocity ($\text{cm} \cdot \text{sec}^{-1}$) of the laminar-flow burner.

Upon combination of all the three above mentioned factors, a complete equation for the ion flux is obtained:

$$J(q,t) = \mu E(q)P(q,t) - D \frac{\partial P(q,t)}{\partial q} + v(q)P(q,t) \quad [4]$$

The change of ion density at point q can be written as follows:

$$\frac{\partial P(q,t)}{\partial t} = - \frac{\partial}{\partial q} \{ J(q,t) - J(q+dq,t) \} \quad [5]$$

where the term $J(q+dq,t)$ is defined as follows:

$$J(q+dq,t) = J(q,t) + \left(\frac{\partial J(q,t)}{\partial q} \right) dq \quad [6]$$

Substitution of equations [5] and [6] into equation [4] yields:

$$\frac{\partial P(q,t)}{\partial t} = D \frac{\partial^2 P(q,t)}{\partial q^2} + \frac{\partial}{\partial q} (h(q)P(q,t)) \quad [7]$$

where $h(q)$ is the so-called "drift function" which is defined as follows:

$$h(q) = - (\mu E(q) + v(q)) \quad [8]$$

Equations [7] and [8] constitute the one-dimensional

Fokker-Planck equation that is suitable for the DLI processes.

C. Analytical Solutions

C-1. Steady-State Approximations

In our laboratory, Lin (2) has proposed a method to solve equation [7] under extreme conditions. By assuming both that the diffusion term is not as important as the migration term under high and constant electric field, and that the convection term is negligible, equation [7] can be reduced as follows:

$$\frac{\partial P(q,t)}{\partial t} = u E \frac{\partial P(q,t)}{\partial q} \quad [9]$$

This equation can be solved by the method of separation of variables. The solution of equation [9] thus is written as follows (2):

$$P(q,t) = n \exp(-q/q_c) * \exp(-\alpha t/q_c) \quad [10]$$

where q_c is the distance between the laser focal point and the lower probe (cathode), as designated in Figure 2-6. The term α ($\text{cm} \cdot \text{sec}^{-1}$) is defined as follows

$$\alpha = \mu E \quad [11]$$

Equation [10] implies that the ion density function has been assumed to be a steady-state distribution when the method of separation of variables was adopted. In addition, the ion density function decays exponentially with time. Lin et al. were able to calculate the mobility coefficients of ions with the aid of equations [10] and [11].

Under the condition that the electric field is absent, equation [7] can be reduced to:

$$\frac{\partial P(q,t)}{\partial t} = D \frac{\partial^2 P(q,t)}{\partial q^2} \quad [12]$$

The analytical solution of equation [12] has already been given in equation [31], chapter III. For ions, that equation can be re-written as follows:

$$P(q,t) = \frac{n\pi}{2q_c} * \exp\left(-\frac{t}{\tau}\right) * \cos\left(\frac{q\pi}{2q_c}\right) \quad [13]$$

where τ is the lifetime of this process and was defined as:

$$\tau = 4 \pi^{-2} D_a^{-1} q_c^2 \quad [14]$$

In equation [14], D_a stands for the ambipolar diffusion coefficient for the ions only. The interpretation of this equation has been discussed in detail as in chapter III.

From the above brief discussion, it is clear that Lin was solving the one-dimensional Fokker-Planck equation

separately. The outcome of Lin's work is quite satisfactory and the current work takes advantage of his investigations. The result from his work assumes that ambipolar diffusion always applies in the DLI process. However, from the experimental results obtained here, it can be concluded that what Lin observed was the electron signal rather than the ion signal. Nevertheless, due to the effectiveness of the ambipolar diffusion, the later part of the electron signal possesses the same diffusion coefficient as ions.

C-2 Path Integral Formalism

A full understanding of the DLI signal detection process relies on treating all of the diffusion, migration, and convection terms together. Due to the level of complexity of the mathematics involved, the one-dimensional Fokker-Planck equation is adopted.

Functional path integral techniques are extremely powerful for solving the Fokker-Planck equation. A brief review of the development of the path integral was given in Chapter I, Section B-4. Path integral techniques are frequently coupled with the Onsager-Machlup-Laplace (OML) approximation. The OML approximation is exact when the drift function $h(q)$ is linear. A later part of this chapter will show that the OML approximation is also exact for

piece-wise linear drift functions.

For the Fokker-Planck equation with a constant diffusion coefficient D , the path integral techniques yields (5,6):

$$P(q_f, t_f | q_0, t_0) = \int D[q(t)] * \exp \left\{ -\frac{1}{2D} \int_{t_0}^{t_f} L(q, \dot{q}, t) dt \right\} \quad [15]$$

The term $P(q_f, t_f | q_0, t_0)$ is the conditional propagator (cm^{-1}) which indicates the probability of observing the value q_f for the stochastical variable q at time t_f . At time $t=0$ (t_0), the conditional propagator is a Dirac delta function.

$$P(q_f, t_f | q_0, t_0) = \delta(q_f - q_0) \quad [16]$$

The integration of equation [15] runs over all functions $q(t)$ under the following designations:

$$q(t_0) = q_0 \quad [17]$$

and

$$q(t_f) = q_f \quad [18]$$

A differentiable path that minimizes the thermodynamic action S always satisfies the Euler-Lagrange equation. If there is only one such path, it determines the OML approximation as follows (5-12):

$$P(q_f, t_f | q_0, t_0) = (4\pi D)^{-1/2} \left(\frac{dq_f}{d\dot{q}_0} \right)^{-1/2} \exp\left(-\frac{S(q^c)}{2D} \right) \quad [19]$$

where

$$S(q^c) = \int_{t_0}^{t_f} L(q, \dot{q}, t) dt \quad [20]$$

The term $L(q, \dot{q}, t)$ is the Lagrangian, which, in turn is described as follows:

$$L(q, \dot{q}, t) = \frac{1}{2} [(\dot{q}(t) + h(q))^2 - 2Dh'(q)] \quad [21]$$

Equation [20] should be evaluated along the path $q^c(t)$ for which the action is minimum.

All the analytical solutions and numerical solutions of the Fokker-Planck equations with various drift functions in this chapter were solved according to the algorithm defined above.

C-3 Constant Drift Function

As mentioned in the previous chapter, the electric field in the laminar-flow hydrogen-oxygen-argon flame is, in

fact, super-saturated. If we further assume that the burning velocity of the flame is a constant along the q -coordinate, i.e. the convection term is no longer a function of q , we may rewrite the drift function as follows:

$$h = -\alpha \quad [22]$$

where

$$\alpha = \mu E + v \quad [23]$$

The solution of equation [7] is given as follows:

$$P(q_f, t_f | q_0, t_0) = \frac{1}{[4\pi Dt_f]^{1/2}} \exp \left\{ -\frac{(q_f - \alpha t_f)^2}{4Dt_f} \right\} \quad [24]$$

Notice the unit of the conditional propagator $P(q_f, t_f | q_0, t_0)$ is cm^{-1} . Equation [24] is an exact solution of equation [7] with a constant drift function and it is already normalized.

Equation [24] is evidently of a Gaussian form. The physical interpretation of equation [24] is clear. The conditional propagator can be viewed as the ion density distribution which changes with time. Since the solution is always Gaussian in the time span, the spreading process is, in fact, a pure diffusion process. The numerator of the exponential term implies that the peak maximum is moving with a constant velocity v_{ion} where

$$\begin{aligned} v_{\text{ion}} &= \alpha \\ &= \mu E + v \end{aligned} \quad [25]$$

Equation [24] nicely offers a less complicated and fairly intuitive interpretation of the DLI process. A pictorial interpretation of equation [24] is given in Figure 4-1.

However, since the DLI processes occur on the microsecond time scale and the position of the cathode is fixed, i.e. it is not possible to physically scan the probe along the q -coordinate in such a short time period, equation [24] is not that useful in modelling the DLI processes. A conditional propagator with the units of sec^{-1} is, in fact, much more useful. The following section is thus devoted to deriving a conditional propagator with the more appropriate units.

C-4 Practical Modification

If we assume that the cathode behaves like an infinite sink which can absorb ions infinitely fast and thus does not impose any extra charge to distort the electric field near the surface of the electrode, the conditional propagator given in equation [24] can be modified to have the units of sec^{-1} .

Since equation [24] offers a normalized distribution function for ions, we may relate the time-dependent total

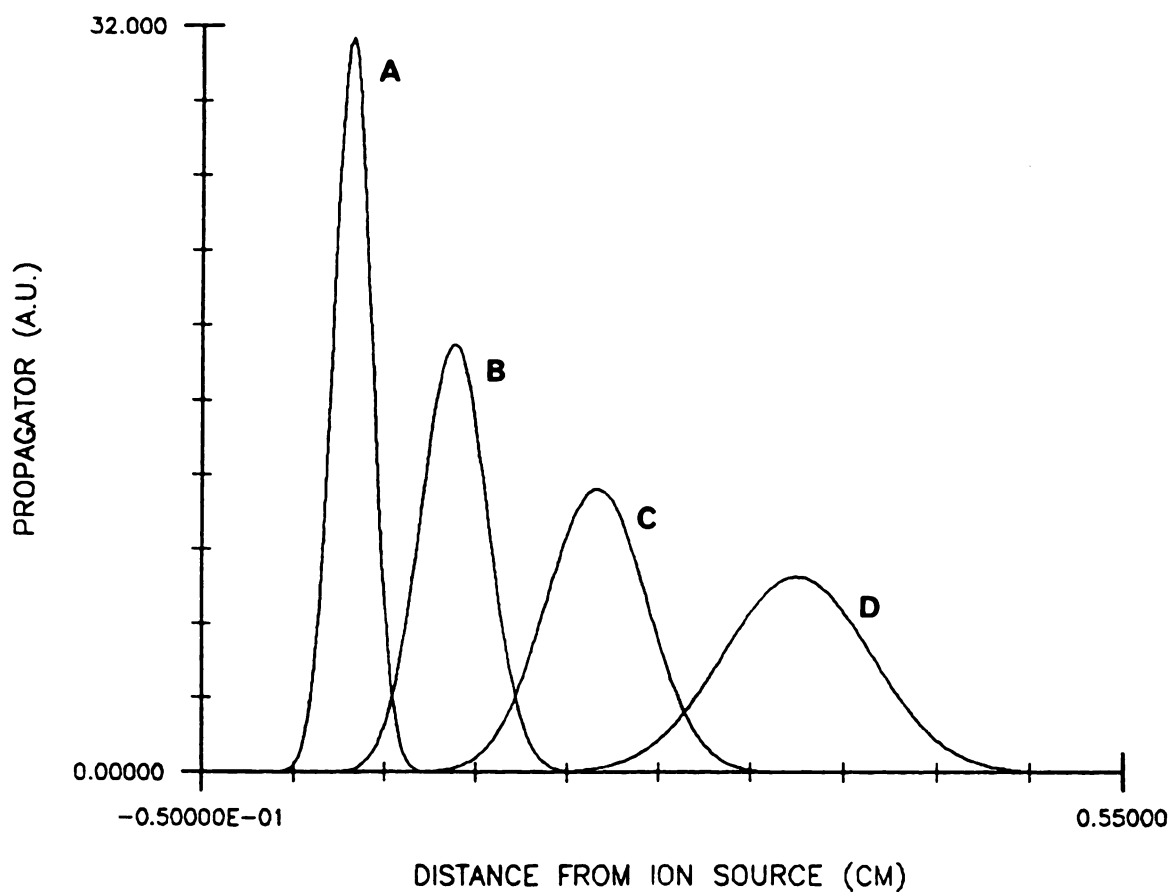


Figure 4-1. Ion distribution versus time diagram. This diagram was drawn from equation [24] by assuming $D = 11.3 \text{ cm}^2 \cdot \text{sec}^{-1}$ and $u = 30.4 \text{ cm}^2 \cdot \text{sec}^{-1} \cdot \text{volt}^{-1}$.

A, 5 μs ; B, 10 μs ; C, 15 μs ; D, 20 μs after the laser pulse.

DLI signal, S_{total} , to the distribution function as follows:

$$S_{\text{total}} = 1 - \int_q^{q_f} P(q_f, t_f | q_0, t_0) dq \quad [26]$$

Therefore the DLI signal, S_{time} , collected by the cathode over a time interval dt can be defined as follows:

$$S_{\text{time}} = \frac{dS_{\text{total}}}{dt_f} \quad [27]$$

S_{time} can be viewed as the ion flux which passes the cathode. Substitution of equation [26] into equation [27] yields:

$$S_{\text{time}} = - \frac{d}{dt} \int_q^{q_f} P(q_f, t_f | q_0, t_0) dq \quad [28]$$

According to the Leibnitz rule, equation [28] can be rewritten as:

$$S_{\text{time}} = - \int_q^{q_f} \frac{d}{dt} P(q_f, t_f | q_0, t_0) dq \quad [29]$$

The integral given in equation [29] has to run from negative infinity to q_f in order to assure the normalization of the distribution function. If q is chosen to be negative infinity, equation [29] yields:

$$S_{\text{time}} = \frac{(q_f + at_f)}{4[\pi D]^{1/2} t_f^{3/2}} \exp \left\{ -\frac{(q_f - at_f)^2}{4Dt_f} \right\} \quad [30]$$

Equation [30] is normalized and has units of sec^{-1} . The physical interpretation of equation [30] is, in fact, very different from that of equation [24]; however, it still provides insight.

Equation [30] has a few interesting implications. First, it predicts that the ion peak will appear when

$$q_f = \alpha t_f \quad [31]$$

This implication agrees with the point charge approximation. Second, the value of Equation [30] approaches zero when t_f approaches zero, i.e. there is no signal at time zero. Mathematically, this implication can be expressed as follows:

$$\lim_{t \rightarrow 0} S_{\text{time}} = 0 \quad [32]$$

Equation [32] can be proved by applying L'Hospital's rule to the right hand side of equation [30].

The idea of deriving a complementary conditional propagator with a unit of sec^{-1} can help treat the skewness of the DLI signals. Besides, the physical interpretation, in fact, makes perfect sense. A plot of equation [30] versus time is given in Figure 4-2.

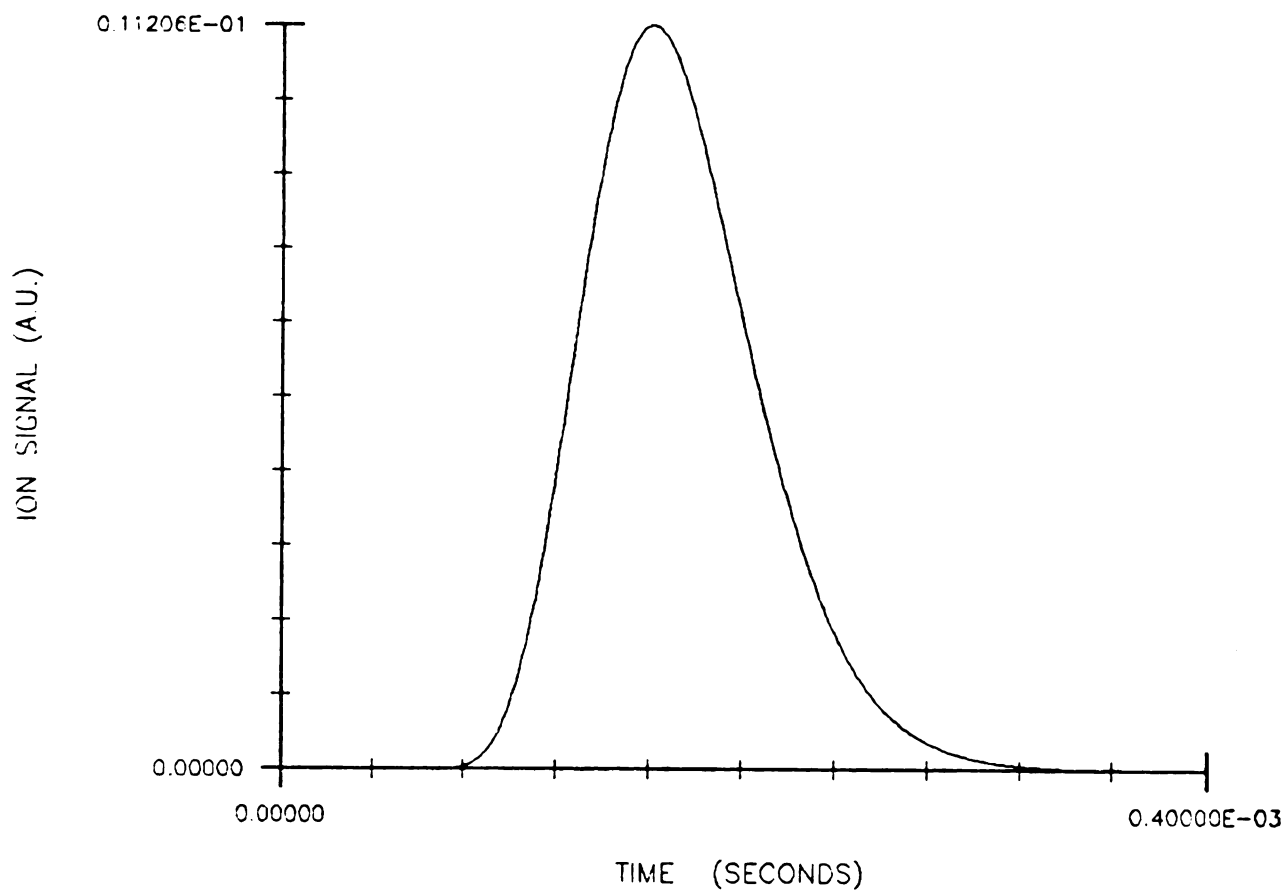


Figure 4-2. Calculated ion signal versus time. This diagram is calculated from equation [30] by assuming $D = 11.3 \text{ cm}^2 \cdot \text{sec}^{-1}$ and $u = 30.4 \text{ cm}^2 \cdot \text{sec}^{-1} \cdot \text{volt}^{-1}$. Notice the skewness of the calculated signal.

C-5 Linear Drift Function

As mentioned in Section B-2, Chapter III, when the electric field is saturated, it can be expressed as follows:

$$E = A_s (q_a - q), \quad -q_c \leq q \leq q_a \quad [33]$$

where A_s is defined in equation [4], Chapter III. This provides a linear drift function,

$$h = -\mu A_s (q_a - q) \quad [34]$$

This is, in fact, the well-known Ornstein-Uhlenbeck process (13). The analytical solution of this case has been given in equations [17] and [18], Chapter I.

C-6 Piece-wise Linear Drift Function

When the electric field is sub-saturated, it can be described as follows:

$$E = A_s (q_s - q), \quad q \leq q_s \quad [35]$$

and

$$E = 0, \quad q_s < q \leq q_a \quad [36]$$

The term A_s is defined in equation [4], Chapter III, and all

the q -coordinates were designated in Figure 2-6, while q_s is the thickness of the space charge sheath around the cathode. The electric field described by equations [35] and [36] is called a piece-wise linear field since the slope of the electric field changes at point q_s . When the laser focal point is inside the non-zero electric field region, the piece-wise linear case still allows ions, through random motion, to enter the zero electric field region. If the ion carries enough momentum upon entering the zero electric field region, it may never turn back and reach the cathode. That is the reason why in this case the analytical solution of the Ornstein-Uhlenbeck process (13) cannot be applied, even when the laser focal point is inside the non-zero electric field region. In the Ornstein-Uhlenbeck processes, all the ions eventually reach the cathode since space extends to infinity.

The analytical solution of the piece-wise linear case was obtained by path integral techniques with the Onsager-Machlup-Laplace (OML) approximation. The formalism described in Section C-2 of this chapter was followed. The solution reads as follows:

$$P(q_f, t_f | q_0, t_0) = (4\pi D)^{-1/2} m^{-1/2} \int_{-\infty}^{\infty} \frac{dq_f}{dp_0}^{-1/2} \exp\left(-\frac{S(q^C)}{2D}\right) \quad [37]$$

where

$$\left(-\frac{dq_f}{dp_0}\right) = \frac{q_f}{mAq_0 + p_0} - \frac{q_0}{mAq_f + p_f} \quad [38]$$

and

$$S(q^C) = ADt_f + \frac{1}{2m} (q_f p_f - q_0 p_0) - \frac{A}{2} (q_f^2 - q_0^2) \quad [39]$$

where D is the diffusion coefficient ($\text{cm}^2 \cdot \text{sec}^{-1}$). The term A (sec^{-1}) is defined as follows:

$$A = \mu A_s \quad [40]$$

The terms p_0 and p_f ($\text{g} \cdot \text{cm} \cdot \text{sec}^{-1}$) are the initial and final momenta of the ions. They are defined as follows:

$$p_0 = \frac{m A (2q_f e^{At_f} - q_0 (e^{2At_f+1}))}{e^{2At_f} - 1} \quad [41]$$

and

$$p_f = \frac{m A (q_f (e^{2At_f} + 1) - 2q_0 e^{At_f})}{e^{2At_f} - 1} \quad [42]$$

Notice that the conditional propagator has the units of cm^{-1} and is only a function of the q -coordinate and time. The validity of equations [37] through [42] has been confirmed by comparing the predicted values (propagator versus time)

at various q_f with those from the numerical method described in Section E of this chapter.

Since substitution of equations [37] through [42] back into equation [7] makes both sides of equation [7] identical, the analytical solution of the Fokker-Planck equation with a piece-wise linear drift function is exact. Taking the limit of A approaching zero, the result of a Wiener process (14), equation [14], chapter I, can be recovered.

D. Further Treatments

D-1. Introduction

Close examination of the assumptions made in the previous sections indicates that the analytical solutions of the Fokker-Planck equations with various drift functions can give reasonable approximations for the detection processes of DLI signals. A few assumptions are indeed over-simplified from the real DLI process. From the outcomes of the curve fitting methods described in the next chapter, it is obvious that further treatment beyond the Fokker-Planck formalism is needed.

One of the unrealistic assumptions that over-simplified the treatment of the real DLI processes is from equation

[16] of this chapter. The assumption that the DLI process starts from a Dirac delta function has two implications. In the scale of time, the laser pulses are assumed to be extremely short in comparison with that of DLI process. In the scale of space, the ions are assumed to be confined in a volume which is negligible compared to the distance between the laser focal point and the cathode, q_c . Examination of Figure 2-4 shows that the length of the temporal overlap of the nitrogen laser and the dye laser is only 3.1 nanoseconds, which is negligible when compared with the microsecond time scale of the DLI experiment. However, as indicated in Section B, Chapter II, the focal area of the dye laser through the lens was determined to be $(1.0 \pm 0.3) \times 10^{-3} \text{ cm}^2$, i.e. the diameter of the corresponding focal area is $(0.36 \pm 0.03) \text{ mm}$ (15). The dimensions of the laser focal point are not negligible with respect to q_c .

Also, in the previous sections, the burning velocity v was almost always assumed to be insignificant in the DLI process. This assumption is not necessarily true, either. The burning velocity of the hydrogen-oxygen-argon flame from the Meker burner is about $500 \text{ cm} \cdot \text{sec}^{-1}$ (16). If we assume that the mobility coefficient of the analyte ion is about $25.0 \text{ cm}^2 \cdot \text{volt}^{-1} \cdot \text{sec}^{-1}$, this factor will be comparable to the ion mobility if the bias voltage applied to the electrodes is less than 20 volts when the distance between anode and cathode is 1.00 cm. Usually, this factor will cause at

least 10 % error.

The results of curve fitting revealed that there exist strong mutual repulsion forces among ions in the early stage of the DLI process. This mutual repulsion was also not accounted for by the drift functions chosen for solving the Fokker-Planck equations.

In order to compensate for the errors caused by the over-simplified assumptions of the treatment of DLI process mentioned above, further treatment is required.

D-2. Convolution Method

To account for the finite dimensions of the laser focal point, convolution of the analytical solution with a reasonable initial space function is a natural choice. If the interaction among ions can be ignored, the laser focal point can be represented by a summation of infinitely thin slices which drift and diffuse independently. Therefore, the DLI signals at any time t_f can be represented by the integration of conditional propagators with different q_0 values. This treatment can be expressed as follows:

$$P_{DLI}(t_f) = \int_0^{q_{1p}} P(q_f, t_f | q_0 - \xi, t_0) V(\xi) d\xi \quad [43]$$

where q_{lp} is the diameter of the laser focal point and $V(\xi)$ is the space distribution function of ions at the laser focal point at the very instant when the laser pulses went off. However, since the mutual repulsion of ions at the laser focal point cannot be omitted, a time-independent space distribution function is not very suitable.

However, if we view the transition from the electron-depletion and charge-separation stage to the ambipolar-diffusion stage (mentioned in Section D-2, Chapter III) as a random mixing process, a time-based exponential decay function can be used to account for much of the oversimplified assumptions we have made. The exponential decay is well-known as the result of a mixing process with an infinite mixing rate in a chamber of finite and fixed dimensions. The time constant of the exponential decay often can be interpreted as a function of the size of the mixing chamber.

Also, as mentioned in Section C-3, a conditional propagator with a unit of sec^{-1} may give better simulation of the DLI signals. Therefore we suggest that a modified conditional propagator convoluted with a time based exponential decay function may give the best description of the ion peaks of DLI signals. Indeed, the results of the curve fitting methods described in the next chapter confirm this proposal.

E. Numerical Solutions

E-1. Introduction

This section describes the computer algorithm which can provide numerical solutions of the Fokker-Planck equations with various drift functions. The computer algorithm is designed according to path integral techniques with the Onsager-Machlup-Laplace (OML) approximation. The formalism described in Section C-2 of this chapter was followed.

The numerical method has many advantages, as it can treat nearly any kind of drift function. Indeed, this is the most general method available that can give good approximate solutions to the Fokker-Planck equations with non-linear drift functions. In addition, numerical approximations can be used to verify the validity of complicated analytical solutions of the Fokker-Planck equations.

E-2. Computer Algorithm

This section gives a brief overview of the programming strategy and a concise algorithm which can be followed step-

by-step to construct a working program. A list of FORTRAN source code which contains all details of this algorithm is given in Appendix A.

To find the conditional propagator at time t_f numerically, a differentiable classical trajectory $q^C(t)$ has to be defined first. This trajectory must start from point q_0 at time t_0 and end at point q_f by time t_f . It may not be unique; however, it usually carries the minimum thermodynamic action $S(q^C)$ and satisfies the Euler-Lagrange equation. Usually, the minimal-action path can be found by providing an approximate initial momentum p_0 , then iteratively adjusting the value until the trajectory ends within a tolerable interval at q_f by time t_f . After the minimal-action path $q^C(t)$ is determined and the initial momentum p_0 is known, the preexponential factor can be rearranged as follows and calculated by the central difference method.

$$\left(\frac{dq_f}{dq_0}\right)^{1/2} = m^{1/2} * \left(\frac{dq_f}{dp_0}\right)^{1/2} \quad [44]$$

Then the minimum thermodynamic action can be obtained by integrating the thermodynamic Lagrangian along the minimal-action path $q^C(t)$.

The computer algorithm can be summarized step-by-step as follows:

(i) Design the drift function $h(q)$ that can describe the chemical system appropriately.

(ii) According to the drift function $h(q)$ designed in step (i), express the following equations analytically in terms of q :

$$V(q) = - \frac{m}{2} (h(q)^2 - 2Dh'(q)) \quad [45]$$

$$L(q, \dot{q}, t) = - \frac{1}{2} ((q + h(q))^2 - 2Dh'(q)) \quad [46]$$

$$\frac{dq}{dt} = \frac{p}{m} \quad [47]$$

$$\frac{\partial p}{\partial t} = - \frac{\partial V(q)}{\partial q} \quad [48]$$

$$\frac{dS(q^C)}{dt} = L(q, \dot{q}, t) \quad [49]$$

(iii) Set up two integrators:

<1> The first shall solve equations [47] and [48] simultaneously. (i.e., integrate both equations simultaneously versus time).

<2> The second shall solve equations [47] to [49] simultaneously

(iv) Use Newton's method to determine the correct initial momentum iteratively.

- <1> Supply an estimated initial momentum p_0 .
- <2> Call the first integrator established in step (iii) and evaluate the integrations of $q(t)$ and $p(t)$ from t_0 to t_f .
- <3> Compare the q outcome from step <2> with q_f .
If the difference is within the tolerance range, go to step (v).
- <4> Use Newton's method to estimate a new initial momentum p_0 .
- <5> Go to <1>.

(v) Call the second integrator set up in step (iii) with the p_0 from <5>, step (iv) to evaluate the thermodynamic action $S(q^C)$ along the the minimal-action path.

(vi) Use the central difference method iteratively to evaluate the preexponential factor according to equation [44].

(vii) Calculate the numerical value of the conditional propagator $P(q_0, t_0 | q_f, t_f)$ according to equation [19].

The FORTRAN source code and related input and output documents are given in Appendix A. The integrator used is the subroutine DVERK from the IMSL library pack. DVERK is a differential equation solver which is designed according to the Runge-Kutta-Verner fifth and sixth order method. All the source codes were run on a DEC VAX 11/750 computer.

F. Conclusion

In this chapter, the relationships between the Fokker-Planck equations and the signal detection process of dual laser ionization (DLI) were discussed. A one-dimensional Fokker-Planck equation was derived in accordance with the ion transport phenomena prevalent in DLI. Various analytical solutions to the Fokker-Planck equations with different drift functions were given. The implications of each drift function mentioned were discussed. Also, a different interpretation of the models and results published by Lin, et al. (2) was suggested. A modified form of the conditional propagator with units of sec^{-1} was proposed, and its physical implications were discussed. An exponentially modified conditional propagator was proposed and the validity of that treatment was also examined. A brief description of the numerical method was given at the end of the chapter and the related FORTRAN source code was included in Appendix A.

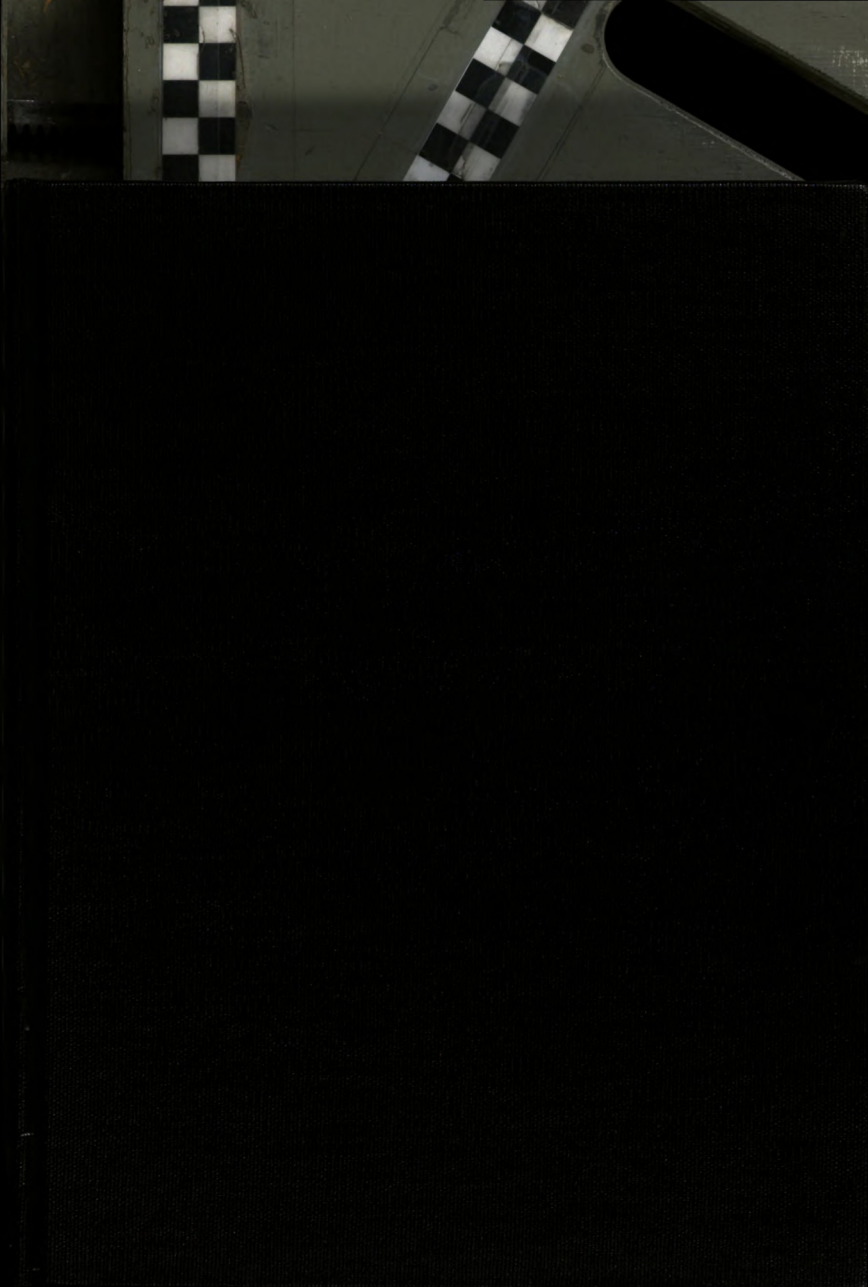
The transport processes in DLI are, in fact, much more complicated than the simple, one-dimensional Fokker-Planck equations presented in this chapter can manage. However, the results of curve fitting to be presented in next chapter suggest that the Fokker-Planck formalism is indeed the correct approach. More research is needed before the transport processes in DLI can be fully understood.

CHAPTER IV

REFERENCES

1. F.M. Curran, C.A. vanDijk, and S.R. Crouch, Appl. Spectrosc. 37, 385 (1983).
2. K.C. Lin, P.M. Hunt, and S.R. Crouch, Chem. Phys. Lett. 90, 111 (1982).
3. T. Berthoud, J. Lipinski, P. Camus, and J.-L. Stehle, Anal. Chem. 55, 959 (1983).
4. G. J. Havrilla, P.K. Schenck, J.C. Travis, and G.C. Turk, Anal. Chem. 56, 186 (1984).
5. K.L.C. Hunt and J. Ross, J. Chem. Phys. 75, 976 (1981).
6. P.M. Hunt, K.L.C. Hunt, and J. Ross, J. Chem. Phys. 79, 3765 (1983).
7. L. Onsager and S. Machlup, Phys. Rev. 91, 1505 (1953).
8. S. Machlup and L. Onsager, Phys. Rev. 91, 1512 (1953).
9. F.W. Wiegel, Physica 33, 734 (1967); *ibid.* 37, 105 (1967).
10. F. Langouche, D. Reokaerts, and E. Tirapegui, Physica A97, 195 (1979).
11. M. Moreau, Physica A90, 410 (1978).
12. B.H. Lavenda, Phys. Lett. A71, 304 (1979).
13. G.E. Uhlenbeck and L.S. Ornstein, Phys. Rev. 36, 823 (1930).
14. H. Risken, "The Fokker-Planck Equation, Methods of Solution and Applications" (Springer-Verlag, Berlin, 1984).

15. K.C. Lin, Ph.D. Dissertation (Michigan State University, 1982).
16. C.Th.J. Alkemade, Tj. Hollander, W. Snelleman, and P.J.Th. Zeegers, "Metal Vapours in Flames" (Pergamon Press, Oxford, 1982).



2253 6298

THESIS

V.2

LIBRARY
Michigan State
University

This is to certify that the

dissertation entitled

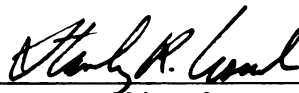
Experimental and Theoretical Studies in Dual
Laser Ionization (DLI) In Flames

presented by

Yen-Yuan James Wu

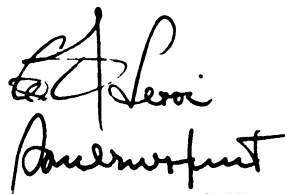
has been accepted towards fulfillment
of the requirements for

Ph.D. degree in Chemistry



Major professor

Date October 17, 1988



MSU is an Affirmative Action/Equal Opportunity Institution

O-12771



RETURNING MATERIALS:

Place in book drop to
remove this checkout from
your record. FINES will
be charged if book is
returned after the date
stamped below.

--	--	--

EXPERIMENTAL AND THEORETICAL STUDIES OF
DUAL LASER IONIZATION (DLI) IN FLAMES

Volume II

by

Yen-Yuan James Wu

A DISSERTATION

Submitted to
Michigan State University
in partial fulfillment of the requirements
for the degree of

DOCTOR OF PHILOSOPHY

Department of Chemistry

1988

CHAPTER V

FLAME TEMPERATURE MEASUREMENT

A. Introduction

One of the important applications of the dual laser ionization (DLI) technique is making flame temperature measurement (1). As mentioned in the previous chapters, signal collection in DLI involves both ion mobility and diffusion. Since the ion transport phenomena of DLI can be modelled well by the one-dimensional Fokker-Planck equations with appropriate drift functions, both mobility and diffusion coefficients can be extracted from the ion peaks of the DLI signals through proper curve fitting methods. The flame temperature thus can be calculated with the Einstein relation (2-3).

The main purpose of this chapter is to demonstrate the capability of the previously-proposed Fokker-Planck formalism in modelling the DLI process. In this chapter, a series of time-resolved DLI signals collected under various bias voltages were modelled by an exponentially modified

Fokker-Planck propagator. Results from curve fitting of the data to the model are presented and interpreted. The outcome of the data treatment revealed a dependence of the ion diffusion coefficients upon the bias voltage. A rough model thus is constructed to explain this phenomenon.

B. Theoretical

In order to simultaneously treat ion mobility, ion diffusion, and especially the interaction between them during DLI signal collection, the Fokker-Planck formalism is adopted. As mentioned in Section D-5, Chapter III, the hydrogen-oxygen-argon flame used in this study can easily reach the so-called "super-saturation" (4) even if only a moderate bias voltage was applied to the electrode pair. In this study, the bias voltages (V_a) used were as high as 870 volts, which were far beyond the requirement of reaching the super-saturation. The electric field thus can be expressed as follows:

$$E_a = \frac{V_a}{q_a + q_c} \quad [1]$$

where E_a (volts·cm⁻¹) is the electric field between the probes, q_a is the distance between the upper probe (anode) and the laser focal point, and q_c is the distance between the lower probe (cathode) and the laser focal point. The

probe configuration with term designations is depicted in Figure 2-6. The Fokker-Planck equation is thus as follows:

$$\frac{\partial P(q,t)}{\partial t} = D \frac{\partial^2 P(q,t)}{\partial q^2} + \frac{\partial}{\partial q} (h(q)P(q,t)) \quad [2]$$

where $P(q,t)$ is the conditional propagator (cm^{-1}), D is the diffusion coefficient ($\text{cm}^2 \cdot \text{sec}^{-1}$) of the analyte ions, and $h(q)$ is the associated drift function ($\text{cm} \cdot \text{sec}^{-1}$). It can be defined as follows:

$$h(q) = -\alpha \quad [3]$$

where

$$\alpha = \mu E + v_f(q) \quad [4]$$

here μ is the mobility coefficient ($\text{cm}^2 \cdot \text{volt}^{-1} \cdot \text{sec}^{-1}$) of the analyte ion and the term $v_f(q)$ is the upward burning velocity ($\text{cm} \cdot \text{sec}^{-1}$) of the flame. Since the magnitude of the burning velocity and its variation versus the q -coordinate, which is defined along the direction of flame propagation (refer to Figure 2-6), are relatively small in comparison to the first term at the right hand side of equation [2], the term $v_f(q)$ is thus assumed to be independent of the q -coordinate throughout this study. Notice that equation [4] thus shows that the drift function $h(q)$ is no longer a function of the q -coordinate.

The exact analytical solution of equation [2] under the

conditions defined by equations [3] and [4] can be obtained by applying the functional path integral techniques with the Onsager-Machlup-Laplace (OML) approximation (5-12). The details of the OML approximation were given in Chapter IV, Section C-2. The solution is given as follows:

$$P(q,t) = \frac{1}{(4\pi Dt)^{1/2}} \exp \left(-\frac{(q-\alpha t)^2}{4Dt} \right) \quad [5]$$

The units of the conditional propagator $P(q,t)$ are cm^{-1} .

As mentioned in Section C-3, Chapter VI, a conditional propagator with units of sec^{-1} is more appropriate for the modelling of the time-resolved DLI signals. According to the mathematical procedures described in that section, equation [5] can be modified to give:

$$P_t(q_f,t) = \frac{(q_f + \alpha t)}{(4\pi D)^{1/2} t^{3/2}} \exp \left\{ -\frac{(q_f - \alpha t)^2}{4Dt} \right\} \quad [6]$$

The conditional propagator of equation [6] can be interpreted as the DLI ion signal at time t when the cathode is located at point q_f . However, equation [6] assumes that at time zero (i.e. the very moment the laser pulses went off) the ion cluster can be treated as a point charge. As mentioned in Section D-1, Chapter IV, the diameter of the laser focal point is about 0.36 mm, which is not small at all in comparison to the distance between the laser focal point and the cathode q_c . In addition, during the

transition stage, which is before a steady-state ambipolar diffusion of electrons has been reached, the ions in the laser focal point can be viewed as being in a mixing chamber. To compensate for the indefinite thickness and the effect of the mixing process, equation [6] must be modified. An exponentially modified conditional propagator is thus adopted. The modified model can be expressed mathematically as follows:

$$P_i(q_f, t) = \int_0^{\infty} \frac{(q_f + \alpha(t-\xi))}{(4\pi D)^{1/2} (t-\xi)^{3/2}} * \exp\left(-\frac{(q_f - \alpha(t-\xi))^2}{4D(t-\xi)}\right) * \exp\left(-\frac{\xi}{\tau_i}\right) d\xi \quad [7]$$

where ξ is a dummy variable for the integration and τ_i is the time constant of the convoluted exponential decay.

The electron peak of the DLI signals, as already discussed in Section D-2, Chapter III, can be described as follows:

$$P_e(q_f, t) = \exp\left(-\frac{t}{\tau_e}\right) \quad [8]$$

where τ_e is the time constant of the electron peak of the DLI signal.

The combination of equations [7] and [8] yields a mathematical model which can describe the DLI signals

reasonably. The equation reads:

$$P_{DLI}(q_f, t) = C_i P_i(q_f, t) + C_e P_e(q_f, t) + C_b \quad [9]$$

where C_i is the amplitude of the ion peak, C_e is the amplitude of the electron signal, and C_b is the baseline of the DLI signal.

C. Experimental

C-1 Apparatus

A complete description of the DLI experimental system used in this study has been given elsewhere (13-15). In all cases, the ions were produced by focusing two lasers at the same point in the flame (approximately 1.2 cm above the burner head) and well away from the combustion region. One laser is a nitrogen laser (Model 0.5-150, NRG, Inc. Madison, WI) with a fixed wavelength (337.1 nm). The other is a Hänsch-type tunable dye laser which was pumped by part of the beam from the nitrogen laser. The dye laser was tuned to a resonance transition to excite the analyte atoms and the nitrogen laser was used to photoionize the excited atoms. For sodium, the dye laser was tuned to the $3S_{1/2} - 3P_{3/2}$ transition (589.0 nm). The nitrogen laser beam is focused by a quartz lens; the focal area was determined to be $(2.0 \pm 0.4) \times 10^{-4} \text{ cm}^2$ (14). The focal area of the dye

laser was $(1.0 \pm 0.3) \times 10^{-3} \text{ cm}^2$. The length of the laser pulse is about 5 nanoseconds. The laser powers were adjusted to ensure the ionization rate of the analyte in the flame was constant.

In this study, a relatively cool hydrogen-oxygen-argon flame was burned from a laminar flow, premixed, circular Meker burner (16). The flame was shielded by a mantle flame of the same composition as the central flame to prevent the entrainment of air. The burning velocity of the flame was approximately $10^3 \text{ cm} \cdot \text{sec}^{-1}$ (17). The hydrogen-oxygen-argon flame was adjusted to be fuel-rich (Argon $3.2 \text{ L} \cdot \text{min}^{-1}$, hydrogen $1.2 \text{ L} \cdot \text{min}^{-1}$, oxygen $0.5 \text{ L} \cdot \text{min}^{-1}$) throughout this study. Atomic sodium was obtained by nebulizing a 20.0 ppm sodium chloride solution into the flame with a pneumatic nebulizer. The ion density of the flame was about $10^8 - 10^{10} \text{ cm}^{-3}$ when the laser pulses were off (17).

The DLI signals were detected by a pair of 0.7 mm diameter nichrome probes. Throughout the studies described in this chapter, the upper probe was connected to the virtual ground of an operational amplifier. It collected electrons and served as the anode. A negative voltage from a high-voltage power supply (Model 3K10B, Power Designs, Inc., Westbury) was supplied to the lower probe. The lower probe collected ion signals and served as the cathode. The probe configuration with term designations is depicted in

Figure 2-6.

All the data were collected by a boxcar integrator (Model 162-164, Princeton Applied Research Corp. Princeton, New Jersey) and stored in a microcomputer. A more complete description of the microcomputer interfaced boxcar integrator system has been presented previously in section F, Chapter II. Briefly, the microcomputer with an associated interface board controlled the scan function of the boxcar integrator through its back panel and read the output from the boxcar integrator. Multiple readings at each aperture delay in a scan were taken and stored in the microcomputer in order to average the noise due to the variation of laser pulse powers. Since all the DLI current signals were converted into voltage by an operational amplifier current follower circuit, all the signals shown in this chapter are inverted, i.e. the DLI signals are drawn downward and all baselines are placed at the top of the plots.

C-2 Reagents

All solutions are prepared from reagent grade sodium chloride dissolved in distilled, deionized water. The laser dye chosen for this study was rhodamine 6G (Eastman Kodak Co.) with a concentration of 7.5×10^{-3} M in absolute

ethanol. It was used without further purification. In order to maintain the stability of the dye laser output, the dye solutions were replaced approximately every ten hours of the working time.

C-3 Experimental Conditions

In order to demonstrate the capability of the Fokker-Planck formalism in extracting the mobility and diffusion coefficients of various ions in a fuel-rich hydrogen-oxygen-argon flame, a set of DLI signals was taken at various bias voltages. The atomic ion was chosen to be sodium since there are sufficient literature values available for comparison. The applied bias voltages ranged from 10 to 870 volts. The distance, q_c , between the laser focal point and the lower probe (cathode) was 3.00 mm. The distance between the upper probe (anode) and lower probe was 4.50 mm. The boxcar aperture duration was chosen to be 5 microseconds with an aperture delay range of 50 microseconds. The % Ini knob was set at 2.0 % (i.e. 1.0 microsecond initial delay). The scan increment between each data points was 0.9766 microseconds; and the microcomputer recorded 30 points per data point.

D. Data Treatment

The data fitting program was constructed by calling appropriate subroutines from the well-known MINPACK package released by the Argonne National Laboratory, Argonne, Illinois (4). For the calculation of the integral contained in equation [7], subroutines from the IMSL package were called.

Briefly, MINPACK is a package of FORTRAN subroutines for the numerical solution of systems of nonlinear equations and nonlinear least squares problems. In this study, the double precision version of the LMDIF subroutine was chosen to fit the experimental results from DLI measurements. Subroutine LMDIF is designed to minimize the sum of the squares of residuals of M nonlinear functions in N variables. Its main algorithm is a modification of the Lavenberg-Marquardt algorithm (18). This subroutine can determine the minimum of the surface of the sum of the squares of residuals effectively. LMDIF does not require the user to supply the set of equations that calculate the Jacobian of the functions versus each parameter, hence it may not be able to reach the minimum as quickly as other subroutines in the same pack, such as LMDER. Due to this deficiency, a curve fitting of about 100 data points may

take hours of CPU time when the program is implemented on a DEC VAX 11/750 minicomputer.

The algorithm of the main driver of the curve fitting program can be summarized as follows:

- (i) Input experimental results.
- (ii) Input initial estimates of all parameters.
- (iii) Input experimental conditions.
- (iv) Call LMDIF subroutine from MINPACK-1 to search for the minimum of the sum of the squares of residuals.
- (v) LMDIF calls an external function to evaluate the residual for each data point.
- (vi) To evaluate the exponentially modified Fokker-Planck propagator, the external function called by LMDIF calls the DVERK subroutine from the IMSL package.
- (vii) Output results.

A complete list of FORTRAN source code of the main driver ZMIDF3 and related input and output file formats are given in Appendix B.

The greatest drawback of all curve fitting algorithms currently available , especially the Lavenberg-Marquardt algorithm (18) adopted by MINPACK-1, is the low tolerance of improper initial estimates of parameters. Unfortunately,

they have to be supplied by the user. Improper initial estimates may cause a divergence of one or more of the parameter values. Since LMDIF possesses so low a tolerance to the improper initial estimates, a version of the curve fitting program which is based on equation [9], but with a Fokker-Planck propagator which is not modified by the exponential decay function, was constructed to supply the initial estimates. A series of external functions based on equation [9], written with different constraints, are also included in Appendix B.

To evaluate the parameters properly, occasionally the data points must be weighted by their standard deviations in order to obtain more information about the data sets for future treatments. The standard deviation of each data point, which is due to the variation of laser pulse powers, was calculated from the multiple points taken by the boxcar integrator at the same aperture delay during the DLI measurement. A different version of curve fitting program which can weight each data point according to its standard deviation was also constructed. Related subroutines are included in Appendix B.

In this study, the experimental data were fit according to equation [9]. There are seven parameters to be specified by the data fitting procedure. The following is a summary of these seven parameters:

- (i) C_b - the baseline of the DLI signals which can be adjusted from the front panel.
- (ii) C_i - the amplitude of the ion peak.
- (iii) C_e - the amplitude of the electron peak.
- (iv) D - the diffusion coefficient of the analyte ions.
- (v) α - the velocity of the analyte ions during the signal collection period.
- (vi) τ_i - the time constant of the exponential decay function which is convolved with the DLI ion peaks.
- (vii) τ_e - the time constant of the electron peak.

E. Results

Figure 5-1 shows the relationship between the moving velocity α ($\text{cm} \cdot \text{sec}^{-1}$) of sodium ions due to the influence of the electric field and the applied bias voltage (V_a). To calculate the mobility coefficient of the sodium ion, equation [1] may be substituted into equation [4] to yield the following relation:

$$\alpha = \left(\frac{\mu}{q_c + q_a} \right) V_a + v_f \quad [10]$$

Thus the slope is:

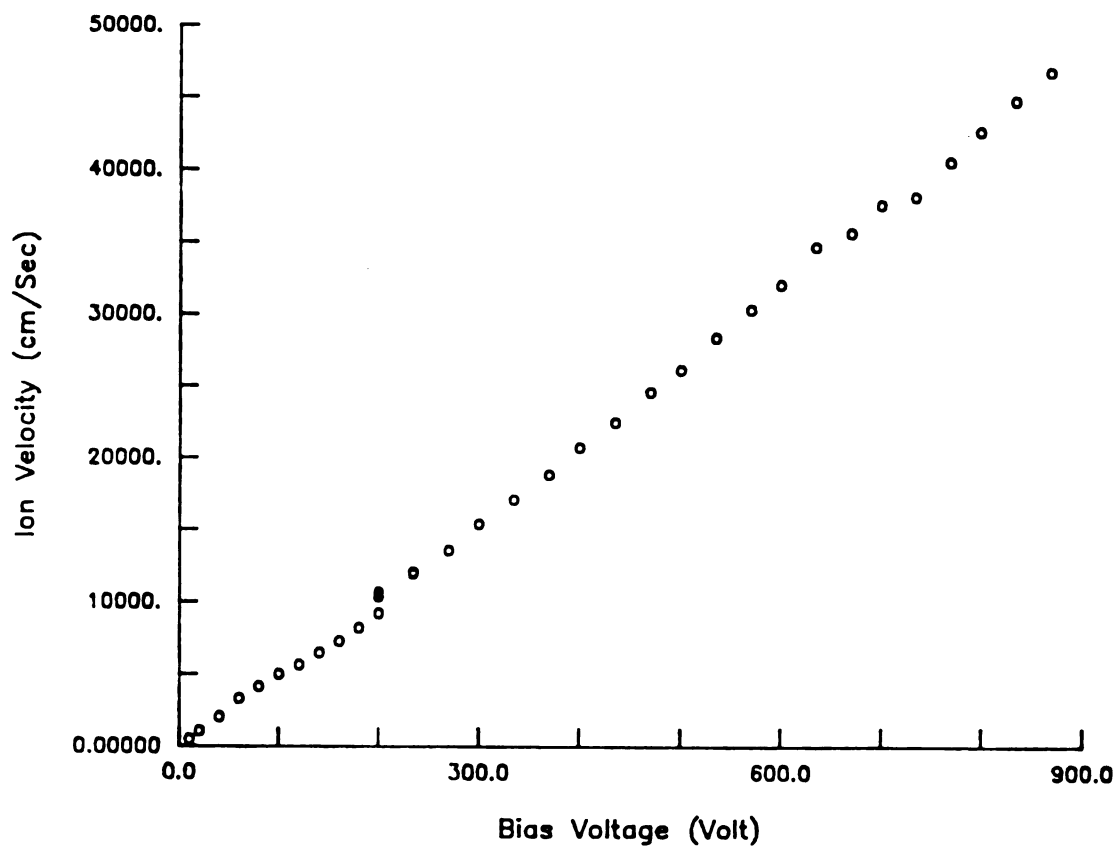


Figure 5-1. Ion velocity versus bias voltage diagram for sodium cations. The slope of the straight line is $54.06 \text{ cm} \cdot \text{sec}^{-1} \cdot \text{volt}^{-1}$, which gives a mobility coefficient of $24.33 \text{ cm}^2 \cdot \text{sec}^{-1} \cdot \text{volt}^{-1}$. The intercept is about $-680 \text{ cm} \cdot \text{sec}^{-1}$, which gives a burning velocity of $680 \text{ cm} \cdot \text{sec}^{-1}$.

$$\text{slope} = \frac{\mu}{q_c + q_a} \quad [11]$$

and the intercept is:

$$\text{intercept} = v_f \quad [12]$$

Linear regression yields a slope of (54.06 ± 0.66) $\text{cm} \cdot \text{sec}^{-1} \cdot \text{volt}^{-1}$ and an intercept of $-680 \text{ cm} \cdot \text{sec}^{-1}$. This gives a mobility coefficient $(24.33 \pm 0.30) \text{ cm}^2 \cdot \text{sec}^{-1} \cdot \text{volt}^{-1}$ and a flame burning velocity of $680 \text{ cm} \cdot \text{sec}^{-1}$. A comparison of this results with the literature values reported by other workers is given in Table 5-1 (1,19,20).

Figure 5-2 shows the relationship between diffusion coefficient (D) of sodium ion and the applied bias voltages (V_a). A dependence of the diffusion coefficient on the applied bias voltage is cleared revealed. This indicates that the mutual repulsion among ions must not be ignored. However, fitting the diffusion coefficients into a power series and taking the extrapolation to the zero voltage gives the ambipolar diffusion coefficient (1). An ambipolar diffusion coefficient of $(8.23 \pm 0.05) \text{ cm}^2 \cdot \text{sec}^{-1}$ thus is yielded. Therefore, the diffusion coefficient can be determined to be $4.10 \text{ cm}^2 \cdot \text{sec}^{-1}$. A comparison of the diffusion coefficient from this work with the reported literature values is given in Table 5-2 (21-23).

TABLE 5-1. A Comparison of Mobility Coefficients for
Sodium Cations in $\text{H}_2/\text{O}_2/\text{Ar}$ Flames

Author	Mobility Coefficient	Reference
Wu	$24.3 \text{ cm}^2 \cdot \text{V}^{-1} \cdot \text{sec}^{-1}$	this work
Tyndall	$25.4 \text{ cm}^2 \cdot \text{V}^{-1} \cdot \text{sec}^{-1}$	(19)
Mallard (2350K)	$25.8 \text{ cm}^2 \cdot \text{V}^{-1} \cdot \text{sec}^{-1}$	(20)
Langevin Theory	$25.8 \text{ cm}^2 \cdot \text{V}^{-1} \cdot \text{sec}^{-1}$	(20)
Lin	$30.2 \text{ cm}^2 \cdot \text{V}^{-1} \cdot \text{sec}^{-1}$	(1)

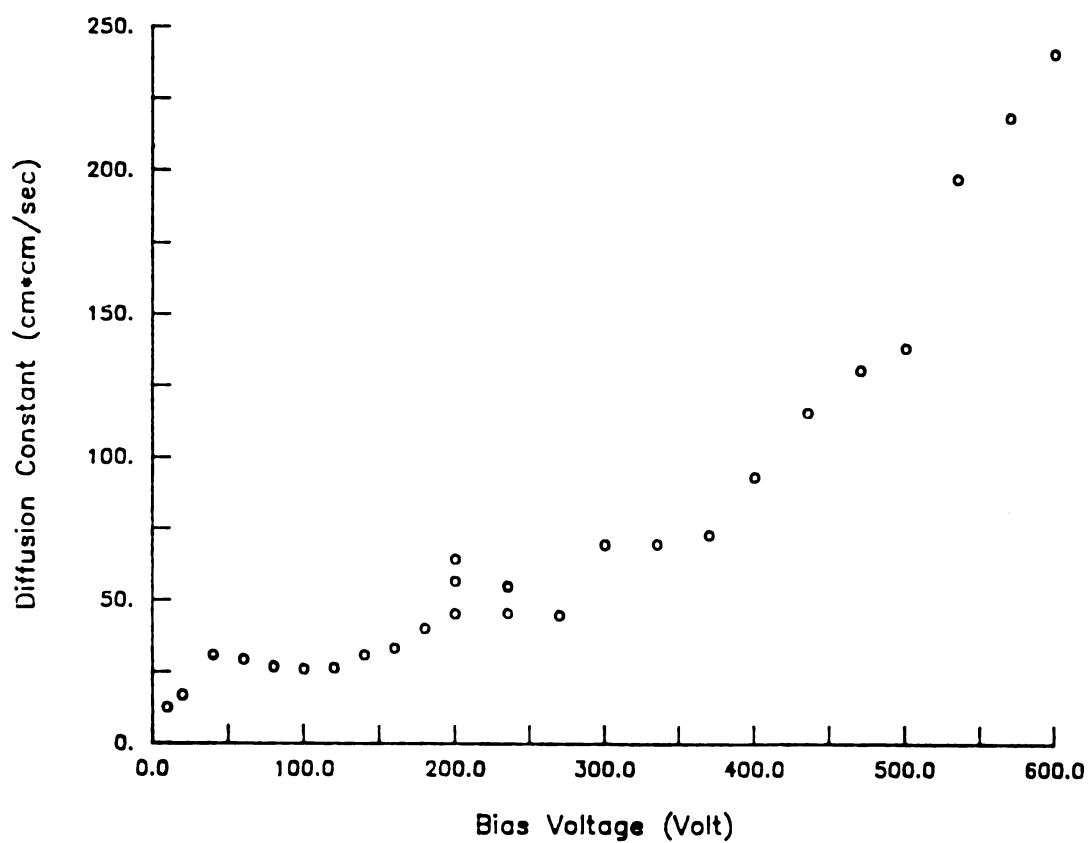


Figure 5-2. Diffusion coefficient versus bias voltage for sodium cations. Extrapolation back to zero voltage gives an ambipolar diffusion coefficient of $8.24 \text{ cm}^2 \cdot \text{sec}^{-1}$.

TABLE 5-2. A Comparison of Diffusion Coefficients for
Sodium Cations in $\text{H}_2/\text{O}_2/\text{Ar}$ Flames

Author	Diffusion Coefficient	Reference
Ginsel	$3.2 \text{ cm}^2 \cdot \text{sec}^{-1}$	(21)
Wu	$4.1 \text{ cm}^2 \cdot \text{sec}^{-1}$	this work
Lin	$5.7 \text{ cm}^2 \cdot \text{sec}^{-1}$	(1)
Ashton	$5.5 - 13 \text{ cm}^2 \cdot \text{sec}^{-1}$	(22)
Snelleman	$9.9 \text{ cm}^2 \cdot \text{sec}^{-1}$	(23)

The flame temperature can be obtained by applying the Einstein relation (2):

$$T = \frac{eD}{k\mu} \quad [13]$$

where T is the temperature (degree K) of the flame, e is the electron charge (coulomb), and k is the Boltzmann constant ($\text{Joule} \cdot \text{K}^{-1}$). Equation [13] yields a flame temperature of (1967 ± 27) K at a 95% confidence level. A comparison of the flame temperatures for similar hydrogen-oxygen-argon flames obtained by line-reversal and dual laser ionization methods with the data from this work is given in Table 5-3 (24,25).

F. Discussion

To explain the relationship between the diffusion coefficient D obtained from curve fittings and the bias voltages V_a applied to the electrodes, mutual repulsion among the positive ions in the flame environment has to be considered. The following is a rough model which can be used to justify the observations shown in Figure 5-2.

According to the data shown in Figure 5-2, we may assume that in the beginning stage of the ion transport process the displacements of the analyte ions due to

TABLE 5-3. A Comparison of $H_2/O_2/Ar$ Flame Temperatures

Author	Temperature	Method	Reference
Wu	1967 K	DLI Na^+	this work
Hooymayers	1990 K	Line Reversal	(24)
Lijnse	2000 K	Line Reversal	(25)
Lin	2014 K	DLI Li^+	(1)
Hooymayers	2070 K	Line Reversal	(24)
Lijnse	2136 K	Line Reversal	(25)
Lin	2171 K	DLI Na^+	(1)
Hooymayers	2210 K	Line Reversal	(24)

diffusion are very small, in comparison to those due to the mutual repulsion among ions, and thus can be ignored for a primary treatment. The initial ion density (c_0 , esu·cm⁻³) is assumed to be in thermal equilibrium with the flame and is uniform throughout the laser focal point at the very moment when the laser pulse shut off. Equation [2] can be reduced as follows:

$$\frac{\partial c}{\partial t} = \frac{\partial}{\partial q} (v_i c) \quad [14]$$

where v_i is the drift velocity (cm·sec⁻¹) due to mutual repulsion among ions. Partial differentiation gives the following form:

$$\frac{\partial c}{\partial t} = c \frac{\partial v_i}{\partial q} + v_i \frac{\partial c}{\partial q} \quad [15]$$

The second term in equation [15] can be dropped immediately since the mutual repulsion of ions in which we are interested will prevent the ion density c from varying rapidly with q in a short time period (26). This gives:

$$\frac{\partial c}{\partial t} = c \frac{\partial v_i}{\partial q} \quad [16]$$

The relation between v_i and the mobility coefficient is as follows:

$$v_i = \mu E_r \quad [17]$$

where E_r is the electric field due to mutual repulsion of ions. Poisson's law gives:

$$\frac{\partial^2 V_r}{\partial q^2} = - 4 \pi c \quad [18]$$

where V_r is the electrical potential (volts) due to mutual repulsion of ions. Also we have:

$$E_r = - \frac{dV_r}{dq} \quad [19]$$

Combining equations [18] and [19] gives the following:

$$\frac{dE_r}{dq} = 4 \pi c \quad [20]$$

Substitution of equations [17] and [20] into equation [16] yields:

$$- \frac{dc}{dt} = 4 \pi \mu c^2 \quad [21]$$

Rearrangement of equation [21] gives the relation between the ion density c and time t .

$$- \frac{dc}{c^2} = 4 \pi \mu dt \quad [22]$$

Integration of equation [22] gives the following equation:

$$\frac{1}{c} - \frac{1}{c_0} = 4 \pi \mu t \quad [23]$$

Rearrangement of equation [23] yields:

$$c = \frac{c_0}{4 \pi \mu c_0 t + 1} \quad [24]$$

A numerical estimate shows that if the initial ion density is about $10^8 \text{ esu} \cdot \text{cm}^{-3}$ in a collision-free environment, it will take 32 microseconds for the ion density to decrease by a factor of 100 provided that the mobility coefficient of the ion is chosen to be $25 \text{ cm}^2 \cdot \text{volt}^{-1} \cdot \text{sec}^{-1}$. Notice that this value falls right into the time scale of the DLI signals.

The mutual repulsion, which is the main factor causing the ion cluster to spread, is directly proportional to the ion density c . Equation [24] clearly indicates that the ion density decreases versus time.

We may assume that the ion cluster has a width of d_i (cm). Viewed from along the q -coordinate, the sheath is seen to contain a charge e_i , and can be expressed as follows:

$$e_i = d_i c \quad [25]$$

According to Gauss's theorem, the electric field outside the laser focal point can be written as:

$$E = 2 \pi e_i \quad [26]$$

The analyte ions at the edge of the ion cluster thus will be moving under the influence of the electric field defined by equation [26], and the drift velocity can be written as follows:

$$v_i = 2 \pi \mu e_i \quad [27]$$

The distance that the ions at the edge of the ion cluster may move along the q-coordinate can thus be expressed as:

$$q = 2 \pi \mu e_i t \quad [28]$$

However, it is well known that the displacement of ions through diffusion can also be written as follows:

$$q = (2D_i t)^{1/2} \quad [29]$$

where D_i is the corresponding diffusion coefficient due to mutual repulsion of ions. Combination of equations [28] and [29] gives the following relation:

$$D_i = 2 \pi^2 \mu^2 e_i^2 t \quad [30]$$

Substitution of equations [24] and [25] into equation [30] gives the following equation:

$$D_i = \frac{2 \pi^2 \mu^2 d_i^2 c_0^2 t}{(4 \pi \mu c_0 t + 1)^2} \quad [31]$$

Equation [31] indicates that D_i decreases when t increases. Since D_i is a function of time, we may interpret the contribution of mutual repulsion of ions to the observed

diffusion coefficient D , which is designates as $(D_i)_t$, as an average of D_i over a time period t_f . The term $(D_i)_t$ thus can be calculated as follows:

$$(D_i)_t = \frac{1}{t_f} \int_0^{t_f} \frac{2 \pi^2 \mu^2 d_i^2 c_0^2 t}{(4 \pi \mu c_0 t + 1)^2} dt \quad [32]$$

Integration of equation [32] yields:

$$(D_i)_t = \frac{d_i^2}{8t_f} (\ln(4\pi\mu c_0 t_f + 1) + \frac{1}{4\pi\mu c_0 t_f + 1} - 1) \quad [33]$$

Since c_0 is at is sufficiently large (26) after the laser pulse goes off, it takes only nanoseconds to make the following condition be valid:

$$4 \pi \mu c_0 t \gg 1 \quad [34]$$

The second and third terms of the right hand side of equation [33] can be dropped. Thus equation [33] can be rewritten as follows:

$$(D_i)_t \approx \frac{d_i^2}{8t_f} \ln(4\pi\mu c_0 t_f) \quad [35]$$

Equation [35] indicates that when t_f is increased, the time-averaged diffusion coefficient $(D_i)_t$ due to mutual repulsion will decrease since the first derivative of $(D_i)_t$ versus time is negative. Also,

$$q_c = \mu E_a t_f \quad [36]$$

where q_c (cm) is the distance between the laser focal point the the cathode (lower probe) and E_a is the electric field between the probes. Also, E_a can be expressed as follows:

$$E_a = \frac{V_a}{q_c + q_a} \quad [37]$$

Substitution of equation [37] into equation [36] yields the following equation:

$$t_f = \frac{q_c (q_c + q_a)}{\mu V_a} \quad [38]$$

Substitution of equation [38] into [35] thus yields an equation which shows the relation between the time-averaged diffusion coefficient $(D_i)_t$ and the applied voltages V_a . The equation reads:

$$(D_i)_t = A \mu V_a \ln \left(\frac{B}{V_a} \right) \quad [39]$$

where

$$A = \frac{d_i^2}{8q_c (q_c + q_a)} \quad [40]$$

and

$$B = 4\pi\epsilon_0 q_c (q_c + q_a) \quad [41]$$

Equation [39] shows that when the bias voltage V_a is increased, the time-averaged diffusion coefficient $(D_i)_t$

also increases. This is because when V_a is increased, the ion transport time t_f will decrease according to equation [38], hence the bigger D_i from the early stages of mutual ion repulsion takes more weight in the time averaging of D_i and in turn makes $(D_i)_t$ bigger. Figure 5-3 shows a set of mutual-repulsion versus q -coordinate curves made by the simulation program described in the next chapter. Curves at various times after the laser pulses shut off are plotted to illustrate how the mutual repulsion decays versus time. Figure 5-4 shows the values of $(D_i)_t$ versus applied voltage V_a with various mobility coefficients μ . It clearly shows that the time-averaged diffusion coefficient $(D_i)_t$ increases dramatically versus V_a . Additional mathematical investigations of this phenomenon should be pursued in the future. In the next chapter a simulation program, which also confirms the importance of the effect of mutual repulsion, will be presented.

G. Conclusion

This chapter has demonstrated the capability of the Fokker-Planck formalism to model the DLI process. Through curve fitting methods, the mobility coefficient and diffusion constant of sodium ion in the hydrogen-oxygen-argon flame were calculated. Also the temperature of the flame was calculated by the Einstein relation. The

Figure 5-3. Ion repulsion versus space coordinate at various times. The laser focal point is located at the position $x=0$, the cathode is placed at the positive x -coordinate and the anode is placed at negative. The ion repulsion is a measure of the electric field due to neighbor ions and each grid scale on the y -axis stands for 1.0×10^6 volts cm^{-1} . Positive ion repulsion values means that the electric field due to mutual ion repulsion will push ions toward the cathode. Notice that the ion clusters moves toward cathode and disperses when time elapses.

A, 0.167 μs ; B, 1.00 μs ; C, 10.0 μs ; D, 30.0 μs after laser pulses went off.

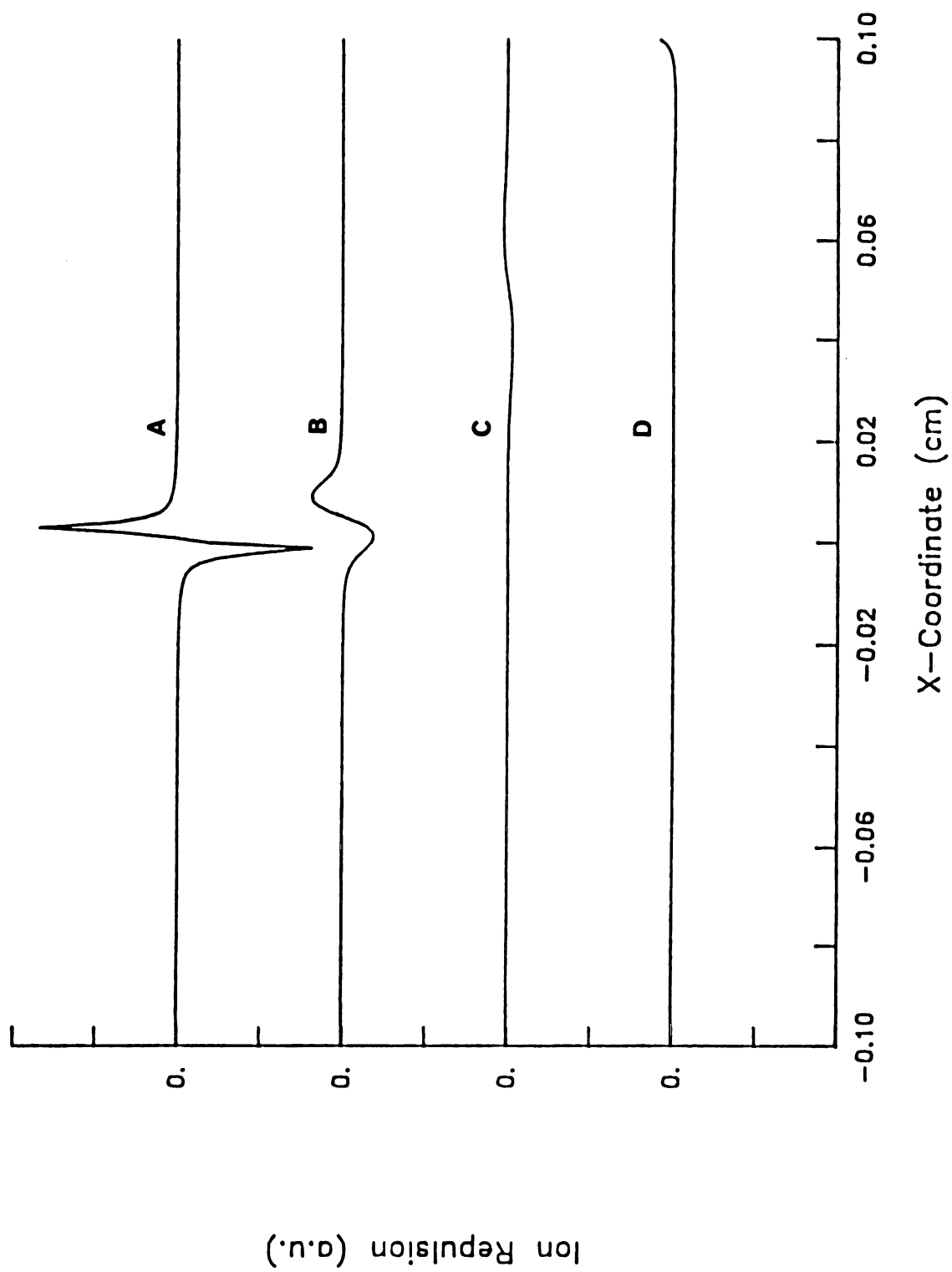


Figure 5-3.

Figure 5-4. Time-averaged diffusion coefficient $(D_i)_t$ versus applied voltages V_a for various ion mobilities. This plot is drawn from equation [39]. Notice that even if the ion mobility is small, the time-averaged diffusion coefficient $(D_i)_t$ still changes dramatically with V_a and gives values over $100 \text{ cm}^2 \cdot \text{sec}^{-1}$, in contrast with the $4.1 \text{ cm}^2 \cdot \text{sec}^{-1}$ for sodium cation. ($c_0 \approx 1.0 \times 10^{11} \text{ esu} \cdot \text{cm}^{-3}$, $q_c = 0.2 \text{ cm}$, $q_a = 0.3 \text{ cm}$, $d_i \approx 0.1 \text{ cm}$)

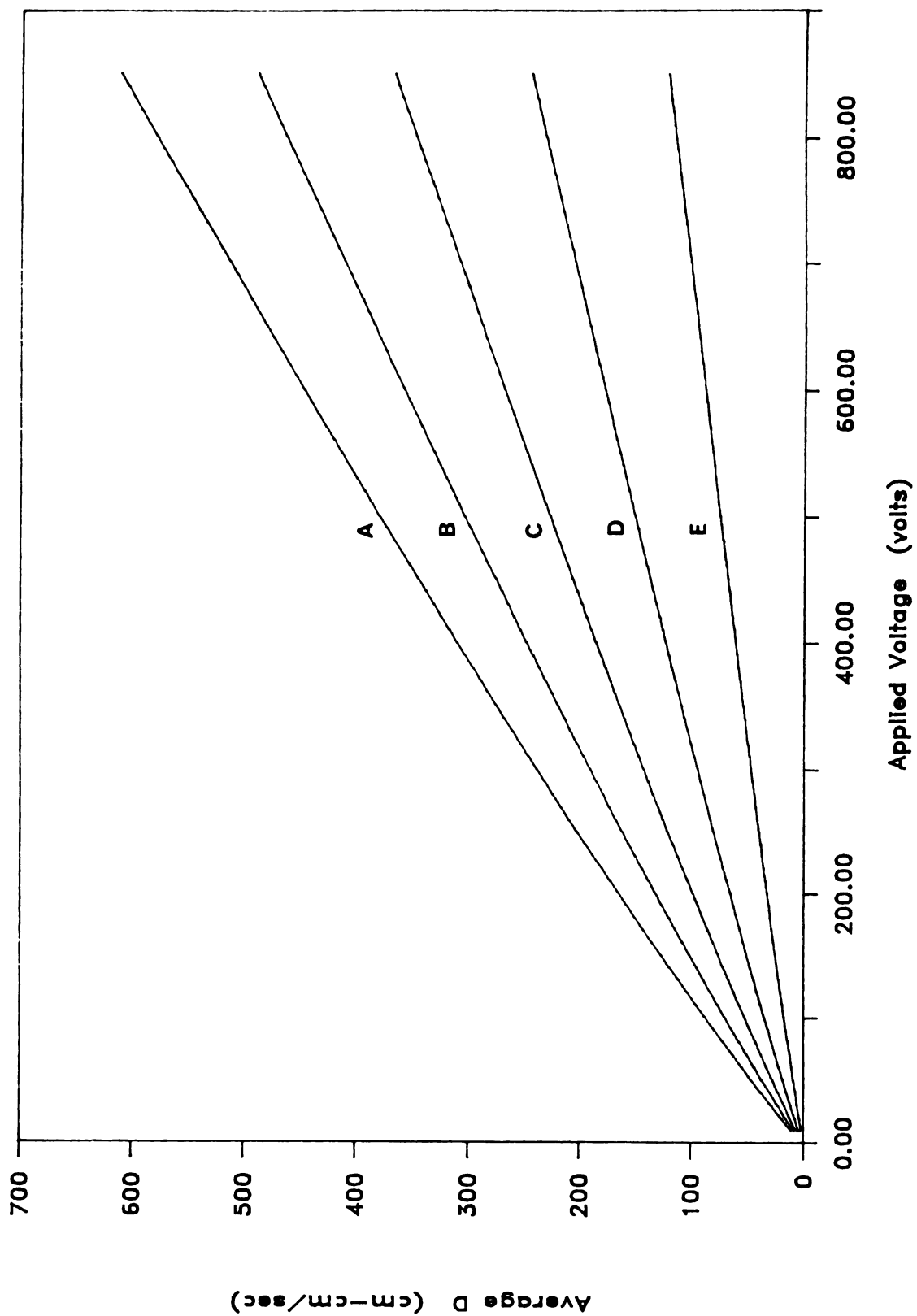


Figure 5-4.

dependence between the diffusion coefficient and bias voltage was also discussed.

CHAPTER V

REFERENCES

1. K.C. Lin, P.M. Hunt, and S.R. Crouch, Chem. Phys. Lett. 90, 111 (1982).
2. E.W. McDaniel and E.A. Mason, "The Mobility and Diffusion of Ions in Gases" (Wiley, New York, 1973).
3. E. Nasser, "Fundamentals of Gaseous Ionization and Plasma Electronics" (Wiley, New York, 1971).
4. J.J. More, B.S. Garbow, and K.E. Hillstrom, "User Guide for MINPACK-1", ANL-80-74 (Argonne National Laboratory, Argonne, Illinois, 1980).
5. K.L.C. Hunt and J. Ross, J. Chem. Phys. 75, 976 (1981).
6. P.M. Hunt, K.L.C. Hunt, and J. Ross, J. Chem. Phys. 79, 3765 (1983).
7. L. Onsager and S. Machlup, Phys. Rev. 91, 1505 (1953).
8. S. Machlup and L. Onsager, Phys. Rev. 91, 1512 (1953).
9. F.W. Wiegel, Physica 33, 734 (1967); *ibid.* 37, 105 (1967).
10. F. Langouche, D. Reokaerts, and E. Tirapegui, Physica A97, 195 (1979).
11. M. Moreau, Physica A90, 410 (1978).
12. B.H. Lavenda, Phys. Lett. A71, 304 (1979).
13. C.A. van Dijk, F.M. Curran, K.C. Lin and S.R. Crouch, Anal. Chem. 53, 1275 (1981).
14. K.C. Lin, Ph.D. Thesis (Michigan State University, 1982).

15. F.M. Curran, Ph.D. Thesis (Michigan State University, 1983).
16. C. van Tricht, Tj. Hollander, and C.Th.J. Alkemade, J. Quant. Spectry. Radiative Transfer 5 813 (1965).
17. C.Th.J. Alkemade, Tj. Hollander, W. Snellsman, and P.J.Th. Zeegers, "Metal Vapors in Flames" (Pergamon Press, Oxford, 1982).
18. J.J. More, "Numerical Analysis", Lecture Notes in Mathematics 630, pp. 105 (Spring-Verlag, Berlin, 1982).
19. A.M. Tyndall, "The Mobility of Positive Ions in Gases" (Cambridge Univ. Priss, London, 1938).
20. W.G. Mallard and K.C. Smyth, Combust. Flame 44, 61 (1982).
21. L.A. Ginsel, Thesis, Utrecht (1933).
22. A.F. Ashton and A.N. Hayhurst, J. Chem. Soc. Faraday Trans. I 69, 652 (1973)
23. W. Snelleman, Thesis, Utrecht (1965).
24. P.L. Lijnse and R.J. Elsenarr, J. Quantum Spectry. Radiat. Transfer 12, 1115 (1972).
25. H.P. Hooymayers and C.Th.J. Alkemade, J. Quantum Spectry. Radiat. Transfer 6, 847 (1966).
26. E.W. McDaniel, "Collison Phenomena in Ionized Gases" (John Wiley & Sons, New York, 1964).

CHAPTER VI

SIMULATION STUDIES OF MUTUAL REPULSION OF IONS

A. INTRODUCTION

The technique of dual laser ionization (DLI) spectrometry has been developed in our laboratory, and is now well established as a very sensitive analytical tool and a most versatile flame diagnostic method (1-6). In DLI measurements, analyte atoms are nebulized into a flame and photoionized by two simultaneous laser pulses. Electrons and ions generated by the laser pulses are then collected by a pair of nichrome probes on which a bias voltage is applied. However, as mentioned in the previous chapter, the DLI signal collection process not only involves ion mobility and diffusion, as commonly suggested, but also involves the mutual interactions among ions and electrons in a flame environment. These interactions are not yet clearly understood. Experimental results show that under high bias voltages, ions tend to diffuse more quickly than expected. Mutual repulsion among ions was proposed as a major reason for this phenomenon. Hence one of the main purposes of this

chapter is using computer simulation to show the effect of the mutual repulsion of ions on DLI signal detection.

We may consider the hydrogen-oxygen-argon flame used in our experiments as a gas-filled cavity to which an electric field is applied. The electrons move to the anode (upper electrode) while the positive ions move to the lower probe (cathode). In studies of such cavities the interaction between the negative and positive charges can be neglected provided that the ion density is lower than 10^7 to 10^8 ions·cm⁻³; otherwise the space charge effects produced by the Coulomb forces become important and must be taken into account.

In order to investigate the space charge effects, the Fokker-Planck equations were adopted. However, many of the partial differential equations which result from non-equilibrium thermodynamic systems cannot be readily solved by analytical methods. The one-dimensional Fokker-Planck equation (FPE) with a nonlinear drift function is one of the well-known examples. Consequently, a knowledge of the methods for obtaining numerical solutions to these partial differential equations is very important to the chemistry community.

To solve the Fokker-Planck equations with different drift functions, two approaches have been used. The first

approach was to solve the FPE by the functional path integral techniques (7-8) coupled with the Onsager-Machlup-Laplace (OML) approximation (9-14). The conditional propagators associated with the process of interest thus can be obtained. The second approach was to simulate the initially defined stochastic variables in a time frame. The latter approach is perhaps more direct and intuitive. In addition, it is always possible to expand the simulation algorithms from one-dimensional to three-dimensional systems for more sophisticated conditions.

B. THE FOKKER-PLANCK EQUATION

A one dimensional Fokker-Planck equation can be written as follows:

$$\frac{\partial P(q,t)}{\partial t} = D \frac{\partial^2}{\partial q^2} P(q,t) + \frac{\partial}{\partial q} h(q) P(q,t) \quad [1]$$

where $P(q,t)$ is the conditional propagator or, in this chapter, the ion density matrix (cm^{-3}) at coordinate q and time t , D is the diffusion coefficient ($\text{cm}^2 \cdot \text{sec}^{-1}$), and $h(q)$ is the drift function ($\text{cm} \cdot \text{sec}^{-1}$).

Throughout this chapter, a constant diffusion coefficient is assumed in order to distinguish its contribution to the spreading of ion peaks from those due to

the mutual repulsion of ions. Also, the ion-ion mutual repulsion was viewed as part of the drift function and the algorithms for simulating the diffusion and drift processes were employed separately.

C. ALGORITHM FOR DIFFUSION

C-1 Introduction

The purpose of this section is to find a generalized finite difference equation that can simulate the diffusion term of a Fokker-Planck equation with higher accuracy. The conventional algorithm are reviewed and examined; a new and effective algorithm derived from Lagrange polynomials is examined and implemented.

C-2 Basic Definitions

Any discussion of the digital simulation of problems involving diffusion begins with a consideration of the combined form of Fick's second law (15).

$$\frac{\partial}{\partial t} P(q,t) = D \frac{\partial^2}{\partial q^2} P(q,t) \quad [2]$$

Equation [2] is also commonly called the equation of

continuity; and indeed it is the Fokker-Planck equation with a vanishing drift function. Its analytical solution can be expressed as follows:

$$P(q, t) = \frac{1}{(4\pi D(t-t_0))^{1/2}} \exp\left(-\frac{(q-q_0)^2}{4D(t-t_0)}\right) \quad [3]$$

where

$$q_0 = q(t_0) \quad [4]$$

Equation [3] can be derived from numerous ways. It was given first by Albert Einstein (16) and is now commonly called the particular solution of the equation of continuity. This particular solution requires that the ion density matrix starts as a Dirac delta function at time zero and turns into a Gaussian distribution at time greater than zero.

It will be shown later that the simulation of a Gaussian process is a rather difficult subject, even today. In fact, when the mutual repulsion among ions must be considered, none of the commonly-used algorithms reported in the literature (17-19) gives satisfactory results. In order to make the discussion in this chapter clear, we begin with the basic or commonly-used algorithms.

A generalized finite difference equation, which is a combination of both forward difference and backward

difference approximations (17), can be written as follows to represent equation [2]:

$$\begin{aligned} \frac{1}{\tau} [u(q, t+\tau) - u(q, t)] \\ = -\frac{D}{\delta^2} [\Omega U(t) + (1-\Omega)U(t+\tau)] \end{aligned} \quad [5]$$

where τ indicates the time propagation interval, δ indicates the space interval between each cell element of the ion density matrix being considered, and Ω is the degree of implicitness of equation [5]. Also, $u(q, t)$ indicates the cell element of the ion density matrix, $P(q, t)$, at any given space coordinate q and time t , of which the value is already normalized. The term $U(t)$ represents the finite difference format of the second derivative of $P(q, t)$ at time t , which will be discussed in more detail later. Equation [5] may be readily rearranged to yield:

$$u(q, t+\tau) - (1-\Omega)D_m U(t+\tau) = U(q, t) + \Omega D_m U(t) \quad [6]$$

where

$$D_m = -\frac{D\tau}{\delta^2} \quad [7]$$

The critical dimensionless parameter D_m is conventionally called the "model diffusion coefficient" (20) which, along with the degree of implicitness r , will determine the stability of equation [6]. Although the assignment of a

value to D_m is arbitrary, it is by no means unrestricted. An optimum value of D_m has to be chosen to prevent the the divergence of the ion density matrix (19).

C-3 Conventional methods

To make the computer algorithm work efficiently, a few parameters should be chosen very carefully. The first parameter, which determines the effectiveness of the entire algorithm, is the finite difference format of the second derivative $U(t)$. The second parameter, which determines the stability of the performance of the algorithm, is the degree of implicitness Ω . The third parameter, which determines the speed of the algorithm, is the model diffusion coefficient D_m . We shall examine these parameters individually in order to obtain a method for optimizing them.

Conventionally, the term $U(t)$ can be defined as follows:

$$U(t) = u(q-\delta, t) - 2u(q, t) + u(q+\delta, t) \quad [8]$$

If Ω is chosen to be zero, we have the so-called "pure forward difference algorithm" (19). Equation [6] thus can be rearranged as follows:

$$u(q, t+\tau) = u(q, t) + D_m [u(q-\delta, t) - 2u(q, t) + u(q+\delta, t)] \quad [9]$$

Equation [9] contains only one unknown value, $u(q, t+\tau)$, and is written explicitly for this unknown. For an array $u(q)$ with a dimension n , it is reasonable to impose zeros on both $u(q_1, t)$ and $u(q_n, t)$ as boundary conditions at any time t . The numerical computation of the values of the dependent variable can thus be made one point a time.

Equation [9] is certainly a simple one to formulate, and it is especially easy to use for computing the values of $u(q, t)$ at each point in time. In addition, since the finite difference analog is correct to the second-order in the variable q , reasonable results can be expected. However, for a numerical analog to be of any merit, it must converge to the solution of the corresponding differential equation when the finite increments, δ and τ , are decreased in size. Analysis has shown (17) that a very restrictive relationship between the sizes of δ and τ must be satisfied in order to make the outcomes of equation [9] approach the real solution of equation [2]. This restrictive relationship can be formulated as follows (17):

$$\frac{1}{2} \geq D_m > 0 \quad [10]$$

Equation [10] is rather critical. In order to minimize the truncation errors in the q analogs, the size of δ must be small. If the value of D_m is chosen to be larger than 0.5, divergence is almost always guaranteed. However, due to the truncation errors, even if equation [10] is strictly followed, oscillation may still occur (17). Reported values of D_m usually are about 0.2 (20). It is obvious that this restriction will limit the speed of the time propagation seriously if high accuracy is demanded.

To relieve the algorithm from the restriction of equation [10], one of the natural choices is to assign Ω a value other than 0. Usually, the value of Ω can be chosen as 0.5. This choice is the so-called Crank-Nicholson formulation (18). Equation [6] can thus be rearranged as follows:

$$\begin{aligned} D_m u(q-\delta, t+\tau) + (-2-2D_m)u(q, t+\tau) + D_m u(q+\delta, t+\tau) \\ = -D_m u(q-\delta, t) + (-2+2D_m)u(q, t) - D_m u(q+\delta, t) \end{aligned} \quad [11]$$

The same boundary conditions imposed on equation [9] can also be applied to equation [11]. The resulting set of equations thus can be generalized as follows:

$$A \times P(q, t+\tau) = A' \times P(q, t) \quad [12]$$

where A and A' are tridiagonal coefficient matrices. The matrices $P(q, t)$ and $P(q, t+\tau)$ are column matrices of which

the elements are the cell elements $u(q,t)$ and $u(q,t+\tau)$, respectively. Since all the values on the right hand side of equation [11] are known, this equation can be readily solved by the Thomas method (18). This method requires more computation per time step than the forward difference method. However, a larger time increment can be used for this algorithm (20). Since equation [12] is the result of successive applications of the forward and backward equations and thus will be stable for any value of D_m . As a consequence, fewer time steps are required to compute values of the dependent variable for a given elapsed time. In general, equation [12] is always preferred for obtaining numerical solutions to parabolic differential equations.

To evaluate the effectiveness of equation [11], a FORTRAN program was written based on the Thomas method to simulate equation [2]. Parameters chosen for this trial program are listed in Table I.

Two comparisons are made between the results from the FORTRAN program and those calculated by Einstein's particular solution of the equation of continuity. Since the kinetics of the stochastic processes under investigation are strongly affected by the mutual repulsion among ions, the values of the ion density matrix in the high density regime are much more important than those in the low density regime. Thus a comparison of the maximum peak height can

TABLE 6-1. Parameters Chosen for Simulation of Diffusion

Item	Value	Units
Diffusion Coefficient	5.65	$\text{cm}^2 \cdot \text{sec}^{-1}$
Cell Width	1.00×10^{-4}	cm
Laser Pulse Length	5.00	ns
Starting Time	5.00	ns
Ending Time	10.0	ns

serve as an indicator in order to show how effective equation [11] is. Also, the base-line peak width is also a good indicator to show how much the simulation peaks are skewed. The comparisons of peak heights versus various D_m is depicted in Figure 6-1, and the comparison of peak width versus D_m is shown in Figure 6-2.

Figure 6-1 shows that equation (8) gives rather unstable values of maximum peak height when the value of D_m is large. Although decreasing the D_m values causes the peak height to converge to a value of 1193.5, in comparison with the true value of 1186.8, a positive 0.56% error still exists. Inevitably, the mutual repulsion calculated according to this ion density matrix will be larger than it should be, and thus the dispersing rate will also be greater. Even worse, Figure 6-2 shows that equation [11] makes the dispersing rate of ions faster in the low density regime than those in the high density regime. As a result of these two effects, the ion density matrix will disperse faster than it should. It is also rather interesting to note that equation [11] requires D_m be smaller than 0.03 to assure a stable result of the second-order differentiation. This value is obviously much smaller than 0.2, the commonly reported value (20). There is thus no advantage over the Crank-Nicholson method.

It can be concluded that equation [11] is not the best

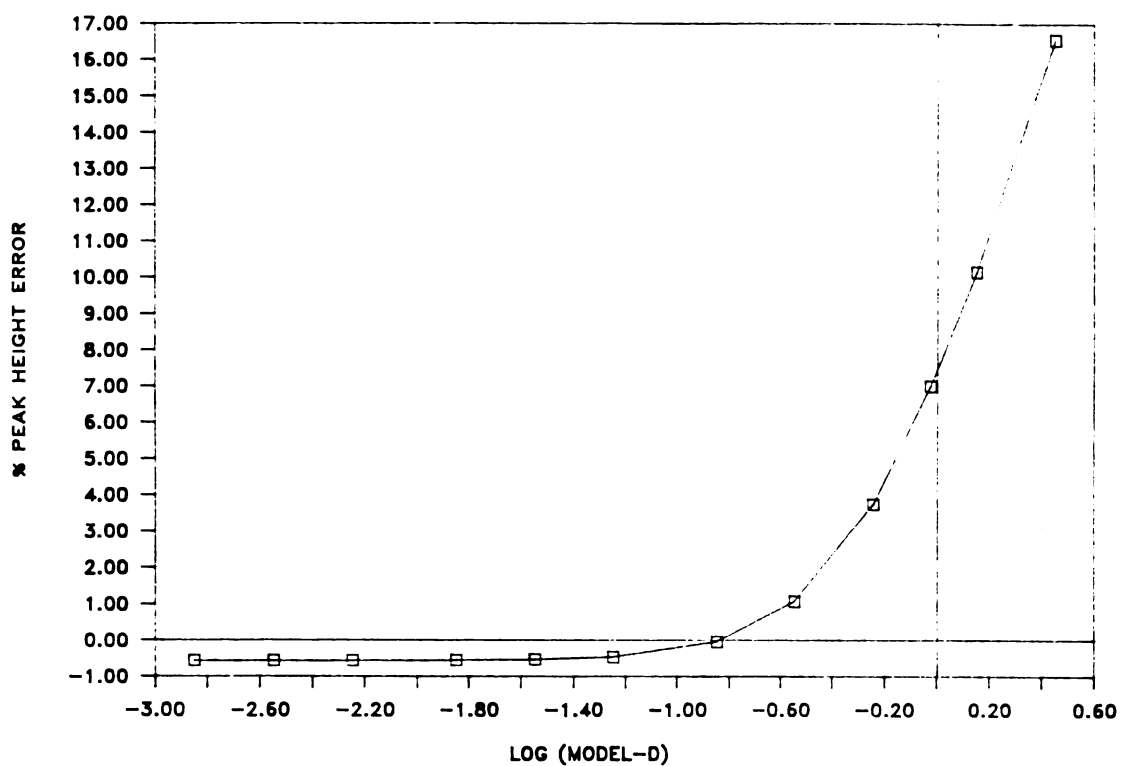


Figure 6-1. Deviations of the maximum peak height versus the logarithm of the model diffusion coefficient. The simulated peak heights were obtained by implementing equation [11] in the simulation program. The theoretical peak height was calculated by equation [3].

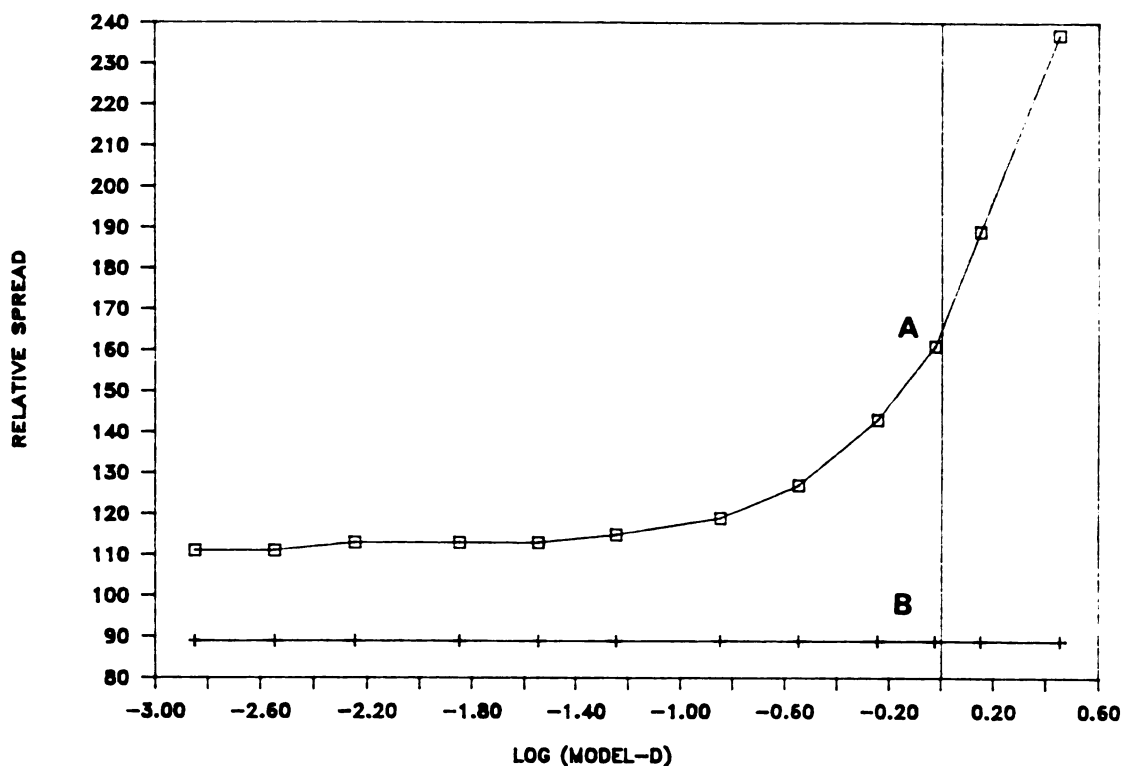


Figure 6-2. Peak width at baseline versus the logarithm of the model diffusion coefficient. The simulated peak widths were obtained by implementing equation [11] in the simulation program. The theoretical peak width was calculated by equation [3].

A, simulated data; B, theoretical values.

choice for handling Gaussian shape peaks. Other more effective methods must be sought.

C-4 Development of a New Algorithm

Numerical differentiation is usually used to estimate the derivative of a function for which selected values are stored in a matrix. It is generally recommended (17) that numerical differentiation be avoided whenever possible, because approximate values of derivatives will inevitably be less accurate than the functional values from which they are derived. In fact, the derivative is the limit of the difference quotient, and in the latter we normally divide the difference of two similar quantities by a relatively small number. Furthermore, if a given function is estimated by a polynomial, the difference in the values calculated may be small, but the derivatives may differ considerably. Hence it is plausible to conclude that numerical differentiation is delicate, in contrast to numerical integration. In fact, numerical integration usually is affected much less by the inaccuracies of function values since it normally smooths the functional values.

The problem the new algorithm encounter is how it can perform numerical differentiation delicately. It has been suggested in the previous section that the conventional

methods are not satisfactory even if the function is smooth. One way to improve the accuracy is to decrease the size of the space interval δ . This choice is impractical since it will require more memory than a mini-mainframe can afford. Another choice is to smooth the function via interpolation and extrapolation after polynomial fitting. The latter guarantees accuracy; however, a great deal of CPU time will be consumed. Thus the compromise is to seek a function that can partially smooth the curve while taking the second derivative at each point.

It is well-known (17) that the Lagrange polynomial can describe most non-linear functions effectively. Since the explicit form of Lagrange's classical formula usually smooths the function to a certain extent, a more accurate approximation can be expected by differentiating suitable Lagrange polynomials. In this study, a fifth-order Lagrange polynomial was chosen as a compromise between speed and accuracy. Thus the term $U(t)$ can be defined as follows:

$$U(t) = \left(\frac{1}{12} \right) [-u(q+2\delta, t) + 16u(q+\delta, t) - 30u(q, t) + 16u(q-\delta, t) - u(q-2\delta, t)] \quad [13]$$

From the discussion in the previous section, inserting equation [13] into the Crank-Nicholson formulation ($\Omega=0.5$) will be a natural choice in order to increase the stability of the performance of the algorithm. Thus equation [6] can

be readily rearranged as follows:

$$\begin{aligned} & C_2 u(q+2\delta, t+\tau) + C_1 u(q+\delta, t+\tau) + C_D u(q+\delta, t+\tau) + \\ & C_1 u(q-\delta, t+\tau) + C_2 u(q-2\delta, t+\tau) \\ & = C_2' u(q+2\delta, t) + C_1' u(q+\delta, t) + C_D' u(q+\delta, t) + \\ & C_1' u(q-\delta, t) + C_2' u(q-2\delta, t) \end{aligned} \quad [14]$$

where:

$$C_D = 24 + 30D_m \quad [15-1]$$

$$C_1 = -16D_m \quad [15-2]$$

$$C_2 = D_m \quad [15-3]$$

and:

$$C_D' = 24 - 30D_m \quad [15-4]$$

$$C_1' = 16D_m \quad [15-5]$$

$$C_2' = -D_m \quad [15-6]$$

Equation [14] along with equations [15-1] to [15-6] give second-order accuracy in both the space coordinate and in time. From the experience gained in dealing with conventional methods, we learned that a different degree of implicitness will give a different stability of the performance of the algorithm, and a different ability of determining the second derivative around the inflection

point. In order to optimize the parameters involved both $\Omega=0.4$ and $\Omega=0.6$, in addition to $\Omega=0.5$, were tested, too.

When the implicitness Ω changes, equation [14] is still valid, only the definitions of the coefficients have to be rearranged. When $\Omega=0.4$, the coefficient sets for equation [14] are as follows:

$$C_D = 60 + 90D_m \quad [16-1]$$

$$C_1 = -48D_m \quad [16-2]$$

$$C_2 = 3D_m \quad [16-3]$$

and:

$$C_D' = 60 - 60D_m \quad [16-4]$$

$$C_1' = 32D_m \quad [16-5]$$

$$C_2' = -2D_m \quad [16-6]$$

When $\Omega=0.6$, the coefficient sets of equation [14] are as follows:

$$C_D = 60 + 60D_m \quad [17-1]$$

$$C_1 = -32D_m \quad [17-2]$$

$$C_2 = 2D_m \quad [17-3]$$

and:

$$C_D' = 60 - 90D_m \quad [17-4]$$

$$C_1' = 48D_m \quad [17-5]$$

$$C_2' = -3D_m \quad [17-6]$$

In these implementations, it is again reasonable to impose the following boundary conditions:

$$u(q_a, t) = 0 \quad [18-1]$$

$$u(q_a + \delta, t) = 0 \quad [18-2]$$

$$u(q_c, t) = 0 \quad [18-3]$$

$$u(q_c - \delta, t) = 0 \quad [18-4]$$

where q_a and q_c , according to the designations in Figure 2-6, are the coordinates of the anode and the cathode, respectively. The term δ is the thickness of each cell of the ion density matrix. In programming, q_a and q_c stand for the first and nth elements of the one-dimensional array while δ is designated as a "counter" integer.

The resulting set of equations for each implementation with different implicitness can be thus generalized as follows:

$$A \times P(q, t + \tau) = A' \times P(q, t) \quad [19]$$

Where A and A' are fifth-order positive definite band symmetrical matrices, while $P(q, t)$ and $P(q, t + \tau)$ are referred to as column matrices, of which the elements are the cell

elements $u(q,t)$ and $u(q,t+\tau)$, respectively. Since all the values on the right hand side of equation [19] are known, this equation can be readily solved by calling subroutines from the IMSL FORTRAN library. Although this algorithm is much more time consuming than conventional methods, the accuracy of the differentiation is improved. In addition, the choice of the size of the time propagation interval, τ , can be increased by orders of magnitude.

In order to evaluate the effectiveness of equation [14] with different degrees of implicitness, a series of FORTRAN programs were written and tested. All the parameters chosen for the testing programs were the same as those listed in Table I, this chapter.

The results from the simulations were compared with each other and with those from Einstein's particular solution of the equation of continuity. Figure 6-3 shows that all the three degrees of implicitness give very good approximations of the maximum peak heights, provided that the value of D_m is sufficiently small. Notice that the value of D_m can be as large as 1.0 with reasonable results. Comparing the range of values that can be assigned to D_m , it is obvious that the new algorithm behaves much better than the conventional Crank-Nicholson method.

Figure 6-4 shows that the different degrees of

Figure 6-3. Deviations of the maximum peak height versus the logarithm of the model diffusion coefficient. The simulated peak heights were obtained by implementing equation [14] in the simulation program with different degrees of implicitness. The theoretical peak height was calculated by equation [3].

- A: 40 % implicitness ($\Omega=0.4$)
- B: 50 % implicitness ($\Omega=0.5$)
- C: 60 % implicitness ($\Omega=0.6$).

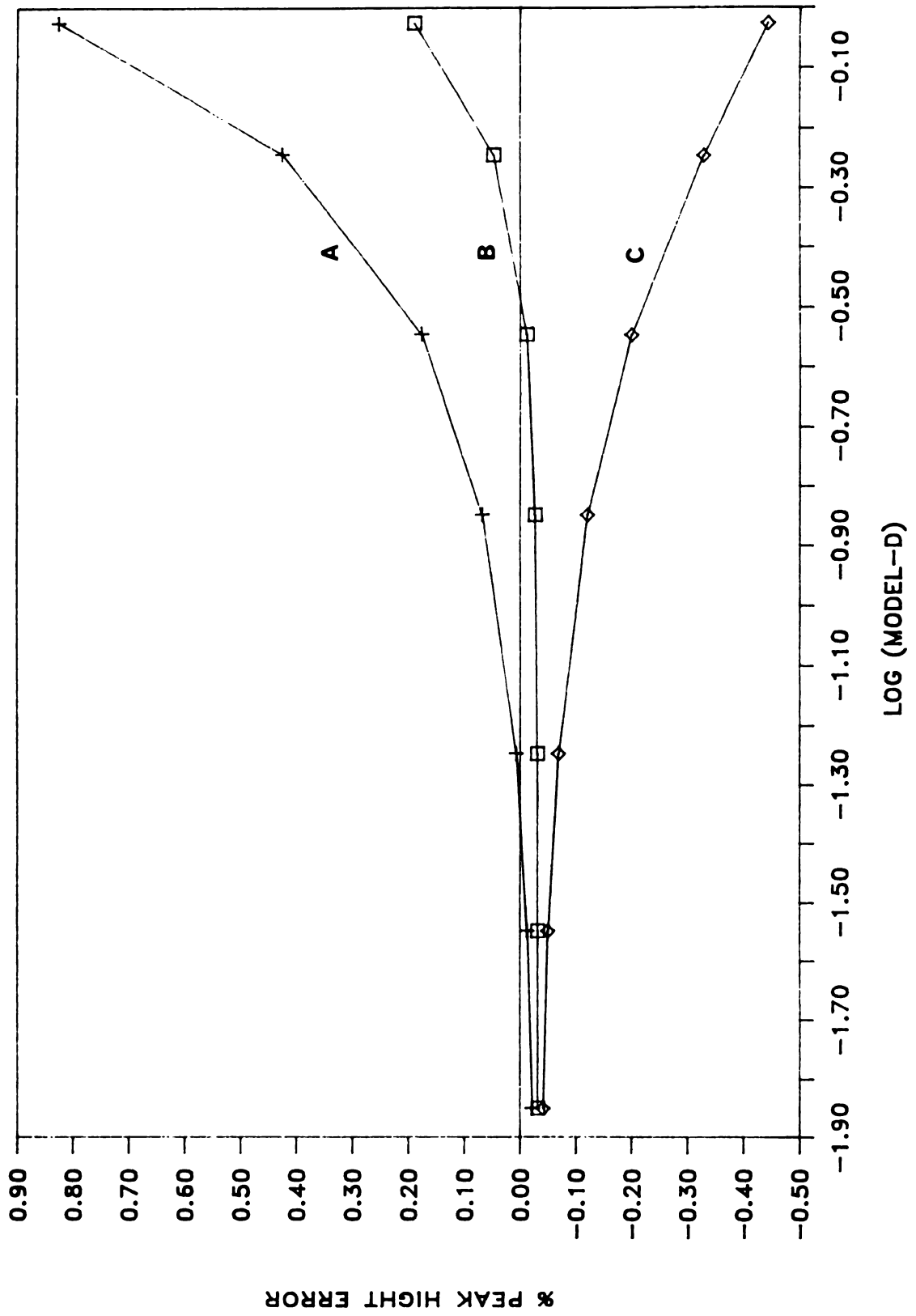


Figure 6-3.

Figure 6-4. Peak width at baseline versus the logarithm of the model diffusion coefficient. The simulated peak widths were obtained by implementing equation [14] in the simulation program with different degrees of implicitness. The theoretical peak width was calculated by equation [3].

- A: 40 % implicitness ($Q=0.4$)
- B: 50 % implicitness ($Q=0.5$)
- C: 60 % implicitness ($Q=0.6$).
- D: Theoretical value.

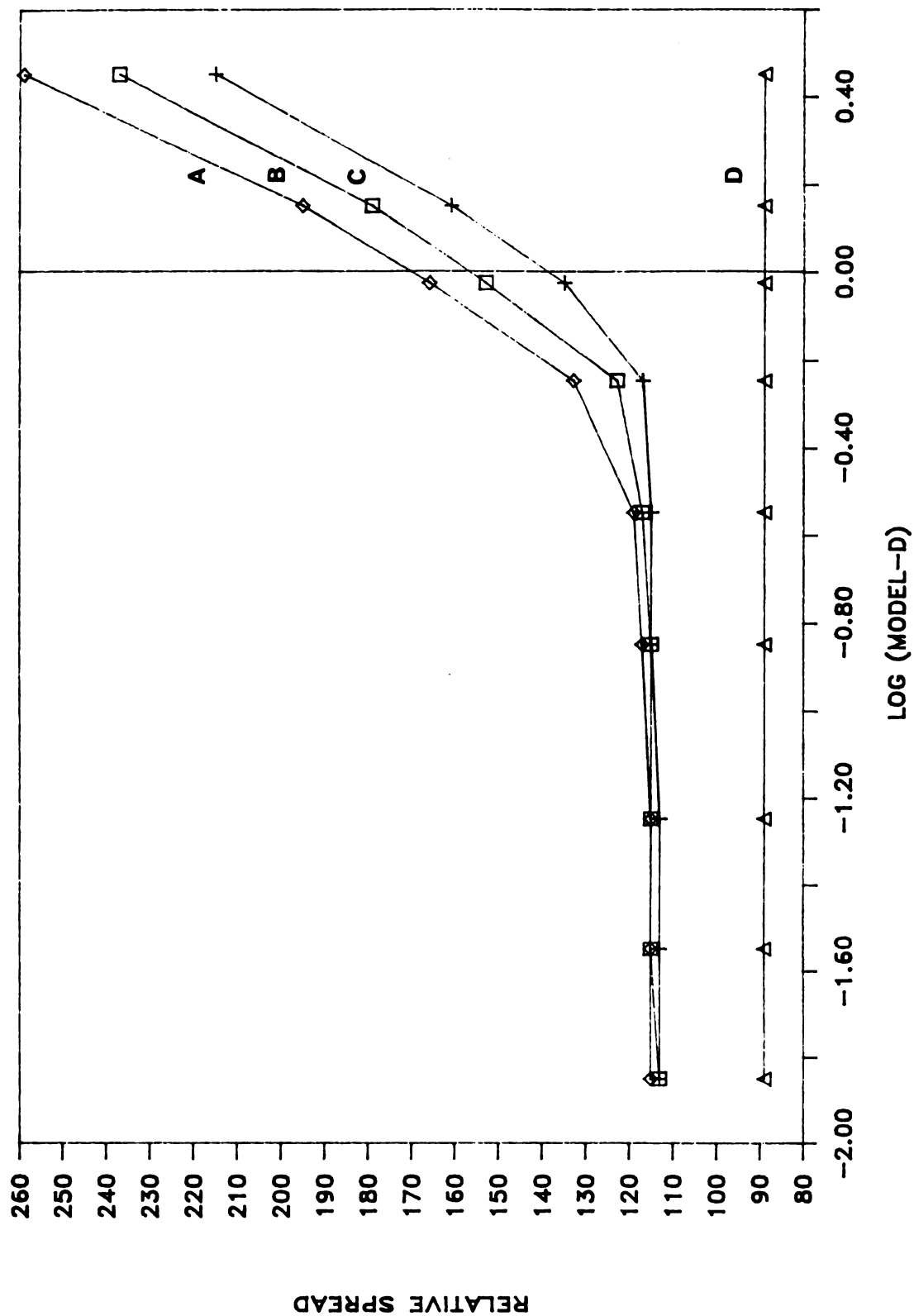


Figure 6-4.

implicitness give roughly the same base-line peak width. This reveals that each algorithm tend to disperse the Gaussian peaks more quickly than it should in the low density regime. Thus other comparisons should be made in order to find the best degree of implicitness.

A third comparison was made by calculating the average square deviation for each simulation according to the following equation:

$$\Theta = \frac{1}{n-1} \sum_{j=0}^{j=n} [u(q_j, t_f) - c(q_j, t_f)]^2 \quad [20]$$

where Θ is the sum of squares of deviations between the numerical approximations and the real values. The variable t_f indicates the time when the ion density matrix was examined. The term $c(q_j, t_f)$ is the numerical value calculated by equation [3] at position q_j and time t_f , where the term j serves as the integer counter. The number of cell elements n in the one-dimensional ion density matrix is defined as follows:

$$n = \frac{(q_c - q_a)}{\delta} + 1 \quad [21]$$

also,

$$u(q_j, t_f) = u(q_a + j\delta, t_f) \quad [22]$$

$$c(q_j, t_f) = c(q_a + j\delta, t_f) \quad [23]$$

Figure 6-5 shows the relation between the average square deviation and D_m for the implementations with different degrees of implicitness. This comparison shows that the implementation with higher implicitness ($\Omega=0.6$) perform better than that with less implicitness ($\Omega=0.4$) when the value of D_m is large. However, in order to extend the effectiveness of the algorithm to a wide D_m range, the implicitness of $\Omega=0.5$ is adopted for later programming. Figure 6-6 shows a comparison of % errors of maximum peak heights between the conventional Crank-Nicholson algorithm and the new algorithm developed in this section. The conventional algorithm has a much narrower working range in terms of model diffusion coefficient and tends to disperse more quickly than the new algorithm. From Figure 6-6, we may indeed claim that the new algorithm is a real improvement over the conventional the Crank-Nicholson algorithm.

D. DRIFT FUNCTION

D-1 Introduction

The purpose of this section is to find a generalized finite difference equation that can simulate the drift term of the Fokker-Planck equation with higher accuracy. The conventional algorithm is reviewed; a new and effective

Figure 6-5. The logarithm of the average of the squares of the deviations between the simulated and theoretical values versus the logarithm of the model diffusion coefficient. The simulated values were obtained by implementing equation [14] in the simulation program with different degrees of implicitness. The theoretical values were calculated by equation [3].

A: 60 % implicitness ($\Omega=0.4$)

B: 50 % implicitness ($\Omega=0.5$)

C: 40 % implicitness ($\Omega=0.6$).

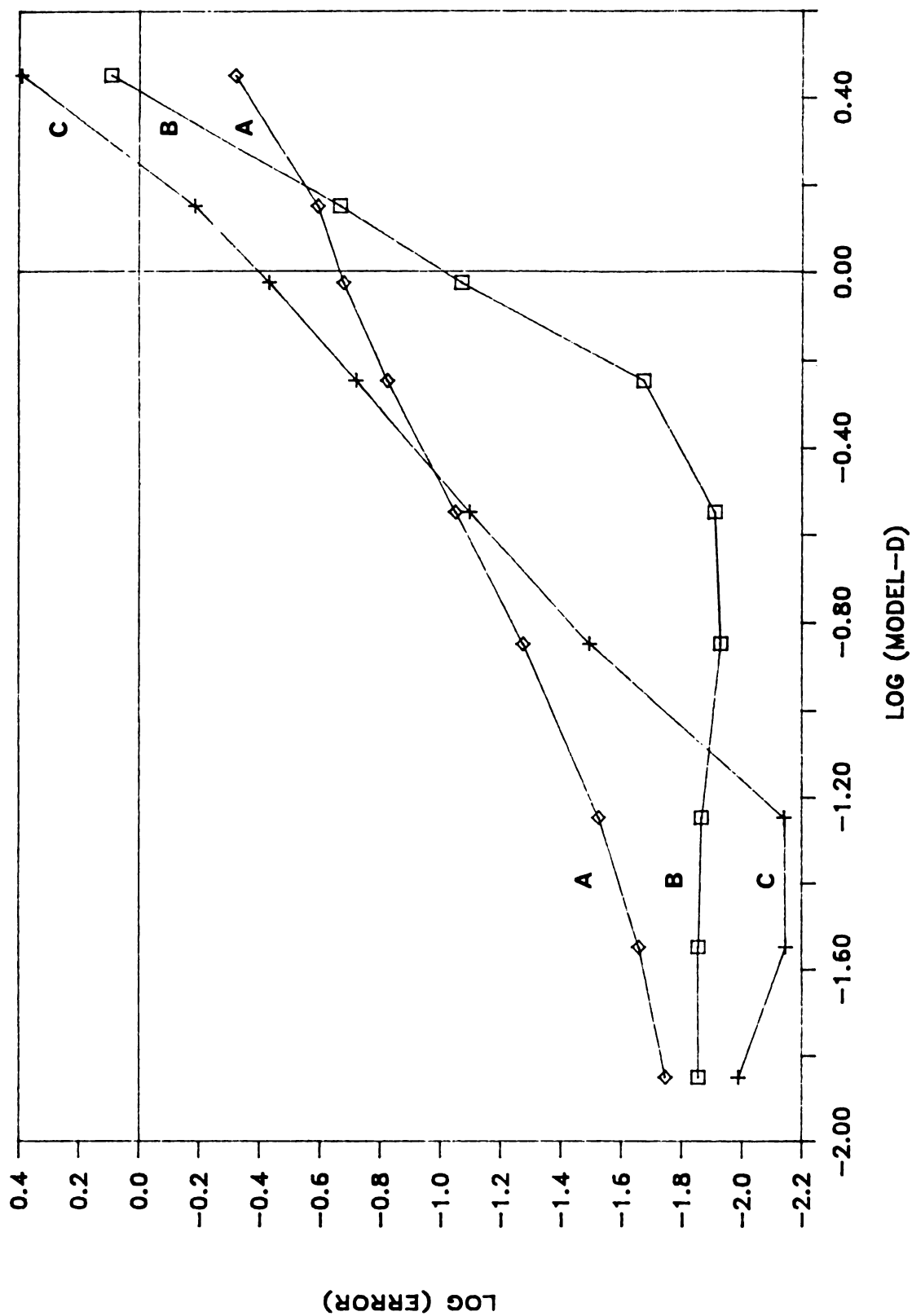


Figure 6-5.

Figure 6-6. A comparison of the deviations of the maximum peak heights from different simulation algorithms. The x-axis is the logarithm of the model diffusion coefficient.

A: 50 % implicitness ($\Omega=0.4$), equation [11];

B: 40 % implicitness ($\Omega=0.4$), equation [14];

C: 50 % implicitness ($\Omega=0.5$), equation [14];

D: 60 % implicitness ($\Omega=0.6$), equation [14].

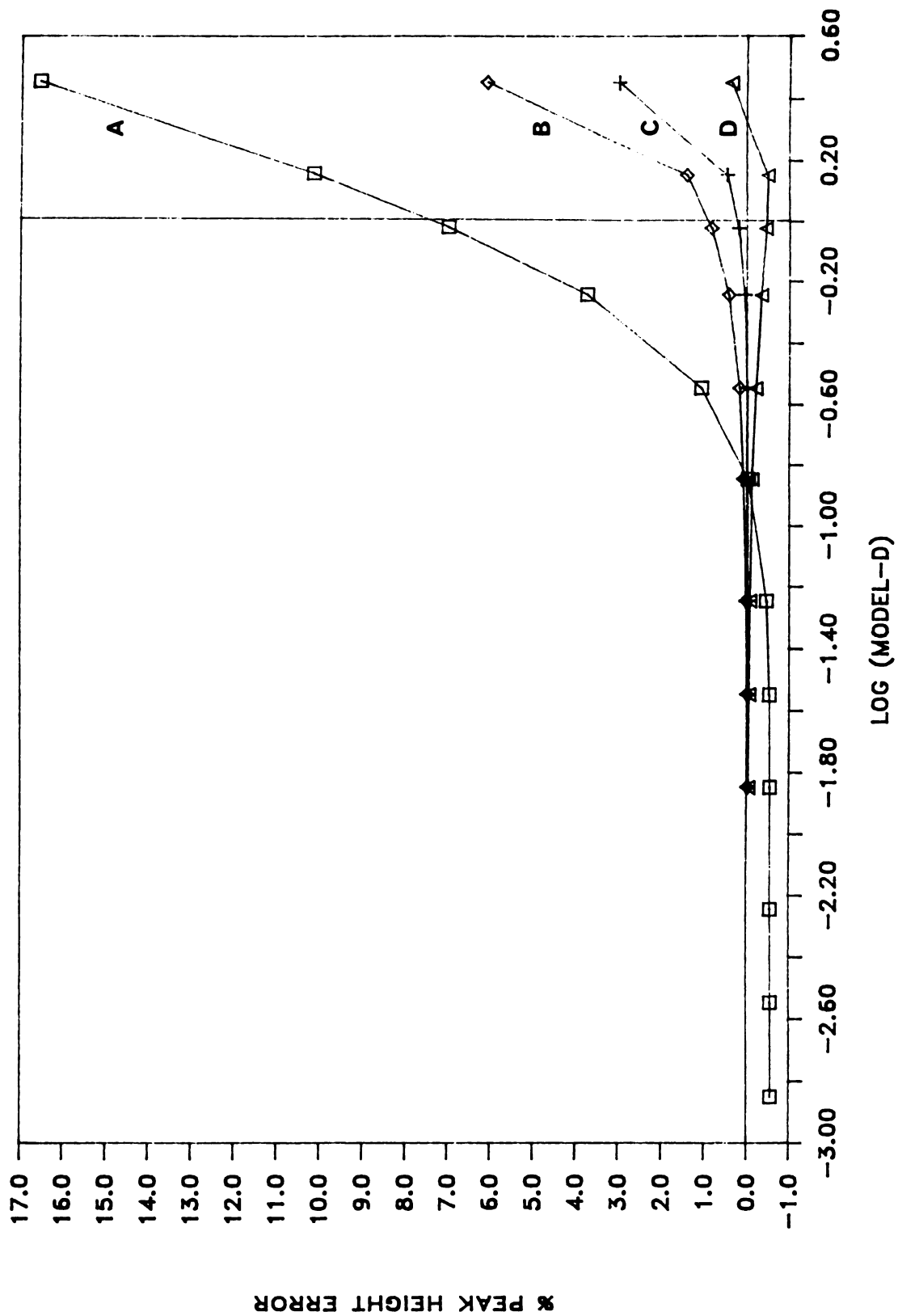


Figure 6-6.

algorithm is derived in order to deal with the complications associated with the introduction of the drift function.

D-2 Basic Definitions

In this section, the intention is to find an algorithm that can simulate the following equation effectively.

$$\frac{\partial}{\partial t} P(q,t) = \frac{\partial}{\partial q} h(q)P(q,t) \quad [24]$$

where $P(q,t)$ is the conditional propagator or the ion density matrix (cm^{-3}) at coordinate q and time t . The term $h(q)$ is the drift function ($\text{cm}\cdot\text{sec}^{-1}$) of the ion propagation under the influence of an electric field.

Conventionally, the basic simulation algorithm only handles first-order differentiation with a constant drift function. Equation [24] must be rewritten by the following formulation if the conventional algorithm is adopted.

$$\frac{\partial}{\partial t} P(q,t) = -b \frac{\partial}{\partial q} P(q,t) \quad [25]$$

where b ($\text{cm}\cdot\text{sec}^{-1}$) is a constant. However, the mutual repulsion of ions varies along with the q -coordinate. In other words, the conventional algorithm is not suitable for

our purpose.

Equation [24] must be written in the following form if the drift function is dependent on the q-coordinate.

$$\frac{\partial}{\partial t} P(q,t) = h(q) \frac{\partial}{\partial q} P(q,t) + P(q,t) \frac{\partial}{\partial q} h(q) \quad [26]$$

Equation [26], indeed, obliges us to derive a new algorithm in order to deal with the non-constant drift function. However, before we start to invent an applicable algorithm the conventional "centered difference method" has to be reviewed.

D-3 Conventional Algorithm

For the centered difference method, the finite difference analogs are centered in both space and time with respect to the grid points at which the values of the dependent variables are determined. In accordance with the conventional Crank-Nicholson formulation, the space derivative at the $(t_k + \tau/2)$ time level is approximated as the average of the space derivatives at the time levels for t_k and $(t_k + \tau)$. This analog can be expressed mathematically by the following equations and term designations.

For the sake of clarity, we begin with defining some fundamental terms. In order to overcome the complexity of mathematics involved in this section, more strict term designations are used.

$$r = \frac{\delta}{2} \quad [27]$$

$$s = \frac{\tau}{2} \quad [28]$$

$$\frac{\partial}{\partial q} u(q,t) = u_q(q_j-r, t_k+s) \quad [29]$$

$$\frac{\partial}{\partial t} u(q,t) = u_t(q_j-r, t_k+s) \quad [30]$$

where δ (cm) indicates the space interval between each cell element of the ion density matrix, and τ (sec) indicates the time propagation interval, which are the same as before. Also, the term $u(q,t)$ indicates the cell element of the ion density matrix, $P(q,t)$, at any given space coordinate q_j and time t_k , of which the value is already normalized. The subscript j and k are integer counters for space and time, respectively. According to the term designation from equation [29], the space derivative at point (q_j-r, t_k+s) can be written as follows:

$$u_q(q_j-r, t_k+s) = \frac{1}{2} \left(\frac{u(q_j, t_k+\tau) - u(q_j-\delta, t_k+\tau)}{\delta} + \frac{u(q_j, t_k) - u(q_j-\delta, t_k)}{\delta} \right) \quad [31]$$

Notice that a 50% implicitness is implied in equation [31].

In a similar manner, the time derivative at the space coordinate $(q_j-\delta/2)$ is approximated by the average of the time derivatives at the space positions for q_j and $(q_j-\delta)$. It can be written as follows:

$$u_t(q_j-r, t_k+s) = \frac{1}{2} \left(\frac{u(q_j, t_k+\tau) - u(q_j, t_k)}{\tau} + \frac{u(q_j-\delta, t_k+\tau) - u(q_j-\delta, t_k)}{\tau} \right) \quad [32]$$

Both equations [31] and [32] can be proved as correct to the second-order (17). Consequently, substitution of equations [31] and [32] into equation [25] yields:

$$\begin{aligned} \left(\frac{b}{\delta} + \frac{1}{\tau} \right) u(q_j, t_k+\tau) = \\ \left(\frac{b}{\delta} - \frac{1}{\tau} \right) (u(q_j-\delta, t_k+\tau) - u(q_j, t_k)) + \\ \left(\frac{b}{\delta} + \frac{1}{\tau} \right) u(q_j-\delta, t_k) \end{aligned} \quad [33]$$

It has been shown (17) that equation [33] is stable for any ratio of δ/τ .

Equation [33] describes equation [25] in finite difference elements explicitly. For a typical set of initial and boundary conditions, $u(q_j, t_k)$ will be known for all values of q at time zero and for all values of t at the boundary points. It is thus interesting to point out that the values of $u(q_j, t_k)$ at the first space position could be computed for as many time levels as desired before any values at the second space position were computed. This characteristic may be used in simulating the decay of Gaussian distributions with a vanishing diffusion coefficient. For instance, the ideal condition of the output from the uv detector of a flow injection analysis.

D-4 Development of a New Algorithm

The main purpose of this section is to derive a new finite difference equation that can describe equation [26] effectively. The derivation is rather complicated, hence only the basic term designations and results are given here.

Again, we start from designate some fundamental terms for the new algorithm that can deal with a drift function of which the functional values are dependent on the q -

coordinate.

$$u_t(q_j - r, t_k + s) = \frac{1}{2} \left(\frac{u(q_j, t_k + \tau) - u(q_j, t_k)}{\tau} + \frac{u(q_j - \delta, t_k + \tau) - u(q_j - \delta, t_k)}{\tau} \right) \quad [34]$$

$$u_q(q_j - r, t_k + s) = \frac{1}{2} \left(\frac{u(q_j, t_k + \tau) - u(q_j - \delta, t_k + \tau)}{\delta} + \frac{u(q_j, t_k) - u(q_j - \delta, t_k)}{\delta} \right) \quad [35]$$

$$\begin{aligned} \frac{\partial}{\partial q} h(q) &= h_q(q_j - r, t_k + s) \\ &= \frac{h(q_j) - h(q_j - \delta)}{\delta} \end{aligned} \quad [36]$$

$$h(q) = \frac{h(q_j) - h(q_j - \delta)}{2} \quad [37]$$

$$\begin{aligned} u(q, t) &= \frac{1}{4} \left(u(q_j, t_k + \tau) + u(q_j - \delta, t_k + \tau) + \right. \\ &\quad \left. u(q_j, t_k) + u(q_j - \delta, t_k) \right) \end{aligned} \quad [38]$$

where the terms $u_t(q_j - r, t_k + s)$ and $u_q(q_j - r, t_k + s)$ have the same meanings as before. Substitution of equations [34] through [38] into equation [26] gives a surprisingly neat format:

$$\begin{aligned}
 & \left(\frac{h(q_j)}{\delta} + \frac{1}{\tau} \right) u(q_j, t_k + \tau) = \\
 & \left(\frac{h(q_j - \delta)}{\delta} - \frac{1}{\tau} \right) u(q_j - \delta, t_k + \tau) - \\
 & \left(\frac{h(q_j)}{\delta} - \frac{1}{\tau} \right) u(q_j, t_k) + \\
 & \left(\frac{h(q_j - \delta)}{\delta} - \frac{1}{\tau} \right) u(q_j - \delta, t_k) \quad [39]
 \end{aligned}$$

Equation [39] is conservative in so far as the boundary conditions defined in equations [18-1] through [18-4] are met.

E. THE SIMULATION PROGRAM

E-1 Introduction

The simulation of DLI signal detection involves diffusion, drift due to the electric field, and drift due to mutual repulsion of ions. The interactions between ions and electrons are not included since they can be nicely managed by the model of ambipolar diffusion.

Due to the complexity of the new diffusion algorithm, an effective matrix manipulation subroutine was required in

order to speed up the computation. The development of such a subroutine is beyond the scope of this thesis; hence subroutine LEQ2PB was called from the IMSL library package. Given an n by n positive definite symmetric band matrix A and an n by m matrix B , subroutine LEQ2PB solves the set of linear equations $AX = B$ for X . A is stored in symmetric band storage mode and B in full storage mode. Subroutine LEQ2PB also invokes iterative refinement to improve the accuracy of the solution. In fact, subroutine LEQ2PB supplies more flexibility than is really needed; hence it dramatically slows down the speed of the diffusion algorithm. However, the accuracy of the simulation may be improved.

In the simulation, the mutual repulsion of ions is treated in accordance with the time-dependent electric field. For each cell element, the effective electric field can be calculated by summing up the electric fields induced by all other cell elements. The induced electric field $E(q_j, t_k)$ (volt \cdot cm $^{-1}$) at position q_j , time t_k is calculated according to the following equation:

$$E(q_j, t_k) = \beta \left(\sum_{i=1}^{i=j-1} \frac{u(q_i, t_k)}{(j-i)^2 \delta^2} - \sum_{i=j+1}^{i=n} \frac{u(q_i, t_k)}{(i-j)^2 \delta^2} \right) \quad [37]$$

where $u(q_i, t_k)$ is the ion density (ions \cdot cm $^{-3}$) at position q_i , time t_k . The term β is a proportional constant which is used to adjust the units.

In the algorithm described in this section, diffusion and drift are treated separately. At the beginning of each time propagation step, diffusion is simulated first. The simulation of the drift term is then based on the new ion density matrix generated by the diffusion algorithm. After the time interval t_k was propagated, the curve fitting program introduced in Section D, Chapter V, was then used to extract the "effective" diffusion coefficient to which both diffusion and mutual repulsion contribute.

E-2 Description of the Simulation Program

The simulation program can be summarized as follows:

- (i) Define program and simulation parameters.
- (ii) Assume that the ion distribution is Gaussian at 5 nanoseconds. Calculate the initial ion density matrix array by using equation [3].
- (iii) Set up the coefficient matrix for calculating the diffusion term according to equations [13] through [15]. Call subroutine LEQ2PB from IMSL to perform the matrix calculation.
- (iv) Record the fraction of ions that has reached the detector.
- (v) Calculate the electric field due to the mutual repulsion of ions based on the ion density

matrix calculated in step (iii) for each cell element to construct the drift function $h(q)$ numerically.

- (vi) Calculate the drift term. If the electric field is too strong, divide this step into sub-steps in order to reduce truncation errors.
- (vii) Report the fraction of ions that has reached the detector.
- (viii) Normalize the ion density matrix. Go to step (iii) for another step of time propagation.
- (ix) Output.

The simulation program is listed in Appendix C. All of the technical details are documented along with the FORTRAN source code.

F. RESULTS AND DISCUSSION

The simulation program described in the previous section has been employed to investigate the contribution of mutual repulsion of ions to the "effective" diffusion coefficient. The test runs assumed that the laser pulses were off after 5 nanoseconds and at that time the ion density matrix simulates a Gaussian peak. The diffusion coefficient was chosen to be $5.0 \text{ cm}^2 \cdot \text{sec}^{-1}$ and the mobility coefficient was chosen to be $25.0 \text{ cm}^2 \cdot \text{volt}^{-1} \cdot \text{sec}^{-1}$. Since

the burning velocity is very small in comparison with the contribution of the electric field, it was left out. The distance between probes was assumed to be 5.00 mm while the distance between the laser focal point and the lower probe (cathode) was assumed to be 2.00 mm. The ion density in the flame, which determines the intensity of mutual repulsion of ions, was assumed to be $1.0 \times 10^{10} \text{ ions}\cdot\text{cm}^{-3}$. The output from the simulation program was then treated by the curve fitting program ZMDIF3 in order to extract the "effective" diffusion coefficient. The program ZMDIF3 was described in Section D, Chapter V.

Figure 6-7 shows the relation between the ion velocity ($\text{cm}\cdot\text{sec}^{-1}$) and the bias voltage (volts). The plot shows a rather straight line of which the slope is $(51.71 \pm 0.48) \text{ cm}\cdot\text{volt}^{-1}\cdot\text{sec}^{-1}$. In accordance with equation [11], Chapter V, the "effective" mobility coefficient of ions is $(25.86 \pm 0.24) \text{ cm}^2\cdot\text{volt}^{-1}\cdot\text{sec}^{-1}$. It is only about 3% different from the initial setting. This result can be viewed as an evidence showing that equation [39] is highly successful as a new algorithm.

Figure 6-8 (a) shows the "effective" diffusion coefficients generated with the same set of parameters as Figure 6-7. The values are rather unstable and are roughly all the same. This indicates that mutual repulsion of ions was not important in this case. A second series of

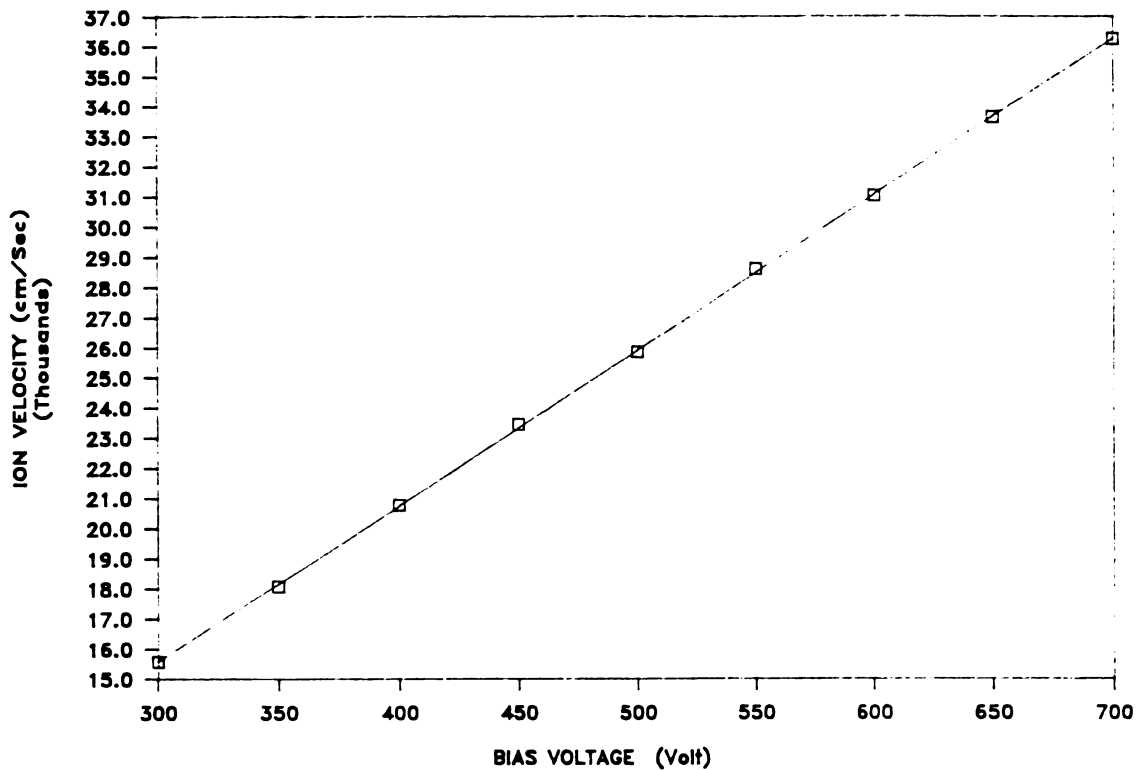


Figure 6-7. Ion velocity versus bias voltage plot. The velocities were obtained from the simulation program. The slope of the plot is 51.71 ± 0.48 which yields a mobility coefficient of $25.86 \pm 0.24 \text{ cm}^2 \cdot \text{volt}^{-1} \cdot \text{sec}^{-1}$.

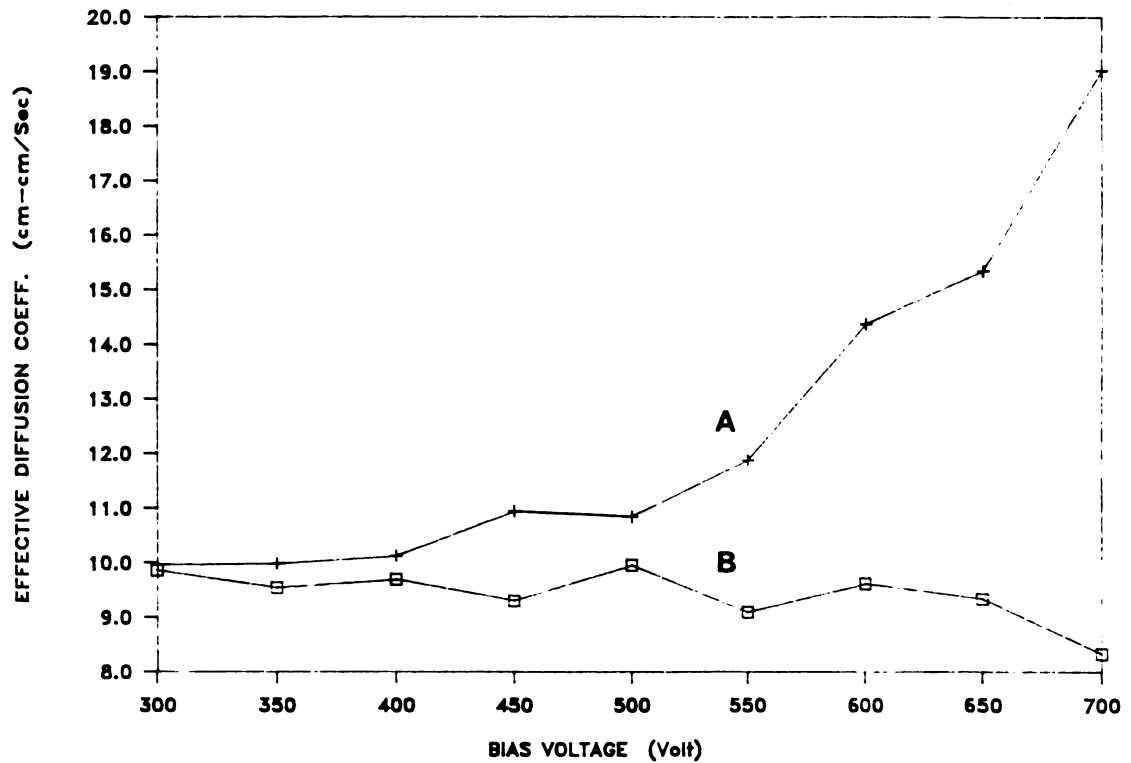


Figure 6-8. Ion diffusion coefficient versus bias voltage plot. The ion diffusion coefficient were obtained from the simulation program.

A: ion density is 1.0×10^{11} ions \cdot cm $^{-3}$;

B: ion density is 1.0×10^{10} ions \cdot cm $^{-3}$.

simulations was then performed. Curve (b) shows the "effective" diffusion coefficients generated under the same parameters as the previous simulation series except the ion density was increased to $1.0 \times 10^{11} \text{ ions}\cdot\text{cm}^{-3}$. Curve (b) shows a tendency for increasing values of the "effective" diffusion coefficient as the bias voltage is increased. This tendency supports the proposal made in the previous chapter that the relationship between diffusion coefficients and bias voltages is due to the mutual repulsion of ions. However, at 700 V, the "effective" diffusion coefficient is only $19 \text{ cm}^2\cdot\text{sec}^{-1}$, which is much smaller than the experimental result of $892 \text{ cm}^2\cdot\text{sec}^{-1}$.

Reducing the distance between the lower electrode and the laser focal point may efficiently increase the value of the "effective" diffusion coefficient. A value of $392 \text{ cm}^2\cdot\text{sec}^{-1}$ has been obtained from different settings of parameters with an assumed voltage of 4000 volts. Nevertheless, our simulation program was not able to duplicate the values obtained by experiments exactly. Additional efforts in optimizing the parameter settings in order to simulate the real DLI signal collection process will be required in the future.

G. CONCLUSIONS

In this chapter, the conventional Crank-Nicholson method which solves parabolic partial differential equations numerically was reviewed. A new algorithm which incorporates the smoothing ability of the Lagrange polynomial with the Crank-Nicholson formulation was developed. Tests showed that the new algorithm performs much better than the old method in simulating the diffusion term in the Fokker-Planck equation. Also, a new algorithm that can numerically solve linear hyperbolic partial differential equations and simulate the drift term in the Fokker-Planck equations was derived. Real simulation showed that this new algorithm also works satisfactorily.

A program which simulates the DLI signal collection process was constructed and tested. Results showed that it can simulate the drift term very well. However, the results can only partially support the explanation proposed in the previous chapter that the observed relationship between the "effective" diffusion coefficient and the bias voltage is due to the mutual repulsion of ions. The general trend of the simulated "effective" diffusion coefficient showed that the mutual repulsion of ions may be an important factor under certain circumstances, such as when a very high bias voltage is applied.

CHAPTER III

REFERENCES

1. C.A. van Dijk, F.M. Curran, K.C. Lin and S.R. Crouch, Anal. Chem. 53, 1275 (1981).
2. K.C. Lin, P.M. Hunt, and S.R. Crouch, Chem. Phys. Lett. 90, 111 (1982).
3. F.M. Curran, C.A. vanDijk, and S.R. Crouch, Appl. Spectrosc. 37, 385 (1983).
4. F.M. Curran, K.C. Lin, G.E. Leroy, P.M. Hunt, and S.R. Crouch, Anal. Chem. 55, 2382 (1983).
5. K.C. Lin, Ph.D. Thesis (Michigan State University, 1982).
6. F.M. Curran, Ph.D. Thesis (Michigan State University, 1983).
7. K.L.C. Hunt and J. Ross, J. Chem. Phys. 75, 976 (1981).
8. P.M. Hunt, K.L.C. Hunt, and J. Ross, J. Chem. Phys. 79, 3765 (1983).
9. L. Onsager and S. Machlup, Phys. Rev. 91, 1505 (1953).
10. S. Machlup and L. Onsager, Phys. Rev. 91, 1512 (1953).
11. F.W. Wiegel, Physica 33, 734 (1967); *ibid.* 37, 105 (1967).
12. F. Langouche, D. Reekaerts, and E. Tirapegui, Physica A97, 195 (1979).
13. M. Moreau, Physica A90, 410 (1978).
14. B.H. Lavenda, Phys. Lett. A71, 304 (1979).

15. A. Fick, Ann. Phys. (pogg.) 94, 59 (1855).
16. A. Einstein, "Investigations on the Theory of the Brownian Movements" (Dover, New York, 1956).
17. W.H. Press, B.P. Flannery, S.A. Teukolsky, and W.T. Vetterling, "Numerical Recipes, The Art of Scientific Computing" (Cambridge University Press, London, 1986).
18. L.W. Johnson and R.D. Riess, "Numerical Analysis" 2nd ed. (Addison-Wesley, Reading, Massachusetts, 1982).
19. B. Carnahan, H.A. Luther, and J.O. Wilkes, "Applied Numerical Methods". (Academic Press, New York, 1981).
20. S.W. Feldberg, "Electroanalytical Chemistry, A Series of Advances" ed. by A.J. Bard, pp. 199 (Marcel Dekker, Inc., New York, 1969).

CHAPTER VII

FLAME TEMPERATURE PROFILES

A. INTRODUCTION

This chapter describes dual-laser-ionization (DLI) measurements of the vertical temperature profiles of a laminar-flow hydrogen-oxygen-argon flame at both fuel-rich, non-stoichiometric and stoichiometric conditions.

As detailed in previous chapters, the time-resolved DLI signals collected under various bias voltages can be precisely modelled by the Fokker-Planck equation, and the mobility and diffusion coefficients of the metal ion can thus be extracted by curve fitting methods. The flame temperatures can then be calculated by the Einstein relation (1,2). In this study, various metal ions were utilized in flame temperature measurements in order to demonstrate the the validity and advantages of the DLI method. The results of the temperature measurements are in reasonable accordance with literature values.

B. EXPERIMENTAL

B-1 Flame Cell

A laminar-flow, premixed, hydrogen-oxygen-argon flame was used in this study. Details of the properties of this flame have been covered in Section C, Chapter II. Hence, in this section only a brief description will be given.

The burner is of the Meker type; the gas mixture emanates from the burner head through 631 circular holes of 0.5 mm diameter and 5 mm length, which are arranged in concentric circles with a 2 mm interval between successive rings. The height of the primary combustion zone is approximately 0.5-2 mm. The burner head is cooled by a water jacket. Pre-purified grade hydrogen, oxygen, and argon gases are divided into two branches to form the inner and mantle flames, respectively. The pressures of each branch of the flame are controlled by dual pressure regulators. The analyte is introduced into the inner flame through a pneumatic nebulizer. Argon is the nebulizing gas.

The flow rates of gases are controlled by six precision flowmeters (Series FM-1050, Matheson Instruments, Horsham, PA). When the flame is adjusted to have a fuel-rich, non-stoichiometric composition, the central and mantle argon gas

settings used gave a flow rate of approximately $3.2 \text{ L}\cdot\text{min}^{-1}$. The mantle flame hydrogen and oxygen flow rate settings gave a stoichiometric mixture of $1.0 \text{ L}\cdot\text{min}^{-1}$ and $0.50 \text{ L}\cdot\text{min}^{-1}$, respectively. To obtain maximum DLI signals, the hydrogen and oxygen settings of the central flame usually were adjusted to be $1.6 \text{ L}\cdot\text{min}^{-1}$ and $0.50 \text{ L}\cdot\text{min}^{-1}$, respectively.

For stoichiometric flames, the central and mantle argon gas settings used gave a flow rate of approximately $3.2 \text{ L}\cdot\text{min}^{-1}$. The hydrogen and oxygen flow rate settings of both mantle and central flames were $1.0 \text{ L}\cdot\text{min}^{-1}$ and $0.50 \text{ L}\cdot\text{min}^{-1}$, respectively.

B-2 Apparatus

A complete description of our DLI experimental system has been presented elsewhere (3-5). Details of the procedures and instruments utilized for this study have been covered in Chapter V.

In this study, the laser beams and probes were carefully aligned at the beginning of each laboratory session. The distance between the laser focal point and the upper probe was 2.5 mm, and the distance between probes was always 5.0 mm; i.e., the relative positions of the laser focal point and the electrodes were fixed throughout the

working period. The burner head was moved up and down in order to adjust the position of the laser focal point in the flame; the vertical flame temperature profile can thus be obtained.

At each vertical point in the flame, eight different bias voltages ranging from 50 to 400 volts were used. Multiple data sets were taken when the ion peak was not well resolved. The aperture duration of the boxcar integrator was chosen to be 5 microseconds. The aperture delay ranges were determined according to the shape of each individual peak. Usually, 30 readings were taken at each aperture delay range and later averaged for additional noise reduction. All data taken by the boxcar were stored in the memory of the microcomputer, and then uploaded to the mainframe PDP/11-23 for further treatment.

B-3 Reagents

All solutions were prepared from reagent grade chemicals and dissolved in distilled, deionized water. Solutions containing sodium, lithium, and calcium were prepared from the chloride salts, while the strontium solution was prepared from its nitrate salt.

The following laser dyes were obtained commercially and

used without further purification: Rhodamine 6G (Eastman Kodak Co.; 7.5×10^{-3} M in ethanol; $3s_{1/2} \rightarrow 3p_{3/2}$, 589.0 nm) for sodium analysis; Coumarin 460 (Exciton Chemical Co., Inc.; 1.0×10^{-2} M in ethanol; $5s \rightarrow 5p$, 460.7 nm) for strontium analysis; DCM (Exciton Chemical Co., Inc.; 5.0×10^{-3} M in dimethyl sulfoxide; $2s \rightarrow 2p$, 670.7 nm) for lithium analysis; and Stilbene 420 (Exciton Chemical Co., Inc.; 3.5×10^{-3} M in methanol; $4s \rightarrow 4p$, 422.7 nm) for calcium analysis.

C. RESULTS OF VERTICAL FLAME TEMPERATURE PROFILE MEASUREMENTS

The temperature profiles of both stoichiometric and fuel-rich, non-stoichiometric H_2-O_2-Ar flames are reported according to the vertical height of the laser focal point above the burner head. In this study, sodium, lithium, and calcium ions were used in the measurements of the vertical temperature profile of the fuel-rich, non-stoichiometric H_2-O_2-Ar flame. For the measurements of the temperature profile of the stoichiometric H_2-O_2-Ar flame, sodium and strontium ions were used.

C-1 Non-Stoichiometric Hydrogen-Oxygen-Argon Flame

The results of the DLI measurements of the fuel-rich, non-stoichiometric hydrogen-oxygen-argon flame with sodium ions are given in Table 7-1. The mobility coefficients and diffusion coefficients of sodium ions at various vertical heights (above the burner head) in the flame were calculated according to the methods detailed in Chapter V. The flame temperature at each vertical point in the flame was calculated by the Einstein relation (1,2).

The vertical temperature profile of the fuel-rich hydrogen-oxygen-argon flame measured with sodium shows a smooth trend. The flame temperature reaches a maximum at a position about 10 to 12 mm above the burner head. Ion signals became weaker and noisier above this region. When the vertical height is more than 15 mm above the burner head, ion signals were too weak to be resolved by the curve fitting methods presented in Chapter V; thus no temperature measurements could be made in this region. The vertical temperature profile measured with sodium ions is plotted in Figure 7-1.

The results of the DLI measurements of the fuel-rich, non-stoichiometric hydrogen-oxygen-argon flame with lithium ions are given in Table 7-2. A plot which shows the flame

**Table 7-1. Non-stoichiometric H₂-O₂-Ar Flame Temperature
Profile Measurements with Sodium Ions**

Height (mm)	Mobility	Diffusion	Temperature (K)
	Coefficient (cm ² ·v ⁻¹ ·s ⁻¹)	Coefficient (cm ² ·s ⁻¹)	
7.5	28.84	3.47	1396
7.5	30.16	3.54	1360
8.0	26.00	3.75	1674
8.0	25.27	3.71	1704
9.0	25.23	4.12	1895
10.0	24.33	4.12	1967
10.0	24.07	4.07	1962
10.5	23.77	4.07	1987
11.0	24.09	4.02	1936
11.5	22.93	3.89	1969
12.0	22.29	3.77	1963
12.5	21.16	3.52	1931
13.0	22.58	3.44	1768

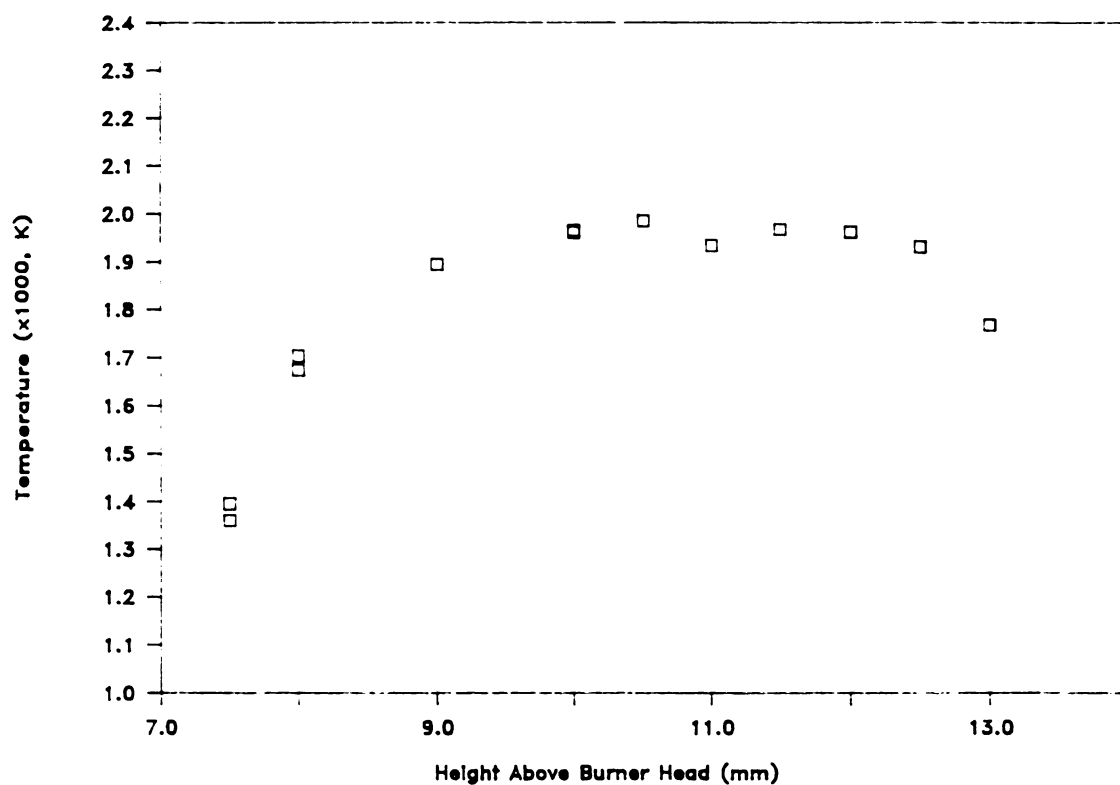


Figure 7-1. Non-stoichiometric $\text{H}_2\text{-O}_2\text{-Ar}$ flame temperature profile measurements with sodium ions at different heights above the burner head.

temperatures measured by lithium ions versus vertical height above the burner head is given in Figure 7-2. Again, a smooth temperature profile is observed. The flame temperature reaches a maximum at a position about 9 to 12 mm above the burner head. Beyond this region, ion signals began to decrease dramatically and the DLI signals became much noisier than those in the high temperature regime. However, ion signals with reasonable strength still could be collected in the region up to 17.5 mm above the burner head. At 20.0 mm above the burner head, no ion signal could be observed.

Measurements of the flame temperature with calcium ions presented some difficulties. Possibly due to the low ion mobility of calcium and/or the formation of CaOH (11) in the flame, the intensities of the ion peaks were almost always low and noisy. Multiple data sets were taken for further averaging. When the laser focal point was placed 12.0 mm or higher above the burner head, no ion signals could be observed. The results of the DLI measurements with calcium ions are given in Table 7-3 and the temperature profile is plotted in Figure 7-3.

Measurements of the flame temperature with strontium ions in the fuel-rich, non-stoichiometric hydrogen-oxygen-argon flame have been tried. However, no ion signal was observed.

**Table 7-2. Non-stoichiometric H₂-O₂-Ar Flame Temperature
Profile Measurements with Lithium Ions**

Height (mm)	Mobility	Diffusion	Temperature (K)
	Coefficient (cm ² ·v ⁻¹ ·s ⁻¹)	Coefficient (cm ² ·s ⁻¹)	
8.5	29.02	4.68	1871
10.5	28.15	4.81	1983
12.0	28.43	4.79	1955
13.5	31.06	4.80	1793
15.5	35.13	3.94	1302
17.5	42.15	2.91	801

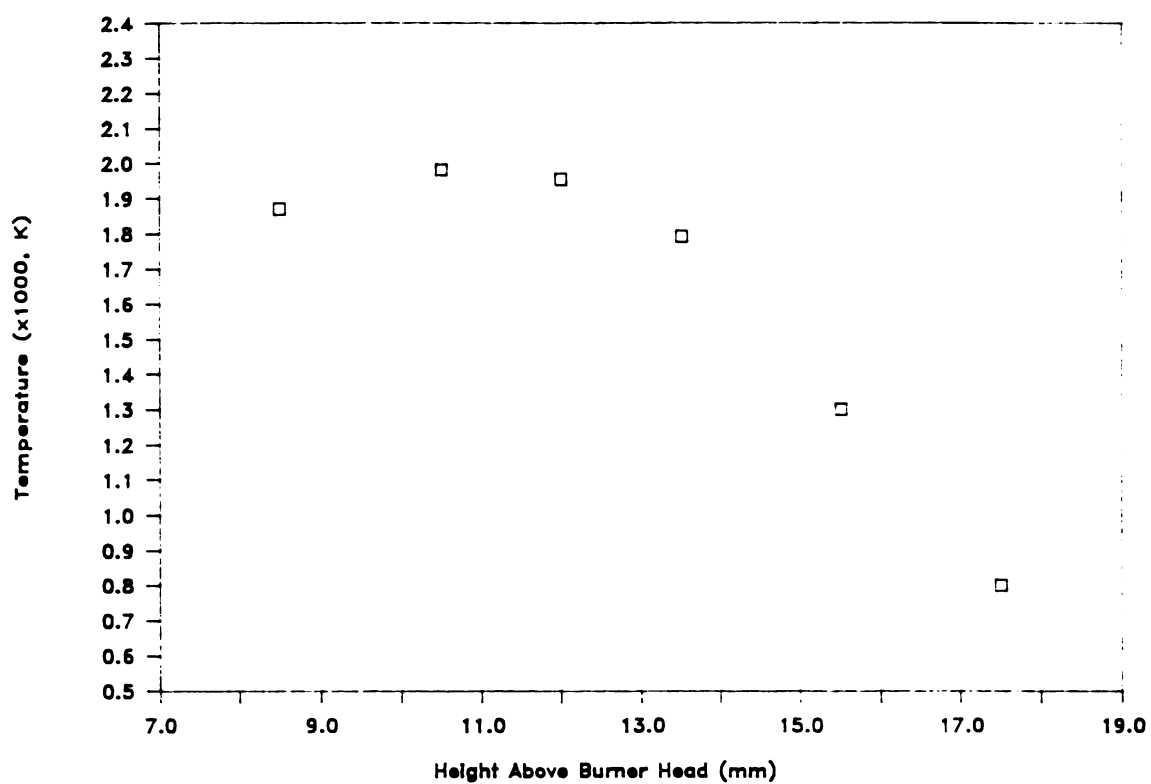


Figure 7-2. Non-stoichiometric H_2-O_2-Ar flame temperature profile measurements with lithium ions at different heights above the burner head.

**Table 7-3. Non-stoichiometric H₂-O₂-Ar Flame Temperature
Profile Measurements with Calcium Ions**

Height (mm)	Mobility	Diffusion	Temperature (K)
	Coefficient (cm ² ·v ⁻¹ ·s ⁻¹)	Coefficient (cm ² ·s ⁻¹)	
7.5	19.36	2.41	1445
9.0	16.13	2.75	1978
11.0	17.01	2.74	1869

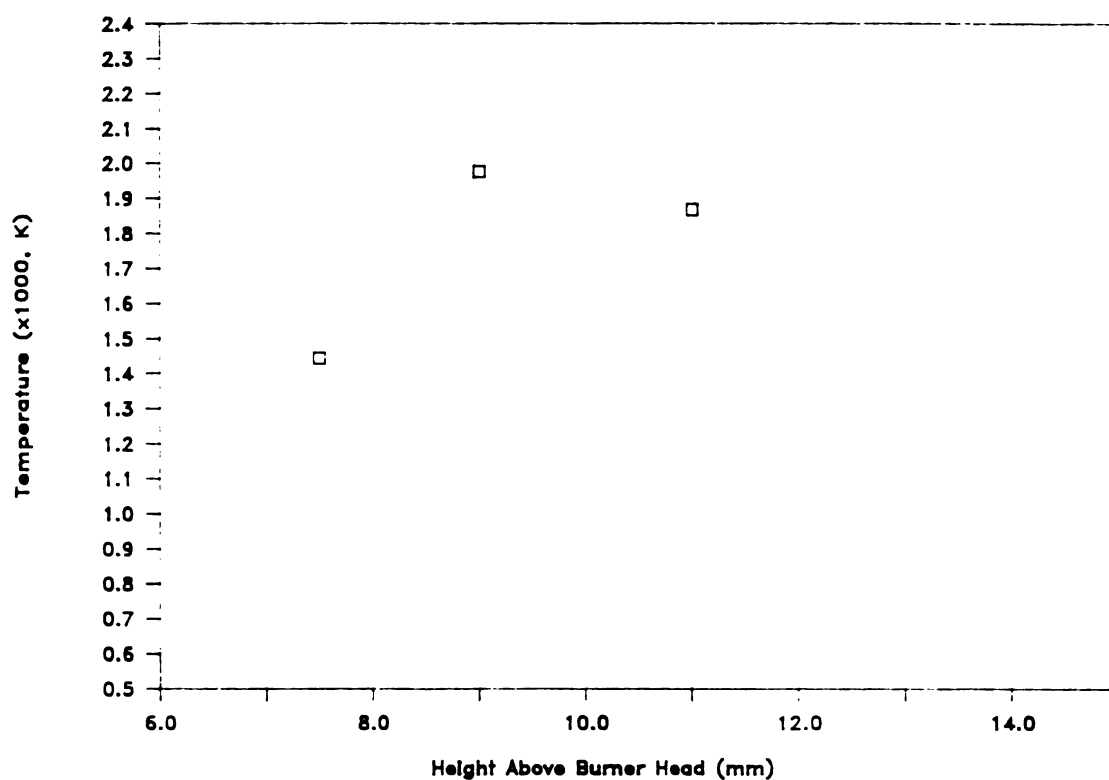


Figure 7-3. Non-stoichiometric $\text{H}_2\text{-O}_2\text{-Ar}$ Flame temperature profile measurements with calcium ions at different heights above the burner head.

The results of the DLI measurements of the fuel-rich, non-stoichiometric hydrogen-oxygen-argon flame with various metal ions mentioned above are given in Table 7-4. A vertical temperature profile measured with various metal ions is plotted in Figure 7-4. Figure 7-4 shows that the DLI temperature measurements with various metal ions at different heights in the flame are generally consistent with one another. However, at the same point in the flame, the flame temperatures measured with different ions may differ as much as 66°C (Table 7-4, 11.0 mm above the burner head). This difference may be attributed to the low ion mobility of calcium ions in the flame.

C-2 Stoichiometric Hydrogen-Oxygen-Argon Flame

The results of DLI temperature measurements of the stoichiometric hydrogen-oxygen-argon flame with sodium ions are given in Table 7-5. In the stoichiometric flame, the flame color became invisible at 15 mm above the burner head. However, reasonable intensities of sodium ion signals still could be collected at 20.5 mm above the burner head. The vertical temperature profile measured with sodium ions is plotted in Figure 7-5.

The results of the DLI temperature measurements of the stoichiometric hydrogen-oxygen-argon flame with strontium

**Table 7-4. Non-stoichiometric H₂-O₂-Ar Flame Temperature
Profile Measurements with Various Ions**

Ion	Height (mm)	Mobility	Diffusion	Flame
		Coefficient (cm ² .v ⁻¹ .s ⁻¹)	Coefficient (cm ² .s ⁻¹)	Temperature (K)
Na ⁺	7.5	28.84	3.47	1396
Na ⁺	7.5	30.16	3.54	1360
Ca ⁺	7.5	19.36	2.41	1450
Na ⁺	8.0	26.00	3.75	1674
Na ⁺	8.0	25.27	3.71	1704
Li ⁺	8.5	29.02	4.68	1870
Na ⁺	9.0	25.23	4.12	1895
Ca ⁺	9.0	16.13	2.75	1980
Na ⁺	10.0	24.33	4.12	1967
Na ⁺	10.0	24.07	4.07	1962
Li ⁺	10.5	28.15	4.81	1985
Na ⁺	10.5	23.77	4.07	1987
Na ⁺	11.0	24.09	4.02	1936
Ca ⁺	11.0	17.01	2.64	1870
Na ⁺	11.5	22.93	3.89	1969
Na ⁺	12.0	22.29	3.77	1963
Li ⁺	12.0	28.43	4.79	1957
Na ⁺	12.5	21.16	3.52	1931
Na ⁺	13.0	22.58	3.44	1768
Li ⁺	13.5	31.06	4.60	1793
Li ⁺	15.5	35.13	3.94	1304
Li ⁺	17.5	42.15	2.91	802

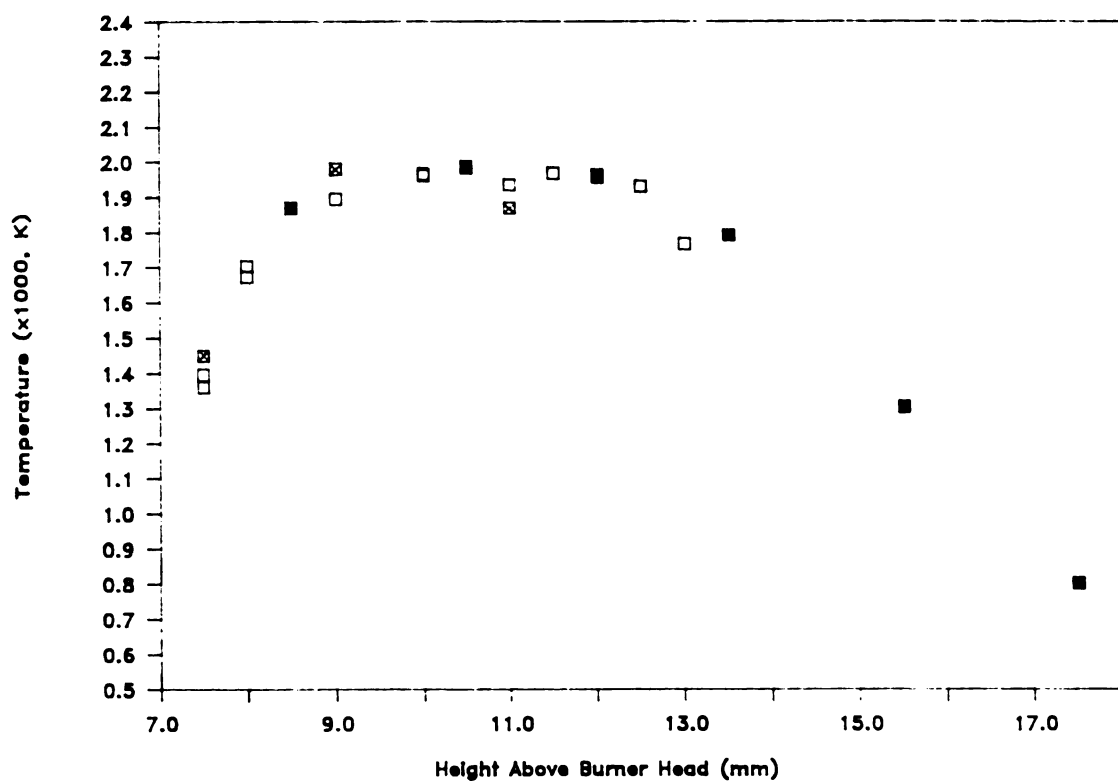


Figure 7-4. Non-stoichiometric H_2-O_2-Ar flame temperature profile measurements with various ions at different heights above the burner head. (\square : sodium; \blacksquare : lithium; \boxtimes : calcium).

**Table 7-5. Stoichiometric H₂-O₂-Ar Flame Temperature
Profile Measurements with Sodium Ions**

Height (mm)	Mobility	Diffusion	Temperature (K)
	Coefficient (cm ² .v ⁻¹ .s ⁻¹)	Coefficient (cm ² .s ⁻¹)	
5.5	27.51	4.44	1873
8.5	30.20	5.57	2140
11.5	30.48	5.52	2102
14.5	30.57	5.61	2130
16.5	30.35	5.57	2130
17.5	28.70	5.49	2220
20.5	29.53	5.88	2311

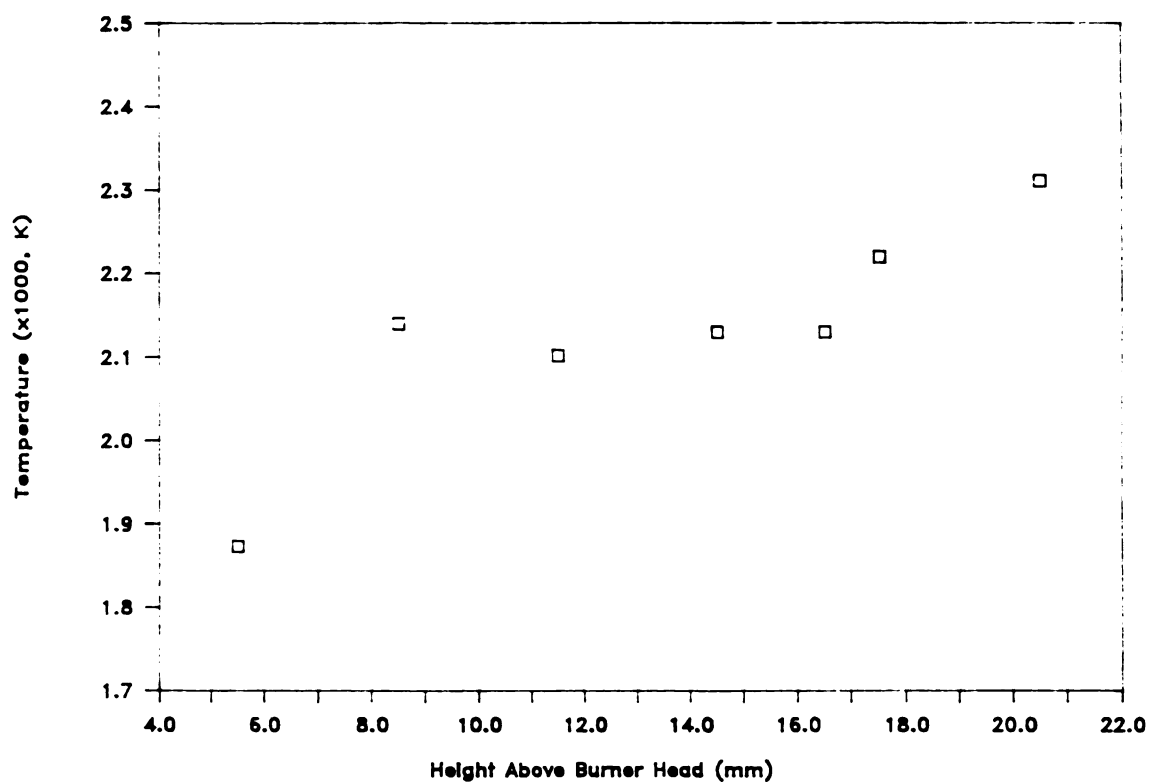


Figure 7-5. Stoichiometric $\text{H}_2\text{-O}_2\text{-Ar}$ flame temperature profile measurements with sodium ions at different heights above the burner head.

ions are given in Table 7-6. Reasonable intensities of strontium ion signals could only be collected up to 14.5 mm above the burner head. The vertical temperature profile measured with strontium ions is plotted in Figure 7-6.

The results of the DLI temperature measurements of the stoichiometric hydrogen-oxygen-argon flame with both sodium and strontium ions are given in Table 7-7. The vertical temperature profile measured with both metal ions is plotted in Figure 7-7. Figure 7-7 shows that the DLI temperature measurements with both metal ions at various heights in the flame are reasonably consistent with each other. However, at the same point in the flame, the flame temperatures measured with different ions may differ as much as 40°C (Table 7-7, 14.5 mm above the burner head), and the results from repeated measurements with the strontium ion may differ as much as 38°C (Table 7-7, 6.5 mm above the burner head). This difference may be, again, attributed to the low ion mobility of strontium ions in the flame.

D. DISCUSSION

As shown in Figure 7-4 and 7-7, it is evident that the flame temperatures measured with heavy metal ions (i.e., calcium and strontium) are not as reliable as those from lighter metal ions. For the fuel-rich, non-stoichiometric

**Table 7-6. Stoichiometric H₂-O₂-Ar Flame Temperature
Profile Measurements with Strontium Ions**

Height (mm)	Mobility	Diffusion	Temperature (K)
	Coefficient (cm ² ·v ⁻¹ ·s ⁻¹)	Coefficient (cm ² ·s ⁻¹)	
6.5	17.29	2.67	1792
6.5	17.13	2.59	1754
7.5	15.45	2.51	1885
10.0	14.53	2.55	2036
12.5	14.41	2.71	2183
14.5	13.32	2.49	2170

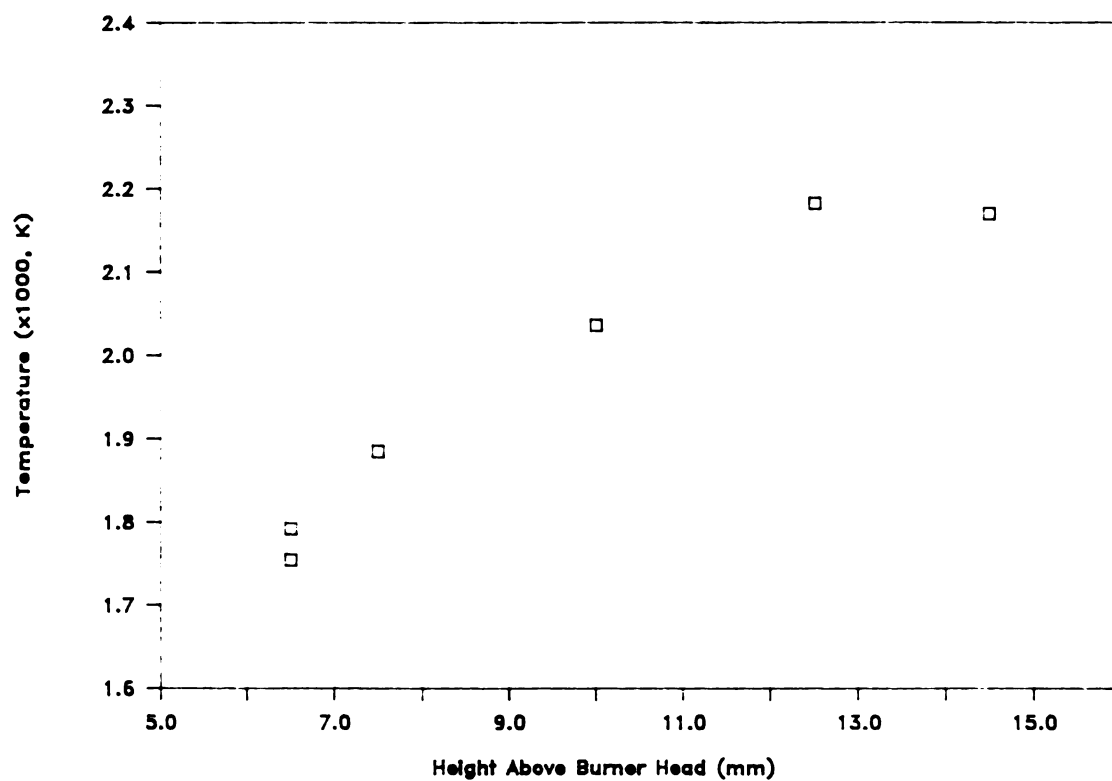


Figure 7-6. Stoichiometric H_2-O_2-Ar flame temperature profile measurements with strontium ions at different heights above the burner head.

**Table 7-7. Stoichiometric H₂-O₂-Ar Flame Temperature
Profile Measurements with Various Ions**

Ion	Height (mm)	Mobility	Diffusion	Flame
		Coefficient (cm ² .v ⁻¹ .s ⁻¹)	Coefficient (cm ² .s ⁻¹)	Temperature (K)
Na ⁺	5.5	27.51	4.44	1873
Sr ⁺	6.5	17.29	2.67	1792
Sr ⁺	6.5	17.13	2.59	1754
Sr ⁺	7.5	15.45	2.51	1885
Na ⁺	8.5	30.20	5.57	2140
Sr ⁺	10.0	14.53	2.55	2036
Na ⁺	11.5	30.48	5.52	2102
Sr ⁺	12.5	14.41	2.71	2183
Na ⁺	14.5	30.57	5.61	2130
Sr ⁺	14.5	13.32	2.49	2170
Na ⁺	16.5	30.35	5.57	2130
Na ⁺	17.5	28.70	5.49	2220
Na ⁺	20.5	29.53	5.88	2311

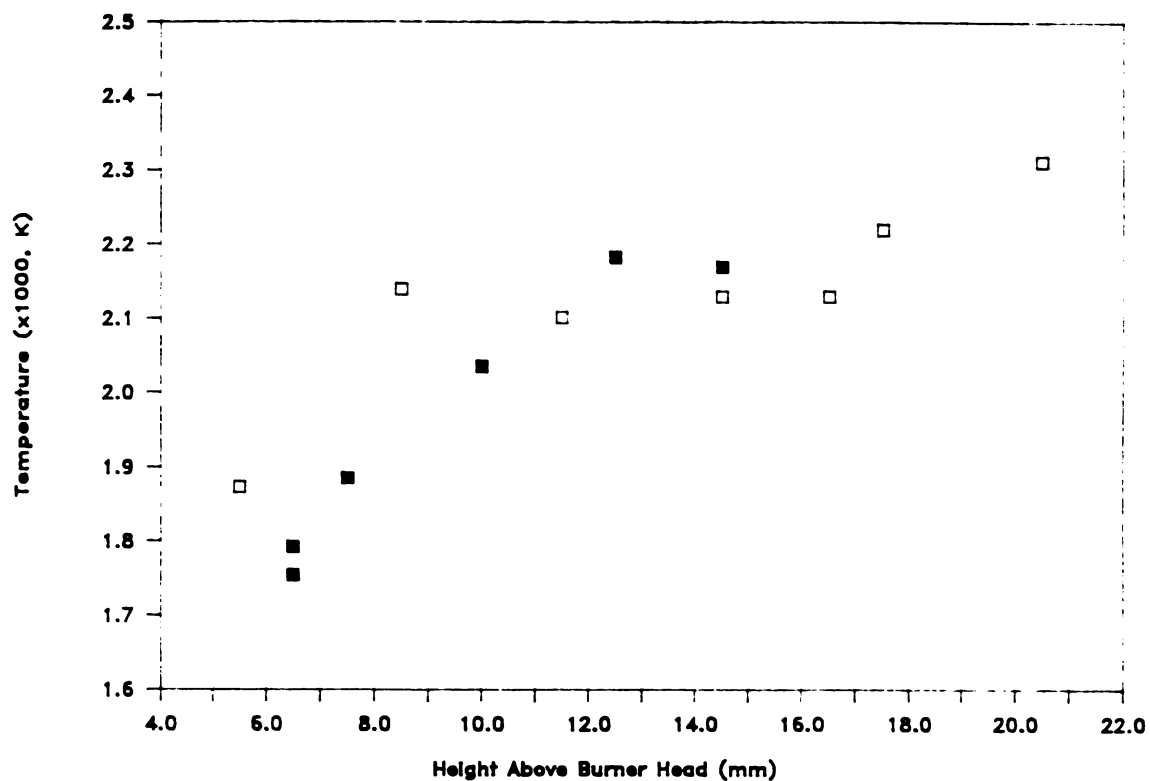


Figure 7-7. Stoichiometric H_2-O_2-Ar flame temperature profile measurements with various ions at different heights above the burner head.
(□: sodium; ■: Strontium)

hydrogen-oxygen-argon flame, in the region about 9 to 12 mm above the burner head the temperature measurements with lithium and calcium are only reasonably consistent with one another. The temperature measured with calcium at 11.0 mm above the burner head is significantly lower than the surrounding measurements. Also, the flame temperature with calcium ion measured at 9.0 mm above the burner head seems too high. For the stoichiometric hydrogen-oxygen-argon flame, the flame temperatures measured with strontium ions in the region about 7 to 11 mm above the burner head appears to be too low in comparison with those measured with sodium ions. However, considering the maximum 5 percent difference among the flame temperature measurements with various ions, we see that DLI can provide very reasonable and consistent temperature data in laminar-flow flames.

A comparison of the mobility and diffusion coefficients of sodium ions from this study with previously reported values (6-9) is given in Table 7-8. The range of both diffusion and mobility coefficients measured at various heights in two different hydrogen-oxygen-argon flame compositions are consistent with the literature values.

A comparison of the mobility and diffusion coefficients of lithium ions from this study with the reported literature values (1,7,8,10) is given in Table 7-9. The range of the mobility coefficients measured at various heights in the

Table 7-8. A Comparison of Diffusion and Mobility
Coefficients of Sodium in Various Flames

Author	Mobility Coefficient ($\text{cm}^2 \cdot \text{v}^{-1} \cdot \text{s}^{-1}$)	Diffusion Coefficient ($\text{cm}^2 \cdot \text{s}^{-1}$)	Reference
Ginsel ^(a)	---	3.2	(6)
Wu ^(b)	21.2 - 30.2	3.4 - 4.1	Table 7-1
Smyth ^(c)	25.7	---	(7)
Langevin ^(c)	25.8	---	(7)
Lin ^(d)	30.2	5.65	(1)
Wu ^(e)	27.5 - 30.6	4.4 - 5.9	Table 7-5
Ashton ^(f)	---	5.5 - 13	(8)
Snelleman ^(g)	---	9.9	(9)

(a) $\text{H}_2\text{-O}_2\text{-Ar}$ flame, 2100 K; (b) $\text{H}_2\text{-O}_2\text{-Ar}$ flame, 1360-1987 K; (c) $\text{C}_2\text{H}_2\text{-Air}$ flame, 2350 K; (d) $\text{H}_2\text{-O}_2\text{-Ar}$ flame, 2171 K; (e) $\text{H}_2\text{-O}_2\text{-Ar}$ flame, 1873-2311 K; (f) $\text{H}_2\text{-O}_2\text{-N}_2$ flame, 1920-2520 K; (g) $\text{C}_2\text{H}_2\text{-O}_2\text{-N}_2$ flame, 2440 K.

Table 7-9. A Comparison of Diffusion and Mobility
Coefficients of Lithium in Various Flames

Author	Mobility	Diffusion	Reference
	Coefficient ($\text{cm}^2 \cdot \text{v}^{-1} \cdot \text{s}^{-1}$)	Coefficient ($\text{cm}^2 \cdot \text{s}^{-1}$)	
Wu ^(a)	28.2 - 42.2	2.9 - 4.8	Table 7-2
Smyth ^(b)	32.4	---	(7)
Lin ^(c)	38.6	6.7	(1)
Langevin ^(b)	38.7	---	(7)
Ashton ^(d)	---	8.5	(8)
Ashton ^(d)	---	6.8 - 11.8	(10)

(a) $\text{H}_2\text{-O}_2\text{-Ar}$ flame, 801-1983 K; (b) $\text{C}_2\text{H}_2\text{-Air}$ flame, 2350 K; (c) $\text{H}_2\text{-O}_2\text{-Ar}$ flame, 2014 K; (c) $\text{H}_2\text{-O}_2\text{-N}_2$ flame, 1920-2520 K.

fuel-rich, non-stoichiometric hydrogen-oxygen-argon flame is consistent with the literature values. However, the diffusion coefficients measured in this study appear to be lower than all the reported values. This result may possibly be attributed to the low flame temperature environment, which favors the formation of LiOH in the flame used in this study.

A comparison of the mobility and diffusion coefficients of calcium ions from this study with the reported literature values (7,11) is given in Table 7-10. The range of the mobility coefficients measured at various heights in the fuel-rich, non-stoichiometric hydrogen-oxygen-argon flame are consistent with the literature values. However, the diffusion coefficients measured in this study appear to be lower than all the reported values. Again, this result may be attributable to the low flame temperature environment, which favors the formation of CaOH in the flame.

A comparison of the mobility and diffusion coefficients of strontium ions from this study with the reported literature values (7,11) is given in Table 7-11. The ranges of both mobility and diffusion coefficients measured at various heights in the stoichiometric hydrogen-oxygen-argon flame appear to be lower than the literature values. This result may also be attributed to the low flame temperature environment, which favors the formation of SrOH in the

Table 7-10. A Comparison of Diffusion and Mobility
Coefficients of Calcium in Various Flames

Author	Mobility Coefficient ($\text{cm}^2 \cdot \text{v}^{-1} \cdot \text{s}^{-1}$)	Diffusion Coefficient ($\text{cm}^2 \cdot \text{s}^{-1}$)	Reference
Smyth ^(a)	16.1	---	(7)
Wu ^(b)	17.0 - 19.4	2.4 - 2.7	Table 7-3
Ashton ^(c)	---	3.1 - 5.2	(11)
Langevin ^(a)	22.6	---	(7)

(a) C_2H_2 -Air flame, 2350 K; (b) H_2 - O_2 -Ar flame, 1445-1978 K; (c) H_2 - O_2 - N_2 flame, 1920-2520 K.

Table 7-11. A Comparison of Diffusion and Mobility
Coefficients of Strontium in Various Flames

Author	Mobility Coefficient ($\text{cm}^2 \cdot \text{v}^{-1} \cdot \text{s}^{-1}$)	Diffusion Coefficient ($\text{cm}^2 \cdot \text{s}^{-1}$)	Reference
Wu ^(a)	13.3 - 17.3	2.5 - 2.7	Table 7-6
Ashton ^(b)	---	2.7 - 4.8	(11)
Smyth ^(c)	18.0	---	(7)
Langevin ^(d)	19.9	---	(7)

(a) $\text{H}_2\text{-O}_2\text{-Ar}$ flame, 1754-2183 K; (b) $\text{H}_2\text{-O}_2\text{-N}_2$ flame, 1920-2520 K; (c) $\text{C}_2\text{H}_2\text{-Air}$ flame, 2350 K; (d) CO-O_2 flame, temperature not available.

flame.

A comparison of the flame temperatures obtained in this study with literature values (1,12-14) measured at similar hydrogen-oxygen-argon flame compositions is given in Table 7-12. The temperatures measured with various metal ions at a height of about 10.0 mm above the burner head are chosen for comparison. All the temperatures measured in this study are self-consistent among the different probe ions chosen, although they appear to be slightly lower than the reported values. However, considering the maximum 5 percent difference among the flame temperature measurements with various ions in this study, our results are in reasonable agreement with the literature values.

E. CONCLUSIONS

Earlier in this dissertation it was shown that the Fokker-Planck model can be used to treat time-resolved DLI signals, hence reasonably consistent flame temperatures should be calculatable. The experimental study reported in this chapter confirms the applicability of the Fokker-Planck model in flame temperature measurements. In addition, all data from DLI temperature measurements show that diffusion coefficient increases with increasing temperature while

Table 7-12. A Comparison of H₂-O₂-Ar Flame Temperatures

Flame Composition (Liter·min ⁻¹)			Temperature (K)	Method Employed	Reference
H ₂	O ₂	Ar			
1.6	0.5	3.2	1967 ^(a)	DLI Na ⁺	Table 7-1
1.6	0.5	3.2	1978 ^(b)	DLI Ca ⁺	Table 7-3
1.6	0.5	3.2	1983 ^(c)	DLI Li ⁺	Table 7-2
1.00	0.65	3.45	1990	Line Reversal	(12)
1.5	0.75	4.5	2000	Line Reversal	(13)
1.0	0.5	3.2	2014	DLI Li ⁺	(1)
1.0	0.5	3.2	2036 ^(d)	DLI Sr ⁺	Table 7-6
1.00	0.5	3.45	2070	Line Reversal	(12)
1.0	0.5	3.2	2102 ^(e)	DLI Na ⁺	Table 7-5
2.0	1.0	4.0	2136	Line Reversal	(13)
1.0	0.5	3.2	2171	DLI Na ⁺	(1)
1.30	0.65	3.45	2210	Line Reversal	(12)

(a) 10.0 mm; (b) 9.0 mm; (c) 10.5 mm; (d) 10.0 mm;

(e) 11.5 mm above the burner head.

mobility coefficient increases with decreasing temperature. The smooth trends of both diffusion and mobility coefficients versus flame temperature are in agreement with the theoretical predications (2,14). Although the temperatures reported in this study are somewhat lower than the literature values, they are very consistent with one another, and they may in fact be the most accurate measurements to date.

This study also suggests that the exponential function has over-compensated the thickness of the laser focal area which would make the extrapolations of the diffusion coefficients smaller than the true values. It is also worth pointing out that the standard deviations of the mobility coefficients measured in our laboratory are almost always much smaller than those reported by others (1,7,14). However, the calculated diffusion coefficient usually contributes the major portion of the standard deviation of each temperature calculation. A better model, which could explain the relationship between the calculated diffusion coefficient and bias voltage, is desired in order to make the DLI temperature measurements more accurate.

CHAPTER VII

REFERENCES

1. K.C. Lin, P.M. Hunt, and S.R. Crouch, Chem. Phys. Lett. 90, 111 (1982).
2. E.W. McDaniel and E.A. Mason, "The Mobility and Diffusion of Ions in Gases" (Wiley, New York, 1973).
3. C.A. van Dijk, F.M. Curran, K.C. Lin and S.R. Crouch, Anal. Chem. 53, 1275 (1981).
4. K.C. Lin, Ph.D. Thesis (Michigan State University, 1982).
5. F.M. Curran, Ph.D. Thesis (Michigan State University, 1983).
6. L.A. Ginsel, Thesis, Utrecht (1933).
7. W.G. Mallard and K.C. Smyth, Combust. Flame 44, 61 (1982).
8. A.F. Ashton and A.N. Hayhurst, J. Chem. Soc., Faraday Trans. I 66, 833 (1970).
9. W. Snelleman, Thesis, Utrecht (1965).
10. A.F. Ashton and A.N. Hayhurst, J. Chem. Soc. Faraday Trans. I 69, 652 (1973).
11. A.F. Ashton and A.N. Hayhurst, J. Chem. Soc. Faraday Trans. I 72, 208 (1976).
12. H.P. Hooymayers and C.Th.J. Alkemade, J. Quantum Spectry. Radiat. Transfer 6, 847 (1966).
13. P.L. Lijnse and R.J. Elsenarr, J. Quantum Spectry. Radiat. Transfer 12, 1115 (1972).

14. C.Th.J. Alkemade, Tj. Hollander, W. Snellsman, and P.J.Th. Zeegers, "Metal Vapours in Flames" (Pergamon Press, Oxford, 1982).

CHAPTER VIII

CONCLUSIONS AND FUTURE PROSPECTS

A. REVIEW AND CONCLUSIONS

A-1 Dual Laser Ionization Signals

In this study, we have demonstrated that there are two temporal components in the dual laser ionization (DLI) signal. In a DLI measurement, usually a short and strong electron peak will be detected first, followed by a longer and weaker ion peak some microseconds later. Experimental results were presented to confirm this conclusion. Also, the temporal behavior of DLI signals taken with different bias voltages at various probe positions was discussed. It has been shown that both the bias voltage and the probe position can strongly affect the shape of the DLI signal. The general factors that influence the shape of DLI signals were given in Chapter III.

Theoretical treatment and experimental results showed that under nearly all conditions, the electron signal decays

exponentially versus time. Upon inspection of the shapes of the ion signals, we found that the interaction between ionic mobility and ion diffusion cannot be ignored in most circumstances. Hence the necessity of adopting a sophisticated model, such as the Fokker-Planck equation, was suggested.

Regarding the flame environment, we have also found that in most cases the flame is sufficiently clean to allow the electric field between the probes to reach the so-called "super-saturation condition"; thus the electric field can be viewed as constant along the moving ion's path. In accordance with Lawton's model (1), several approximations for the super-saturation condition were derived and interpreted. All assumptions made were then confirmed by the curve fitting method introduced in Chapter V.

It was also proposed that the mutual repulsion among ions should not be ignored if the applied bias voltages were high. A simulation program was constructed with some newly developed algorithms to demonstrate the importance of the mutual repulsion effect. Additional efforts must be devoted in the future to make the simulation program more flexible and effective, and to apply it to more realistic model systems.

A systematic method based on the Fokker-Planck formalism was developed to extract both ion diffusion coefficients and ionic mobility coefficients from the DLI signals. The flame temperature can thus be calculated with reasonable accuracy by applying the well-known Einstein equation. Flame temperature profiles measured with different metal ions were presented in Chapter VII.

A-2 The Fokker-Planck Equation

The applicability of the Fokker-Planck equation to the DLI technique was confirmed. The theoretical treatment in Chapter IV has shown that a general, one-dimensional Fokker-Planck equation can model the basic characteristics of the DLI signal collection process. Several Fokker-Planck equations with various drift functions were solved analytically. All drift functions were designed in accordance with the different shapes of electric field between the probes; interpretations of the various drift functions were also given.

A modified conditional propagator with units of s^{-1} was derived. In order to handle the indefinite size of the laser focal point, the new propagator was then convoluted with an exponential decay function to form an exponentially modified conditional propagator. Curve fitting results

showed that this new formulation can be used to model the DLI signal collection process effectively.

In this study, the Fokker-Planck formalism was applied widely and successful results were obtained. Certain evidence suggests that the one-dimensional Fokker-Planck equations may not be sophisticated and flexible enough to treat the DLI process thoroughly, there is, however, no doubt that this approach is fundamentally correct and effective.

B. FUTURE PROSPECTS

B-1 DLI Techniques

In this study, we have examined Lawton's model carefully. For each type of electric field proposed by Lawton, a corresponding Fokker-Planck equation with the appropriate drift function was constructed. These equations were either already solved analytically or were susceptible to solution by the numerical method described in Chapter IV. To take advantage of these new mathematical models, a few new projects can be pursued.

As mentioned in Chapter III, an understanding of the time-resolved DLI signals can help scientists determine the

most effective aperture delay and aperture duration, in order to obtain maximum ion signal and at the same time block out most of the noise due to the sample matrix. This approach is definitely worth trying. In addition, since the ion peak can be modelled by the Fokker-Planck equation rather precisely, as demonstrated in Chapter V, it is possible to use software to subtract the electron signal from the total DLI signal. This approach should make the DLI technique more sensitive if all the experimental variables can be optimized.

In order to gain a more thorough understanding of the DLI ion collection process, additional experiments should be performed, such as adding more easily ionized elements to the analyte solution to remove the super-saturation condition. Observation of the behavior of the DLI time-resolved signals under such conditions can help confirm the applicability of the Fokker-Planck formalism.

A better understanding of the dependence of the bias voltage and diffusion coefficient is also worth pursuing. An improved version of the simulation program which can also deal with the interaction between electrons and ions may help explain the dependence more effectively.

B-2 Fokker-Planck Formalism

In recent years the investigation of chromatographic peak profiles has become increasingly important, especially from the viewpoint of understanding and characterizing the chromatographic process, and ultimately optimizing resolution (2). A chromatographic column is normally assumed to act as a Gaussian operator, broadening a delta-function input into a Gaussian distribution as it passes through the column. However, ideal Gaussian profiles are rarely, if ever, observed since a number of intracolumn and extracolumn processes may lead to peak asymmetry (3). Thus, in practice peaks are usually skewed. The exponentially modified Gaussian (EMG) peak shape model is widely accepted as a more accurate model for real chromatographic peaks than a simple Gaussian function. The development, characterization, and the theoretical and experimental justification of the EMG model have been thoroughly reviewed (4). Unfortunately, nearly every chromatographer realizes that the EMG model does not have a strong theoretical background. It is just an empirical tool that works well. Other functions besides the EMG have been introduced to characterize chromatographic peak profiles (5); however, only limited success has been obtained.

Theoretically, the chromatographic processes can be modelled in detail by solving the Fokker-Planck equation with suitable drift functions. In our laboratory, we have found that chromatographic peak profiles can be skewed even when only the Gaussian operator is applied. This discovery is strong evidence that the EMG actually over compensates the skewing effect from the chromatographic processes. Also, HPLC data taken by a microcomputer has been fit by both the EMG and the exponentially modified Fokker-Planck equation. Results show that the latter can supply better parameter sets with reasonable physical interpretation. Moreover, the Fokker-Planck equation can be decomposed into a form that will be easier to use in computer programming. More interestingly, clues have been found that EMG can be proven as one of the solutions of the Fokker-Planck equation with an alternative drift function. Examination of the drift function that induces the EMG may then show that the EMG is no more than a particular solution of the Fokker-Planck equation that oversimplifies the true chromatographic process.

The Fokker-Planck formalism can be applied also to the time-of-flight mass spectroscopy (TOF-MS), which is one of the major categories of mass spectrometry. In this technique, the spread of electron beams caused by space-charge forces is the chief limiting factor. On account of space charge, repulsive forces exist so that beams, parallel

at their origin, become divergent, or beams originally convergent fail to converge (6). In the best case, the resolution of the spectra is still relatively lower than that of other mass spectroscopic techniques.

Since the TOF-MS has a delta-function-like ion source, a Fokker-Planck equation with a suitable drift function (7) can serve as an ideal model to describe the ion motion. The effort can be initiated with the simulation of the ion-moving process (8) in a TOF mass spectrometer, by modifying an existing computer algorithm which has already been developed for simulating the dual laser ionization (DLI) process. The results can be used to construct a new algorithm which can deconvolute the peaks from the TOF mass spectrum and, hence, the resolution can be increased (9).

CHAPTER VIII

REFERENCES

1. J. Lawton and F.J. Weinberg, "Electrical Aspects of Combustion" (Clarendon Press, Oxford, 1969)
2. J.J. Kirkland, W.W. Yau, H.J. Stoklosa, and C.H. Dilks, Jr., J. Chromatog. Sci. 15, 303 (1977).
3. C.H. Lochmuller and M. Sumner, J. Chromatog. Sci. 18, 159 (1980).
4. V. Maynard and E. Grushka, Anal. Chem. 44, 1427 (1972); E. Grushka, Anal. Chem. 44, 1733 (1972); R.E. Pauls and L.B. Rogers, Anal. Chem. 49, 625 (1977); Sep. Sci. Technol. 12, 395 (1977).
5. S.N. Chesler and S.P. Cram, Anal. Chem. 45, 1354 (1973) and references therein.
6. E.E. Watson, Phil. Mag. 3, 849 (1927); E.G. Linder and K.G. Hernqvist, J. Appl. Phys. 21, 1088 (1950); H.W. Ioup, G.E. Ioup, G.H. Rayborn, Jr., G.M. Wood, Jr., and B.T. Upchurch, Inst. J. Mass Spectro. Ion Proc. 55, 93 (1983).
7. L.G.H. Huxley and R.W. Crompton, "The diffusion and Drift of Electrons in Gases", John Wiley and Sons, New York (1974).
8. R.H. Plumlee, Rev. Sci. Instru. 28, 830 (1957).
9. R.A. Caruana, R.B. Searle, T. Heller and S.I. Schupack, Anal. Chem. 58, 1162 (1986).

APPENDIX A

FOKKER-PLANCK EQUATION NUMERICAL SOLVER

I. FORTRAN LISTING

```

      PROGRAM FPLI
C =====
C
C      YEN-YUAN JAMES WU                                JUL-8-1985
C      DEPARTMENT OF CHEMISTRY
C      MICHIGAN STATE UNIVERSITY
C      EAST LANSING, MICHIGAN 48824
C
C =====
C
C      THIS THE MAIN DRIVER OF PROGRAM FPLII
C
C      THE FOLLOWING DOCUMENTATION SUMMARIZES ALL THE INFORMATION OF THE
C      COMMON BLOCKS.
C
C      DEFAULT REAL*8 FOR ALL VARIABLES UNLESS OTHERWISE SPECIFIED.
C
C =====
C      CHARACTER*10 FLPV
C      INTEGER NFLPV
C      INTEGER PNSTRT, PNPNT, PNNNN
C      LOGICAL FLAG1, FLAG2
C
C -----
C      COMMON BLOCKS FOR PARAMETER INPUT
C -----
C      COMMON /FILNAM/ FLPV
C      COMMON /FILLN/ NFLPV
C      COMMON /PCA/    PCEC, PCAMU, PCVP, PCEMS, PCAJK5
C      COMMON /PCB/    TOLDVR, TOLEQ1, TOLEQ3
C      COMMON /PVA/    PVRC, PVBV, PVVA, PVMOBF, PVAJK5
C      COMMON /PNB/    PNSTRT, PNPNT, PNNNN
C      COMMON /PVB/    PVTI, PVXW, PVXC, PVBJK4, PVBJK5
C      COMMON /PV1/    PVION1, PVDFU1, PVMOB1, PV1JK4
C      COMMON /PV2/    PVION2, PVDFU2, PVMOB2, PV2JK4
```

```

C      COMMON /PVE/      PVDFUE, PVMOBE, PVEJK3
C -----
C COMMON BLOCKS FOR MAIN DRIVER
C -----
C      COMMON /MDRC1/    MDRC1A, MDRC1B
C      COMMON /MDRC1/    FLAG1,  FLAG2
C      COMMON /MDRC2/    MDRC2A
C      COMMON /MDRC2/    PVTI
C -----
C COMMON BLOCKS FOR INDIVIDUAL SUBROUTINE
C -----
* TXT1
C      COMMON /TXT1/     TXT1A,  TXT1B
C      COMMON /TXT1/     DSXS,   DSXA
* EQAI1
C      COMMON /AI1C/     AI1CA,  AI1CB,  AI1CC,  AI1CD
C      COMMON /AI1C/     TOLDVR, TOLY1,  Y1FNL,  GUESS
C      COMMON /AI1M/     AI1MA,  AI1MB,  AI1MC,  AI1MD
C      COMMON /AI1M/     TIME,    XAI,    Y1AI,   Y2AI
* EQAI2
C      COMMON /AI2C/     AI2CA
C      COMMON /AI2C/     TOLDVR
C      COMMON /AI2M/     AI2MA,  AI2MB,  AI2MC,  AI2MD,  AI2ME
C      COMMON /AI2M/     TIME,    XAI,    Y1AI,   Y2AI,   Y3AI
* EQAI3
C      COMMON /AI3C/     AI3CA,  AI3CB,  AI3CC,  AI3CD
C      COMMON /AI3C/     MASS,    TOLDVR, ADELTA, TOLSLP
C      COMMON /AI3M/     AI3MA,  AI3MB,  AI3MC,  AI3MD
C      COMMON /AI3M/     TIME,    Y1AI,   Y2AI,   YRATIO
* FXAI1
C      COMMON /AIF1/     AIF1A,  AIF1B,  AIF1C
C      COMMON /AIF1/     MASS,    HEQ21,  HEQ22
* FXAI2
C      COMMON /AIF2/     AIF2A,  AIF2B,  AIF2C,  AIF2D,  AIF2E,  AIF2F
C      COMMON /AIF2/     MASS,    ADELTA, HEQ21,  HEQ22,  HEQ31,  HEQ32
* EQAE1
C      COMMON /AE1C/     AE1CA,  AE1CB,  AE1CC,  AE1CD,  AE1CE
C      COMMON /AE1C/     TOLDVR, TOLY1,  Y1FNL,  GUESS,  DSXSAE
C      COMMON /AE1M/     AE1MA,  AE1MB,  AE1MC,  AE1MD,  AE1ME
C      COMMON /AE1M/     TIME,    XAE,    Y1AE,   Y2AE,   XENDMD
* EQAE2
C      COMMON /AE2C/     AE2CA
C      COMMON /AE2C/     TOLDVR
C      COMMON /AE2M/     AE2MA,  AE2MB,  AE2MC,  AE2MD,  AE2ME
C      COMMON /AE2M/     TIME,    XAE,    Y1AE,   Y2AE,   Y3AE
* FXAE1
C      COMMON /AEF1/     AEF1A,  AEF1B,  AEF1C,  AEF1D
C      COMMON /AEF1/     DSXSAE, MASS,    HEQ21,  HEQ22
* FXAE2
C      COMMON /AEF2/     AEF2A,  AEF2B,  AEF2C,  AEF2D,  AEF2E,  AEF2F,
C      +                AEF2G,  AEF2H
C      COMMON /AEF2/     DSXSAE, MASS,    ADELTA, HEQ21,  HEQ22,  HEQ31,
C      +                HEQ32,  HEQ33

```

```

C
C =====
C
      IMPLICIT REAL*8 (A-H, O-Z)
C
      CHARACTER*10 FLPV
C
      INTEGER NFLPV
      INTEGER PNSTRT, PNPNT, PNNNN
      INTEGER NCOUNT
C
      REAL*8 PVTI
      REAL*8 AI1MA, AI1MB, AI1MC, AI1MD
      REAL*8 AI2MA, AI2MB, AI2MC, AI2MD, AI2ME
      REAL*8 AI3MA, AI3MB, AI3MC, AI3MD
      REAL*8 TIME
      REAL*8 XAI, Y1AI, Y2AI, Y3AI, RRAI
C
      COMMON /FILNAM/ FLPV
      COMMON /FILLN/ NFLPV
      COMMON /PNB/ PNSTRT, PNPNT, PNNNN
      COMMON /MDRC2/ PVTI
      COMMON /AI1M/ AI1MA, AI1MB, AI1MC, AI1MD
      COMMON /AI2M/ AI2MA, AI2MB, AI2MC, AI2MD, AI2ME
      COMMON /AI3M/ AI3MA, AI3MB, AI3MC, AI3MD
      COMMON /AI4M/ AI4MA, AI4MB, AI4MC, AI4MD, AI4ME
C
***** SECTION 1 *****
C
      CALL GTCML
      CALL PAR
      CALL CNST
      CALL TXT1
      CALL TXT2
      CALL OPEN7
C
      DO 800, NCOUNT = PNSTRT, PNSTRT+PNPNT-1
        TIME = FLOAT(NCOUNT) * PVTI
C
        AI1MA = TIME
        CALL EQAI1
        XAI = AI1MB
        Y1AI = AI1MC
        Y2AI = AI1MD
C
        AI2MA = TIME
        AI2MB = 0.0
        AI2MC = 0.0
        AI2MD = Y2AI
        AI2ME = 0.0
        CALL EQAI2
        Y3AI = AI2ME
C

```

[illegible]

SUBROUTINE PAR

```

C
C =====
C
C PCA(1) = PCEC      ; ELEMENTARY CHARGE
C PCA(2) = PCAMU     ; ATOMIC MASS UNIT
C PCA(3) = PCVP      ; VACUUM PERMITTIVITY
C PCA(4) = PCEMS     ; REST MASS OF ELECTRONS
C PCA(5) =           ;
C
C PCB(1) = TOLDVR     ; TOLERANCE OF DVERK
C PCB(2) = TOLEQ1     ; TOLERANCE OF EQXX1 FOR MOMENTUM SHOOTING
C PCB(3) = TOLEQ3     ; TOLERANCE OF EQXX3 FOR RATIO CALCULATION
C
C PVA(1) = PVRC       ; VOLUME IONIZATION RATE
C PVA(2) = PVBV       ; BURNING VELOCITY
C PVA(3) = PVVA       ; VOLTAGE APPLIED ACROSS ELECTRODES
C PVA(4) = PVMOBF     ; DIFFU COEF BKGRND ION
C PVA(5) =           ;
C
C PNB(1) = PNSTRT     ; STARTING POINT
C PNB(2) = PNPNT      ; NUMBER OF POINTS
C PNB(3) =           ;
C
C PVB(1) = PVTI       ; TIME INTERVAL BETWEEN EACH STEP
C PVB(2) = PVXW       ; DISTANCE BETWEEN PROBES
C PVB(3) = PVXC       ; DISTANCE BETWEEN LASER SPOT AND CATHODE
C PVB(4) =           ;
C PVB(5) =           ;
C
C PV1(1) = PVION1     ; ATOMIC MASS OF ION 1
C PV1(2) = PVDFU1     ; DIFUSSION COEFFICIENT OF ION 1
C PV1(3) = PVMOB1     ; MOBILITY COEFFICIENT OF ION 1
C PV1(4) =           ;
C
C PV2(1) = PVION2     ; ATOMIC MASS OF ION 2
C PV2(2) = PVDFU2     ; DIFUSSION COEFFICIENT OF ION 2
C PV2(3) = PVMOB2     ; MOBILITY COEFFICIENT OF ION 2
C PV2(4) =           ;
C
C PVE(1) = PVDFU2     ; DIFUSSION COEFFICIENT OF ELECTRON
C PVE(2) = PVMOB2     ; MOBILITY COEFFICIENT OF ELECTRON
C PVE(3) =           ;
C
C =====
C
C      IMPLICIT REAL*8 (A-H, O-Z)
C
C      CHARACTER*10 FLPV
C      CHARACTER*40 FLIN1, FLIN2
C
C      INTEGER LUNIN1, LUNIN2
C      INTEGER NFPV

```

```

      INTEGER PNB(3)
      INTEGER PNSTRT, PNPNT, PNNNN
C
      REAL*8 PCA(5), PCB(3)
      REAL*8 PVA(5), PVB(5), PV1(4), PV2(4), PVE(3)
      REAL*8 PCEC, PCAMU, PCVP, PCEMS, PCAJK5
      REAL*8 TOLDVR, TOLEQ1, TOLEQ3
      REAL*8 PVRC, PVBV, PVVA, PVMOBF, PVAJK5
      REAL*8 PVTI, PVXW, PVXC, PVBJK4, PVBJK5
      REAL*8 PVION1, PVDFU1, PVMOB1, PV1JK4
      REAL*8 PVION2, PVDFU2, PVMOB2, PV2JK4
      REAL*8 PVDFUE, PVMOBE, PVEJK3
C
      COMMON /FILNAM/ FLPV
      COMMON /FILLN/ NFLPV
      COMMON /PCA/ PCEC, PCAMU, PCVP, PCEMS, PCAJK5
      COMMON /PCB/ TOLDVR, TOLEQ1, TOLEQ3
      COMMON /PVA/ PVRC, PVBV, PVVA, PVMOBF, PVAJK5
      COMMON /PNB/ PNSTRT, PNPNT, PNNNN
      COMMON /PVB/ PVTI, PVXW, PVXC, PVBJK4, PVBJK5
      COMMON /PV1/ PVION1, PVDFU1, PVMOB1, PV1JK4
      COMMON /PV2/ PVION2, PVDFU2, PVMOB2, PV2JK4
      COMMON /PVE/ PVDFUE, PVMOBE, PVEJK3
C
***** DEFINITION OF LOCAL VARIABLES *****
C
      LUNIN1 = 1
      FLIN1 = 'SYSSSYSDEVICE:[WU.FPLIA.FOR]FPLI.PC'
C
      LUNIN2 = 2
      FLIN2 = 'SYSSSYSDEVICE:[WU.FPLIA.PV]' // FLPV(1:NFLPV) // '.PV'
C
***** SECTION 1 *****
C
      OPEN ( UNIT=LUNIN1, NAME=FLIN1, STATUS='OLD',
+          CARRIAGECONTROL='LIST', ERR=914, READONLY )
C
      READ (LUNIN1, 882, ERR=916, END=918)
      READ (LUNIN1, 882, ERR=916, END=918)
      READ (LUNIN1, 882, ERR=916, END=918)
C
      DO 165, I = 1, 5
      READ (LUNIN1, 882, ERR=916, END=918)
      READ (LUNIN1, 884, ERR=916, END=918) PCA(I)
165  CONTINUE
C
      PCEC = PCA(1)
      PCAMU = PCA(2)
      PCVP = PCA(3)
      PCEMS = PCA(4)
      PCAJK5 = PCA(5)
C
      READ (LUNIN1, 882, ERR=916, END=918)
```



```
      READ (LUNIN1, 882, ERR=916, END=918)
      READ (LUNIN1, 882, ERR=916, END=918)
C
      DO 167, I = 1, 3
      READ (LUNIN1, 882, ERR=916, END=918)
      READ (LUNIN1, 884, ERR=916, END=918) PCB(I)
167  CONTINUE
C
      TOLDVR = PCB(1)
      TOLEQ1 = PCB(2)
      TOLEQ3 = PCB(3)
C
      CLOSE (LUNIN1)
C
***** SECTION 2 *****
C
      OPEN ( UNIT=LUNIN2, NAME=FLIN2, STATUS='OLD',
+          CARRIAGECONTROL='LIST', ERR=924, READONLY )
C
      READ (LUNIN2, 882, ERR=1926, END=928)
      READ (LUNIN2, 882, ERR=1926, END=928)
      READ (LUNIN2, 882, ERR=1926, END=928)
C
      DO 245, I = 1, 5
      READ (LUNIN2, 882, ERR=1926, END=928)
      READ (LUNIN2, 884, ERR=1926, END=928) PVA(I)
245  CONTINUE
C
      PVRC   = PVA(1)
      PVBV   = PVA(2)
      PVVA   = PVA(3)
      PVMOBF = PVA(4)
      PVAJK5 = PVA(5)
C
      READ (LUNIN2, 882, ERR=2926, END=928)
      READ (LUNIN2, 882, ERR=2926, END=928)
      READ (LUNIN2, 882, ERR=2926, END=928)
C
      DO 248, I = 1, 3
      READ (LUNIN2, 882, ERR=2926, END=928)
      READ (LUNIN2, 886, ERR=2926, END=928) PNB(I)
248  CONTINUE
C
      PNSTRT = PNB(1)
      PNPNT  = PNB(2)
      PNNNN  = PNB(3)
C
      READ (LUNIN2, 882, ERR=3926, END=928)
      READ (LUNIN2, 882, ERR=3926, END=928)
      READ (LUNIN2, 882, ERR=3926, END=928)
C
      DO 251, I = 1, 5
      READ (LUNIN2, 882, ERR=3926, END=928)
```

```
      READ (LUNIN2, 884, ERR=3926, END=928) PVB(I)
251  CONTINUE
C
      PVTI   = PVB(1)
      PVXW   = PVB(2)
      PVXC   = PVB(3)
      PVBJK4 = PVB(4)
      PVBJK5 = PVB(5)
C
      READ (LUNIN2, 882, ERR=4926, END=928)
      READ (LUNIN2, 882, ERR=4926, END=928)
      READ (LUNIN2, 882, ERR=4926, END=928)
C
      DO 255, I = 1, 4
      READ (LUNIN2, 882, ERR=4926, END=928)
      READ (LUNIN2, 884, ERR=4926, END=928) PV1(I)
255  CONTINUE
C
      PVION1 = PV1(1)
      PVDFU1 = PV1(2)
      PVMOB1 = PV1(3)
      PV1JK4 = PV1(4)
C
      READ (LUNIN2, 882, ERR=5926, END=928)
      READ (LUNIN2, 882, ERR=5926, END=928)
      READ (LUNIN2, 882, ERR=5926, END=928)
C
      DO 265, I = 1, 4
      READ (LUNIN2, 882, ERR=5926, END=928)
      READ (LUNIN2, 884, ERR=5926, END=928) PV2(I)
265  CONTINUE
C
      PVION2 = PV2(1)
      PVDFU2 = PV2(2)
      PVMOB2 = PV2(3)
      PV2JK4 = PV2(4)
C
      READ (LUNIN2, 882, ERR=5926, END=928)
      READ (LUNIN2, 882, ERR=5926, END=928)
      READ (LUNIN2, 882, ERR=5926, END=928)
C
      DO 275, I = 1, 3
      READ (LUNIN2, 882, ERR=5926, END=928)
      READ (LUNIN2, 884, ERR=5926, END=928) PVE(I)
275  CONTINUE
C
      PVDFUE = PVE(1)
      PVMOBE = PVE(2)
      PVEJK3 = PVE(3)
C
      CLOSE (LUNIN2)
C
***** THE RETURN STATEMENT *****
```

```

C
      RETURN
C
***** ERROR STATEMENTS *****
C
  914  STOP 'LIPAR ERR=914 : CANNOT OPEN FPLI.PC FILE'
  916  STOP 'LIPAR ERR=916 : READING ERROR IN FPLI.PC FILE'
  918  STOP 'LIPAR ERR=918 : NOT ENOUGH DATA IN FPLI.PC FILE'
C
  924  STOP 'LIPAR ERR=924 : CANNOT OPEN FPLI.PV FILE'
  1926 STOP 'LIPAR ERR=1926 : READING ERROR IN FPLI.PV FILE - PVA'
  2926 STOP 'LIPAR ERR=2926 : READING ERROR IN FPLI.PV FILE - PNB'
  3926 STOP 'LIPAR ERR=3926 : READING ERROR IN FPLI.PV FILE - PVB'
  4926 STOP 'LIPAR ERR=4926 : READING ERROR IN FPLI.PV FILE - PV1'
  5926 STOP 'LIPAR ERR=5926 : READING ERROR IN FPLI.PV FILE - PV2'
  928  STOP 'LIPAR ERR=928 : NOT ENOUGH DATA IN FPLI.PV FILE'
C
***** FORMATS *****
C
  882  FORMAT ( ' ' )
  884  FORMAT (48X, G15.8)
  886  FORMAT (48X, I6)
C
***** THE END STATEMENT *****
C
C -- -- -- -- -- -- -- -- -- -- -- -- -- -- -- -- -- -- -- --
C THE FOLLOWING STATEMENT IS THE LAST CARD OF SUBROUTINE PAR
C -- -- -- -- -- -- -- -- -- -- -- -- -- -- -- -- -- -- -- --
      END
      SUBROUTINE CNST
C
C =====
C
C THIS SUBROUTINE SETS UP ALL THE NECESSARY CONSTANTS AND PUT THE
C VALUES INTO SEPARATE COMMON BLOCKS
C
C =====
C
      IMPLICIT REAL*8 (A-H, O-Z)
C
      REAL*8 PCEC, PCAMU, PCVP, PCEMS, PCAJK5
      REAL*8 TOLDVR, TOLEQ1, TOLEQ3
      REAL*8 PVRC, PVBV, PVVA, PVMOBF, PVAJK5
      REAL*8 PVTI, PVXW, PVXC, PVBJK4, PVBJK5
      REAL*8 PVION1, PVDFU1, PVMOB1, PV1JK4
      REAL*8 PVION2, PVDFU2, PVMOB2, PV2JK4
      REAL*8 PVDFUE, PVMOBE, PVEJK3
C
      REAL*8 PI, DELTA, DELTA1, DELTA2, DELTAE, DSXS, DSXA
C
      REAL*8 MDRC2A
      REAL*8 TXT1A, TXT1B
      REAL*8 AI1CA, AI1CB, AI1CC, AI1CD

```

```

REAL*8  AI2CA
REAL*8  AI3CA,  AI3CB,  AI3CC,  AI3CD
REAL*8  AI4CA,  AI4CB
REAL*8  AIF1A,  AIF1B,  AIF1C
REAL*8  DSXSAI
REAL*8  AIF2A,  AIF2B,  AIF2C,  AIF2D,  AIF2E,  AIF2F
REAL*8  AE1CA,  AE1CB,  AE1CC,  AE1CD,  AE1CE
REAL*8  AE2CA
REAL*8  AEF1A,  AEF1B,  AEF1C,  AEF1D
REAL*8  AEF2A,  AEF2B,  AEF2C,  AEF2D,  AEF2E,  AEF2F,
+      AEF2G,  AEF2H
C
COMMON /PCA/  PCEC,  PCAMU,  PCVP,  PCEMS,  PCAJK5
COMMON /PCB/  TOLDVR,  TOLEQ1,  TOLEQ3
COMMON /PVA/  PVRC,  PVBV,  PVVA,  PVMOBF,  PVAJK5
COMMON /PVB/  PVTI,  PVXW,  PVXC,  PVBJK4,  PVBJK5
COMMON /PV1/  PVION1,  PVDFU1,  PVMOB1,  PV1JK4
COMMON /PV2/  PVION2,  PVDFU2,  PVMOB2,  PV2JK4
COMMON /PVE/  PVDFUE,  PVMOBE,  PVEJK3
C
COMMON /MDRC2/  MDRC2A
COMMON /TXT1/  TXT1A,  TXT1B
COMMON /AI1C/  AI1CA,  AI1CB,  AI1CC,  AI1CD
COMMON /AI2C/  AI2CA
COMMON /AI3C/  AI3CA,  AI3CB,  AI3CC,  AI3CD
COMMON /AI4C/  AI4CA,  AI4CB
COMMON /AIF1/  AIF1A,  AIF1B,  AIF1C
COMMON /AIF2/  AIF2A,  AIF2B,  AIF2C,  AIF2D,  AIF2E,  AIF2F
C
COMMON /AE1C/  AE1CA,  AE1CB,  AE1CC,  AE1CD,  AE1CE
COMMON /AE2C/  AE2CA
COMMON /AEF1/  AEF1A,  AEF1B,  AEF1C,  AEF1D
COMMON /AEF2/  AEF2A,  AEF2B,  AEF2C,  AEF2D,  AEF2E,  AEF2F,
+      AEF2G,  AEF2H
C
C -----
C UNIVERSAL CONSTANTS
C =====
C
PI      = 3.141592653589793
C
DELTA   = SQRT ( (PVRC * PCEC) / (PCVP * PVMOBF) )
C
DELTA1  = PVMOB1 * DELTA
C
DELTA2  = PVMOB2 * DELTA
C
DELTAE  = PVMOBE * DELTA
C
DSXS    = SQRT ( 2.0 * PVVA / DELTA )
C
DSXA    = PVXW - PVXC
C

```

```

C =====
C FPLITXT1.FOR
C -----
C      COMMON /TXT1/   TXT1A,  TXT1B
C      COMMON /TXT1/   DSXS,   DSXA
C -----
C
C      TXT1A  = DSXS
C
C      TXT1B  = DSXA
C
C -----
C FPLI.FOR
C =====
C      COMMON /MDRC1/   MDRC1A, MDRC1B
C      COMMON /MDRC1/   FLAG1,  FLAG2
C      COMMON /MDRC2/   MDRC2A
C      COMMON /MDRC2/   PVTI
C -----
C
C      MDRC2A = PVTI
C
C -----
C FPLIEQAI1.FOR
C =====
C      COMMON /AI1C/   AI1CA,  AI1CB,  AI1CC,  AI1CD
C      COMMON /AI1C/   TOLDVR, TOLY1,  Y1FNL,  GUESS
C -----
C
C      AI1CA  = TOLDVR
C
C      AI1CB  = TOLEQ1
C
C      AI1CC  = PVXC
C
C      AI1CD  = SQRT ( 3.0 * PCAMU * PVION1 * 1.38E-16 * 1700.0 )
C
C -----
C FPLIEQAI2.FOR
C =====
C      COMMON /AI2C/   AI2CA
C      COMMON /AI2C/   TOLDVR
C -----
C
C      AI2CA  = TOLDVR
C
C -----
C FPLIEQAI3.FOR
C =====
C      COMMON /AI3C/   AI3CA,  AI3CB,  AI3CC,  AI3CD
C      COMMON /AI3C/   MASS,    TOLDVR, DELTA1, TOLSLP
C -----
C

```

```
C      AI3CA = PCAMU * PVION1
C
C      AI3CB = TOLDVR
C
C      AI3CC = DELTA1
C
C      AI3CD = TOLEQ3
C
C -----
C FPLIEQAI4.FOR
C =====
C      COMMON /AI4C/   AI4CA,  AI4CB
C      COMMON /AI4C/   HEAD,   PVDFU1
C -----
C
C      AI4CA = 4.0 * PI * PVDFU1
C      AI4CA = 1.0 / SQRT(AI4CA)
C      AI4CB = PVDFU1
C
C -----
C FPLIFXAI1.FOR
C =====
C      COMMON /AIF1/   AIF1A,  AIF1B,  AIF1C
C      COMMON /AIF1/   MASS,   HEQ21,  HEQ22
C -----
C
C      AIF1A = PCAMU * PVION1
C
C      AIF1B = AIF1A * DELTA1 * DELTA1
C
C      DSXSAI = DSXS - PVXC
C      AIF1C = AIF1B * DSXSAI - AIF1A * DELTA1 * PVBV
C
C -----
C FPLIFXAI2.FOR
C =====
C      COMMON /AIF2/   AIF2A,  AIF2B,  AIF2C,  AIF2D,  AIF2E,  AIF2F
C      COMMON /AIF2/   MASS,   DELTA1, HEQ21,  HEQ22,  HEQ31,  HEQ32
C -----
C
C      AIF2A = PCAMU * PVION1
C
C      AIF2B = DELTA1
C
C      AIF2C = AIF2A * DELTA1 * DELTA1
C
C      DSXSAI = DSXS - PVXC
C      AIF2D = AIF2C * DSXSAI - AIF2A * DELTA1 * PVBV
C
C      AIF2E = DELTA1 * DSXSAI - PVBV
C
C      AIF2F = 2.0 * PVDFU1 * DELTA1
C
```

```

C =====
C FPLIEQAE1.FOR
C -----
C      COMMON /AE1C/   AE1CA, AE1CB, AE1CC, AE1CD, AE1CE
C      COMMON /AE1C/   TOLDVR, TOLY1, Y1FNL, GUESS, DSXSAE
C -----
C
C      AE1CA = TOLDVR
C
C      AE1CB = TOLEQ1
C
C      AE1CC = DSXA
C
C      AE1CD = SQRT ( PCEMS ) * SQRT ( 3.0 * 1.38E-16 * 1700.0 )
C
C      AE1CE = DSXS + DSXA - PVXW
C
C =====
C FPLIEQAE2.FOR
C -----
C      COMMON /AE2C/   AE2CA
C      COMMON /AE2C/   TOLDVR
C -----
C
C      AE2CA = TOLDVR
C
C =====
C FPLIFXAE1.FOR
C -----
C      COMMON /AEF1/   AEF1A, AEF1B, AEF1C, AEF1D
C      COMMON /AEF1/   DSXSAE, MASS, HEQ21, HEQ22
C -----
C
C      AEF1A = DSXS + DSXA - PVXW
C
C      AEF1B = PCEMS
C
C      AEF1C = PCEMS * DELTAE * DELTAE
C
C      AEF1D = AEF1C * AEF1A + PCEMS * DELTAE * PVBV
C
C =====
C FPLIFXAE2.FOR
C -----
C      COMMON /AEF2/   AEF2A, AEF2B, AEF2C, AEF2D, AEF2E, AEF2F,
C      +               AEF2G, AEF2H
C      COMMON /AEF2/   DSXSAE, MASS, DELTAE, HEQ21, HEQ22, HEQ31,
C      +               HEQ32, HEQ33
C -----
C
C      AEF2A = DSXS + DSXA - PVXW
C
C      AEF2B = PCEMS

```

```

C      AEF2C  = DELTAE
C
C      AEF2D  = PCEMS * DELTAE * DELTAE
C
C      AEF2E  = AEF2D * AEF2A + PCEMS * DELTAE * PVBV
C
C      AEF2F  = DELTAE * AEF2A + PVBV
C
C      AEF2G  = 2.0 * PVDFUE * DELTAE
C
C      AEF2H  = PVBV
C
C  --*-- --*-- --*-- --*-- --*-- --*-- --*-- --*-- --*-- --*-- --*-- --*-- --*-- --*-- --*--
C  THE FOLLOWING STATEMENT IS THE LAST CARD OF SUBROUTINE CNST
C  --*-- --*-- --*-- --*-- --*-- --*-- --*-- --*-- --*-- --*-- --*-- --*-- --*-- --*-- --*--
C      END
C      SUBROUTINE TXT1
C
C  =====
C  THIS SUBROUTINE WILL WRITE THE FIRST PART OF THE TEXT PAGE
C  THE LOGIC UNIT NUMBER FOR WRITING THE TEXT FILE WILL BE ALWAYS 01
C  =====
C
C      IMPLICIT REAL*8 (A-H, O-Z)
C
C      CHARACTER*10 FLPV
C      CHARACTER*40 FLTXT
C
C      INTEGER NFLPV
C      INTEGER LUNTXT
C      INTEGER PNSTRT, PNPNT, PNNNN
C
C      REAL*8  PCEC,   PCAMU,   PCVP,   PCEMS,   PCAJK5
C      REAL*8  TOLDVR, TOLEQ1, TOLEQ3
C      REAL*8  PVRC,   PVBV,   PVVA,   PVMOBF, PVAJK5
C      REAL*8  PVTI,   PVXW,   PVXC,   PVBJK4, PVBJK5
C      REAL*8  PVION1, PVDFU1, PVMOB1, PV1JK4
C      REAL*8  PVION2, PVDFU2, PVMOB2, PV2JK4
C      REAL*8  PVDFUE, PVMOBE, PVEJK3
C      REAL*8  DSXS,   DSXA
C      REAL*8  TIMES,  TIMEE
C
C      COMMON /FILNAM/ FLPV
C      COMMON /FILLN/  NFLPV
C      COMMON /PCA/    PCEC,   PCAMU,   PCVP,   PCEMS,   PCAJK5
C      COMMON /PCB/    TOLDVR, TOLEQ1, TOLEQ3
C      COMMON /PVA/    PVRC,   PVBV,   PVVA,   PVMOBF, PVAJK5
C      COMMON /PNB/    PNSTRT, PNPNT, PNNNN
C      COMMON /PVB/    PVTI,   PVXW,   PVXC,   PVBJK4, PVBJK5
C      COMMON /PV1/    PVION1, PVDFU1, PVMOB1, PV1JK4

```



```
COMMON /PV2/      PVION2, PVDFU2, PVMOB2, PV2JK4
COMMON /PVE/      PVDFUE, PVMOBE, PVEJK3
COMMON /TXT1/     DSXS,   DSXA

C
***** SECTION 1 *****
C
      LUNTXT = 1
      FLTXT= 'SYSSSYSDEVICE:[WU.FPLIA.TXT]' // FLPV(1:NFLPV) // '.TXT'

C
      OPEN ( UNIT=LUNTXT, NAME=FLTXT, STATUS='NEW',
+          CARRIAGECONTROL='LIST', ERR=9024 )

C
***** SECTION 2 *****
C
210  FORMAT ( ' ' )
211  FORMAT ( '-----',
+          '-----')
212  FORMAT ( '=====',
+          '=====')

C
      WRITE (LUNTXT, 212)
      WRITE (LUNTXT, 214) FLPV(1:NFLPV), FLPV(1:NFLPV), FLPV(1:NFLPV)
214  FORMAT ('FILENAME : ', A10, 10X, A10, 10X, A10)
      WRITE (LUNTXT,212)

C
      WRITE (LUNTXT, 215)
215  FORMAT('SPECIAL COMMENTS ON THIS DATA SET:')
      WRITE (LUNTXT, 210)
      WRITE (LUNTXT, 210)
      WRITE (LUNTXT, 210)
      WRITE (LUNTXT, 210)
      WRITE (LUNTXT, 211)

C
      WRITE (LUNTXT, 210)
      WRITE (LUNTXT, 220) PCEC, PCAMU, PCVP
220  FORMAT ('PCEC =', G14.6, ' PCAMU =', G14.6,
+          ' PCVP =', G14.6)
      WRITE (LUNTXT, 224) PCEMS, PCAJK5
224  FORMAT ('PCEMS =', G14.6, ' PCAJK5=', G14.6)

C
      WRITE (LUNTXT, 210)
      WRITE (LUNTXT, 230) TOLDVR, TOLEQ1, TOLEQ3
230  FORMAT ('TOLDVR=', G14.6, ' TOLEQ1=', G14.6,
+          ' TOLEQ3=', G14.6)

      WRITE (LUNTXT, 210)
      WRITE (LUNTXT, 232) PVRC, PVBV, PVVA
232  FORMAT ('PVRC =', G14.6, ' PVBV =', G14.6,
+          ' PVVA =', G14.6)
      WRITE (LUNTXT, 234) PVMOBF, PVAJK5
234  FORMAT ('PVMOBF=', G14.6, ' PVAJK5=', G14.6)

C
      WRITE (LUNTXT, 210)
```

```

      WRITE (LUNTXT, 240) PVTI, PVXW, PVXC
240  FORMAT ('PVTI =', G14.6, '    PVXW =', G14.6,
+         '    PVXC =', G14.6)
      WRITE (LUNTXT, 244) DSXS, DSXA
244  FORMAT ('DSXS =', G14.6, '    DSXA =', G14.6)
C
      WRITE (LUNTXT, 210)
      WRITE (LUNTXT, 246) PVION1, PVDFU1, PVMOB1
246  FORMAT ('PVION1=', G14.6, '    PVDFU1=', G14.6,
+         '    PVMOB1=', G14.6)
      WRITE (LUNTXT, 248) PVION2, PVDFU2, PVMOB2
248  FORMAT ('PVION2=', G14.6, '    PVDFU2=', G14.6,
+         '    PVMOB2=', G14.6)
      WRITE (LUNTXT, 250) PCEMS, PVDFUE, PVMOBE
250  FORMAT ('PCEMS =', G14.6, '    PVDFUE=', G14.6,
+         '    PVMOBE=', G14.6)
C
      WRITE (LUNTXT, 210)
      WRITE (LUNTXT, 256) PNSTRT, PNPNT, PNSTRT+PNPNT-1
256  FORMAT (' START ', I14, ' ', RANGE ' ', I14, ' ', END ' ', I14)
      TIMES = FLOAT(PNSTRT) * PVTI
      TIMEE = FLOAT(PNPNT) * PVTI
      WRITE (LUNTXT, 258) TIMES, PVTI, TIMEE
258  FORMAT (7X, G14.6, ' ', G24.6, ' ', G22.6)
      WRITE (LUNTXT, 210)
C
      RETURN
C
***** ERROR STATEMENTS *****
C
9024  STOP 'FPLI ERR=9024 : CANNOT OPEN FPLI***.TXT FILE'
C
C --- --- --- --- --- --- --- --- --- --- --- --- --- --- ---
C THE FOLLOWING STATEMENT IS THE LAST CARD OF SUBROUTINE TXT1
C --- --- --- --- --- --- --- --- --- --- --- --- --- --- ---
      END
      SUBROUTINE TXT2
C
C =====
C
C THIS SUBROUTINE WILL WRITE THE SECOND PART OF THE TEXT PAGE
C THE LOGIC UNIT NUMBER FOR WRITING THE TEXT FILE WILL BE ALWAYS 01
C
C =====
C
      IMPLICIT REAL*8 (A-H, O-Z)
C
      INTEGER LUNTXT
C
      REAL*8 AIF2A, AIF2B, AIF2C, AIF2D, AIF2E, AIF2F
C
      COMMON /AIF2/ AIF2A, AIF2B, AIF2C, AIF2D, AIF2E, AIF2F
*      COMMON /AIF2/ MASS, ADELTA, HEQ21, HEQ22, HEQ31, HEQ32

```

```

COMMON /AEF2/  AEF2A, AEF2B, AEF2C, AEF2D, AEF2E, AEF2F,
+             AEF2G, AEF2H
* COMMON /AEF2/  DSXSAE, MASS,  DELTAE, HEQ21, HEQ22, HEQ31,
*             HEQ32, HEQ33
C
      LUNTXT = 1
C
***** SECTION 1 *****
C
110  FORMAT ( ' ' )
111  FORMAT ( '-----',
+         '-----')
C
      WRITE (LUNTXT, 111)
      WRITE (LUNTXT, 120)
120  FORMAT ('EQUATIONS USED IN FCNXXX ROUTINE')
      WRITE (LUNTXT, 111)
C
      WRITE (LUNTXT, 110)
      WRITE (LUNTXT, 130)
130  FORMAT ('EQAI1: YPRIME(1) = Y(2) / MASS')
      WRITE (LUNTXT, 140)
140  FORMAT ('EQAI2: YPRIME(2) = HEQ21 * Y(1) + HEQ22')
      WRITE (LUNTXT, 150)
150  FORMAT ('EQAI3: HEQ3 = YPRIME(1) + DELTAI * Y(1) + HEQ31')
      WRITE (LUNTXT, 152)
152  FORMAT ('      YPRIME(3) = 0.5 * ( HEQ3 * HEQ3 - HEQ32 )')
C
      WRITE (LUNTXT, 110)
      WRITE (LUNTXT, 160) AIF2A, AIF2C, AIF2D
160  FORMAT ('MASS =', G14.6, '      HEQ21 =', G14.6,
+         '      HEQ22 =', G14.6)
      WRITE (LUNTXT, 162) AIF2B, AIF2E, AIF2F
162  FORMAT ('DELTAI=', G14.6, '      HEQ31 =', G14.6,
+         '      HEQ32 =', G14.6)
      WRITE (LUNTXT, 110)
      WRITE (LUNTXT, 111)
C
      WRITE (LUNTXT, 110)
      WRITE (LUNTXT, 230)
230  FORMAT ('EQAE1: YPRIME(1) = Y(2) / MASS')
      WRITE (LUNTXT, 240)
240  FORMAT ('EQAE2: YPRIME(2) = HEQ21 * Y(1) - HEQ22')
      WRITE (LUNTXT, 242)
242  FORMAT ('      YPRIME(2) = 0.00')
      WRITE (LUNTXT, 250)
250  FORMAT ('EQAE3: HEQ3A = YPRIME(1) + DELTAE * Y(1) + HEQ31')
      WRITE (LUNTXT, 252)
252  FORMAT ('      YPRIME(3) = 0.5 * ( HEQ3A * HEQ3A - HEQ32 )')
      WRITE (LUNTXT, 254)
254  FORMAT ('EQAEB: HEQ3B = YPRIME(1) + HEQ33')
      WRITE (LUNTXT, 256)
256  FORMAT ('      YPRIME(3) = 0.5 * ( HEQ3B * HEQ3B )')

```

```

C      WRITE (LUNTXT, 110)
      WRITE (LUNTXT, 260) AEF2A, AEF2D, AEF2E
260  FORMAT ('DSXSAE=', G14.6, '   HEQ21 =', G14.6,
+        '   HEQ22 =', G14.6)
      WRITE (LUNTXT, 262) AEF2B, AEF2F, AEF2G
262  FORMAT ('MASS  =', G14.6, '   HEQ31 =', G14.6,
+        '   HEQ32 =', G14.6)
      WRITE (LUNTXT, 266) AEF2C, AEF2H
266  FORMAT ('DELTAE=', G14.6, '   HEQ33 =', G14.6)
      WRITE (LUNTXT, 110)
      WRITE (LUNTXT, 111)

C
      WRITE (LUNTXT, 350) 12
350  FORMAT (A1)

C
C      CLOSE (LUNTXT)
C

      RETURN
C  -- -- -- -- -- -- -- -- -- -- -- -- -- -- -- -- -- -- -- -- -- --
C  THE FOLLOWING STATEMENT IS THE LAST CARD OF SUBROUTINE TXT2
C  -- -- -- -- -- -- -- -- -- -- -- -- -- -- -- -- -- -- -- -- -- --
      END
      SUBROUTINE OPEN7

C
C  =====
C
C  THIS SUBROUTINE WILL OPEN CHENNEL 7 WITH EXTENSION .TMP
C  =====
C
      IMPLICIT REAL*8 (A-H, O-Z)

C
      CHARACTER*10 FLPV
      CHARACTER*40 FLTXT

C
      INTEGER NFLPV

C
      COMMON /FILNAM/ FLPV
      COMMON /FILLN/ NFLPV

C
***** SECTION 1 *****
C
      FLTXT= 'SYSSSYSDEVICE:[WU.FPLIA.TXT]' // FLPV(1:NFLPV) // '.TXT'
      FLTXT= 'SYSSSYSDEVICE:[WU.FPLIA.FOR]' // FLPV(1:NFLPV) // '.TMP'

C
      OPEN ( UNIT=7, NAME=FLTXT, STATUS='UNKNOWN',
+        CARRIAGECONTROL='LIST', ERR=9024 )

C
      RETURN

C
9024  STOP 'OPEN7 ERR=9024 : CANNOT OPEN FPLI***.TMP FILE'
C

```

```

C  --  --  --  --  --  --  --  --  --  --  --  --  --  --  --  --  --  --
C  THE FOLLOWING STATEMENT IS THE LAST CARD OF SUBROUTINE OPEN7
C  --  --  --  --  --  --  --  --  --  --  --  --  --  --  --  --  --  --
      END
      SUBROUTINE OPEN8
C
C  =====
C  THIS SUBROUTINE WILL OPEN CHENNEL 8 WITH EXTENSION .MUL
C  AFTER THE OPERATION IS DONE, THE .TMP FILE WILL BE DELETED
C  =====
C
      IMPLICIT REAL*8 (A-H, O-Z)
C
      CHARACTER*10 FLPV
      CHARACTER*40 FLTXT
C
      INTEGER NFLPV
C
      COMMON /FILNAM/ FLPV
      COMMON /FILLN/ NFLPV
C
      ***** SECTION 1 *****
C
      FLTXT= 'SYS$SYSDEVICE:[WU.FPLIA.TXT]' // FLPV(1:NFLPV) // '.MUL'
C
      OPEN ( UNIT=8, NAME=FLTXT, STATUS='NEW',
+          CARRIAGECONTROL='LIST', ERR=9024 )
C
      RETURN
C
      9024  STOP 'OPEN8 : ERR=9024 : CANNOT OPEN FPLI***.MUL FILE'
C
C  --  --  --  --  --  --  --  --  --  --  --  --  --  --  --  --  --  --
C  THE FOLLOWING STATEMENT IS THE LAST CARD OF SUBROUTINE OPEN8
C  --  --  --  --  --  --  --  --  --  --  --  --  --  --  --  --  --  --
      END
      SUBROUTINE EQAI1
C
C  =====
C
C  THIS SUBROUTINE WILL FIND THE CORRECT MOMENTUM, Y(2), FOR FIXED TIME
C  INTERVAL (TIME) AND DISTANCE (Y1FNL) UNDER CONDITION A FOR ION I.
C
C  XAI      : RETURN VALUE OF X, WHEN RETURN EQUALS TIME OR XEND
C            ; SECOND
C
C  X        : TIME, FOR DVERK USE
C            ; THEORETICALLY, IT REALLY COULD BE STARTED FROM
C              0.0 SECOND WITHOUT LOSING GENERALITY
C            ; AFTER THIS ROUTINE IS COMPLETED, X SHOULD HAVE
C              THE SAME VALUE AS XEND. OR A NEGATIVE IND
C              VALUE WILL BE ISSUED
C
C

```

```

C  TIME      : VALUE SET UP BY MAIN DRIVER FOR XEND
C              ; SECOND
C              ; SHOULD NOT BE CHANGED BY THIS SUBROUTINE
C
C  XEND       : TIME INTERVAL, FOR DVERK USE
C              ; SECOND
C              ; THE OUTPUT VALUE AFTER CALL DVERK COULD BE SMALLER
C              ; THAN THE ORIGINAL SET UP
C
C  Y1FNL      : DISTANCE BETWEEN LASER SPOT AND PROBE
C              ; CENTIMETER
C
C  Y1AI       : RETURN VALUE OF Y(1)
C              ; CENTIMETER
C              ; POSITION OF ION AT TIME XEND
C              ; WHEN SUBROUTINE FPEQ1 IS FINISHED, WE SHOULD HAVE
C              ; Y1AI = Y1FNL WHERE TOLY1 = TOLEQ1
C
C  Y(1)       : POSITION, FOR DVERK USE
C              ; CENTIMETER
C
C  Y2AI       : RETURN VALUE OF Y(2)
C              ; GRAM * CENTIMETER / SECOND
C              ; INITIAL MOMENTUM OF THE ION THAT WILL REACH "Y1FNL"
C              ; POSITION AT "TIME" SECONDS
C              ; ACTUALLY, Y2AI IS THE VALUE THIS SUBROUTINE WANTS TO
C              ; SHOOT.
C
C  Y(2)       : MOMENTUM, FOR DVERK USE
C
C  TOLY1      : TOLERANCE OF THE POSITION
C              ; TOLY1 = ABS(Y1AI-Y1FNL)
C
C  GUESS      : THE INITIAL MOMENTUM OF IONS
C              ; ACTUALLY, THIS IS A NUMBER THE USER SHOULD GUESS
C              ; NOW IS CALCULATED BY SUBROUTINE CNST

```

```

C =====

```

```

C  IMPLICIT REAL*8 (A-H, O-Z)
C
C  INTEGER N, IND, NW, IER
C
C  REAL*8 TOLDVR, TOLY1, Y1FNL, GUESS
C  REAL*8 TIME, XAI, Y1AI, Y2AI, Y3AI
C  REAL*8 X, Y(2), XEND, TOL, C(24), W(2,9)
C  REAL*8 Y1OLD1, Y1OLD2, Y2OLD1, Y2OLD2, Y2SAVE
C  REAL*8 YT1, YT2, YT3, YT4, YDIF
C
C  COMMON /AI1C/ TOLDVR, TOLY1, Y1FNL, GUESS
C  COMMON /AI1M/ TIME, XAI, Y1AI, Y2AI

```

```

      EXTERNAL FCNAI1
C
      NW      = 2
      N       = 2
      IND     = 1
      TOL     = TOLDVR
C
C
***** SECTION 1 *****
C
C
C  FIND DATA POINTS FOR FIRST SLOPE
C
      X      = 0.00
      Y(1)   = 0.00
      Y(2)   = 0.00
      XEND   = TIME
      Y2OLD1 = Y(2)
C
      IND = 1
      CALL DVERK(N,FCNAI1,X,Y,XEND,TOL,IND,C,NW,W,IER)
      IF (IND.LT.0 .OR. IER.GT.0) GO TO 999
      Y1OLD1 = Y(1)
C
      X      = 0.0
      Y(1)   = 0.0
      Y(2)   = GUESS
      XEND   = TIME
      Y2OLD2 = Y(2)
C
      IND =1
      CALL DVERK(N,FCNAI1,X,Y,XEND,TOL,IND,C,NW,W,IER)
      IF (IND.LT.0 .OR. IER.GT.0) GO TO 999
      Y1OLD2 = Y(1)
C
C
***** SECTION 2 *****
C
C
C  HERE IS THE ITERATION LOOP WHICH WILL SHOOT THE CORRECT YFCN1(2)
C  VALUE
C  THIS ALGORITHM ASSUMES THAT YFCN1(1) IS A FUNCTION OF YFCN1(2)
C  AND THIS FUNCTION IS REASONABLLY SMOOTH
C
C  THIS THE CORE OF THE SHOOTING LOOP
C
C
200  CONTINUE
      X      = 0.00
      Y(1)   = 0.00
      YT1    = Y2OLD2 - Y2OLD1
      YT2    = Y1OLD2 - Y1OLD1
```


SUBROUTINE EQAI2

```

C
C =====
C
C THIS SUBROUTINE WILL CLACULATE THE LAGRANGIAN OF THE WINNING PROCESS
C UNDER CONDITION A FOR ION I
C
C =====
C
C      IMPLICIT REAL*8 (A-H, O-Z)
C
C      INTEGER N, IND, NW, IER
C
C      REAL*8 TOLDVR
C      REAL*8 TIME,  XAI,  Y1AI,  Y2AI,  Y3AI
C      REAL*8 X, Y(3), XEND, TOL, C(24), W(3,9)
C
C      COMMON /AI2C/ TOLDVR
C      COMMON /AI2M/ TIME,  XAI,  Y1AI,  Y2AI,  Y3AI
C
C      EXTERNAL FCNAI2
C
C      N      = 3
C      IND    = 1
C      NW     = 3
C      TOL    = TOLDVR
C
C      X      = XAI
C      Y(1)   = Y1AI
C      Y(2)   = Y2AI
C      Y(3)   = Y3AI
C      XEND   = TIME
C
C
C ***** SECTION 1 *****
C
C      FIND THE LAGRANGIAN
C
C
C      CALL DVERK(N,FCNAI2,X,Y,XEND,TOL,IND,C,NW,W,IER)
C      IF (IND.LT.0 .OR. IER.GT.0) GO TO 999
C
C      XAI = X
C      Y3AI = Y(3)
C
C      RETURN
C
C ***** SECTION 2 *****
C
C      GOD BLESS YOU.....

```

```

C OTHERWISE YOU WILL HAVE TO USE THIS STUPID PART REALLY OFTEN
C
C
  999  CONTINUE
        WRITE (6, 1000) IND, IER
1000  FORMAT (' IND= ', I3, ' IER= ', I4)
        TYPE*, 'YOU STUPID KID, TRY AGAIN!'
        TYPE*, ' '
        TYPE*, 'OR YOU WANT TO GO HOME NOW.'
        STOP 'FPLIEQAI2.FOR. SO, WHAT HAPPENS?'
C --- --- --- --- --- --- --- --- --- --- --- --- --- ---
C THE FOLLOWING STATEMENT IS THE LAST CARD OF SUBROUTINE EQAI2
C --- --- --- --- --- --- --- --- --- --- --- --- --- ---
      END
      SUBROUTINE EQAI3
C
C =====
C
C THIS SUBROUTINE CALCULATES THE PARTIAL DIFFERENTIATION OF THE FINAL
C Y1AI VS. THE INITIAL MOMENTUM (Y2AI/MASS) BY THE CENTRAL DIFFERENCE
C METHOD FOR ION I UNDER CONDITION A
C
C =====
C
      IMPLICIT REAL*8 (A-H, O-Z)
C
      INTEGER N, IND, NW, IER
C
      REAL*8 MASS,   TOLDVR, ADELTA, TOLSLP
      REAL*8 TIME,   Y1AI,   Y2AI,   YRATIO
      REAL*8 X,      Y(2),   XEND,   TOL,   C(24), W(3,9)
      REAL*8 Y2RTIO, YSLPR
      REAL*8 Y1H,    Y2H,    YSLPH
      REAL*8 Y1L,    Y2L,    YSLPL
C
      COMMON /AI3C/  MASS,   TOLDVR, ADELTA, TOLSLP
      COMMON /AI3M/  TIME,   Y1AI,   Y2AI,   YRATIO
C
      EXTERNAL FCNAI1
C
      NW      = 2
      N       = 2
      TOL     = TOLDVR
C
C ***** SECTION 1 *****
C
C
      Y2RTIO = 1.0E-01
C
120  X      = 0.0
      Y(1) = 0.0
      Y(2) = Y2AI * ( 1.0 + Y2RTIO)

```

```

XEND = TIME
IND =1
Y2H = Y(2)
CALL DVERK(N,FCNAI1,X,Y,XEND,TOL,IND,C,NW,W,IER)
IF (IND.LT.0 .OR. IER.GT.0) GO TO 999
Y1H = Y(1)

C
YSLPH = (Y1H - Y1AI) / (Y2H - Y2AI)

C
X      = 0.0
Y(1) = 0.0
Y(2) = Y2AI * ( 1.0 - Y2RTIO)
IND =1
Y2L = Y(2)
CALL DVERK (N,FCNAI1,X,Y,XEND,TOL,IND,C,NW,W,IER)
IF (IND.LT.0 .OR. IER.GT.0) GO TO 999
Y1L = Y(1)

C
YSLPL = (Y1AI - Y1L) / (Y2AI - Y2L)

C
YSLPR = ABS(1.0 - YSLPH/YSLPL)
Y2RTIO = Y2RTIO * 0.10
IF (YSLPR .LT. TOLSLP) GO TO 140
GO TO 120

C
140  YRATIO = 0.50 * (YSLPH + YSLPL) * MASS

C
      RETURN

C
C ***** SECTION 3 *****
C
C GOD BLESS YOU.....
C OTHERWISE YOU WILL HAVE TO USE THIS STUPID PART REALLY OFTEN
C
C
999  CONTINUE
      WRITE (6, 1000) IND, IER
1000  FORMAT (' IND= ', I3, ' IER= ', I4)
      TYPE*, 'YOU STUPID KID, TRY AGAIN!'
      TYPE*, ' '
      TYPE*, 'OR YOU WANT TO GO HOME NOW.'
      STOP 'FPLIEQAI3.FOR. WELL, SOMETHING FOR YOU TO THINK.'
C --* --* --* --* --* --* --* --* --* --* --* --* --* --* --* --*
C THE FOLLOWING STATEMENT IS THE LAST CARD OF SUBROUTINE EQAI3
C --* --* --* --* --* --* --* --* --* --* --* --* --* --* --* --*
      END
      SUBROUTINE EQAI4

C
C =====
C THIS PROGRAM WILL CALCULATE THE VALUE OF PROPAGATOR
C =====

```

```

C      IMPLICIT REAL*8 (A-H, O-Z)
C
C      CHARACTER*10 FLPV
C
C      INTEGER NFLPV
C      INTEGER NCOUNT
C
C      REAL*8  TIME,   Y1AI,   Y2AI,   Y3AI,   RRAI
C      REAL*8  HEAD,   PVDFU1
C      REAL*8  HEADT,  RRAIT,  Y3AIT
C
C      COMMON /FILNAM/ FLPV
C      COMMON /FILLN/ NFLPV
C      COMMON /AI4C/  HEAD, PVDFU1
C      COMMON /AI4M/  TIME,  Y1AI,  Y2AI,  Y3AI,  RRAI
C
C      HEADT = LOG(HEAD)
C      RRAIT = LOG(1.0 / SQRT(RRAI))
C      Y3AIT = -1.0 * Y3AI / (2.0 * PVDFU1)
C      PROP = HEADT + RRAIT + Y3AIT
C  ADDED ON APR-07-86
C      PROPR = DEXP(PROP)
C
C  CHANGED ON APR-07-86
C      WRITE (1, 720) TIME, Y1AI, Y2AI, Y3AI, RRAI, PROP
C  720  FORMAT (2E13.4, 4E20.11)
C      WRITE (1, 720) TIME, Y1AI, Y2AI, Y3AI, RRAI, PROP, PROPR
C  720  FORMAT (2E13.4, 5E20.11)
C      WRITE (7, 730) TIME, PROP
C  730  FORMAT (' ', 2E20.11)
C
C      RETURN
C  -- -- -- -- -- -- -- -- -- -- -- -- -- -- -- -- -- -- -- --
C  THE FOLLOWING STATEMENT IS THE LAST CARD OF SUBROUTINE EQAI4
C  -- -- -- -- -- -- -- -- -- -- -- -- -- -- -- -- -- -- -- --
C      END
C      SUBROUTINE EQAI5
C
C      =====
C  THIS PROGRAM WILL CALCULATE THE VALUE OF PROPAGATOR
C      =====
C
C      IMPLICIT REAL*8 (A-H, O-Z)
C
C      REAL*8  TIME,   PROP
C      REAL*8  TIMEM,  PROPM, DIF
C
C      READ (7, 120) TIME, PROP
C  120  FORMAT (1X, 2E20.11)
C      TIMEM = TIME
C      PROPM = PROP
C

```


[illegible]

II. COMMAND FILES

II-1 FPLI.COM File

```
$ FOR FPLI
$ FOR FPLIGTCML
$ FOR FPLIPAR
$ FOR FPLICNST
$ FOR FPLITXT1
$ FOR FPLITXT2
$ FOR FPLIEQAI1
$ FOR FPLIEQAI2
$ FOR FPLIEQAI3
$ FOR FPLIEQAI4
$ FOR FPLIEQAI5
$ FOR FPLIFXAI1
$ FOR FPLIFXAI2
$ FOR FPLIOPEN
$ LINK FPLI, FPLIGTCML, FPLIPAR, -
FPLITXT1, FPLICNST, FPLITXT2, -
FPLIEQAI1, FPLIEQAI2, FPLIEQAI3, -
FPLIEQAI4, FPLIEQAI5, -
FPLIFXAI1, FPLIFXAI2, -
FPLIOPEN, -
IMSL/LIB
```

III. INPUT FILES

III-1 FPLI.PC File

```
=====
/PCA/
=====
C
  Elementary Charge          PCEC =          +0.16021917E-18
C
  Atomic Mass Unit           PCAMU =          +0.16605310E-23
C
  Vacuum Permittivity        PCVP =          +0.88544000E-13
C
  Rest Mass of Electron      PCEMS =          +0.91095345E-27
C
                                   +0.00000000E+00
=====
/PCB/
=====
C
  Tolerance of DVERK         TOLDVR =          +0.10000000E-08
C
  Tolerance of EQXX1         TOLEQ1 =          +0.10000000E-05
C
  Tolerance of EQXX3         TOLEQ3 =          +0.10000000E-05
```


	/PVA/ =====		
C	Volume Ionization Rate r(c)	PVRC =	+0.20000000E+14
C	Burning Velocity v(B)	PVBV =	+0.50000000E+03
C	Voltage Applied V(a)	PVVA =	+0.10000000E+03
C	Bkgrnd Ion Mobi Coef (Na)	PVMOBF =	+0.30200000E+02
C			+0.00000000E+00
	/PNB/ -----		
C	Starting Point (>= 1)	PNSTRT =	+1
C	Number of Points	PNPNT =	+30
C			+0
	/PVB/ -----		
C	Time Interval	PVTI =	+0.10000000E-05
C	Distance Between Probes X(w)	PVXW =	+0.60000000E+00
C	Laser Cathode Distance X(c)	PVXC =	+0.20000000E+00
C			+0.00000000E+00
C			+0.00000000E+00
	/PV1/ -----		
C	Mass of Ion 1, (Na)	PVION1 =	+0.22989770E+02
C	Diffusion Coefficient (Na)	PVDFU1 =	+0.56500000E+01
C	Mobility Coefficient (Na)	PVMOB1 =	+0.30200000E+02
C			+0.00000000E+00
	/PV2/ -----		
C			

- 328 -

C	Mass of Ion 2, (*)	PVION2 =	+0.00000000E+00
C	Diffusion Coefficient (*)	PVDFU2 =	+0.00000000E+00
C	Mobility Coefficient (*)	PVMOB2 =	+0.00000000E+00
C			+0.00000000E+00

/PVE/

C	Diff. Coef. of Electrons	PVDFUE =	+0.10000000E+04
C	Mobi. Coef. of Electrons	PVMOBE =	+0.50000000E+04
C			+0.00000000E+00

IV. OUTPUT FILE

IV-1 FPLI.TXT File

```
=====
FILENAME :   LOWFIELD           LOWFIELD           LOWFIELD
=====
SPECIAL COMMENTS ON THIS DATA SET:
```

```
-----
PCEC  =  0.160219E-18   PCAMU =  0.166053E-23   PCVP  =  0.885440E-13
PCEMS =  0.910953E-27   PCAJK5=  0.000000E+00
TOLDVR=  0.100000E-08   TOLEQ1=  0.100000E-05   TOLEQ3=  0.100000E-05
PVRC   =  0.800000E+14   PVBV  =    500.000       PVVA  =    200.000
PVMOBF=   24.3300       PVAJK5=  0.000000E+00
PVTI   =  0.100000E-05   PVXW  =    0.450000       PVXC  =    0.300000
DSXS   =  0.404953      DSXA  =    0.150000
PVION1=   22.9898       PVDFU1=    4.12000       PVMOB1=   24.3300
PVION2=  0.000000E+00   PVDFU2=  0.000000E+00   PVMOB2=  0.000000E+00
PCEMS  =  0.910953E-27   PVDFUE=   1000.00       PVMOBE=   5000.00

START           15,      RANGE           1,      END           15
              0.150000E-04,      0.100000E-05,      0.100000E-05
-----
```

EQUATIONS USED IN FCNXXX ROUTINE

```
-----
EQAI1: YPRIME(1) = Y(2) / MASS
EQAI2: YPRIME(2) = HEQ21 * Y(1) + HEQ22
EQAI3: HEQ3 = YPRIME(1) + DELTAI * Y(1) + HEQ31
      YPRIME(3) = 0.5 * ( HEQ3 * HEQ3 - HEQ32 )

MASS  =  0.381752E-22   HEQ21 =  0.134453E-12   HEQ22 =  0.129784E-13
DELTAI=   59346.3      HEQ31 =   5728.55       HEQ32 =   489014.
-----
```

```
-----
EQAE1: YPRIME(1) = Y(2) / MASS
EQAE2: YPRIME(2) = HEQ21 * Y(1) - HEQ22
      YPRIME(2) = 0.00
EQAE3: HEQ3A = YPRIME(1) + DELTAE * Y(1) + HEQ31
      YPRIME(3) = 0.5 * ( HEQ3A * HEQ3A - HEQ32 )
-----
```

EQAEB: HEQ3B = YPRIME(1) + HEQ33
YPRIME(3) = 0.5 * (HEQ3B * HEQ3B)

DSXSAE= 0.104953 HEQ21 = 0.135500E-12 HEQ22 = 0.142266E-13
MASS = 0.910953E-27 HEQ31 = 0.128051E+07 HEQ32 = 0.243922E+11
DELTA E= 0.121961E+08 HEQ33 = 500.000

APPENDIX B

CURVE FITTING PROGRAM WITH MINPACK-1

I. FORTTRAN LISTING

```

C      PROGRAM LMDIFD      ! DOUBLE PRECISION VERSION
C -----
C      YEN-YUAN JAMES WU      JUNE 22, 1986
C      DEPARTMENT OF CHEMISTRY
C      MICHIGAN STATE UNIVERSITY
C      EAST LANSING, MICHIGAN 48824
C -----
C      FILENAME: ZMDIF3.FOR
C      FUNCTION: 9 PARAMETERS, 9 CONSTANTS, 300 DATA POINTS
C      CHANGING: YX(M) = YX(M) * 1.0E-06
C -----
C      1. PURPOSE.
C      THE PURPOSE OF LMDIFD IS TO MINIMIZE THE SUM OF THE SQUARES OF M
C      NONLINEAR FUNCTIONS IN N VARIABLES BY A MODIFICATION OF THE
C      LEVENBERG-MARQUARDT ALGORITHM. THE USER MUST PROVIDE A
C      SUBROUTINE WHICH CALCULATES THE FUNCTIONS. THE JACOBIAN IS THEN
C      CALCULATED BY A FORWARD-DIFFERENCE APPROXIMATION.
C
C      2. PROGRAM PARPMETERS.
C      MAXIMUM NUMBER OF PARAMETERS THIS PROGRAM CAN HANDLE: 9
C      MAXIMUM NUMBER OF DATA POINTS THIS PROGRAM CAN TAKE: 300
C      INPUT DATA FILE FORMAT: (2X,2G15.6), OR MULPLT COMPATIBLE
C      OUTPUT DATA FILE 1: *.FIT FILE, CONTAINS ALL FITTING PARAMETERS
C      OUTPUT DATA FILE 2: *.MUL FILE, A MULPLT COMPATIBLE FILE
C      OUTPUT DATA FILE 3: *.??? NOT USED
C      ALL THE REAL NUMBERS HERE ARE OF DOUBLE PRECISION
C
C      3. DESCRIPTION OF THE MAIN SUBROUTINE.
C      THE MAIN SUBROUTINE CALLED FROM MINPACK IS LMDIF.FTN(MD12.FTN).
C      IT SHOULD BE CALLED ACCORDING TO THE FOLLOWING STATEMENTS.
C      SUBROUTINE LMDIF(FCN,M,N,X,FVEC,FTOL,XTOL,GTOL,MAXFEV,EPSFCN,
C      *                DIAG,MODE,FACTOR,NPRINT,INFO,NFEV,FJAC,LDFJAC,
C      *                IPVT,QTF,WA1,WA2,WA3,WA4)
C      INTEGER M,N,MAXFEV,MODE,NPRINT,INFO,NFEV,LDFJAC
```

```

C      INTEGER IPVT(N)
C      DOUBLE PRECISION FTOL,XTOL,GTOL,EPSFCN,FACTOR
C      DOUBLE PRECISION X(N),FVEC(M),DIAG(N),FJAC(LDFJAC,N),QTF(N),
C      *      WA1(N),WA2(N),WA3(N),WA4(M)
C      EXTERNAL FCN
C      PARAMETERS DESIGNATED AS INPUT PARAMETERS MUST BE SPECIFIED ON
C      ENTRY TO LMDIF AND ARE NOT CHANGED ON EXIT, WHILE PARAMETERS
C      DESIGNATED AS OUTPUT PARAMETERS NEED NOT BE SPECIFIED ON ENTRY
C      AND ARE SET TO APPROPRIATE VALUES ON EXIT FROM LMDIF.
C
C 4. USER SUPPLIED FCN
C      FCN IS THE NAME OF THE USER-SUPPLIED SUBROUTINE WHICH CALCULATES
C      THE FUNCTIONS. FCN MUST BE DECLARED IN AN EXTERNAL STATEMENT
C      IN THE USER CALLING PROGRAM, AND SHOULD BE WRITTEN AS FOLLOWS.
C      SUBROUTINE FCN(M,N,X,FVEC,IFLAG)
C      INTEGER M,N,IFLAG
C      DOUBLE PRECISION X(N),FVEC(M)
C      - - - - -
C      CALCULATE THE FUNCTIONS AT X AND
C      RETURN THIS VECTOR IN FVEC.
C      - - - - -
C      RETURN
C      END
C      THE VALUE OF IFLAG SHOULD NOT BE CHANGED BY FCN UNLESS THE
C      USER WANTS TO TERMINATE EXECUTION OF LMDIF. IN THIS CASE SET
C      IFLAG TO A NEGATIVE INTEGER.
C
C 5. OTHER SUBPROGRAMS REQUIRED FROM MINAPCK.
C      DPMPAR.FTN(MINPACK.004), ENORM.FTN(MD03.FTN),
C      FDJAC2.FTN(MD05.FTN), LMPAR.FTN(MD14.FTN), QRFAC.FTN(MD18.FTN),
C      QRSOLV.FTN(MD19.FTN)
C
C 6. THE IMAGE FILE CAN BE BUILT BY USING THE FOLLOWING COMMAND LINES
C      .; 'P1' = DRIVER.FTN, WHICH IS THE MAIN DRIVER SUPPLIED BY THE
C      .; USER. FCN SUBROUTINE SHOULD BE INCLUDED IN DRIVER.FTN
C      .ENABLE SUBSTITUTION
C      .IF P1 = "" .ASKS P1 DRIVER NAME
C      FOR 'P1'='P1'/-TR
C      FOR MD12=MD12/-TR
C      FOR MINPACK04=MINPACK.004/-TR
C      .; FOR PDP/11, USE THE FOLLOWING COMMAND
C      FOR MD03=MD03A/-TR
C      .; FOR VAX/11, USE THE FOLLOWING COMMAND
C      .; FOR MD03=MD03/-TR
C      FOR MD05=MD05/-TR
C      FOR MD14=MD14/-TR
C      FOR MD18=MD18/-TR
C      FOR MD19=MD19/-TR
C      .OPEN TTKB.CMD
C      .DATA 'P1'='P1',MD12,MINPACK04,MD03,MD05,MD14,MD18,MD19
C      .DATA /
C      .DATA CLSTR=F77CLS,FCSRES:RO
C      .DATA //

```

```

C      .CLOSE TTKB.CMD
C      PIP 'P1'.TSK;*/DE
C      TKB @TTKB
C      PIP TTKB.CMD;*/DE,'P1'.OBJ;*

C      .EXIT
C -----
      IMPLICIT DOUBLE PRECISION (A-H,O-Z)
      IMPLICIT INTEGER (I-N)
      INTEGER J,M,N,MAXFEV,MODE,NPRINT,INFO,NFEV,LDFJAC,NWRITE
      INTEGER IPVT(9)
      INTEGER TI, KB, IN, IOIN, OUT1, OUT2, OUT3
      INTEGER LINLEN
      DOUBLE PRECISION FTOL,XTOL,GTOL,EPSFCN,FACTOR,FNORM
      DOUBLE PRECISION X(9),FVEC(300),DIAG(9),FJAC(300,9),QTF(9)
      DOUBLE PRECISION WA1(9),WA2(9),WA3(9),WA4(300)
      DOUBLE PRECISION ENORM,DPMPAR
      DOUBLE PRECISION YX(300),YY(300),CSTFCN(9)
      EXTERNAL FCN
      BYTE BINFL(80),BOTFL1(80),BOTFL2(80),BOTFL3(80)
      BYTE LINTXT(80)
      COMMON /DATA1/ YX,YY,CSTFCN
C SET FTOL AND XTOL TO THE SQUARE ROOT OF THE MACHINE PRECISION AND
C GTOL TO ZERO. UNLESS HIGH PRECISION SOLUTIONS ARE REQUIRED, THESE ARE
C THE RECOMMENDED SETTINGS.
      FTOL = DSQRT(DPMPAR(1))
      XTOL = DSQRT(DPMPAR(1))
      GTOL = 0.0D+00
C      DATA FTOL,XTOL,GTOL
C      *      /0.526835606386175D-08, 0.526835606386175D-08, 0.0D+00/
      DATA FACTOR,MAXFEV,MODE,NPRINT,EPSCN,M
      *      /1.0D+02, 800, 1, 0, 0.0D+00, 0/
      DATA KB,TI,IN,OUT1,OUT2,OUT3 /5, 6, 4, 1, 2, 3/
C -----
C ASK FOR DATA FILE NAME
C -----
      WRITE (TI, 120)
120  FORMAT ('$DATA FILE NAME: ')
      READ (KB, 140) IOIN, (BINFL(I),I=1,80)
140  FORMAT (Q80A1)
      BINFL(IOIN+1) = 0
C
      OPEN (UNIT=IN, NAME=BINFL, STATUS='OLD',
+         CARRIAGECONTROL='LIST', ERR=9000,
+         READONLY)
C READ IN THE DATA
150  M = M + 1
160  READ (IN, 170, END=180, ERR=9010) LINLEN, LINTXT
170  FORMAT(Q80A1)
      IF (LINTXT(1).NE.'R' .OR. LINTXT(2).NE.'D') GOTO 160
      DECODE (LINLEN,177,LINTXT,ERR=9010) YX(M), YY(M)
177  FORMAT (2X, 2G15.6)
      YX(M) = YX(M) * 1.0E-06

```

```

      GOTO 150
180  CLOSE (IN)
      M = M - 1
      WRITE (TI, 190) M
190  FORMAT (/, ' *** THERE ARE', I4, ' DATA POINTS ***', /)
      LDFJAC = M
C -----
C OPEN THE .FIT OUTPUT FILE
C -----
      DO 310, I=1, IOIN-3
        BOTFL1(I)=BINFL(I)
310  CONTINUE
        BOTFL1(IOIN-2) = 'F'
        BOTFL1(IOIN-1) = 'I'
        BOTFL1(IOIN)   = 'T'
        BOTFL1(IOIN+1) = 0
        OPEN (UNIT=OUT1, NAME=BOTFL1, STATUS='UNKNOWN',
+           CARRIAGECONTROL='LIST', ERR=9030,
+           ACCESS='APPEND')
        WRITE (OUT1, 330) 1, (BINFL(I), I=1, IOIN), 2
330  FORMAT (A1, 'DATA FILE: ', 80A1, A1)
        WRITE (OUT1, 335)
335  FORMAT (/, ' THIS FITTING IS DONE BY ZMDIF3.FOR!')
        WRITE (OUT1, 350) M
350  FORMAT (/, ' THIS DATA FILE HAS', I4, ' POINTS.')
C -----
C TAKE INITIAL ESTIMATES X(N)
C -----
      WRITE (TI, 510)
510  FORMAT ('$NUMBER OF PARAMETERS (MAXIMUM 9): ')
      READ (KB, 520) N
520  FORMAT(I1)
C
      TYPE*, ' '
      DO 550, I= 1, N
        WRITE (TI, 530) I
530  FORMAT ('$      X(', I1, '): ')
        READ (KB, 540) X(I)
540  FORMAT (G20.0)
550  CONTINUE
        WRITE (OUT1, 570) N
570  FORMAT (' THIS FITTING HAS', I2, ' PARAMETERS.', /)
        WRITE (OUT1, 580) (X(I), I=1,N)
580  FORMAT (' INITIAL APPROXIMATION OF PARAMETERS:', /)
      *      3X, 'X(1) - X(3) = ', 3D15.7, /
      *      3X, 'X(4) - X(6) = ', 3D15.7, /
      *      3X, 'X(7) - X(9) = ', 3D15.7, /)
        WRITE (TI, 585) (X(I), I=1,N)
585  FORMAT (//, ' INITIAL APPROXIMATION OF PARAMETERS:', /)
      *      3X, 'X(1) - X(3) = ', 3D15.7, /
      *      3X, 'X(4) - X(6) = ', 3D15.7, /
      *      3X, 'X(7) - X(9) = ', 3D15.7)

```



```

C -----
C TAKE CONSTANTS CSTFCN(NCNST)
C -----
      TYPE*, ' '
      WRITE (TI, 610)
610   FORMAT ('$NUMBER OF CONSTANTS (MAXIMUM 9): ')
      READ (KB, 620) NCNST
620   FORMAT(I2)
C
      TYPE*, ' '
      DO 650, I= 1, NCNST
      WRITE (TI, 630) I
630   FORMAT ('$      CSTFCN(', I1, '): ')
      READ (KB, 640) CSTFCN(I)
640   FORMAT (G15.0)
650   CONTINUE
      WRITE (OUT1, 670) NCNST
670   FORMAT (/, ' THIS FITTING HAS', I2, ' CONSTANTS.', /)
      WRITE (OUT1, 680) (CSTFCN(I), I=1,NCNST)
680   FORMAT (' VALUES OF CONSTANTS:', //
*         3X, 'C(1) - C(3) = ', 3D15.7, /
*         3X, 'C(4) - C(6) = ', 3D15.7, /
*         3X, 'C(7) - C(9) = ', 3D15.7, /)
      WRITE (TI, 685) (CSTFCN(I), I=1,NCNST)
685   FORMAT (//, ' VALUES OF CONSTANTS:', /
*         3X, 'C(1) - C(3) = ', 3D15.7, /
*         3X, 'C(4) - C(6) = ', 3D15.7, /
*         3X, 'C(7) - C(9) = ', 3D15.7, /)
C -----
C CALLING LMDIF (MD12)
C -----
      IFLAG = 1
      CALL FCN(M,N,X,FVEC,IFLAG)
      FNORM = ENORM(M,FVEC)
      WRITE (OUT1, 710) FNORM
710   FORMAT (/, ' THE INITIAL L2 NORM OF THE RESIDUALS ',D15.7 /)
      WRITE (TI, 720) FNORM
720   FORMAT (' THE INITIAL L2 NORM OF THE RESIDUALS ',D15.7)
      TYPE*, ' '
      TYPE*, ' I AM WORKING VERY HARD NOW. BE PATIENT, PLEASE!'
      CALL LMDIF(FCN,M,N,X,FVEC,FTOL,XTOL,GTOL,MAXFEV,EPSFCN,
*              DIAG,MODE,FACTOR,NPRINT,INFO,NFEV,FJAC,LDFJAC,
*              IPVT,QTF,WA1,WA2,WA3,WA4)
C
      FNORM = ENORM(M,FVEC)
C -----
C WRITE OUT THE RESULTS
C -----
      WRITE (OUT1, 920)
920   FORMAT (/, ' RESULTS FROM LMDIF CURVE FITTING ')
      WRITE (OUT1, 930) FNORM,NFEV,INFO,(X(J),J=1,N)
930   FORMAT (/, 2X,31H FINAL L2 NORM OF THE RESIDUALS,D15.7 //
*           2X,31H NUMBER OF FUNCTION EVALUATIONS,I10 //

```

```

*      2X,15H EXIT PARAMETER,16X,I10 //
*      2X,27H FINAL APPROXIMATE SOLUTION //
*      3X, 'X(1) - X(3) = ', 3D15.7, /
*      3X, 'X(4) - X(6) = ', 3D15.7, /
*      3X, 'X(7) - X(9) = ', 3D15.7, /)
      WRITE (TI, 940) FNORM,NFEV,INFO,(X(J),J=1,N)
940   FORMAT (/, 2X,31H FINAL L2 NORM OF THE RESIDUALS,D15.7 /
*      2X,31H NUMBER OF FUNCTION EVALUATIONS,I10 /
*      2X,15H EXIT PARAMETER,16X,I10 //
*      2X,27H FINAL APPROXIMATE SOLUTION /
*      3X, 'X(1) - X(3) = ', 3D15.7, /
*      3X, 'X(4) - X(6) = ', 3D15.7, /
*      3X, 'X(7) - X(9) = ', 3D15.7, /)
      WRITE (OUT1, 950) (BOTFL1(I), I=1,IOIN)
      WRITE (TI, 950) (BOTFL1(I), I=1,IOIN)
950   FORMAT (/, ' RESULTS IN: ', 80A1)
C -----
C OPEN THE MULPLOT FILE
C -----
      DO 1110, I=1, IOIN-3
        BOTFL2(I)=BINFL(I)
1110   CONTINUE
        BOTFL2(IOIN-2) = 'M'
        BOTFL2(IOIN-1) = 'U'
        BOTFL2(IOIN)    = 'L'
        BOTFL2(IOIN+1) = 0
        OPEN (UNIT=OUT2, NAME=BOTFL2, STATUS='NEW',
+          CARRIAGECONTROL='LIST', ERR=9030)
        WRITE (OUT1, 1130) (BOTFL2(I), I=1,IOIN)
        WRITE (TI , 1130) (BOTFL2(I), I=1,IOIN)
1130   FORMAT (' PLOT IN: ', 80A1)
        WRITE (OUT1, 1140) 12
1140   FORMAT (A1)
C -----
C MAKE THE MULPLOT FILE
C FORMAT ('RD', 4G15.6) X, Y, FIT_VALUE, Y-FIT_VALUE
C -----
      IFLAG = 1
      CALL FCN(M,N,X,FVEC,IFLAG)
      DO 1303, I=1,M
        FJAC(I,1) = FVEC(I)
1303   CONTINUE
        IFLAG = 97
        CALL FCN(M,N,X,FVEC,IFLAG)
        WRITE (OUT2, 1305) (BINFL(I), I=1,IOIN)
1305   FORMAT ('TX THE DATA FILE IS: ', 30A1)
        WRITE (OUT2, 1306)
1306   FORMAT ('TX THIS FITTING IS DONE BY ZMDIF3.FOR!')
        WRITE (OUT2, 1307) M
1307   FORMAT ('TX NUMBER OF DATA POINTS: ', I3)
        DO 1330, I = 1, M
          WRITE (OUT2, 1310) YX(I), YY(I), FVEC(I), FJAC(I,1)
1310   FORMAT ('RD', 4G15.6)

```

```

1330  CONTINUE
      CLOSE (OUT1)
      CLOSE (OUT2)
C -----
C ERROR MESSAGES
C -----
      GOTO 9999
9000  TYPE*, ' '
      TYPE*, ' *** LMDIFD: CAN NOT FIND THE DATA FILE ***'
      GOTO 9999
9010  TYPE*, ' '
      TYPE*, ' *** LMDIFD: DATA FILE FORMAT WRONG ***'
      GOTO 9999
9030  TYPE*, ' '
      TYPE*, ' *** LMDIFD: CANNOT OPEN FILE ***'
9999  WRITE (TI,9998) 7, 7, 7
9998  FORMAT (/, ' *** EXCELLENT JOB, DEAR! ***', 3A1)
      STOP
C LAST CARD OF DRIVER FOR WLF.FTN
C =====
      END
      SUBROUTINE FCN(M,N,X,FVEC,IFLAG)
C -----
C ZMDIF2, UNNORMALIZED FPE EQN, SIMPLEST VERSION
C -----
      IMPLICIT DOUBLE PRECISION (A-H,O-Z)
      IMPLICIT INTEGER (I-N)
      INTEGER M,N,IFLAG
      INTEGER I
      DOUBLE PRECISION X(N),FVEC(M)
      DOUBLE PRECISION YX(300), YY(300), CSTFCN(9)
      DOUBLE PRECISION CC11, CC12, CC1, CC21, CC22, CC2, CC
      DOUBLE PRECISION BB2, BB3
      COMMON /DATA1/ YX, YY, CSTFCN
      DATA PI /3.141592653589793238462643/
      IF (IFLAG .EQ. 97) GO TO 97
      IF (IFLAG .NE. 0) GO TO 5
C INSERT PRINT STATEMENTS HERE WHEN NPRINT IS POSITIVE.
      RETURN
C -----
C CALCULATE ERROR SURFACE
C -----
5 CONTINUE
      X(1) = ABS(X(1))
      X(2) = ABS(X(2))
      X(3) = ABS(X(3))
      X(4) = ABS(X(4))
      X(5) = ABS(X(5))
      DO 10 I = 1, M
          CC11 = CSTFCN(1) + X(2) * YX(I)
          CC12 = 4.0 * SQRT(PI*X(3)*YX(I)) * YX(I)
          CC1 = CC11 / CC12
          CC21 = CSTFCN(1) - X(2)*YX(I)

```

```

      CC22 = 4.0 * X(3) * YX(I)
      CC2 = DEXP(-CC21*CC21/CC22)
      CC3 = X(4) * DEXP(-YX(I)/X(5))
      CC = -X(1) * CC1 * CC2 - CC3 + X(6)
      FVEC(I) = YY(I) - CC
10    CONTINUE
      GO TO 100
C -----
C CALCULATE FITTING VALUE
C -----
97    CONTINUE
      X(1) = ABS(X(1))
      X(2) = ABS(X(2))
      X(3) = ABS(X(3))
      X(4) = ABS(X(4))
      X(5) = ABS(X(5))
      DO 90 I = 1, M
          CC11 = CSTFCN(1) + X(2) * YX(I)
          CC12 = 4.0 * SQRT(PI*X(3)*YX(I)) * YX(I)
          CC1 = CC11 / CC12
          CC21 = CSTFCN(1) - X(2)*YX(I)
          CC22 = 4.0 * X(3) * YX(I)
          CC2 = DEXP(-CC21*CC21/CC22)
          CC3 = X(4) * DEXP(-YX(I)/X(5))
          CC = -X(1) * CC1 * CC2 - CC3 + X(6)
          FVEC(I) = CC
90    CONTINUE
100   CONTINUE
      RETURN
C LAST CARD OF SUBROUTINE FCN FOR LMDIFD.FTN
C =====
      END
      SUBROUTINE FCN(M,N,PAR,FVEC,IFLAG)
C =====
C 1. SUBROUTINE FCN FOR ZMDIF3.FOR.
C 2. THIS PROGRAM IS MODIFIED FROM [WU.FPE.FD23PACK]FXFPT.FOR;2
C 3. THIS SUBROUTINE WILL CALCULATE THE EM-FP-T FUNCTION VALUE
C 4. CALLED BY ZMDIF3.FOR (LMDIF).
C =====
      IMPLICIT REAL*8 (A-H,O-Z)
      IMPLICIT INTEGER (I-N)
      INTEGER TI, KB, IN, IOIN, OUT1, OUT2, OUT3
C THE LMDIF PART
      INTEGER M,N,IFLAG
      REAL*8 PAR(N),FVEC(M)
C THE DVERK PART
      INTEGER NEQ, IND, NW, IER
      REAL*8 X, Y(2), XEND, TOL, C(24), W(2,9)
      REAL*8 TOLDVR
C FOR THIS ROUTINE
      INTEGER MFLAG, NPAR
      REAL*8 CORE, SQT, BLP, BUP, PROP
C COMMON BLOCK

```

```

DOUBLE PRECISION YX(300), YY(300), CSTFCN(9)
REAL*8 IRTIO1, IAPHA2, IDIFU3, ERTIO4, ETAO5, BASE6, ITAO7
REAL*8 QF, TIME, HEAD
COMMON /DATA1/ YX, YY, CSTFCN
COMMON /DATA2/ IRTIO1, IAPHA2, IDIFU3, ITAO7, QF, TIME, HEAD
EXTERNAL EQZM3
C -----
      IF (MFLAG .EQ. 89) GOTO 11
C  CONSTANTS FOR DVERK
      DATA KB,TI,IN,OUT1,OUT2,OUT3 /5, 6, 4, 1, 2, 3/
      NW   = 2
      NEQ  = 2
      TOL  = 0.10E-07
      PI   = 3.141592653589793238462643
      Y(2) = 0.00
      MFLAG = 89
      QF = CSTFCN(1)
C
      11  IF (IFLAG .EQ. 97) GO TO 217
          IF (IFLAG .NE. 0) GO TO 105
C  INSERT PRINT STATEMENTS HERE WHEN NPRINT IS POSITIVE.
      RETURN
C
      105  CONTINUE
          IRTIO1 = ABS(PAR(1))
          IAPHA2 = ABS(PAR(2))
          IDIFU3 = ABS(PAR(3))
          ERTIO4 = ABS(PAR(4))
          ETAO5  = ABS(PAR(5))
          BASE6  = -ABS(PAR(6))
          ITAO7  = ABS(PAR(7))
C
C      WRITE (TI,109) (PAR(NPAR), NPAR=1,N)
C      WRITE (OUT1,109) (PAR(NPAR), NPAR=1,N)
      109  FORMAT (' ', 7G15.6)
C
          CORE = QF + 175.0*IDIFU3/IAPHA2
          SQT  = SQRT(CORE*CORE - QF*QF)
          BUP  = (CORE+SQT) / IAPHA2
          BLP  = (CORE-SQT) / IAPHA2
          HEAD = 1.0 / (4.0 * DSQRT(PI))
          DO 198 I = 1, M
              TIME = YX(I)
C      IF ((TIME.LE.BLP) .OR. (TIME.GE.BUP)) GOTO 170
          IF (TIME.LE.BLP) GOTO 170
          XEND = TIME - BLP
          X    = 0.00
          Y(1) = 0.00
          IND  = 1
          CALL DVERK(NEQ,EQZM3,X,Y,XEND,TOL,IND,C,NW,W,IER)
          IF (IND.LT.0 .OR. IER.GT.0) GO TO 999
          PROP = -Y(1) - ERTIO4 * DEXP(-TIME/ETAO5) + BASE6
          GOTO 180

```

```

170     PROP = -ERTIO4 * DEXP(-TIME/ETA05) + BASE6
180     FVEC(I) = YY(I) - PROP
198     CONTINUE
        RETURN
C -----
C CALCULATE ERROR SURFACE
C -----
217     CONTINUE
        IRTIO1 = ABS(PAR(1))
        IAPHA2 = ABS(PAR(2))
        IDIFU3 = ABS(PAR(3))
        ERTIO4 = ABS(PAR(4))
        ETA05  = ABS(PAR(5))
        BASE6  = -ABS(PAR(6))
        ITAO7  = ABS(PAR(7))
C
        CORE = QF + 175.0*IDIFU3/IAPHA2
        SQT  = SQRT(CORE*CORE - QF*QF)
        BUP  = (CORE+SQT) / IAPHA2
        BLP  = (CORE-SQT) / IAPHA2
        HEAD = 1.0 / (4.0 * DSQRT(PI))
        DO 298, I = 1, M
            TIME = YX(I)
            IF ((TIME.GE.BUP) .OR. (TIME.LE.BLP)) GOTO 270
            XEND = TIME - BLP
            X     = 0.00
            Y(1) = 0.00
            IND = 1
            CALL DVERK(NEQ,EQZM3,X,Y,XEND,TOL,IND,C,NW,W,IER)
            IF (IND.LT.0 .OR. IER.GT.0) GO TO 999
            PROP = -Y(1) - ERTIO4 * DEXP(-TIME/ETA05) + BASE6
        GOTO 280
270     PROP = -ERTIO4 * DEXP(-TIME/ETA05) + BASE6
280     FVEC(I) = PROP
298     CONTINUE
        RETURN
C
C GOD BLESS YOU.....
C OTHERWISE YOU WILL HAVE TO USE THIS STUPID PART REALLY OFTEN
999     CONTINUE
        WRITE (6, 1000) IND, IER
1000    FORMAT (' IND= ', I3, ' IER= ', I4)
        TYPE*, ' '
        STOP ' EQZM3.FOR, I HOPE YOU CAN FIGURE OUT WHAT HAPPENED.'
C
C LAST CARD OF ZMDIF3.FCN (SUBROUTINE FCN FOR ZMDIF3.FOR).
C =====
        END
        SUBROUTINE EQZM3 (N, X, Y, YPRIME)
C =====
C 1. THIS SUBROUTINE IS MODIFIED FROM EQFPT.FOR
C 2. THIS SUBROUTINE WILL BE CALLED FROM DVERK
C 3. FP-EM-T CASE

```

```

C =====
      IMPLICIT REAL*8 (A-H, O-Z)
      INTEGER N
      REAL*8 X, Y(N), YPRIME(N)
      REAL*8 DIFF, PART1, P21, P22, PART2, P31, PART3
C
      REAL*8 IRTIO1, IAPHA2, IDIFU3, ITAO7, QF, TIME, HEAD
      COMMON /DATA2/ IRTIO1, IAPHA2, IDIFU3, ITAO7, QF, TIME, HEAD
C
      DIFF = TIME - X
      PART1 = (QF+IAPHA2*DIFF) / (DSQRT(IDIFU3*DIFF)*DIFF)
      P21 = QF - IAPHA2*DIFF
      P22 = 4.0 * IDIFU3 * DIFF
      PART2 = DEXP(-P21*P21/P22)
      P31 = X / ITAO7
      PART3 = DEXP(-P31)
      YPRIME(1) = IRTIO1 * HEAD * PART1 * PART2 * PART3
      YPRIME(2) = 0.0
C
      RETURN
C
C LAST CARD OF ZMDIF3.EQN (SUBROUTINE EQZM3 FOR ZMDIF3.FOR).
C =====
      END
      SUBROUTINE FCN(M,N,PAR,FVEC,IFLAG)
C =====
C 1. SUBROUTINE FCN FOR ZMDIF4.FOR
C 2. THIS PROGRAM IS MODIFIED FROM [WU.FPE.FD23PACK]FXFPT.FOR;2
C 3. THIS SUBROUTINE WILL CALCULATE THE EM-FP-T FUNCTION VALUE
C 4. CALLED BY ZMDIF4.FOR (LMDIF).
C =====
      IMPLICIT REAL*8 (A-H,O-Z)
      IMPLICIT INTEGER (I-N)
      INTEGER TI, KB, IN, IOIN, OUT1, OUT2, OUT3
C THE LMDIF PART
      INTEGER M,N,IFLAG
      REAL*8 PAR(N),FVEC(M)
C THE DVERK PART
      INTEGER NEQ, IND, NW, IER
      REAL*8 X, Y(2), XEND, TOL, C(24), W(2,9)
      REAL*8 TOLDVR
C FOR THIS ROUTINE
      INTEGER MFLAG, NPAR
      REAL*8 CORE, SQT, BLP, BUP, PROP
C COMMON BLOCK
      DOUBLE PRECISION YX(300), YY(300), YS(300), CSTFCN(9)
      REAL*8 IRTIO1, IAPHA2, IDIFU3, ERTIO4, ETAO5, BASE6, ITAO7
      REAL*8 QF, TIME, HEAD
      COMMON /DATA1/ YX, YY, YS, CSTFCN
      COMMON /DATA2/ IRTIO1, IAPHA2, IDIFU3, ITAO7, QF, TIME, HEAD
      EXTERNAL EQZM3
C -----
      IF (MFLAG .EQ. 89) GOTO 11

```

C CONSTANTS FOR DVERK

```
DATA KB, TI, IN, OUT1, OUT2, OUT3 /5, 6, 4, 1, 2, 3/
NW   = 2
NEQ  = 2
TOL  = 0.10E-07
PI   = 3.141592653589793238462643
Y(2) = 0.00
MFLAG = 89
QF   = CSTFCN(1)
```

C

```
11  IF (IFLAG .EQ. 97) GO TO 217
    IF (IFLAG .NE. 0) GO TO 105
```

C INSERT PRINT STATEMENTS HERE WHEN NPRINT IS POSITIVE.
RETURN

C

```
105 CONTINUE
    IRTIO1 = ABS(PAR(1))
    IAPHA2 = ABS(PAR(2))
    IDIFU3 = ABS(PAR(3))
    ERTIO4 = ABS(PAR(4))
    ETAO5  = ABS(PAR(5))
    BASE6  = -ABS(PAR(6))
    ITAO7  = ABS(PAR(7))
```

C

```
WRITE (TI, 109) (PAR(NPAR), NPAR=1, N)
```

C

```
WRITE (OUT1, 109) (PAR(NPAR), NPAR=1, N)
```

C

```
109 FORMAT (' ', 7G15.6)
```

C

```
    CORE = QF + 175.0*IDIFU3/IAPHA2
    SQT  = SQRT(CORE*CORE - QF*QF)
    BUP  = (CORE+SQT) / IAPHA2
    BLP  = (CORE-SQT) / IAPHA2
    HEAD = 1.0 / (4.0 * DSQRT(PI))
    DO 198 I = 1, M
        TIME = YX(I)
C      IF ((TIME.LE.BLP) .OR. (TIME.GE.BUP)) GOTO 170
        IF (TIME.LE.BLP) GOTO 170
        XEND = TIME - BLP
        X    = 0.00
        Y(1) = 0.00
        IND  = 1
        CALL DVERK(NEQ, EQZM3, X, Y, XEND, TOL, IND, C, NW, W, IER)
        IF (IND.LT.0 .OR. IER.GT.0) GO TO 999
        PROP = -Y(1) - ERTIO4 * DEXP(-TIME/ETAO5) + BASE6
        GOTO 180
```

```
170 PROP = -ERTIO4 * DEXP(-TIME/ETAO5) + BASE6
```

```
180 FVEC(I) = (YY(I) - PROP) / YS(I)
```

```
198 CONTINUE
    RETURN
```

C

C -----
C CALCULATE ERROR SURFACE
C -----

```
217 CONTINUE
```



```

      IRTIO1 = ABS(PAR(1))
      IAPHA2 = ABS(PAR(2))
      IDIFU3 = ABS(PAR(3))
      ERTIO4 = ABS(PAR(4))
      ETAO5  = ABS(PAR(5))
      BASE6  = -ABS(PAR(6))
      ITAO7  = ABS(PAR(7))

C
      CORE = QF + 175.0*IDIFU3/IAPHA2
      SQT  = SQRT(CORE*CORE - QF*QF)
      BUP  = (CORE+SQT) / IAPHA2
      BLP  = (CORE-SQT) / IAPHA2
      HEAD = 1.0 / (4.0 * DSQRT(PI))
      DO 298, I = 1, M
        TIME = YX(I)
        IF ((TIME.GE.BUP) .OR. (TIME.LE.BLP)) GOTO 270
        XEND = TIME - BLP
        X     = 0.00
        Y(1) = 0.00
        IND = 1
        CALL DVERK(NEQ,EQZM3,X,Y,XEND,TOL,IND,C,NW,W,IER)
        IF (IND.LT.0 .OR. IER.GT.0) GO TO 999
        PROP = -Y(1) - ERTIO4 * DEXP(-TIME/ETAO5) + BASE6
      GOTO 280
270    PROP = -ERTIO4 * DEXP(-TIME/ETAO5) + BASE6
280    FVEC(I) = PROP
298    CONTINUE
      RETURN

C
C GOD BLESS YOU.....
C OTHERWISE YOU WILL HAVE TO USE THIS STUPID PART REALLY OFTEN
999    CONTINUE
      WRITE (6, 1000) IND, IER
1000   FORMAT (' IND= ', I3, ' IER= ', I4)
      TYPE*, ' '
      STOP ' EQZM3.FOR, I HOPE YOU CAN FIGURE OUT WHAT HAPPENED.'

C
C LAST CARD OF ZMDIF4.FCN (SUBROUTINE FCN FOR ZMDIF4.FOR).
C =====
      END

      SUBROUTINE EQZM3 (N, X, Y, YPRIME)
C =====
C 1. THIS SUBROUTINE IS MODIFIED FROM EQFPT.FOR
C 2. THIS SUBROUTINE WILL BE CALLED FROM DVERK
C 3. FP-EM-T CASE
C =====
      IMPLICIT REAL*8 (A-H, O-Z)
      INTEGER N
      REAL*8 X, Y(N), YPRIME(N)
      REAL*8 DIFF, PART1, P21, P22, PART2, P31, PART3

C
      REAL*8 IRTIO1, IAPHA2, IDIFU3, ITAO7, QF, TIME, HEAD

```

```
C      COMMON /DATA2/ IRTIO1, IAPHA2, IDIFU3, ITAO7, QF, TIME, HEAD

      DIFF = TIME - X
      PART1 = (QF+IAPHA2*DIFF) / (DSQRT(IDIFU3*DIFF)*DIFF)
      P21 = QF - IAPHA2*DIFF
      P22 = 4.0 * IDIFU3 * DIFF
      PART2 = DEXP(-P21*P21/P22)
      P31 = X / ITAO7
      PART3 = DEXP(-P31)
      YPRIME(1) = IRTIO1 * HEAD * PART1 * PART2 * PART3
      YPRIME(2) = 0.0

C      RETURN

C
C LAST CARD OF ZMDIF4.EQN (SUBROUTINE EQZM3 FOR ZMDIF4.FOR).
C =====
      END
```

II. OUTPUT FILES

DATA FILE: [WU.LASER.DATB3]GAA01A.SSD

THIS FITTING IS DONE BY ZMDIF2.FOR!

THIS DATA FILE HAS 52 POINTS.
THIS FITTING HAS 6 PARAMETERS.

INITIAL APPROXIMATION OF PARAMETERS:

X(1) - X(3) = 0.1902570D-04 0.1751380D+04 0.8911500D+02
X(4) - X(6) = 0.2177590D+00 0.1891410D-03 -0.3133050D+01

THIS FITTING HAS 1 CONSTANTS.

VALUES OF CONSTANTS:

C(1) - C(3) = 0.2000000D+00

THE INITIAL L2 NORM OF THE RESIDUALS 0.9528573D+00

RESULTS FROM LMDIF CURVE FITTING

FINAL L2 NORM OF THE RESIDUALS 0.3015916D-01

NUMBER OF FUNCTION EVALUATIONS 79

EXIT PARAMETER 1

FINAL APPROXIMATE SOLUTION

X(1) - X(3) = 0.6052223D-05 0.2584936D+04 0.7187254D+02
X(4) - X(6) = 0.6111747D-01 0.1187015D-03 -0.3152037D+01

RESULTS IN: [WU.LASER.DATB3]GAA01A.FIT

PLOT IN: [WU.LASER.DATB3]GAA01A.MUL

DATA FILE: [WU.LASER.DATB3]GAA01A.SSD

THIS FITTING IS DONE BY ZMDIF3.FOR!

THIS DATA FILE HAS 52 POINTS.
THIS FITTING HAS 7 PARAMETERS.

INITIAL APPROXIMATION OF PARAMETERS:

X(1) - X(3) = 0.1306570D+03 0.2585650D+04 0.7200700D+02
X(4) - X(6) = 0.6113190D-01 0.1185060D-03 -0.3152050D+01
X(7) - X(9) = 0.4633640D-07

THIS FITTING HAS 1 CONSTANTS.

VALUES OF CONSTANTS:

C(1) - C(3) = 0.2000000D+00

THE INITIAL L2 NORM OF THE RESIDUALS 0.3018972D-01

RESULTS FROM LMDIF CURVE FITTING

FINAL L2 NORM OF THE RESIDUALS 0.3017522D-01

NUMBER OF FUNCTION EVALUATIONS 805

EXIT PARAMETER 5

FINAL APPROXIMATE SOLUTION

X(1) - X(3) = 0.2501513D+03 0.2584719D+04 0.7196516D+02
X(4) - X(6) = 0.6106031D-01 0.1181542D-03 -0.3152121D+01
X(7) - X(9) = 0.2421763D-07

RESULTS IN: [WU.LASER.DATB3]GAA01A.FIT
PLOT IN: [WU.LASER.DATB3]GAA01A.MUL

APPENDIX C

SIMULATION PROGRAM

FORTRAN LISTING

PROGRAM CN5A3

```
C =====
C THIS PROGRAM SIMULATES THE CONCENTRATION VERSUS TIME CURVE.
C (1) DIFFUSION IS SIMULATED BY CRANK-NICHOLSON METHOD ALONG WITH
C THE LAGRANGE'S DIFFERENTIATED 5-POINT POLYNOMIAL TO ADDRESS
C THE SECOND DERIVATIVE
C (2) THE DRIFT FUNCTION IS SIMULATED BY 5-POINT CENTERED DIFFERENCE
C APPROXIMATION.
C (3) THE SIGNAL IS CALCULATED BY AN IMPOSED BOUNDARY CONDITION.
C =====
      IMPLICIT REAL*8 (A-H,O-Z)
      INTEGER TI
      INTEGER NTSTEP
      INTEGER NDO, NBLANK, NORIGN, NDIMEN, NSTART, NEND
      INTEGER QPN, QPNC, QPIA, QPIB, QPM, QPIDGT, QPIER
      REAL*8 PI
      REAL*8 CEQU(205)
      REAL*8 QPAA(205,3), QPBB(205), QPWK(205,5), QPXX(205)
      REAL*8 QPD1, QPD2
      REAL*8 DIFFUS, DMODEL, ALPHA, AMODEL
      REAL*8 CWIDTH, TRANGE, TWIDTH, TLASER
      REAL*8 CNAAD, CNAAL, CNAAR, CNBB1, CNBB2
      REAL*8 CEQUH, QPXXH, QPXXL
C =====
C INTEGERS OF DIMENSIONS OF ARRAYS AND MATRICES
C -----
C NDO      : The number of space points. This number is preferred to be
C            an odd number.
C NBLANK   : Number of buffer points on each end of the distribution
C            matrix. NBLANK = 2 for the 5-point Crank-Nicholson Method.
C NORIGN   : The space point index of the pulse ion-source space point.
C            For the 5-point Crank-Nicholson Method, NORIGN is preferred
C            to be an integer ends with a 3 if NDO is a multiple of 10.
C NDIMEN   : The dimension of all working arrays. (NDIMEN=NDO+2*NBLANK)
```

C NSTART : The starting point index of DO LOOPS. (NSTART=NBLANK+1)
 C NEND : The end point index of DO LOOPS. (NEND=NDO+BLANK)

C ARRYS AND MATRICES

C CEQU : (OUTPUT) The working array of the distribution matrix which
 C is calculated by the analytical solution of Fokker-Planck
 C Equation. (NDIMEN)
 C QPAA : (INPUT of LEQ2PB) The coefficient matrix of the diffusion
 C function. This matrix is stored in Band Symmetric Storage
 C Mode. (NDIMEN,3)
 C QPBB : (INPUT/OUTPUT of LEQ2PB) The Input and output array of the
 C distribution matrix. (NDIMEN)
 C QPWK : (OUTPUT of LEQ2PB) Vector or matrix having QPN*(QPNC+3)
 C locations used as work storage. On return, the first
 C QPN*(QPNC+1) locations of QPWK will contain the matrix QPL
 C stored in Band Storage Mode where QPAA = QPL * transp-QPL
 C Note that the diagonal elements of QPL are stored in
 C reciprocal form. (NDIMEN,5)
 C QPDD : (INPUT/OUTPUT) Working array of the coefficients of the
 C drift function. (NDIMEN)
 C QPXX : Temporary working array of the distribution matrix for drift
 C function calculations. (NDIMEN)

C PARAMETERS FOR CALLING IMSL LEQ2PB

C QPN : (INPUT of LEQ2PB) Order of QPAA and the number of rows in
 C QPBB. (QPN=NDIMEN)
 C QPNC : (INPUT of LEQ2PB) Number of upper or lower co-diagonals in
 C QPAA. QPNC = 2 for the 5-point Crank-Nicholson Method.
 C QPIA : (INPUT of LEQ2PB) Row dimension of the coefficient matrix.
 C (QPIA=NDIMEN)
 C QPIB : (INPUT of LEQ2PB) Row dimension of the distribution matrix.
 C (QPIB=NDIMEN)
 C QPM : (INPUT of LEQ2PB) Number of right hand side columns in the
 C distribution matrix. QPM = 1 for the 5-point Crank-
 C Nicholson Method.
 C QPIDGT : (OUTPUT of LEQ2PB) The number of digits in the answer which
 C were unchanged after the first iterative improvement.
 C QPD1 : (OUTPUT of LEQ2PB) Components of the determinant of QPAA.
 C QPD2 : (OUTPUT of LEQ2PB) Det(QPAA) = QPD1 * 2.0 ** QPD2.
 C QPIER : (OUTPUT of LEQ2PB) Error Parameter.
 C QPIER = 0 indicates a successful run.
 C QPIER = 129 indicates that the matrix QPAA is
 C algorithmically not positive definite.
 C QPIER = 130 indicates that iterative improvement failed to
 C converge. The matrix QPAA is too ill-conditioned.

C SYSTEM DEFINING PARAMETERS

C DIFFUS : Diffusion coefficient of the ion. (cm*cm/sec)
 C DMODEL : Model diffusion coefficient of the ion. (dimensionless)
 C DMODEL=DIFFUS*TWIDTH/(CWIDTH)**2

```

C ALPHA : Drift constant of the ion which is composed of the flow rate
C          of the carrier gas, the electrical field applied through
C          biased voltage on the probes, and the attraction/repulsion
C          forces among electrons and ions. (cm/sec)
C AMODEL : Model drift constant of the ion. (dimensionless)
C          AMODEL=(AMODL1-AMODL2)/(AMODL1+AMODL2) where
C          AMODL1=ALPHA/CWIDTH and AMODL2=1.0/TWIDTH
C TLASER : The laser pulse lifetime (sec)
C TRANGE : The propagating time interval of the simulation. (sec)
C NTSTEP : Number of steps for time propagation.
C TWIDTH : The width of each propagating time step. (sec)
C          TWIDTH=(TRANGE-TLASER)/FLOAT(NTSTEP)
C CWIDTH : The width of the one-dimensional space cell. (cm)
C CEQUH : The sum of the space distribution (probability function)
C          over the whole space that is calculated by the theoretical
C          method. This number should equal to 1.00 exactly.
C QPXXH : The sum of the space distribution (probability function)
C          over the whole space that is calculated by the theoretical
C          method at TIME=TLASER. This number may not equal to 1.00
C          exactly due to the limitation from the finite difference
C          method. Further adjustment is usually required.
C QPXXL : The sum of the space distribution (probability function)
C          over the whole space at TIME=TLASER after adjustment. This
C          number should equal to 1.00 exactly.
C -----
C COEFFICIENTS FROM 5-POINT CRANK-NICHOLSON METHOD
C -----
C CNAAD : The value of the diagonal array of the coefficient matrix
C          QPAA.
C CNAA1 : The value of the first off-diagonal array of the coefficient
C          matrix QPAA.
C CNAA2 : The value of the second off-diagonal array of the
C          coefficient matrix QPAA.
C CNBBB : The value of the diagonal array of the distribution matrix
C          QPBB.
C CNBB1 : The value of the first off-diagonal array of the
C          distribution matrix QPBB.
C CNBB2 : The value of the second off-diagonal array of the
C          distribution matrix QPBB.
C =====
C
C HERE COMES THE REAL PROGRAMMING
C
C -----
C DEFINE THE LUN NUMBER FOR VAX/VMS
C -----
C          TI = 5
C -----
C THE OFFICIAL PI VALUE FROM ABRAWOWITZ AND STEGUN
C -----
C          PI = 3.1415926535

```

```
C -----
C DEFINE THE DIMENSION OF ALL WORKING ARRAYS WITH BUFFER POINTS
C -----
      NDO      = 501
      NBLANK   = 2
C      NORIGN  = (NDO-1)/2 + (NBLANK+1)
      NORIGN   = 300 + (NBLANK+1)
      NDIEN    = NDO + 2 * NBLANK
C -----
C THE FIRST AND LAST NBLANK CELLS ARE RESERVED FOR BOUNDARY CONDITIONS
C -----
      NSTART   = NBLANK + 1
      NEND     = NDO + NBLANK
      NQRIIA   = 50
C -----
C DIFFUS: DIFFUSION CONSTANT (cm*cm/Sec)
C ----- User define term -----
      DIFFUS   = 5.00
C -----
C CMOBIL: MOBILITY COEFFICIENT (cm*cm/Sec/Volt)
C ----- User define term -----
      CMOBIL   = 25.0
C -----
C ALPHA: GAS FLOW RATE (cm/Sec)
C ----- User define term -----
      ALPHA    = CMOBIL * 700.0 / 0.50
C -----
C TLASER: LASER PULSE LENGTH (Sec)
C ----- User define term -----
      TLASER   = 0.1000E-06
C -----
C CWIDTH: THE WIDTH OF THE SPACE CELL (cm)
C ----- User define term -----
      CWIDTH   = 0.1000E-02
C -----
C TRANGE: ENDING TIME OF SIMULATION (Micro-Sec)
C ----- User define term -----
      TRANGE   = 1.5000E+01
C -----
C NTSTEP: NUMBER OF PROPAGATING STEPS
C ----- User define term -----
      NTSTEP   = 90
      NJUMP    = 1
C -----
C RICNST: CONSTANT FOR CALCULATING REPULSION FORCE AMONG IONS
C      RI01   : 1.439 860 521 025 E-07 (VOLT/CM)
C      RI02   : TOTAL NUMBER OF IONS
C      RI02A  : ION DENSITY (IONS/CC)
C      RI02B  : VOLUME OF LASER FOCAL POINT (CC)
C      RI02C  : TO COMPENSATE THE SLIDE WIDTH (= CWIDTH)
C      RI03   : TO COMPENSATE THE SLIDE DISTANCE
C -----
      RI01     = 1.439860521025E-07
```



```

      RI02A = 1.00E+11
      RI02B = 2.00E-06
      RI02C = CWIDTH
      RI02 = RI02A * RI02B * RI02C
      RI03 = CWIDTH * CWIDTH
      RICNST = CMOBIL * RI01 * RI02 / RI03
C -----
C NUMBER ADJUSTMENT FOR USER'S CONVENIENCE
C -----
      TRANGE = TRANGE / 1.0E+06
      TWIDTH = (TRANGE) / FLOAT(NTSTEP)
      DRIFTH = CWIDTH / TWIDTH
      DMODEL = DIFFUS * TWIDTH / (CWIDTH)**2
C -----
C CLEAN UP THE BOUNDARY CELLS (THIS PART IS FOR SOME SHAKY COMPILERS
C AND BLURRY BRAINS)
C -----
      DO 1020, I = 1, NBLANK
        CEQU(I) = 0.0
        QPBB(I) = 0.0
        QPXX(I) = 0.0
        QRII(I) = 0.0
        QRXX(I) = 0.0
1020  CONTINUE
C
      DO 1022, I = NDIMEN-NBLANK+1, NDIMEN
        CEQU(I) = 0.0
        QPBB(I) = 0.0
        QPXX(I) = 0.0
        QRII(I) = 0.0
        QRXX(I) = 0.0
1022  CONTINUE
C
C =====
C
C HERE IS THE THEORETICAL CALCULATION
C
C =====
C -----
C USE THE ANALYTICAL SOLUTION FROM FOKKER-PLANCK EQUATION TO CALCULATE
C THE THEORETICAL DISTRIBUTION MATRIX
C -----
C * FOKKER-PLANCK EQUATION = FPE-CF-X
C -----
      TIME = TRANGE
      CEQU1 = 1.0 / ( 2.0 * DSQRT( PI * DIFFUS * TIME ))
      CEQU2 = 4.0 * DIFFUS * TIME
      CEQU3 = ALPHA * TIME
      CEQUH = 0.0
      DO 1200, I = NSTART, NEND
        QSIM = CWIDTH * FLOAT(I-NORIGN) - CEQU3
        CEQU(I) = CEQU1 * DEXP(-QSIM*QSIM / CEQU2)

```

```

                CEQUH = CEQUH + CEQU(I)
1200    CONTINUE
                CEQUH = CEQUH * CWIDTH
C
C =====
C
C HERE IS THE SIMULATION
C
C =====
C -----
C CALCULATE THE STARTING DISTRIBUTION MATRIX BY USING GAUSSIAN
C DISTRIBUTION FUNCTION AT TIME=TLASER, ie. THE SIMULATION IS
C ALWAYS STARTED AFTER TLASER SECONDS
C -----
                TIME = TLASER
                QPXX1 = 1.0 / ( 2.0 * DSQRT( PI * DIFFUS * TIME ))
                QPXX2 = 4.0 * DIFFUS * TIME
                QPXXH = 0.0
                DO 2200, I = NSTART, NEND
                    QSIM = CWIDTH * FLOAT(I-NORIGN)
                    QPXX(I) = QPXX1 * DEXP(-QSIM*QSIM / QPXX2)
                    QPXXH = QPXXH + QPXX(I)
2200    CONTINUE
                QPXXH = QPXXH * CWIDTH
C -----
C FOR FINITE DIFFERENCE METHOD CASE, THE SUM OF THE CONTENTS IN EACH
C SPACE CELL OF THE DISTRIBUTION MATRIX CAN BE OFF-NORMALIZATION.
C HERE WE FIX AND REPORT THIS PROBLEM.
C -----
                QPXXL = 0.0
                DO 2400, I = NSTART, NEND
                    QPXX(I) = QPXX(I) / QPXXH
                    QPXXL = QPXXL + QPXX(I)
2400    CONTINUE
                QPXXL = QPXXL * CWIDTH
C
                WRITE (TI, 2420) QPXXH, QPXXL
2420    FORMAT ( ' QPXXH = ', G15.6, 6X, 'QPXXL = ', G15.6)
C -----
C SET UP THE NECESSARY CONSTANTS FOR 5-POINT CRANK-NICHOLSON METHOD
C WITH THE COEFFICIENTS FROM THE LAGRANGIAN POLYNOMIAL
C -----
C * THE FOLLOWING SETUP COMES FROM 50% EXPLICIT AND 50% IMPLICIT
C DERIVATION.
C -----
                CNAAD = 24.0 + 30.0*DMODEL
                CNAA1 = -16.0 * DMODEL
                CNAA2 = DMODEL
                CNBB1 = 24.0 - 30.0*DMODEL
                CNBB2 = 16.0 * DMODEL
                CNBB2 = -DMODEL
C -----

```

```
C -----
C SET UP THE PARAMETERS FOR CALLING LEQ2PB FROM IMSL
C -----
```

```

C -----
C THE TIME PROPAGATION CYCLE STARTS HERE
C ----- DO 6000 -----

```

```
C      DO 6000, J= 1, NTSTEP
C
C          SIGNLE = 0.0
C          SIGNLI = 0.0
```

```
C -----
C SET UP THE INITIAL DISTRIBUTION MATRIX QPBB
C -----
```

```

C      DO 3240, IDIFU = NSTART, NEND
          IF (QPBB(IDIFU) .LT. 0.0) QPBB(IDIFU)=0.0
3240    CONTINUE
          QPXXH = 0.0
          DO 3242, IDIFU = NSTART, NEND
              IF (QPBB(IDIFU) .EQ. 0.0) THEN
                  QPBB(IDIFU) = (QPBB(IDIFU-2)+QPBB(IDIFU-1) +

```

```

C                                QPBB(IDIFU+1)+QPBB(IDIFU+2))/4.0
                                ELSE
                                END IF
                                QPXXH = QPXXH + QPBB(IDIFU)
3242    CONTINUE                QPXXAJ = 1.0 - TOTALS * CWIDTH
                                QPXXH = QPXXH * CWIDTH / QPXXAJ
                                QPXXL = 0.0
                                DO 3244, IDIFU = NSTART, NEND
                                    QPBB(IDIFU) = QPBB(IDIFU) / QPXXH
                                    QPXXL = QPXXL + QPBB(IDIFU)
3244    CONTINUE                QPXXL = (QPXXL+TOTALS) * CWIDTH
C
                                SIGNLE = SIGNLE + QPBB(NSTART)
                                QPBB(NSTART) = 0.0
                                SIGNLI = SIGNLI + QPBB(NEND)
                                QPBB(NEND) = 0.0
C -----
C NOW TREAT THE DRIFT FUNCTION
C -----
C * FIRST CALCULATE THE REPULSION FORCE AMONG IONS
C -----
                                DO 4200, IQRII = NSTART, NEND
C
                                    RIPUSH = 0.0
                                    RIDRAW = 0.0
C
                                    IF (IQRII .EQ. NSTART) GOTO 4140
C
                                    DO 4120, IPUSH = NSTART, IQRII-1
                                        IRIDST = IQRII - IPUSH
                                        IRIDST = IRIDST * IRIDST
                                        RIPUSH = RIPUSH + DABS(QPBB(IPUSH))/FLOAT(IRIDST)
4120    CONTINUE
C
                                    IF (IQRII .EQ. NEND) GOTO 4180
C
4140    DO 4160, IDRAW = IQRII+1, NEND
                                        IRIDST = IDRAW - IQRII
                                        IRIDST = IRIDST * IRIDST
                                        RIDRAW = RIDRAW + DABS(QPBB(IDRAW))/FLOAT(IRIDST)
4160    CONTINUE
C
4180    QRII(IQRII) = (RIPUSH-RIDRAW) * RICNST
C
4200    CONTINUE
C -----
C * FIND THE MOST +/- DRIFT FACTOR DUE TO ION REPULSION
C -----
                                RILOW = 0.0
                                RIHIGH = 0.0
                                REPULS = 0.0

```

```

DO 4400, IQRII= NSTART, NEND
  IF (QRII(IQRII) .LT. RILOW) THEN
    RILOW = QRII(IQRII)
  ELSE IF (QRII(IQRII) .GT. RIHIGH) THEN
    RIHIGH = QRII(IQRII)
  ELSE
    END IF
    REPULS = REPULS + DABS(QRII(IQRII))
4400  CONTINUE
C -----
C * DETERMINE THE TYPE OF TIME PROPAGATION
C -----
      ZILOW = RILOW
      ZIHIGH = RIHIGH
      RILOW = RILOW + ALPHA
      RIHIGH = RIHIGH + ALPHA
  IF (RILOW .GE. 0.0) THEN
    IF (RIHIGH .LE. DRIFTH) THEN
      GOTO 5100
    ELSE
      GOTO 5200
    END IF
  ELSE
    IBKSTP = INT(DABS(RILOW)/DRIFTH) + 1
    RFORWD = FLOAT(IBKSTP)*DRIFTH
    IDRSTP = INT((RIHIGH+RFORWD)/DRIFTH) + 1
    RQRTIO = FLOAT(IBKSTP)/FLOAT(IDRSTP)
    IF (IDRSTP .LE. NQRIIA) THEN
      GOTO 5400
    ELSE
      GOTO 5500
    END IF
  END IF
C -----
C * RILOW > 0.0 AND RIHIGH < DRIFTH
C -----
5100  IDRFLG = 1
      DO 5120, IQRII = NSTART, NEND
        QRII(IQRII) = QRII(IQRII) + ALPHA
5120  CONTINUE
      QPXXSS = 0.0
      DO 5140, IQRII = NSTART, NEND
        DRCNTX = QRII(IQRII) + DRIFTH
        DRCNTA = (QRII(IQRII-1) - DRIFTH) * QPXX(IQRII-1)
        DRCNTB = (QRII(IQRII) - DRIFTH) * QPBB(IQRII)
        DRCNTC = (QRII(IQRII-1) + DRIFTH) * QPBB(IQRII-1)
        QPXX(IQRII) = (DRCNTA - DRCNTB + DRCNTC) / DRCNTX
        QPXXSS = QPXXSS + QPXX(IQRII)
5140  CONTINUE
      QPXXAJ = 1.0 - (TOTALS+SIGNLI+SIGNLE) * CWIDTH
      IF (QPXXAJ .LE. 1.0E-08) GOTO 6200
      QPXXSS = QPXXSS * CWIDTH / QPXXAJ
      DO 5160, IQRII = NSTART, NEND

```

```

      QPBB(IQR II) = QPXX(IQR II) / QPXXSS
5160  CONTINUE
      SIGNLE = SIGNLE + QPBB(NSTART)
      QPBB(NSTART) = 0.0
      SIGNLI = SIGNLI + QPBB(NEND)
      QPBB(NEND) = 0.0
      GOTO 5800
C -----
C * RILOW > 0.0 AND RIHIGH > DRIFTH
C -----
5200  IDRFLG = 2
      IDRSTP = INT(RIHIGH/DRIFTH) + 1
      DO 5220, IQR II = NSTART, NEND
      QRII(IQR II) = (QRII(IQR II)+ALPHA) / FLOAT(IDRSTP)
5220  CONTINUE
      DO 5280, IDRIFT = 1, IDRSTP
      QPXXSS = 0.0
      DO 5240, IQR II = NSTART, NEND
      DRCNTX = QRII(IQR II) + DRIFTH
      DRCNTA = (QRII(IQR II-1) - DRIFTH) * QPXX(IQR II-1)
      DRCNTB = (QRII(IQR II) - DRIFTH) * QPBB(IQR II)
      DRCNTC = (QRII(IQR II-1) + DRIFTH) * QPBB(IQR II-1)
      QPXX(IQR II) = (DRCNTA - DRCNTB + DRCNTC) / DRCNTX
      QPXXSS = QPXXSS + QPXX(IQR II)
5240  CONTINUE
      QPXXAJ = 1.0 - (TOTALS+SIGNLI+SIGNLE) * CWIDTH
      IF (QPXXAJ .LE. 1.0E-08) GOTO 6200
      QPXXSS = QPXXSS * CWIDTH / QPXXAJ
      DO 5260, IQR II = NSTART, NEND
      QPBB(IQR II) = QPXX(IQR II) / QPXXSS
5260  CONTINUE
      SIGNLE = SIGNLE + QPBB(NSTART)
      QPBB(NSTART) = 0.0
      SIGNLI = SIGNLI + QPBB(NEND)
      QPBB(NEND) = 0.0
5280  CONTINUE
      GOTO 5800
C -----
C * RILOW < 0.0 AND IDRSTP <= NQR IIA (=50)
C -----
5400  IDRFLG = 4
      RFORWD = FLOAT(IBKSTP)*DRIFTH + ALPHA
      KBKSTP = IBKSTP
      A1MODL = DRIFTH * RQRTIO
      A2MODL = A1MODL / CWIDTH
      A3MODL = 1.0 / TWIDTH
      AAMODL = (A2MODL-A3MODL) / (A2MODL+A3MODL)
C
      WARNF = 0.0
      DO 5410, IQR II = NSTART, NSTART+KBKSTP-1
      WARNF = WARNF + QPBB(IQR II)
5410  CONTINUE
      WARNA = 1.0E-06 / CWIDTH

```

```

        WARNB = WARNF * CWIDTH * 1.0E+06
        IF (WARNF. GE. WARNA) GOTO 9524
C
        DO 5420, IQR II = NSTART, NEND-KBKSTP
            KQR II = IQR II + KBKSTP
            QPBB(IQR II) = QPBB(KQR II)
            QR II(IQR II) = (QR II(KQR II)+RFORWD) / FLOAT(IDRSTP)
5420    CONTINUE
        DO 5422, IQR II = NEND-KBKSTP+1, NEND
            QPBB(IQR II) = 0.0
            QR II(IQR II) = DRIFTH
5422    CONTINUE
C
        DO 5480, IDRIFT = 1, IDRSTP
            QPXXSS = 0.0
            DO 5440, IQR II = NSTART, NEND
                DRCNTX = QR II(IQR II) + DRIFTH
                DRCNTA = (QR II(IQR II-1) - DRIFTH) * QPXX(IQR II-1)
                DRCNTB = (QR II(IQR II) - DRIFTH) * QPBB(IQR II)
                DRCNTC = (QR II(IQR II-1) + DRIFTH) * QPBB(IQR II-1)
                QPXX(IQR II) = (DRCNTA - DRCNTB + DRCNTC) / DRCNTX
                QPXXSS = QPXXSS + QPXX(IQR II)
5440    CONTINUE
            DO 5442, IQR II = NSTART, NEND
                QRXX(IQR II) = AAMODL * (QRXX(IQR II-1)-QR II(IQR II))
                    + QR II(IQR II-1)
C
5442    CONTINUE
                QPXXAJ = 1.0 - (TOTALS+SIGNLI+SIGNLE) * CWIDTH
                IF (QPXXAJ .LE. 1.0E-08) GOTO 6200
                QPXXSS = QPXXSS * CWIDTH / QPXXAJ
            DO 5460, IQR II = NSTART, NEND
                QPBB(IQR II) = QPXX(IQR II) / QPXXSS
                QR II(IQR II) = QRXX(IQR II)
5460    CONTINUE
                SIGNLE = SIGNLE + QPBB(NSTART)
                QPBB(NSTART) = 0.0
                SIGNLI = SIGNLI + QPBB(NEND)
                QPBB(NEND) = 0.0
5480    CONTINUE
                GOTO 5800
C -----
C * RILOW < 0.0 AND IDRSTP >= NQR IIA (=50), A REAL HEADACHE
C -----
5500    IDRFLG = 5
            IBKCLE = INT(IDRSTP/NQR IIA)
            RFORWD = FLOAT(IBKSTP)*DRIFTH + ALPHA
            A1MODL = DRIFTH * RQRTIO
            A2MODL = A1MODL / CWIDTH
            A3MODL = 1.0 / TWIDTH
            AAMODL = (A2MODL-A3MODL) / (A2MODL+A3MODL)
            RBKSTP = FLOAT(NQR IIA)*RQRTIO
            KBKSTP = INT(RBKSTP) + 1
            A6MODL = (FLOAT(KBKSTP)-RBKSTP) * DRIFTH

```

```

      A7MODL = A6MODL / CWIDTH
      A8MODL = 1.0 / TWIDTH
      ABMODL = (A7MODL-A8MODL) / (A7MODL+A8MODL)
      KDRSTP = IDRSTP - NQRIIA * IBKCLE
C
      DO 5505, IQR II = NSTART, NEND
        QR II(IQR II) = (QR II(IQR II)+RFORWD) / FLOAT(IDRSTP)
5505  CONTINUE
C
      DO 5590, IIBKCL = 1, IBKCLE
C
      WARNF = 0.0
      DO 5510, IQR II = NSTART, NSTART+KBKSTP-1
        WARNF = WARNF + QPBB(IQR II)
5510  CONTINUE
      WARNA = 1.0E-06 / CWIDTH
      WARNB = WARNF * CWIDTH * 1.0E+06
      IF (WARNF. GE. WARNA) GOTO 9524
C
      DO 5520, IQR II = NSTART, NEND-KBKSTP
        KQR II = IQR II + KBKSTP
        QPBB(IQR II) = QPBB(KQR II)
        QR II(IQR II) = QR II(KQR II)
5520  CONTINUE
      DO 5522, IQR II = NEND-KBKSTP+1, NEND
        QPBB(IQR II) = 0.0
        QR II(IQR II) = DRIFTH
5522  CONTINUE
C
      DO 5530, IQR II = NSTART, NEND
        QPXX(IQR II) = ABMODL * (QPXX(IQR II-1)-QPBB(IQR II))
        + QPBB(IQR II-1)
        QRXX(IQR II) = ABMODL * (QRXX(IQR II-1)-QR II(IQR II))
        + QR II(IQR II-1)
C
5530  CONTINUE
      DO 5532, IQR II = NSTART, NEND
        QPBB(IQR II) = QPXX(IQR II)
        QR II(IQR II) = QRXX(IQR II)
5532  CONTINUE
C
      DO 5580, IDRIFT = 1, NQRIIA
        QPXXSS = 0.0
      DO 5540, IQR II = NSTART, NEND
        DRCNTX = QR II(IQR II) + DRIFTH
        DRCNTA = (QR II(IQR II-1) - DRIFTH) * QPXX(IQR II-1)
        DRCNTB = (QR II(IQR II) - DRIFTH) * QPBB(IQR II)
        DRCNTC = (QR II(IQR II-1) + DRIFTH) * QPBB(IQR II-1)
        QPXX(IQR II) = (DRCNTA - DRCNTB + DRCNTC) / DRCNTX
        QPXXSS = QPXXSS + QPXX(IQR II)
5540  CONTINUE
      DO 5542, IQR II = NSTART, NEND
        QRXX(IQR II) = AAMODL * (QRXX(IQR II-1)-QR II(IQR II))
        + QR II(IQR II-1)
C

```



```

5542     CONTINUE
          QPXXAJ = 1.0 - (TOTALS+SIGNLI+SIGNLE) * CWIDTH
          IF (QPXXAJ .LE. 1.0E-08) GOTO 6200
          QPXXSS = QPXXSS * CWIDTH / QPXXAJ
          DO 5560, IQR II = NSTART, NEND
            QPBB(IQR II) = QPXX(IQR II) / QPXXSS
            QR II(IQR II) = QRXX(IQR II)
5560     CONTINUE
          SIGNLE = SIGNLE + QPBB(NSTART)
          QPBB(NSTART) = 0.0
          SIGNLI = SIGNLI + QPBB(NEND)
          QPBB(NEND) = 0.0
5580     CONTINUE
C
5590     CONTINUE
C
C
          RBKSTP = FLOAT(KDRSTP)*RQRTIO
          KBKSTP = INT(RBKSTP) + 1
          A6MODL = (FLOAT(KBKSTP)-RBKSTP) * DRIFTH
          A7MODL = A6MODL / CWIDTH
          A8MODL = 1.0 / TWIDTH
          ABMODL = (A7MODL-A8MODL) / (A7MODL+A8MODL)
          IDRSTP = KDRSTP
C
          WARNF = 0.0
          DO 5610, IQR II = NSTART, NSTART+KBKSTP-1
            WARNF = WARNF + QPBB(IQR II)
5610     CONTINUE
          WARNA = 1.0E-06 / CWIDTH
          WARNB = WARNF * CWIDTH * 1.0E+06
          IF (WARNF. GE. WARNA) GOTO 9524
C
          DO 5620, IQR II = NSTART, NEND-KBKSTP
            KQR II = IQR II + KBKSTP
            QPBB(IQR II) = QPBB(KQR II)
            QR II(IQR II) = QR II(KQR II)
5620     CONTINUE
          DO 5622, IQR II = NEND-KBKSTP+1, NEND
            QPBB(IQR II) = 0.0
            QR II(IQR II) = DRIFTH
5622     CONTINUE
C
          DO 5630, IQR II = NSTART, NEND
            QRXX(IQR II) = ABMODL * (QRXX(IQR II-1)-QR II(IQR II))
            + QR II(IQR II-1)
C
            QPXX(IQR II) = ABMODL * (QPXX(IQR II-1)-QPBB(IQR II))
            + QPBB(IQR II-1)
C
5630     CONTINUE
          DO 5632, IQR II = NSTART, NEND
            QPBB(IQR II) = QPXX(IQR II)
            QR II(IQR II) = QRXX(IQR II)
5632     CONTINUE

```

```

C
DO 5680, IDRIFT = 1, IDRSTP
    QPXXSS = 0.0
    DO 5640, IQR II = NSTART, NEND
        DRCNTX = QR II(IQR II) + DRIFTH
        DRCNTA = (QR II(IQR II-1) - DRIFTH) * QPXX(IQR II-1)
        DRCNTB = (QR II(IQR II) - DRIFTH) * QPBB(IQR II)
        DRCNTC = (QR II(IQR II-1) + DRIFTH) * QPBB(IQR II-1)
        QPXX(IQR II) = (DRCNTA - DRCNTB + DRCNTC) / DRCNTX
        QPXXSS = QPXXSS + QPXX(IQR II)
5640    CONTINUE
        DO 5642, IQR II = NSTART, NEND
            QRXX(IQR II) = AAMODL * (QRXX(IQR II-1) - QR II(IQR II))
            + QR II(IQR II-1)
C
5642    CONTINUE
            QPXXAJ = 1.0 - (TOTALS+SIGNLI+SIGNLE) * CWIDTH
            IF (QPXXAJ .LE. 1.0E-08) GOTO 6200
            QPXXSS = QPXXSS * CWIDTH / QPXXAJ
            DO 5660, IQR II = NSTART, NEND
                QPBB(IQR II) = QPXX(IQR II) / QPXXSS
                QR II(IQR II) = QRXX(IQR II)
5660    CONTINUE
                SIGNLE = SIGNLE + QPBB(NSTART)
                QPBB(NSTART) = 0.0
                SIGNLI = SIGNLI + QPBB(NEND)
                QPBB(NEND) = 0.0
5680    CONTINUE
            GOTO 5800
C -----
C * REPORT THE ION SIGNAL (SIGNLI) AND JUNK SIGNAL (SIGNLE)
C -----
5800    CONTINUE
            IF (SIGNLI .LT. 0.0) GOTO 5802
            TOTALI = TOTALI + SIGNLI
5802    IF (SIGNLE .LT. 0.0) GOTO 5804
            TOTALE = TOTALE + SIGNLE
5804    TOTALS = TOTALI + TOTALE
            TIME = FLOAT(J) * TWIDTH * (1.0E+06)
            SIGNLI = -SIGNLI * FLOAT(NTSTEP) / (TRANGE*1.0E+06)
            SIGNLE = -SIGNLE * FLOAT(NTSTEP) / (TRANGE*1.0E+06)
            IF (IJUMP .EQ. NJUMP) THEN
                WRITE (2, 5840) TIME, SIGNLI, SIGNLE
5840    FORMAT ('RD', 3G15.6)
                IJUMP = 0
            ELSE
                IJUMP = IJUMP + 1
            END IF
            WRITE (9, 5842) TIME, SIGNLI, TOTALS*CWIDTH,
C
5842    FORMAT (' ', F10.6, 2G15.6, I2, 3G10.2)
            IF (TOTALS*CWIDTH .GE. 1.00) GOTO 6200
C -----
C THE TIME PROPAGATION CYCLE ENDS HERE

```

```
C ----- END DO 6000 -----
6000  CONTINUE
C -----
C REPORT THE TOTAL SIGNAL FOR REFERENCE
C -----
6200      TOTALI = TOTALI * CWIDTH
          TOTALE = TOTALE * CWIDTH
          TOTALS = TOTALS * CWIDTH
          WRITE (9, 6210) TOTALI, TOTALE, TOTALS
6210      FORMAT (' TOTALI = ', F10.6, ' TOTALE = ', F10.6,
C          ' TOTALS = ', F10.6)
C -----
C NOW WRITE OUT THE RESULT, HOPEFULLY THEY WILL MAKE SOME SENSE
C -----
          ERROR1 = 0.0
          ERROR2 = 0.0
          DO 8200, I = NBLANK+1, NEND
              QSIM = CWIDTH * FLOAT(I-NORIGN)
              CEQQ = CEQU(I) - QPXX(I)
              ERRA = CEQQ * CEQQ
              ERROR1 = ERROR1 + ERRA
              IF (I .EQ. NORIGN) GOTO 8100
              ERRB = ERRA / (QSIM*QSIM)
              ERROR2 = ERROR2 + ERRB
8100      WRITE (1, 8120) QSIM, CEQU(I), QPXX(I), CEQQ
8120      FORMAT ('RD', 4G15.6)
8200      CONTINUE
C -----
          EROOT = FLOAT( NNDIMEN - 2 * NBLANK - 1 )
          ERROR1 = DSQRT(ERROR1/EROOT)
          ERROR2 = DSQRT(ERROR2/(EROOT-1.0))
          WRITE (TI, 8220) ERROR1, ERROR2
8220      FORMAT (2X, 'ERROR1 = ', G15.6, 'ERROR2 = ', G15.6)
C -----
C ERROR MESSAGES
C -----
          GOTO 9900
9524      WRITE (TI, 9526) IDRFLG, WARNB
9526      FORMAT (' IDRFLG = ', I2, ' WARNF = ', G15.6)
          STOP 'MORE THAN 1 ppm SIGNAL LOST DUE TO IBKSTP.'
C -----
9900      STOP 'CONGRATULATION, YOU GET BY. DUMMY'
          END
```

APPENDIX D

APPLICATIONS OF THE FOKKER-PLANCK EQUATION TO HPLC DATA

I. INTRODUCTION

This appendix demonstrates the applications of the exponentially modified Fokker-Planck flux equation to the HPLC data.

A chromatographic column is normally assumed to act as a Gaussian operator. The input is commonly referred to as a Dirac delta function, which is broadened into a Gaussian distribution when passing through the column (1). However, pure Gaussian peaks are not found experimentally. This is because noncolumn factors such as dead volume, detector time-constants, and injection profile convolute the Gaussian distribution (2). Schmauch (3), as well as Johnson and Stross (4), have shown that detector dead-volume will exponentially modify a chromatographic peak. The exponentially modified Gaussian function (EMG) hence is utilized to describe the chromatographic peaks:

$$f(t) = \frac{A}{\tau \sigma (2\pi)^{1/2}} \int_0^{\infty} \exp\left(-\frac{(t-t_r-\xi)^2}{2\sigma^2}\right) \exp\left(-\frac{\xi}{\tau}\right) d\xi \quad [1]$$

where A is the peak amplitude, t_r is the center of gravity of the Gaussian component, σ is the standard deviation of the Gaussian, τ is the time constant of the exponential decay, and ξ is the dummy variable of integration. Equation [1] can be alternatively written as follows:

$$f(t) = \frac{A\sigma}{\tau(2)^{1/2}} \exp\left(\frac{1}{2} \left(\frac{\sigma}{\tau}\right)^2 - \frac{(t-t_r)}{\tau}\right) \int_{-\infty}^z \exp(-\xi^2) d\xi \quad [2]$$

where:

$$z = \left(\frac{t-t_r}{\sigma-\sigma/\tau}\right) \left(\frac{1}{(2)^{1/2}}\right) \quad [3]$$

Equation [1], in fact, is the exponentially modified form of the Fokker-Planck propagator (cm^{-1}) with a linear drift function. However, the chromatographic signal is actually a flux function (sec^{-1}) rather than a propagator. Hence the following exponentially modified Fokker-Planck flux function is proposed as a model in the least-square fitting of the chromatographic signals.

$$P(q_f, t) = \int_0^{\infty} \frac{(q_f + \alpha(t-\xi))}{4(\pi D)^{1/2} (t-\xi)^{3/2}} \exp\left(-\frac{(q_f - \alpha(t-\xi))^2}{4D(t-\xi)}\right) \exp\left(-\frac{\xi}{\tau}\right) d\xi \quad [4]$$

where $P(q_f, t)$ is the chromatographic signal, q_f is the column length, α is the moving speed of the analyte, D is the pseudo diffusion coefficient due to retention, t_f is the retention time of the analyte, ξ is a dummy variable for the integration, and τ is the time constant of the convoluted exponential decay. Equation [4] is normalized and has units of sec^{-1} .

II. EXPERIMENTAL

Six HPLC data sets were obtained under various flow rates ranging from 0.5 ml/min to 1.6 ml/min. The specific system was made up of a mobile phase that contained 50% methanol (MeOH) and 50% H_2O . The sample was 0.001 molality phenol (aq) with a volume of 20 microliter. An ODS (C_{18}) column was employed at 25°C .

III. RESULTS AND DISCUSSION

Both equation [1] and equation [4] were used to least-square fit the HPLC data. For computer programming, equation [1] was modified as follows:

$$f(x) = A \left(\frac{1}{2\tau} \right) \exp \left(-\frac{\sigma^2}{2\tau^2} - \frac{t-t_r}{\tau} \right) \left(1 + \operatorname{erf} \left(-\frac{1}{(2)^{1/2}} \left(\frac{t-t_r}{\sigma} - \frac{\sigma}{\tau} \right) \right) \right) + B \quad [5]$$

where B is the signal baseline.

The FORTRAN programs of both equation [4] and [5] are listed in section V.

Through the curve fitting study, it has been found that generally the exponentially modified Fokker-Planck flux function gives better fitting results with smaller average square deviation and thus describe the shape of the liquid chromatographic signal more closely.

Figure D-1 shows the relationship between the moving speed of analyte α and flow rate. The linear relationship indicates that the retention time of the analyte can be predicted by equation [4] rather accurately. Figure D-2 shows the relationship between the pseudo diffusion constant and the flow rate. The linear relationship indicates that the partition coefficient of the analyte in the C_{18} column can be calculated and utilized to predict the shape of the chromatographic signal.

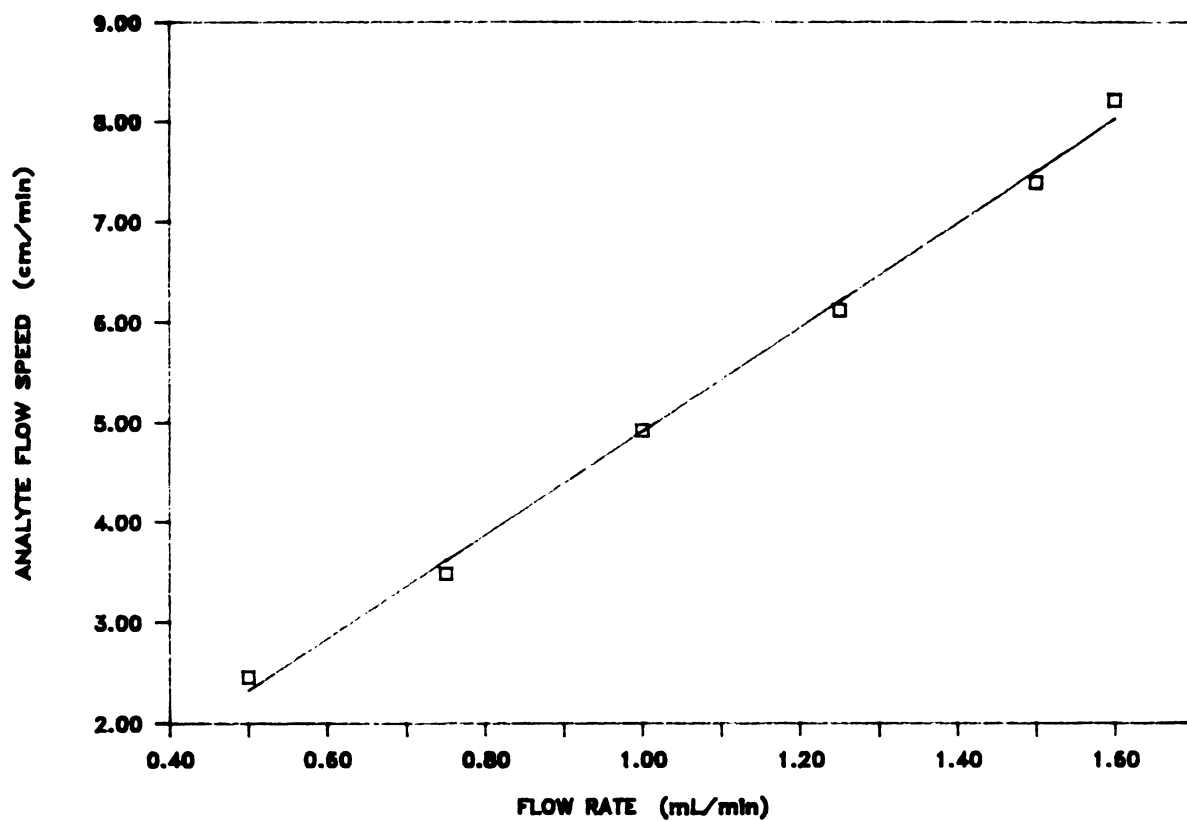


Figure D-1. Analyte flow speed versus flow rate plot.

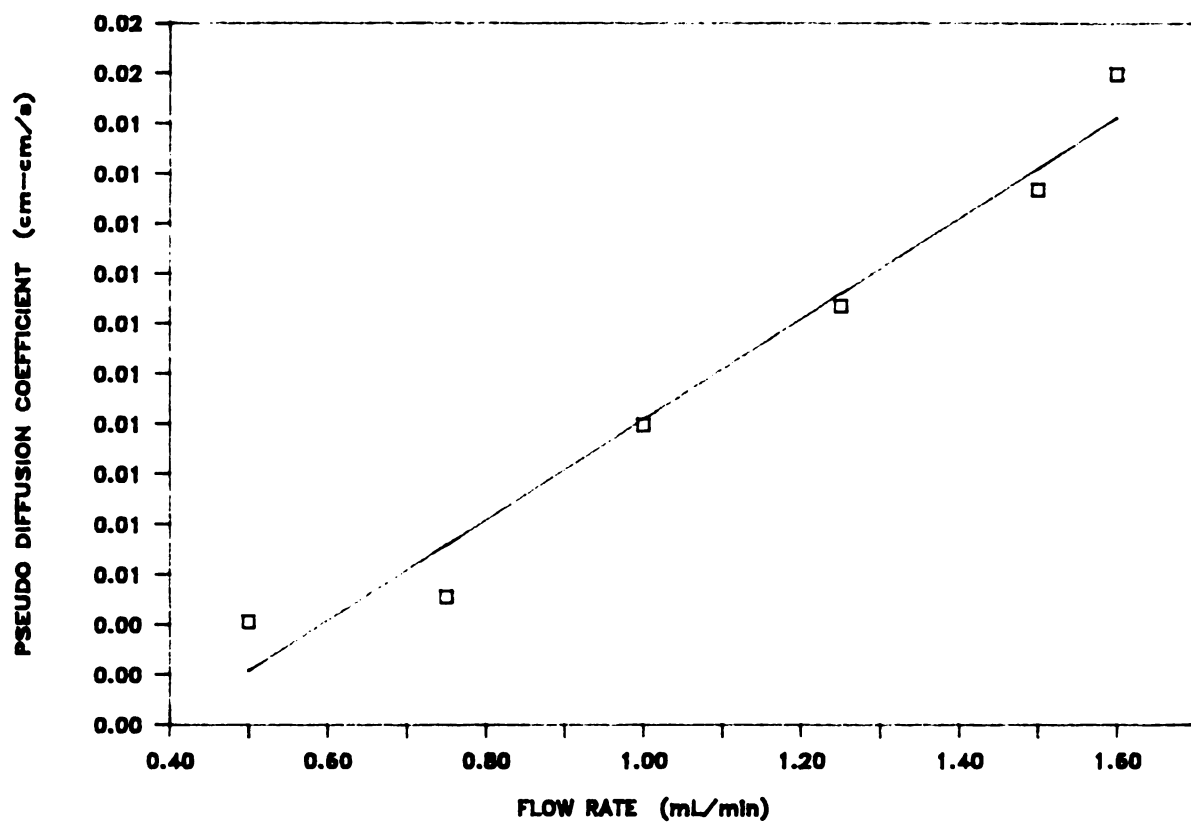


Figure D-2. Pseudo diffusion coefficient versus flow rate plot.

IV. REFERENCES

1. J.P. Foley and J.G. Dorsey, J. Chromatog. Sci. 22, 40 (1984).
2. R.E. Pauls and L.B. Rogers, Anal. Chem. 49, 625 (1977).
3. L.J. Schmauch, Anal. Chem. 31, 225 (1959).
4. H.W. Johnson and F.H. Stross, Anal. Chem. 31, 357 (1959).

V. FORTTRAN LISTING

```

      SUBROUTINE FCN(M,N,PAR,FVEC,IFLAG)
C   FIRST CARD OF FXFPT.FOR. (SUBROUTINE FCN FOR DIFPT.FOR).
C   =====
C   THIS PROGRAM IS MODIFIED FROM FXFPT.FOR
C   1. Only the definition of CNST is changed.
C   =====
C   THIS SUBROUTINE WILL CALCULATE THE NEW EMG FUNCTION VALUE
C   CALLED BY DIFPT.FOR (LMDIF).
C   CASE FP-EM-T
C   =====
      IMPLICIT REAL*8 (A-H,O-Z)
      IMPLICIT INTEGER*4 (I-N)
C   THE LMDIF PART
      INTEGER*4 M,N,IFLAG
      REAL*8 PAR(N),FVEC(M)
C   THE DVERK PART
      INTEGER*4 NEQ, IND, NW, IER
      REAL*8 X, Y(2), XEND, TOL, C(24), W(2,9)
      REAL*8 TOLDVR
C   FOR THIS ROUTINE
      INTEGER*4 MFLAG
      REAL*8 CORE, SQT, BLP, BUP, PROP
C   COMMON BLOCK
      REAL*8 RATIO1, BASLN2, ALPHA3, D4, TAO5
      REAL*8 QF, TIME, CNST
      REAL*8 TT(300), YY(300)
      COMMON /MAIN/ RATIO1, BASLN2, ALPHA3, D4, TAO5,
+           QF, TIME, CNST
      COMMON /DATA/ TT, YY
      EXTERNAL EQFPT
C   -----
      IF (MFLAG .EQ. 89) GOTO 11
C   CONSTANTS FOR DVERK
      NW   = 2
      NEQ  = 2
      TOL  = 0.10E-08
      PI   = 3.141592653589793238462643
      Y(2) = 0.00
      MFLAG = 89
C
      11  IF (IFLAG .EQ. 97) GO TO 217
          IF (IFLAG .NE. 0) GO TO 105
C   INSERT PRINT STATEMENTS HERE WHEN NPRINT IS POSITIVE.
      RETURN
C
      105  CONTINUE
          RATIO1 = ABS(PAR(1))
          BASLN2 = ABS(PAR(2))

```

```

      ALPHA3 = ABS(PAR(3))
      D4      = ABS(PAR(4))
      TAO5    = ABS(PAR(5))
C
      WRITE (6,109) PAR(1), PAR(2), PAR(3), PAR(4), PAR(5)
      WRITE (1,109) PAR(1), PAR(2), PAR(3), PAR(4), PAR(5)
109  FORMAT (' ', 5G15.6)
C
      CORE = QF + 175.0*D4/ALPHA3
      SQT  = SQRT(CORE*CORE - QF*QF)
      BUP  = (CORE+SQT) / ALPHA3
      BLP  = (CORE-SQT) / ALPHA3
C - NEW - - - - -
      CNST  = 1.0 / (4.0 * DSQRT(PI))
C - NEW - - - - -
      DO 198 I = 1, M
        TIME = TT(I)
        IF ((TIME.LE.BLP) .OR. (TIME.GE.BUP)) GOTO 170
C - OLD - - - - -
C      CNST1 = DEXP(-TIME/TAO5)
C      CNST2 = 2.0 * TAO5 * (1.0-CNST1) * ALPHA3 * DSQRT(PI)
C      CNST  = 1.0 / CNST2
C - OLD - - - - -
      XEND = TIME - BLP
      X     = 0.00
      Y(1) = 0.00
      IND = 1
      CALL DVERK(NEQ,EQFPT,X,Y,XEND,TOL,IND,C,NW,W,IER)
      IF (IND.LT.0 .OR. IER.GT.0) GO TO 999
      PROP = Y(1) + BASLN2
      GOTO 180
170  PROP = BASLN2
180  FVEC(I) = YY(I) - PROP
198  CONTINUE
      RETURN
C -----
C CALCULATE ERROR SURFACE
C -----
217  CONTINUE
      RATIO1 = ABS(PAR(1))
      BASLN2 = ABS(PAR(2))
      ALPHA3 = ABS(PAR(3))
      D4      = ABS(PAR(4))
      TAO5    = ABS(PAR(5))
C
      CORE = QF + 175.0*D4/ALPHA3
      SQT  = SQRT(CORE*CORE - QF*QF)
      BUP  = (CORE+SQT) / ALPHA3
      BLP  = (CORE-SQT) / ALPHA3
C - NEW - - - - -
      CNST  = 1.0 / (4.0 * DSQRT(PI))
C - NEW - - - - -
      DO 298, I = 1, M

```

```

      TIME = TT(I)

      IF ((TIME.GE.BUP) .OR. (TIME.LE.BLP)) GOTO 270
C - OLD - - - - -
C      CNST1 = DEXP(-TIME/TAO5)
C      CNST2 = 2.0 * TAO5 * (1.0-CNST1) * ALPHA3 * DSQRT(PI)
C      CNST  = 1.0 / CNST2
C - OLD - - - - -
      XEND = TIME - BLP
      X     = 0.00
      Y(1) = 0.00
      IND = 1
      CALL DVERK(NEQ,EQFPT,X,Y,XEND,TOL,IND,C,NW,W,IER)
      IF (IND.LT.0 .OR. IER.GT.0) GO TO 999
      PROP = Y(1) + BASLN2
      GOTO 280
270     PROP = BASLN2
280     FVEC(I) = PROP
298     CONTINUE
      RETURN
C
C GOD BLESS YOU.....
C OTHERWISE YOU WILL HAVE TO USE THIS STUPID PART REALLY OFTEN
999     CONTINUE
      WRITE (6, 1000) IND, IER
1000    FORMAT (' IND= ', I3, ' IER= ', I4)
      TYPE*, ' '
      STOP ' FPLIEQAI1.FOR, I HOPE YOU CAN FIGURE WHAT HAPPENS.'
C
C LAST CARD OF FXFPT.FOR. (SUBROUTINE FCN FOR DIFPT.FOR).
C =====
      END
SUBROUTINE FCN(M,N,PAR,FVEC,IFLAG)
C FIRST CARD OF FXEMG.FOR. (SUBROUTINE FCN FOR DIEMG.FOR).
C =====
C THIS PROGRAM IS MODIFIED FROM FXFPQ.FOR
C =====
C THIS SUBROUTINE WILL CALCULATE THE EMG FUNCTION VALUE
C CALLED BY DIEMG.FOR (LMDIF).
C CASE EMG
C =====
C CORRESPONDING CHART:
C      RATIO1 = ABS(PAR(1))
C      BASLN2 = ABS(PAR(2))
C      SIGMA3 = ABS(PAR(3))
C      TAO4   = ABS(PAR(4))
C      TG5    = ABS(PAR(5))
C =====
      IMPLICIT REAL*8 (A-H,O-Z)
      IMPLICIT INTEGER*4 (I-N)
C THE LMDIF PART
      INTEGER*4 M,N,IFLAG
      REAL*8 PAR(N),FVEC(M)

```

```

C FOR THIS ROUTINE
      REAL*8 RATIO1, BASLN2, SIGMA3, TAO4, TG5

      REAL*8 PI, TIME, DERF
      REAL*8 PROP
C COMMON BLOCK
      REAL*8 TT(300), YY(300)
      COMMON /DATA/ TT, YY
C -----
      PI      = 3.141592653589793238462643
      RATIO1 = ABS(PAR(1))
      BASLN2 = ABS(PAR(2))
      SIGMA3 = ABS(PAR(3))
      TAO4   = ABS(PAR(4))
      TG5    = ABS(PAR(5))

C
      A1      = SIGMA3 / TAO4
      A2      = 0.5 * A1 * A1
      PART1   = 0.5 / TAO4

C
      11  IF (IFLAG .EQ. 97) GO TO 217
          IF (IFLAG .NE. 0) GO TO 105
C INSERT PRINT STATEMENTS HERE WHEN NPRINT IS POSITIVE.
      RETURN

C
      105  CONTINUE

C
      WRITE (6,109) PAR(1), PAR(2), PAR(3), PAR(4), PAR(5)
      WRITE (1,109) PAR(1), PAR(2), PAR(3), PAR(4), PAR(5)
      109  FORMAT (' ', 5G15.6)

C
      DO 198 I = 1, M
          TIME = TT(I)
          EZ = ( (TIME-TG5)/SIGMA3 - SIGMA3/TAO4 ) / -SQRT(2.0)
          IF (EZ.LT.0.0) GOTO 125
          PART3 = 1.0 - DERF(EZ)
          GOTO 127
      125  PART3 = 1.0 + DERF(-EZ)
      127  AA = (TIME-TG5) / TAO4
          PART2 = EXP( A2-AA )
          PROP = RATIO1 * PART1 * PART2 * PART3 + BASLN2
      180  FVEC(I) = YY(I) - PROP
      198  CONTINUE
          RETURN
C -----
C CALCULATE ERROR SURFACE
C -----
      217  CONTINUE

C
      DO 298 I = 1, M
          TIME = TT(I)
          EZ = ( (TIME-TG5)/SIGMA3 - SIGMA3/TAO4 ) / -SQRT(2.0)
          IF (EZ.LT.0.0) GOTO 225

```

```

      PART3 = 1.0 - DERF(EZ)
      GOTO 227
225    PART3 = 1.0 + DERF(-EZ)

227    AA = (TIME-TG5) / TAO4
      PART2 = EXP( A2-AA )
      PROP = RATIO1 * PART1 * PART2 * PART3 + BASLN2
      FVEC(I) = PROP
298    CONTINUE
      RETURN
C
C GOD BLESS YOU.....
C OTHERWISE YOU WILL HAVE TO USE THIS STUPID PART REALLY OFTEN
999    CONTINUE
      WRITE (6, 1000) IND, IER
1000   FORMAT (' IND= ', I3, ' IER= ', I4)
      TYPE*, ' '
      STOP ' FXEMG.FOR, I HOPE YOU CAN FIGURE WHAT HAPPENS.'
C
C LAST CARD OF FXEMG.FOR. (SUBROUTINE FCN FOR DIFPQ.FOR).
C =====
      END
```